UNIVERSITÀ DEGLI STUDI DI MILANO

Scuola di Dottorato in Fisica, Astrofisica e Fisica Applicata
Dipartimento di Fisica

Corso di Dottorato in Fisica, Astrofisica e Fisica Applicata
Ciclo XXV

Energy calibration and observation of the Higgs boson in the diphoton decay with the ATLAS experiment

Settore Scientifico Disciplinare FIS/04, FIS/01

Supervisori: Dott. Marcello FANTI
Dott.ssa Chiara MERONI

Coordinatore: Professor Marco BERSANELLI

Tesi di Dottorato di:

Ruggero TURRA

Anno Accademico 2011/12

Commission of the final examination:

External Referee:
Prof. Daniel Fournier (Laboratoire de l'Accélérateur Linéaire, IN2P3-CNRS, Orsay, France)

External Members:
Prof. Edoardo Gorini (Università del Salento),
Prof. Tommaso Tabarelli de Fatis (Università degli Studi di Milano-Bicocca)

Internal Member:
Prof.ssa Laura Perini (Università degli Studi di Milano)

Final examination:

February 18, 2013

Università degli Studi di Milano, Dipartimento di Fisica, Milano, Italy

Cover illustration:

Event display of a diphoton with two jets event candidate where both photon candidates are converted. The event number is 24 947 130 and it was recorded during run 204 769 at $\sqrt{s} = 8\,\text{TeV}$. The leading photon has $E_T = 80.1\,\text{GeV}$ and $\eta = 1.01$. The subleading photon has $E_T = 36.2\,\text{GeV}$ and $\eta = -0.17$. The measured diphoton mass is 126.9 GeV. The p_T and p_{Tt} of the diphoton are 44.3 GeV and 6.2 GeV, respectively. The leading jet has $E_T = 120\,\text{GeV}$ and $\eta = -2.9$. The subleading jet has $E_T = 81\,\text{GeV}$ and $\eta = 2.7$. The measured two-jets mass is 1.6 TeV. The $\Delta\phi$ between the diphoton system and the system of the two-jets is 2.9.

MIUR subjects:

FIS/01
FIS/04

PACS:

29.40.Vj
14.80.Bn

Contents

Introduction

In the last three years, during my PhD, I have worked in the ATLAS collaboration focusing on photon physics. ATLAS is one of the four main experiments at the LHC proton-proton accelerator at CERN. I joined the collaboration in 2010 when LHC started to provide collisions at 7 TeV centre of mass energy. Up to now, ATLAS has collected a huge amount of data and in the last year the energy has been raised to 8 TeV. The analyses I have contributed to were driven by the amount of collected luminosity. My first analysis was the measurement of the inclusive isolated prompt photon cross section [1–3] and then with more statistics I moved to the measurement of the isolated diphoton cross section [4]. In 2011 I started to work on the search of the Higgs boson in the diphoton channel [5–12]. In parallel I have studied many topics about the performance of electrons and photons. In particular I worked on the energy calibration, reimplementing the standard method previously developed in Milan, and introducing corrections on top of it. I also developed a different multivariate calibration. Other performance studies I made are: the effect of the material before the calorimeter on the calibration, on the reconstruction and on the identification efficiency; the purity of selected photons using various methods; the photon pointing method using a likelihood and part of the systematic effects on the Higgs mass measurement related with the energy calibration.

This thesis describes two correlated topics: the observation for the Higgs boson in the diphoton channel and the Monte Carlo calibration of electrons and photons. The Higgs boson is a particle predicted by the Standard Model (SM) to explain the mechanism for electroweak symmetry breaking, giving masses to the particles. This theory was developed in the ’60s and a particle compatible with the SM Higgs boson has been discovered by the ATLAS and CMS experiments in 2012. If this new boson is the Higgs boson, all fundamental parameters of the SM are known and, for the first time, it is possible to overconstrain the SM at the electroweak scale and to evaluate its validity.

This thesis is organized as follows: chapter 1 introduces the theory of the SM and the Higgs mechanism, the theoretical and experimental constraints before LHC and an overview of the searches of the Higgs boson at LHC. Chapter 2 and chapter 3 describe the LHC accelerator and the ATLAS experiment, focusing on the photon reconstruction. My work on the energy calibration of electrons and photons with the default technique used in ATLAS is described in chapter 4, while the new technique I have recently developed is presented in chapter 5. Chapter 6 summarizes the results presented by the ATLAS collaboration on the search of the Higgs boson in December 2012, during the Council conference. In this chapter I describe in detail the topics where I gave substantial contribution: the pointing, the background decomposition and the effect of the multivariate calibration described in chapter 5 on the Higgs mass reconstruction.

CHAPTER 1

The Standard Model and the Higgs boson

A coherent description of the electroweak and strong phenomena was achieved with the development of the Standard Model (SM) of particle physics [13–16]. It has been tested by many experiments over the last four decades and has been shown to successfully describe high energy particle interactions. It combines the well established electroweak theory of Glashow, Weinberg and Salam with Quantum Chromodynamics (QCD), the fundamental theory of strong interactions. The SM offers an elegant theoretical framework for the characterization of these interactions at the quantum level: it is perturbative at sufficiently high energies and renormalizable due to its gauge invariant formulation.

The SM Lagrangian cannot accommodate explicit mass terms, without spoiling the electroweak gauge invariance. The Higgs boson is the particle that could explain the mechanism for electroweak symmetry breaking giving masses to the particles.

This chapter gives a very brief overview of the Standard Model and its key ingredients with some attention to the mechanism which predicts the existence of the Higgs particle. These topics are the objects of sections 1.1, 1.2 and 1.3. The state of the art in Higgs searches is reviewed in section 1.4 while a summary of the various Higgs decay channels studied at hadron colliders are part of sections 1.5 and in particular at LHC in 1.6. Finally, extensions and alternatives to the Standard Model are briefly mentioned in section 1.7.

The Higgs search in the diphoton final state is discussed in chapter 6 after the introduction of some theoretical background in the present one. A complete treatment of these subjects is given in refs. [17–20].

1.1 Electromagnetic, strong and weak interactions

According to SM, the main elementary constituents of matter are point-like spin-$\frac{1}{2}$ particles called fermions. Their dynamics is governed by a relativistic quantum theory. The associated field, represented by the four-component spinor $\psi(x)$, obeys the Dirac equation:

$$\left(i\gamma^{\mu}\partial_{\mu} - m\right)\psi(x) = 0 \tag{1.1}$$

where each ψ component is a function of the space-time coordinates x; γ^{μ} are Dirac matrices and m is the fermion mass. In the Lagrangian formalism, this equation of motion can be derived from the Lagrangian:

$$\mathscr{L}_0 = i\bar{\psi}\gamma^{\mu}\partial_{\mu}\psi - m\bar{\psi}\psi \tag{1.2}$$

where $\bar{\psi} = \psi^{\dagger}\gamma_0$ is the adjoint of ψ. In the context of quantum field theory, ψ represents the fermionic field. After quantization, this field can create and annihilate particles of matter and anti-matter (fermions and anti-fermions).

The formulation above is restricted to a free or non-interacting field theory. Interactions are typically introduced invoking the 'gauge principle'. It states that the underlying physics should be invariant under local phase transformations of the fields ($U(1)$ transformation). A redefinition of the field of the form $\psi \to \psi' \equiv e^{i\theta(x)}\,\psi(x)$, where $\theta(x)$ is an arbitrary function, should not alter the Lagrangian by more than a total derivative of a function of the coordinates. This is not the case of equation (1.2), since:

$$\partial_\mu \psi(x) \to \partial_\mu \psi'(x) = e^{i\theta(x)}\,\left[\partial_\mu + i\partial_\mu\theta(x)\right]\psi(x) \tag{1.3}$$

The invariance can be restored with the addition of a spin-1 field $A_\mu(x)$, which transforms as $A_\mu(x) \to A'_\mu(x) \equiv A_\mu(x) - \frac{1}{Q}\partial_\mu\theta$, where Q is a constant, under the same $U(1)$ symmetry. Its transformation law allows the cancellation of the last term on the right-hand side of eq. (1.3). If one now replaces the ordinary derivative by the covariant derivative:

$$D_\mu(x)\psi(x) \equiv \left[\partial_\mu + iQA_\mu(x)\right]\,\psi(x) \tag{1.4}$$

the resulting Lagrangian is invariant under $U(1)$:

$$\mathscr{L} = i\bar{\psi}\gamma^\mu D_\mu\psi - m\bar{\psi}\psi \;= \mathscr{L}_0 - QA_\mu\bar{\psi}\gamma^\mu\psi \tag{1.5}$$

The gauge principle has generated the second term of eq. (1.5), which couples the fermion with the vector field A_μ. The dynamics of the latter is governed by the Maxwell's equations if the kinetic term $-\frac{1}{4}F^{\mu\nu}F_{\mu\nu}$ is added to the Lagrangian, with $F^{\mu\nu} = \partial^\mu A^\nu - \partial^\nu A^\mu$. The strength of the interaction is proportional to Q, which can be interpreted as the charge of the electron. The quantization of this Lagrangian leads to the theory of Quantum Electrodynamics (QED), which is in excellent agreement with experimental data. The fields are identified with the electron and a gauge boson – the photon. The photon is massless, and a mass term of the form $M^2A_\mu A^\mu$ is forbidden in order to preserve gauge invariance.

Quantum Chromodynamics (QCD)

QCD, the theory of strong interactions, explains the existence of a multitude of particles classified as *mesons* and *baryons* – such as pions and protons – by combinations of elementary fermions called *quarks*. Quarks are electrically charged and also carry a new quantum number, colour charge. There are three colours (conventionally noted as red, green and blue) such that the baryons and mesons are colour-singlet combinations of qqq or $q\bar{q}$, respectively.

The interactions among the quarks are derived invoking the gauge principle for a $SU(3)$ symmetry. We notice that there are six different quark flavours, which will be labelled by the subscript f. Starting with the free Lagrangian for a quark triplet of a given flavour, $q_f^t = (q_f^{red}\; q_f^{green}\;\; q_f^{blue})$:

$$\mathscr{L}_0 = \sum_f \bar{q}_f\,(i\gamma^\mu\partial_\mu - m_f)\,q_f \tag{1.6}$$

one is forced to introduce gauge bosons – called *gluons* – to preserve the gauge invariance. The Lagrangian becomes:

$$\mathscr{L}_{QCD} = \mathscr{L}_0 - g_s G_a^\mu \sum_f \bar{q}_f^\alpha \gamma_\mu \left(\frac{\lambda^a}{2}\right)_{\alpha\beta} q_f^\beta - \frac{1}{4}G_a^{\mu\nu}G_{\mu\nu}^a \tag{1.7}$$

The strength of the interaction is g_s, which is universal for all the quark flavours. The second term includes $SU(3)$ matrices λ_a and represents the interaction between the quarks and the gluon field G_a^μ. The kinetic term for the gluons is the third one, with $G_a^{\mu\nu} = \partial^\mu G_a^\nu - \partial^\nu G_a^\mu - g_s f^{abc} G_b^\mu G_c^\nu$, where f^{abc} are the $SU(3)$ structure constants. There are eight gluons which also carry colour charge due to the non-abelian nature of the group. This gives rise to self-interactions between them and is behind the existence of bound-states instead of free quarks (quark confinement).

The electroweak theory

Weak interactions are behind a variety of phenomena like beta decay, decays of charged pions and muons, scattering of neutrinos – neutral and nearly massless fermions – on nuclei, among others. Some of the experimental facts that helped constructing a theory of weak interactions are the following:

- The decays of charged pions, muons and neutrons are governed by a universal strength that involves left-handed (right-handed) fermion (anti-fermion) chiralities[1].
- These decays are identified with charged current interactions: transitions between down and up-type quarks (like $d \to u$) or between charged leptons – like electrons or muons – and the corresponding neutrinos. There are different types (flavours) of neutrinos, one associated with each charged lepton.
- Although neutrinos do not have electric charge, they interact via neutral currents, which can also involve charged fermions. Neutral currents conserve flavour, implying that there is no transition between charged leptons like $\mu \to e\gamma$. Those interactions also distinguish between the different chiralities of the fermions, unlike the electromagnetic interaction.

Electromagnetic and weak phenomena are described in a coherent framework requiring a gauge symmetry group $SU(2)_L \otimes U(1)_Y$. The subscript L refers to left-handed fields. The $U(1)$ symmetry does not correspond to the electromagnetic interaction but it is related to it as it will be shown. Its parameter Y – called hypercharge – is connected to the electric charge by a relation which also involves the charge associated with $SU(2)$, called weak isospin.

The electroweak interactions dictate how the particles of matter are organized. Leptons that only interact electroweakly, and quarks that also interact strongly are grouped in three families with increasing mass:

Leptons: **Quarks:**

$$\begin{pmatrix} \nu_e \\ e \end{pmatrix}, \begin{pmatrix} \nu_\mu \\ \mu \end{pmatrix}, \begin{pmatrix} \nu_\tau \\ \tau \end{pmatrix} \qquad \begin{pmatrix} u \\ d \end{pmatrix}, \begin{pmatrix} c \\ s \end{pmatrix}, \begin{pmatrix} t \\ b \end{pmatrix}$$

The leptons on the upper row are the neutrinos, each one associated with the electron, muon and tau that occupy the lower row. The neutrinos are chargeless while the other leptons have charge $= -1$. The quarks appear in three different colours and carry

---

[1] Chirality is a property of the field defined by the operator γ^5, which is formed by the product of Dirac matrices so that it anti-commutes with all the others. In case of massless particles the chirality corresponds to the helicity: fermions with right-handed (left-handed) helicity are the ones that have the spin pointing in the same (opposite) direction of the momentum. For anti-fermions this convention is reversed.

fractional charge: $+\frac{2}{3}$ for the up (u), charm (c) and top (t) and $-\frac{1}{3}$ for the down (d), strange (s) and bottom (b). Anti-particles for each of the fermions are also included.

Left-handed chiral fields transform as doubles under $SU(2)_L$, while right-handed fields transform as singlets. Right-handed neutrinos do not exist in the minimal version of the theory, only charged leptons, up and down-type quarks.

The interactions among the particles can be derived from the gauge principle. The gauge symmetry implies the existence of two coupling constants – g and g' – and four gauge fields: W_μ^a (with $a = 1, 2, 3$) and B_μ. Taking for instance a quark family given by:

$$\psi_1 = \begin{pmatrix} u \\ d \end{pmatrix}_L \qquad \psi_2 = u_R \qquad \psi_3 = d_R \tag{1.8}$$

with R referring to right-handed fields, the associated Lagrangian can be written under the form:

$$\mathscr{L}_{EW} = \sum_{j=1}^{3} i\bar{\psi}_j \gamma^\mu D_\mu \psi_j - \frac{1}{4} W_{\mu\nu}^a W_a^{\mu\nu} - \frac{1}{4} B^{\mu\nu} B_{\mu\nu} \tag{1.9}$$

where the covariant derivative D_μ is expressed as:

$$D_\mu \, \psi_j(x) = \left[\partial_\mu - ig\frac{\sigma_a}{2} W_\mu^a \delta_{1j} - ig' \frac{Y_j}{2} B_\mu \right] \psi_j(x) \tag{1.10}$$

Here σ_a are the Pauli matrices, Y_j is the hypercharge and $\delta_{ij} = 1$ for $i = j$ and 0 otherwise. The second term, associated with $SU(2)$ transforms only left-handed fields (ψ_1) while the last term, associated with $U(1)$, acts on both chiralities. Moreover:

$$W_a^{\mu\nu} = \partial^\mu W_a^\nu - \partial^\nu W_a^\mu + g\,\epsilon_{abc}\, W_b^\mu \, W_c^\nu \tag{1.11}$$

$$B^{\mu\nu} = \partial^\mu B^\nu - \partial^\nu B^\mu \tag{1.12}$$

Combinations of the first two components of W_μ^i are associated with two charged vector bosons:

$$W_\mu^\pm = \frac{1}{\sqrt{2}} \left(W_\mu^1 \mp i W_\mu^2 \right) \tag{1.13}$$

The remaining component W_μ^3 mixes with B_μ via the Weinberg angle θ_W in such a way to form two neutral bosons: the photon and the Z.

$$\begin{pmatrix} W_\mu^3 \\ B_\mu \end{pmatrix} = \begin{pmatrix} \cos\theta_W & \sin\theta_W \\ -\sin\theta_W & \cos\theta_W \end{pmatrix} \begin{pmatrix} Z_\mu \\ A_\mu \end{pmatrix} \tag{1.14}$$

Again, the non-abelian group symmetry predicts the existence of interactions between the gauge bosons. There are triple gauge couplings and vertices involving four bosons, always with the presence of a W pair.

This Lagrangian describes charged and neutral interactions associated with weak decays, such as the phenomena mentioned in the beginning of the section. It incorporates QED and self-interactions among the gauge bosons. Nevertheless it is in strong disagreement with experimental facts. The $W^\pm$, the Z and the fermions are massive objects, and mass terms for any of these particles violate explicitly the gauge symmetry.

1.2 The Higgs mechanism

The contradiction pointed out in the last section left the theorists with a difficult question: should one brutally add the mass terms to the Lagrangian and abandon gauge invariance with the nice properties associated such as renormalizability, or is there an alternative to generate masses without breaking the symmetry explicitly?

The answer is yes and came from the work of Higgs, Englert, Brout and others [21–23] on the mechanism of spontaneous symmetry breaking. One introduces a doublet of complex scalar fields $\Phi(x)$ and a scalar potential $V(\Phi)$ given by e.g.:

$$\Phi(x) = \begin{pmatrix} \phi^{+}(x) \\ \phi^{0}(x) \end{pmatrix} \tag{1.15}$$

$$V(\Phi) = \mu^2\, \Phi^{\dagger}\Phi + \lambda \left(\Phi^{\dagger}\Phi\right)^2 \tag{1.16}$$

The Lagrangian that includes this potential is invariant under $SU(2)_L \otimes U(1)_Y$ transformations. The existence of minima is guaranteed by taking $\lambda > 0$. The usual choice $\mu^2 > 0$ gives a mass term for Φ and implies a trivial minimum of the potential at $\Phi = 0$. If one chooses $\mu^2 < 0$ on the other hand, the minimum obeys the condition:

$$\langle 0\,|\Phi|\,0\rangle = \begin{pmatrix} 0 \\ \frac{v}{\sqrt{2}} \end{pmatrix} \text{ with } v \equiv \sqrt{-\frac{\mu^2}{2\lambda}} > 0 \tag{1.17}$$

where the ground state of ϕ^{+} was chosen to be zero.

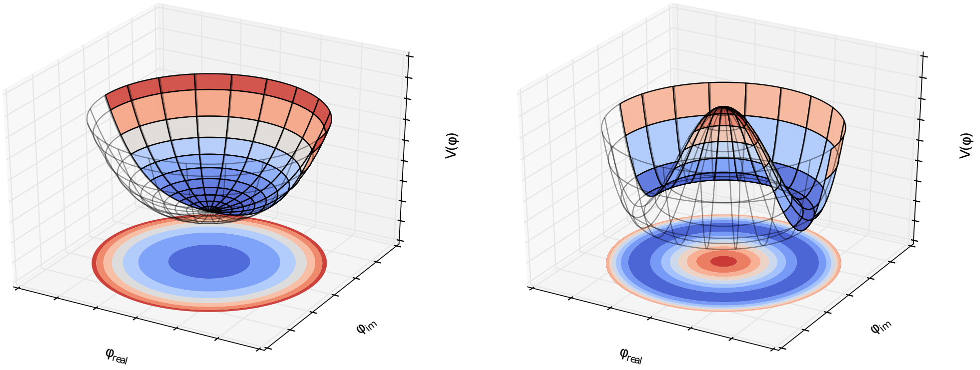

(a) $\mu^2 > 0$.

(b) $\mu^2 < 0$.

Figure 1.1: Illustration of the Higgs potential for a scalar field $\Phi = \varphi_{\text{real}} + i\varphi_{\text{im}}$ with $\mu^2 > 0$ and $\mu^2 < 0$.

Although the Lagrangian remains invariant under $SU(2) \otimes U(1)$, the choice of a particular value for the ground state breaks the symmetry. This is illustrated in Fig. 1.1: the potential on Fig. 1.1b is symmetric under rotations, but any minimum chosen is not. One now has to develop the theory around a point of minimum, so that the scalar doublet can be written in terms of real fields as following:

$$\Phi(x) = \frac{1}{\sqrt{2}} e^{i\frac{\sigma_a}{2}\theta_a(x)} \begin{pmatrix} 0 \\ v + H(x) \end{pmatrix} \tag{1.18}$$

The local $SU(2)$ invariance of the Lagrangian allows any choice of the fields $\theta_i(x)$. In particular, taking $\theta_i = 0$ in the so-called unitary gauge, the kinetic term of the scalar field, using the covariant derivative from equation (1.10), becomes:

$$\left(D_\mu \Phi\right)^\dagger D^\mu \Phi \to \frac{1}{2}\left(\partial_\mu H\right)\left(\partial^\mu H\right) + (v+H)^2 \left[\frac{g^2}{4} W_\mu^\dagger W^\mu + \frac{g^2}{8\cos^2\theta_W} Z_\mu Z^\mu\right] \tag{1.19}$$

We have obtained a kinetic term for a scalar field, interactions between the scalar and the gauge bosons and mass terms for the gauge bosons given by:

$$M_W = M_Z \cos\theta_W = \frac{1}{2} g v \tag{1.20}$$

Out of the four degrees of freedom introduced by the scalar doublet, three were absorbed by the longitudinal components of $W^\pm$ and the Z, and the remaining one is the Higgs particle, with a mass $M_H = \sqrt{-2\mu^2} = \sqrt{2\lambda} v$. All that came from the spontaneous symmetry breaking and the field redefinition in the unitary gauge.

Moreover, mass terms for the fermions (f) that would violate the gauge symmetry are now allowed by the scalar doublet and its charge conjugate. In the unitary gauge they take the form:

$$\mathscr{L}_Y = -\frac{1}{2}(v+H)\lambda_f \bar{f} f \tag{1.21}$$

The couplings between fermions and the Higgs boson λ_f are arbitrary. They are related to the fermion masses via $m_f = \lambda_f \frac{v}{\sqrt{2}}$ which are free parameters of the theory.

1.3 The Standard Model

Combining the electroweak theory with the Higgs mechanism and QCD, one obtains a model that describes strong and electroweak interactions. The gauge symmetry group behind it is $SU(3)_C \otimes SU(2)_L \otimes U(1)_Y$. The first one is associated with the colour charges of quarks and gluons while the other two are related to weak left-handed isospin and hypercharge. The electroweak symmetry is spontaneously broken into the electromagnetic $U(1)_Q$ with the introduction of the scalar field. These are the ingredients of the Standard Model.

The result is the existence of four intermediate vector bosons mediating the electroweak interactions: the photon (γ), $W^{\pm}$ and Z. After symmetry breaking, the photon remains massless while the others acquire masses which are predicted by the theory given some experimental input (e.g. the vacuum expectation value of the scalar field v and the electroweak couplings as in eq. (1.20)). Their experimental values are listed in table 1.1. The gauge sector is completed by 8 gluons (g), mediators of the strong interactions. The scalar sector is represented by the Higgs boson. The Higgs potential and self-interactions are governed by the quadratic and quartic coefficients associated to λ (or μ).

Boson	Mass (GeV)	Electric charge	Associated interaction
γ	0	0	electromagnetic
Z	91.1875 ± 0.0021	0	weak
$W^{\pm}$	80.399 ± 0.023	± 1	
g	0	0	strong

Table 1.1: Properties of the vector bosons of the Standard Model. The experimental values for the masses of the W and Z bosons were extracted from ref. [24].

Quark		Mass	Electric charge
up	(u)	1.1 to 3.3 MeV	+2/3
down	(d)	3.5 to 6.0 MeV	-1/3
charm	(c)	$1.27\,^{+0.07}_{-0.11}$ GeV	+2/3
strange	(s)	$105\,^{+25}_{-35}$ MeV	-1/3
top	(t)	$171.3 \pm 1.1 \pm 1.2$ GeV	+2/3
bottom	(b)	$4.20\,^{+0.17}_{-0.07}$ GeV	-1/3

Lepton		Mass	Electric charge
electron	(e)	0.511 MeV	-1
e-neutrino	(ν_e)	< 2 eV	0
muon	(μ)	105.7 MeV	-1
μ-neutrino	(ν_μ)	< 0.19 eV	0
tau	(τ)	1777 MeV	-1
τ-neutrino	(ν_τ)	< 18.2 eV	0

Table 1.2: Properties of the quarks and leptons of the Standard Model. Only upper limits are given for the masses of the neutrinos, although there is strong experimental evidence that they are massive [25].

The Yukawa sector complements the model, with quarks and leptons acquiring masses through the same mechanism as the gauge fields. This time the masses are free parameters, and their values are listed in table 1.2.

Actually, the quark mass eigenstates do not correspond to the eigenstates of the weak interaction. The quark doublets depicted in the previous section are in fact mixtures of the mass eigenstates through a 3×3 unitary matrix named after Cabbibo, Kobayashi and

Maskawa (CKM). This mechanism introduces three mixing angles between the quark flavours and a phase that allows for the violation of charge conjugation and parity (CP). Reference [18] gives a full description of this effect.

Putting all together, one finds that the SM has 18 free real parameters: 9 fermion masses, 4 CKM parameters, 3 couplings and 2 parameters for the scalar sector. It is more convenient to translate the last five of them into quantities precisely measured experimentally. The QCD coupling was well determined from Z decays in *ee* collisions, and thus it is typically expressed at the Z mass: $\alpha_s(M_Z)$. The other ones can be replaced by the fine structure constant α, measured for instance from the quantum Hall effect [25], the Fermi coupling constant G_F that governs the muon decay, the mass of the Z boson M_Z determined at LEP and SLD, and the Higgs mass M_H which is the only unknown.

Essentially any physical observable can be calculated using this set of parameters. Uncertainties below the percent level can be achieved including loop corrections, given that the Standard Model is renormalizable to all orders in perturbation theory. The result of a calculation is a clear prediction of the model, and extensive tests were performed with many observables. They include the measurement of the W mass and total width, the total and partial widths of the Z boson, asymmetries in its decays from *ee* collisions and others (see refs. [20, 24, 26, 27] for detailed reviews). No serious discrepancies were observed at the per mille level, and the conclusion is that the SM describes the data up to the highest energies achieved experimentally.

Next section discusses the constraints on the Higgs mass both from the theoretical point of view and from the experimental side.

1.4 Constraints on the Higgs boson mass

On the 4th of July, 2012 the discovery of new boson, compatible with the SM Higgs boson, was announced at CERN [28]. The discovery was made at the same time both by CMS [29] and by ATLAS [30]. In this section theoretical constraints, previous direct searches by LEP and Tevatron and indirect limits from electroweak data are presented.

Theoretical constraints

Extending the validity of the Standard Model beyond the energies for which it has been tested imposes some limits on the Higgs mass. The first example is the $W^+W^- \rightarrow W^+W^-$ scattering, which involves the quartic gauge coupling and exchanges of Z, γ and possibly the Higgs. If the Higgs is too heavy or does not exist, the yield of this process at high energies grows proportionally to s, the square of the center of mass energy. Unitarity is violated unless some new physics appears at the scale of around 1 TeV, or if the Higgs is lighter than approximately 800 GeV.

A stronger upper limit is given by the triviality bound. Assuming that the scalar sector of the SM is a ϕ^4 theory, it remains valid as long as the Higgs quartic coupling is finite. As this coupling is expected to increase with energy, a cut-off Λ must be set, after which some new physics takes over. If the SM is restricted to the electroweak scale ($\Lambda \sim 1 \times 10^3$ GeV), the Higgs could have mass up to 1 TeV. On the other hand, if its validity extends up to 1×10^{16} GeV (the scale of the Grand Unification, GUT), masses above $M_H = 200\,\text{GeV}$ are not allowed.

Finally, a lower limit is set by the vacuum stability bound. If again one considers the Higgs self-couplings but this time with a low mass Higgs, loops with fermions and gauge bosons must be included. The most important one involves the top quark and contributes with a negative sign. If M_H is too low, the sign of quartic term in the scalar potential is flipped and there is no minima anymore. As the theory cannot be developed from an unstable vacuum, M_H is required to lie above a certain value depending on the cut-off Λ. For the same scales mentioned above:

$$\begin{aligned} \Lambda \sim 1 \times 10^3\,\text{GeV} &\Rightarrow M_H \gtrsim 70\,\text{GeV} \\ \Lambda \sim 1 \times 10^{16}\,\text{GeV} &\Rightarrow M_H \gtrsim 130\,\text{GeV} \end{aligned} \tag{1.22}$$

Combining all these effects, the theoretical limits on the Higgs mass are represented in Fig. 1.2.

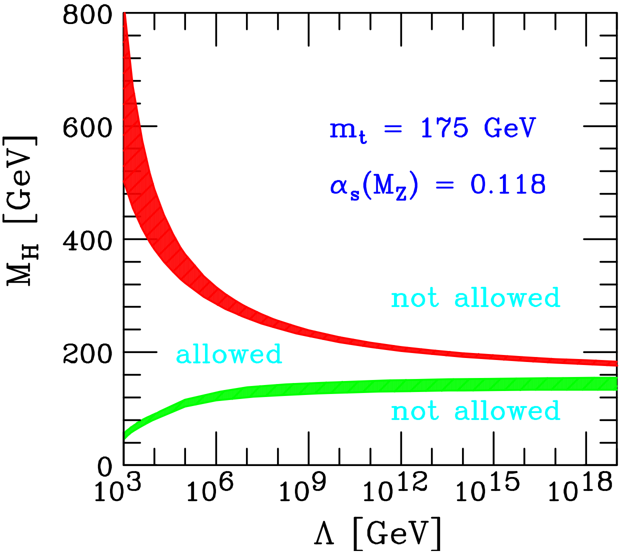

Figure 1.2: Theoretical limits on the Higgs boson mass from the triviality (upper bound) and vacuum stability arguments (lower bound), as a function of the cut-off Λ. The allowed region lies between the bands and the coloured/shaded bands illustrate the impact of various uncertainties. Extracted from ref. [20].

Direct searches from previous experiment

Before LHC the most stringent limits came from direct searches of Higgs boson at Tevatron and at LEP [31]. Operating near the Z mass, the initial phase of the LEP excluded the mass range below 65.2 GeV. The upgraded LEP2 increased the center of mass energy up to 209 GeV, looking for the Higgs produced from off-shell Z boson radiation (“Higgs-strahlung”). The process $ee \to Z^* \to HZ$ is illustrated in Fig. 1.3.

An excess of events close to $M_H = 116\,\text{GeV}$ created great expectations close to the end of LEP operations, but was not enough to claim a discovery. The final analyses reduced the significance of this signal from 2.9σ to 1.7σ. The exclusion limit for $M_H < 114.4\,\text{GeV}$ was set at 95% confidence level (CL), compared with the expected limit at 115.3 GeV, as shown in Fig. 1.4.

The Tevatron operated at $\sqrt{s} = 1.96\,\text{TeV}$ colliding $p + \bar{p}$ until 30 September, 2011. Essentially two regions are distinguished for the searches, according to the dominant decay modes. The decay modes of the Higgs boson and its production in hadron colliders

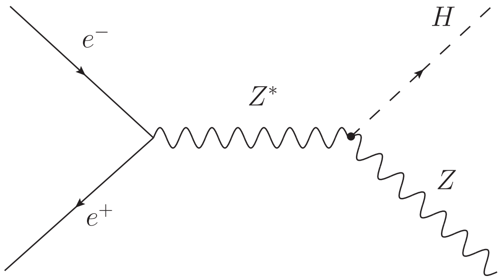

Figure 1.3: Feynman diagram of the dominant production mechanism of the Higgs boson at LEP2.

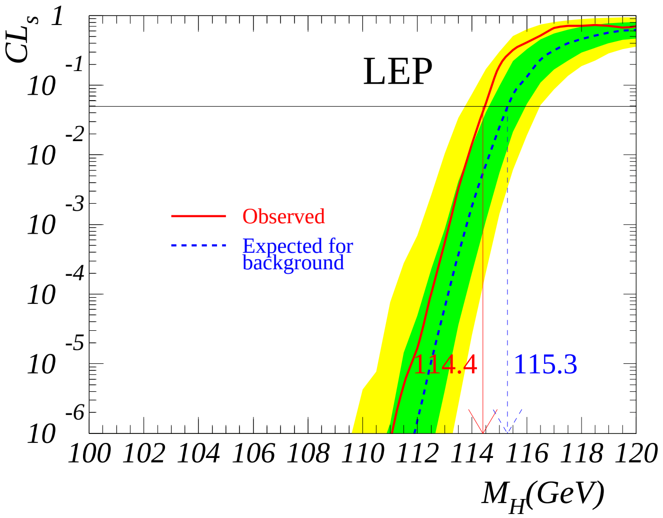

Figure 1.4: Confidence level of signal plus background hypothesis on the Standard Model Higgs boson searches at LEP. Masses below 114.4 GeV, defined by the intersection of the horizontal line at $CL_s = 0.05$ with the observed curve are excluded at 95% CL. Extracted from ref. [31].

will be discussed in section 1.5. In the low mass region ($M_H < 125\,\mathrm{GeV}$), the biggest sensitivity is from the $q\bar{q} \to (W/Z)H$ process where the Higgs decays to $b\bar{b}$ and the W or Z bosons decay leptonically. The associated production with vector bosons, similar to the one used at LEP, is required to fight the overwhelming QCD backgrounds. In the high masses ($M_H > 125\,\mathrm{GeV}$), the decay to a pair of W bosons (one of which possibility virtual, if $m_H < 160\,\mathrm{GeV}$) takes over and all the production channels can be explored. Also other channels have been investigated and used into the combination as: $H \to ZZ$, $H \to \tau\tau$ and $H \to \gamma\gamma$.

Using $10\,\mathrm{fb}^{-1}$ and combining the results from the two experiments, CDF and DØ, the excluded regions at 95% CL is between 100 and 103 GeV and between 147 and 180 GeV [32] as shown in Fig. 1.5. If the Higgs boson did not exist, the expected exclusion regions would be $100 < m_H < 120\,\mathrm{GeV}$ and $139 < m_H < 184\,\mathrm{GeV}$. Higgs boson masses below 100 GeV were not studied. Tevatron quoted an excess at $m_H = 120\,\mathrm{GeV}$ with a p-value for a background fluctuation to produce this excess of 1.5×10^{-3}, corresponding to a local significance of 3.0 standard deviations. The observed and expected p-value for the studied mass range is shown in Fig. 1.6. The global significance (incorporating the look-elsewhere effect) for such an excess anywhere in the full mass range investigated is approximately 2.5 standard deviations. The best sensitivity is reached in the $b\bar{b}$ decay, with a deviation from the background of 3.2σ and it is complementary with the results at LHC. The search of the $H \to \gamma\gamma$ decay is limited by the signal-to-background ratio, the resolution of the Higgs mass in this channel is of the order of 3 %.

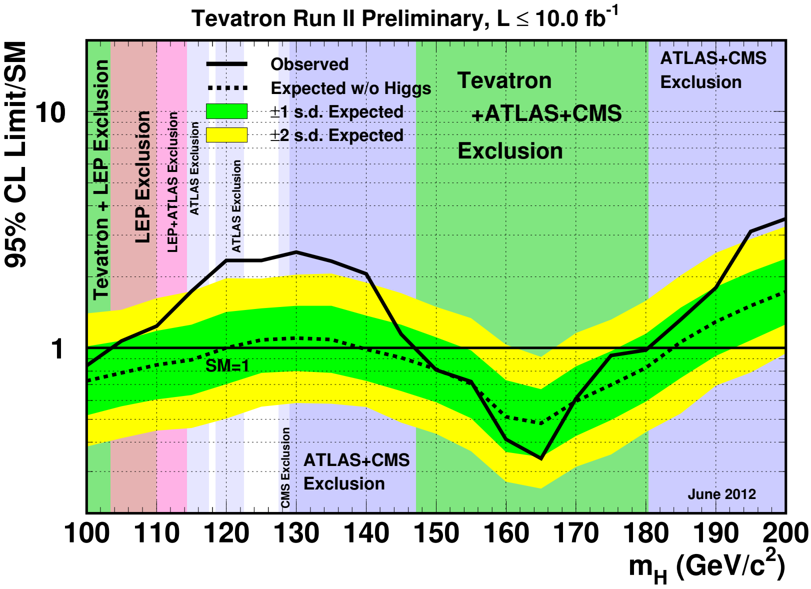

Figure 1.5: Observed and expected 95% CL upper limits on SM Higgs boson production at the Tevatron. Masses between 100 and 103 GeV, and between 147 and 180 GeV, for which the observed curve lies below 1, are excluded at 95% CL. Extracted from ref. [32].

The best fit signal strength, defined as the ratio between the observed and expected cross section, for an hypothesized Higgs boson at 125 GeV is shown in Fig. 1.7 separating the three main subchannels $b\bar{b}$, WW and $\gamma\gamma$.

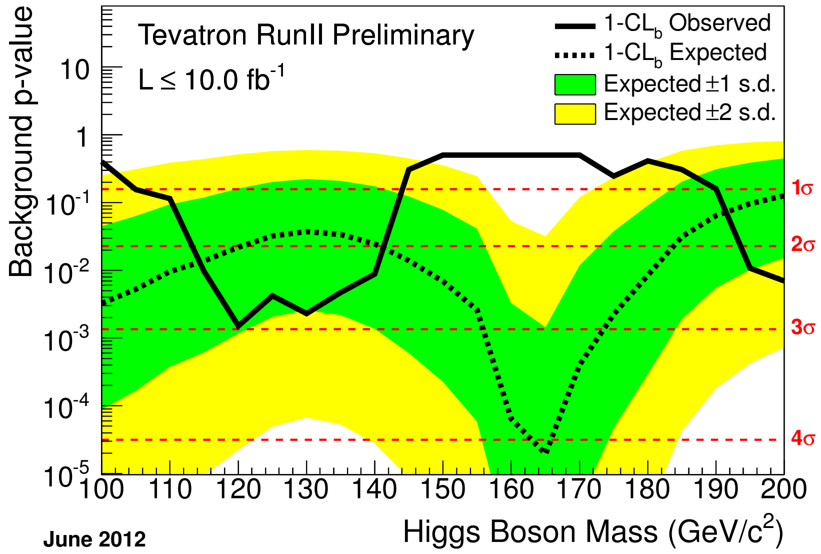

Figure 1.6: The background p-values $1 - CL_b$ as a function of the Higgs boson mass. The green and yellow bands correspond respectively to the regions enclosing 1 s.d. and 2 s.d. fluctuations around the median prediction in the signal plus background hypothesis at each value of m_H. Extracted from ref. [32].

Indirect limits from electroweak precision data

Electroweak precision data offer a very powerful check of the internal consistency of the SM. Given its remarkable accuracy, the performed measurements are sensitive to energy scales beyond the ones achieved experimentally, as high mass particles contribute to the observables via quantum loop corrections. The Higgs boson, for instance, enters the one-loop corrections to the W and Z masses, illustrated in Fig. 1.8. Although the Higgs contribution is logarithmic and much smaller than the component associated to the top quark, the data is precise enough to constrain this parameter.

Stringent limits are set from a global fit using all the observables, historically by the LEP Electroweak Working Group [24] and more recently using the GFitter toolkit [27]. The results from the GFitter group have been updated just after the discovery of the new boson at LHC assuming it to be the SM Higgs boson [33]. Two main results are provided, including or not the constraint from the direct measurement of the Higgs mass from ATLAS and CMS:

$$\begin{aligned} \text{Electroweak precision data only:} \quad & M_H = 94^{+25}_{-22}\,\text{GeV} \\ \text{Including direct searches:} \quad & M_H = (125.7 \pm 0.4)\,\text{GeV} \end{aligned}$$

consistent within 1.3σ. Fig. 1.9 displays the corresponding $\Delta\chi^2$ profile versus the Higgs mass (grey band) compared to the new Higgs mass measurements of ATLAS and CMS (red/orange data points) and the $\Delta\chi^2$ profile of the fit including the Higgs mass measurement (blue curve). The two fits clearly favours a low mass Higgs boson.

Assuming the newly discovered particle to be the SM Higgs boson, all fundamental parameters of the SM are known. It allows, for the first time, to overconstrain the SM at the electroweak scale and to evaluate its validity. The global fit to all the electroweak

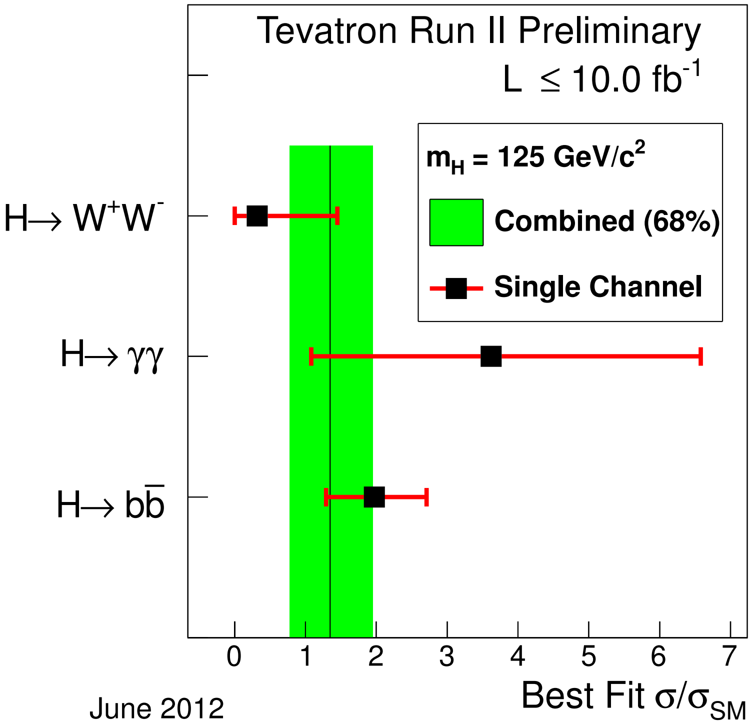

Figure 1.7: Best fit signal strength for Higgs boson at 125 GeV for the combination (black line) and for the three sub-combinations. Extracted from ref. [32].

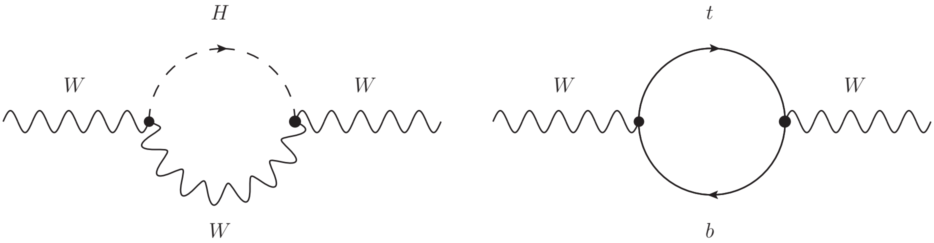

Figure 1.8: One-loop diagrams for the contributions to the W mass involving (a) the Higgs boson and (b) the top quark.

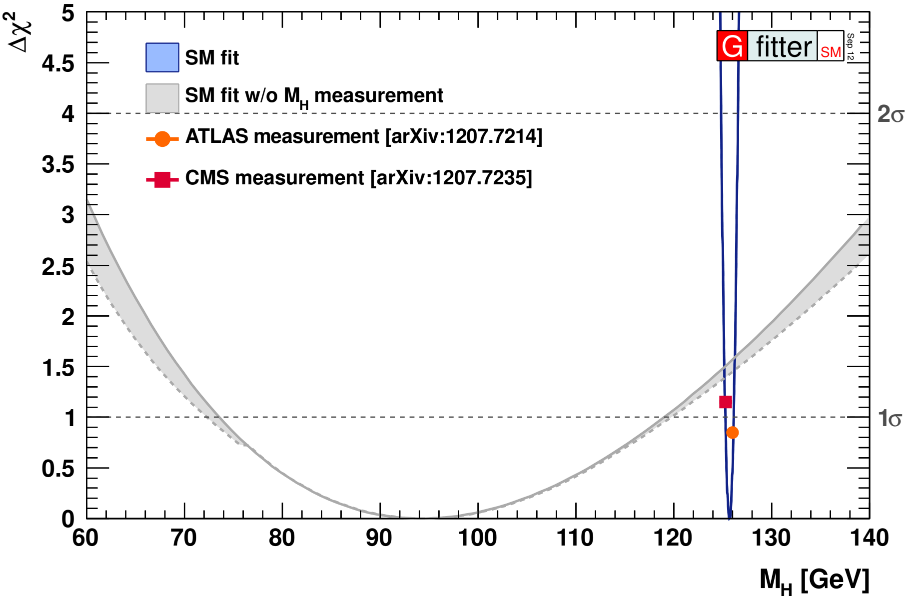

Figure 1.9: $\Delta\chi^2$ profiles as a function of the Higgs mass (gray band)compared with the Higgs mass measurements of ATLAS and CMS (red/orange data points) with their $\pm\sigma$ uncertainties and the $\Delta\chi^2$ profile of the fit including the Higgs mass measurement (blue curve). the solid (dotted) lines illustrate the fit results including (ignoring) theoretical uncertainties in the fit. Extracted from ref. [33].

precision data and the measured Higgs mass results in a goodness-of-fit p-value of 0.07. Only a fraction of the contribution to the "incompatibility" stems from the Higgs mass. It is also possible to indirectly estimate the values of some parameters with a better precision than the direct measurement, for example the mass of the W boson.

1.5 Higgs decay modes and production in hadron colliders

1.5.1 Decay modes and total width

Strong limits on the Higgs boson mass were set by theoretical arguments, direct searches at LEP and the Tevatron, and electroweak precision data. If the new boson discovered by ATLAS and CMS is the SM Higgs boson all the parameter of the model are for the first time known. All the SM Higgs boson properties are completely determined once its mass value is fixed.

In particular, the decay modes to fermions, gauge bosons and decays involving virtual loops are known to next-to-leading order (NLO) or better. At tree level, the Higgs couplings are proportional to the masses of the particles (m_f/v for fermions and M_V^2/v for $V = W, Z$) and thus it tends to decay to the heaviest particles kinematically accessible. Figure 1.10 shows the branching fractions as a function of M_H.

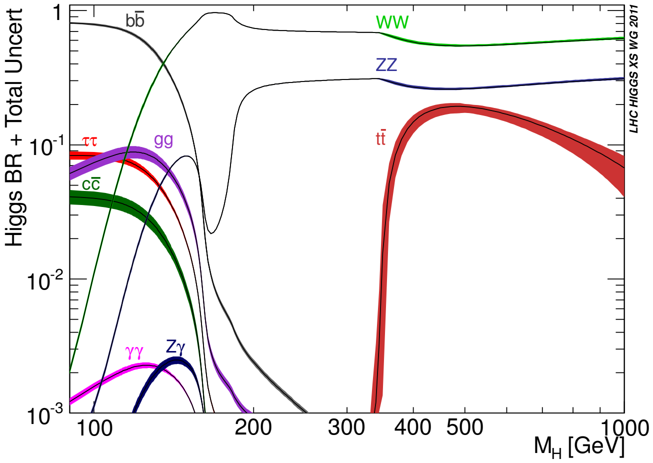

Figure 1.10: Branching ratios of the SM Higgs boson as a function of its mass. Extracted from ref. [34].

In the "low mass" region ($M_H \lesssim 130\,\text{GeV}$), $H \to b\bar{b}$ is the dominant mode, with branching ratios (BR) around 50% – 75%, followed by $H \to \tau^+\tau^-$ with BR $\approx$ 5% to 7%. Decays to massless particles – gluons and photons – proceed through a loop of heavy fermions and/or gauge bosons with the major contribution coming from the top quark in the gluon channel and the W boson in case of photons.

For $130 \lesssim M_H \lesssim 180$, decays to a pair of gauge bosons take over, usually with one of the Ws or Zs still off-shell (noted by the '$*$' superscript). Close to $M_H = 130\,\text{GeV}$, $H \to WW^*$ becomes the dominant mode and is almost exclusive when it turns on-shell, for $M_H > 2M_W$. Meanwhile, $H \to ZZ^*$ remains suppressed by the virtual Z and has its relative importance reduced.

The "high mass" range ($180 \lesssim M_H \lesssim 1000\,\mathrm{GeV}$) is completely dominated by vector bosons, with $H \to WW$ entering with BR $\sim 2/3$ and $H \to ZZ$ with BR $\sim 1/3$. While the latter involves two identical particles (ZZ), the former includes two different ones ($W^\pm W^\mp$), which justifies the factor of 2 between them. Decays to a pair of top quarks open around $M_H \gtrsim 350\,\mathrm{GeV}$ and contribute at most with 20%. While the partial width of this process grows with M_H, the vector boson one is proportional to M_H^3.

The total width (Γ_H), shown in Fig. 1.11, is also a reflex of the previous statement. The Higgs resonance is very narrow at low masses, with $\Gamma_H < 10$ MeV at $M_H = 130\,\mathrm{GeV}$. With the increase of the vector boson decay yields, the width rises quickly to near 1 GeV at $M_H = 180\,\mathrm{GeV}$ and becomes comparable to the Higgs mass for a heavy scalar ($M_H \gtrsim 500\,\mathrm{GeV}$), although such masses are highly disfavoured by electroweak precision data.

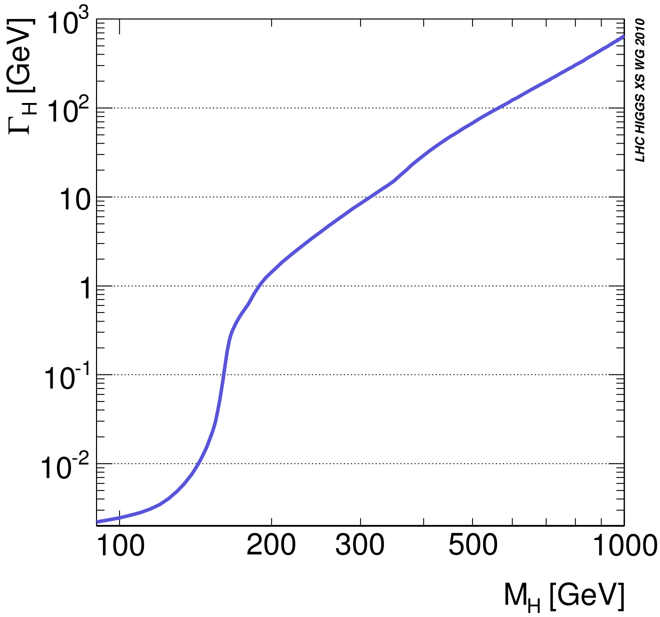

Figure 1.11: Total width of the SM Higgs boson as a function of its mass. Extracted from ref. [34].

1.5.2 Production in hadron colliders

Both at the Tevatron and LHC, the Higgs is produced through four main channels, depicted in Fig. 1.12 and discussed below.

Gluon fusion (also called gluon-gluon fusion) is the dominant one, mediated by a top quark loop and a b-quark loop to a lesser extent. This process receives huge contributions from higher order QCD corrections, with NLO increasing the total cross section by $\sim 70\%$ at $\sqrt{s} = 14\,\mathrm{TeV}$ [35] and NNLO giving extra 30%, while electroweak (EW) corrections are at the percent level [36]. The uncertainties on the total values did not meet a consensus among the theorists, varying from 10% to 40% depending on the prescription used for their calculation.

Vector boson fusion (VBF) is the sub-leading mode at the LHC, with the Higgs produced in association with two quarks. The quarks are expected to give rise to very

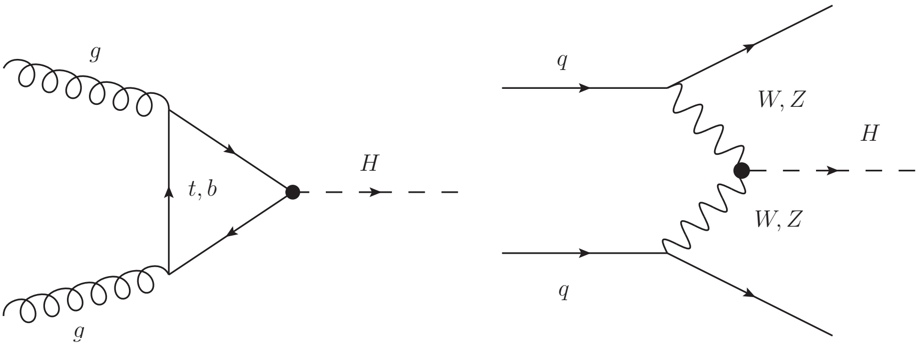

(a) Gluon fusion. **(b)** Vector boson fusion.

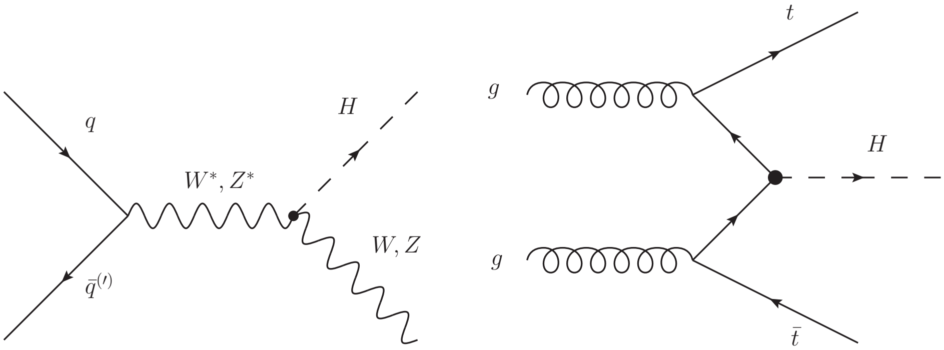

(c) Associated production with *W* or *Z* bosons. **(d)** Associated production with top quarks.

Figure 1.12: Main production modes of the Higgs boson at hadron colliders.

energetic jets located in the forward regions, with a big rapidity gap between them. This is a powerful filter against QCD backgrounds and is explored in some final states. Higher order effects (QCD + EW) have a modest contribution, increasing the cross section by approximately 5 - 10% [37].

Associated production with W or Z bosons is the same process used at LEP, this time initiated by $q\bar{q}$. The decays of the vector bosons to leptons (including neutrinos) provide good trigger efficiency and help reducing QCD backgrounds. It is the second most important production channel at the Tevatron and used to be the most sensitive search mode. Recently it became more attractive at the LHC with the revival of $H \to b\bar{b}$ that will be discussed in the next section. The K-factors[2] (QCD + EW) vary around 30% with uncertainties at the percent level [37].

Associated production with top quarks can be initiated by a pair of gluons or quarks, the Higgs being radiated from a quark line in the latter case. The low yields restrict the interest of this mode to decays that cannot be accessed otherwise, as used to be the case of $H \to b\bar{b}$. This matter will be discussed shortly.

The cross section of each component as a function of the Higgs mass is shown in Fig. 1.13 for $\sqrt{s} = 7\,\text{TeV}$ and $8\,\text{TeV}$. Their relative contribution is not the same in both accelerators due to the increase of gluon-gluon cross section with the center of mass energy, and the presence of valence anti-quarks in $p\bar{p}$ collisions. All the cross sections presented are provided by the LHC Higgs Cross Section Working Group [34].

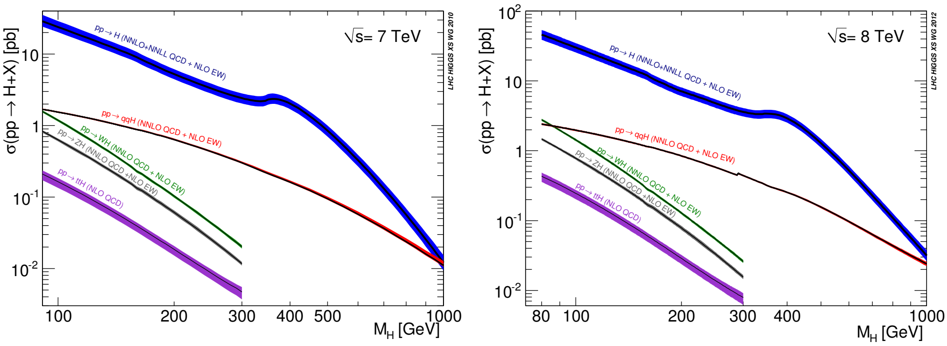

(a) $\sqrt{s} = 7\,\text{TeV}$ **(b)** $\sqrt{s} = 8\,\text{TeV}$

Figure 1.13: Next-to-leading order cross sections for the dominant modes of the production of a SM Higgs at (a) $\sqrt{s} = 7\,\text{TeV}$ and (b) $\sqrt{s} = 8\,\text{TeV}$, as a function of its mass. Extracted from ref. [34].

1.6 Higgs searches at the LHC

One of the main goals of ATLAS and CMS is the discovery the Higgs boson. Both experiments were designed to either exclude or discover the Higgs at 5σ level with a few tens of fb^{-1} in the whole mass range. On July 4th, 2012 both ATLAS and CMS announced the discovery of a new boson with a significance greater than 5σ compatible with the SM Higgs boson with a mass around 125 GeV (see figure 1.14 for the discovery significance).

---

[2] The K-factor is the ratio between higher and lowest order cross sections. e.g. σ_{NLO}/σ_{LO}.

This section briefly discusses the analyses considered by ATLAS. Details can be found in ref. [30, 38], while similar CMS results are reported in ref. [29, 39].

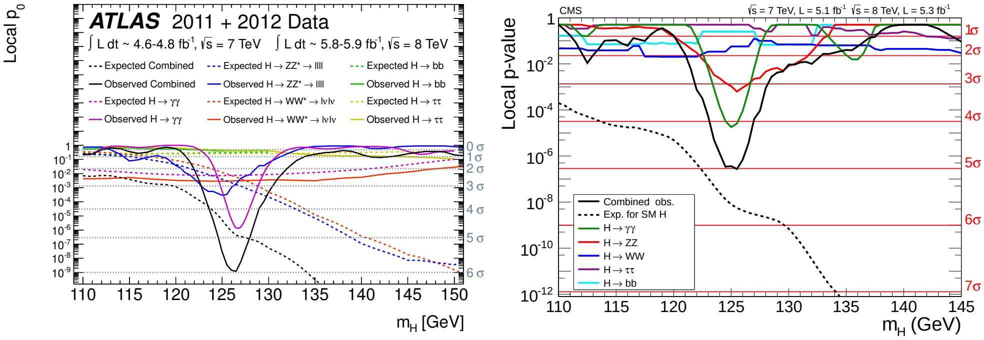

(a) ATLAS **(b)** CMS

Figure 1.14: Local p-value and corresponding significance (see appendix A) for a background-only experiment to be more signal-like than the observation, for individual channels and the combination and as a function of the SM Higgs boson mass for (a) ATLAS and (b) CMS. The dashed line shows the expected local p-values for a SM Higgs boson with a mass m_H. This plots have been presented on July 4th, 2012 when both experiments announced the discovery of the new boson compatible with the SM Higgs boson. Extracted from [30] and [29].

Ideally one would like to use all the combinations between initial and final states on Higgs searches. The overwhelming backgrounds from QCD processes and the low yields for Higgs production restrict the analysis channels to only a few. Efficient trigger require either the presence of leptons or photons, or at least large missing transverse energy and high-p_T jets. Distinctive signatures are also needed in the offline analyses. The most important ones are gauge bosons decaying to leptons, but forward jets and b-quarks can be of great help.

The most interesting decay modes ($H \to b\bar{b}$, $\gamma\gamma$, $\tau^+\tau^-$, WW and ZZ) are briefly discussed in the following, focusing on ATLAS analyses. The expected exclusion for each channel is shown in Fig. 1.15. Other decays, involving a pair of gluons or c-quarks are completely swamped by the hadronic activity and cannot be assessed. $H \to t\bar{t}$ and $H \to \mu^+\mu^-$ have low yields, and would need huge luminosities to be distinguished from the $t\bar{t}$ and $\mu^+\mu^-$ continuum backgrounds.

- $H \to b\bar{b}$ has the highest branching ratio at low masses[3]. On the other hand it suffers from huge QCD backgrounds, many orders of magnitude above the signal. Absence of an efficient trigger already excluded both gluon fusion and VBF. $t\bar{t}H$ disappeared from the list of sensitive channels because of the complex final state and difficulties with combinatorial backgrounds, given the large number of jets, leaving the associated production with vector bosons as the only possibility.

  The current analysis [40] combines leptonic decays of vector bosons ($W \to \ell\nu$, $Z \to \ell\ell$ and $Z \to \nu\nu$, with $\ell = e, \mu$). The analysis is performed for events containing zero, one or two leptons, targeting the three Higgs boson decay channels mentioned above. The channels are split in further categories, depending on the vector boson

---

[3] Following section 1.5, low Higgs masses refer to $M_H < 130\,\mathrm{GeV}$ unless stated otherwise.

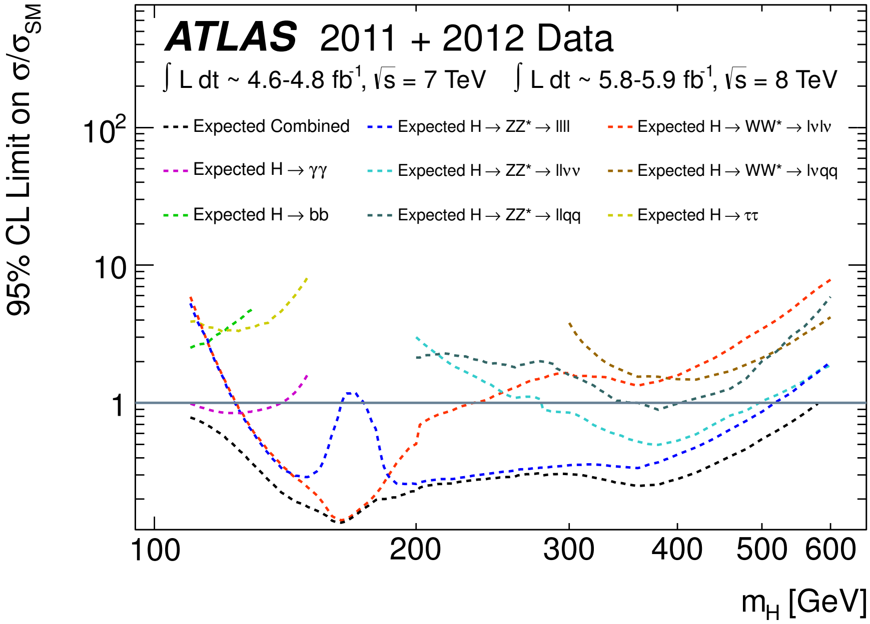

Figure 1.15: The expected 95% CL cross section upper limits for the individual search channels and the combination, normalised to the SM Higgs boson production cross section, as a function of the Higgs boson mass hypothesis. The expected limits are those for the background-only hypothesis i.e. in the absence of a Higgs boson signal. Extracted from [30].

transverse momentum and the number of jets. The analysis relies on the identification of b-quarks (b-tagging), with an efficiency of 70% for b-jets and rejection factors of 5 and 150 for c and light jets, respectively.

- $H \to \gamma\gamma$, despite its very low branching ratios of $\mathcal{O}(10^{-3})$, is one of the most important channels in the low mass range. It has a very distinctive signature with two isolated very energetic photons forming a narrow invariant mass peak. The associated resolution on the Higgs mass is around $1-2$ GeV. Jet rejection factors above 10^3 on photon identification greatly reduce the di-jet and $\gamma +$ jet backgrounds. QCD production of two photons is irreducible. All production modes can be explored, with higher signal over background for associated production modes and higher yields on gluon fusion. A relatively large number of events is expected after selection cuts: 25 for the signal (at $M_H = 120\,\text{GeV}$) and almost 1000 for the background within the signal mass window per fb^{-1}. This provides a robust method for extracting the signal significance from the data using fits on the side-bands[4].

- $H \to \tau^+\tau^-$ has the second highest branching fraction at low masses [41]. The final states depend on the tau decays: 42% of the time both taus decay hadronically, in 46% of the cases one goes to hadrons and the other one to an electron or a muon, and the remaining 12% are fully leptonic modes. The fully hadronic channels are very challenging and require data-driven methods to study the QCD multijet background, while semi-leptonic and leptonic ones can more easily lead to a discovery at LHC using the vector boson fusion production mode. The tau products in the central region and tagging jets from VBF in the forward part of the detector are a rare topology for background events. A central jet veto is explored, although it might be very sensitive to multiple interactions within the same LHC bunch crossing (pile-up). Gluon fusion and W/Z associated analyses, on the other hand, are much more difficult.

  Neutrinos in the final state prevent the full reconstruction of the event and the Higgs mass is estimated by guessing the acollinearity of the invisible decay products with respect to the visible ones using the Missing Mass Calculator (MMC) method [42]. The MMC methods uses as input the kinematics of the visible τ products, the missing energy and the number of jets in the event[5]. Resolutions around 13-20% on M_H are obtained [44]. The main background after the selection cuts is $Z \to \tau\tau$, with an invariant mass peak close to the signal for $M_H \lesssim 125\,\text{GeV}$.

- $H \to WW^{(*)}$ with both $W \to \ell\nu$ has the highest potential from $M_H = 2M_Z$ down to $130\,\text{GeV}$, both at the Tevatron and at the LHC. This is a direct consequence of the large branching ratios and rather clean signature. The presence of two high-p_T isolated leptons and large missing transverse energy provides efficient trigger and great reduction against QCD processes. The dominant backgrounds are WW and $t\bar{t}$ with real leptons and neutrinos in the final state. They can be distinguished from the signal using the jet activity and the angle between the leptons. For the signal,

---

[4] Side-bands are regions were no signal contribution is expected. From the fits one can quantify the amount of background in the signal region.

[5] MMC is a more sophisticated version of the collinear approximation [43] used in the past and today only for $H \to \tau_{\text{lep}}\tau_{\text{lep}}$ for the $\sqrt{s} = 7\,\text{TeV}$ dataset. The main improvement comes from requiring that relative orientations of the neutrinos and other decay products are consistent with the mass and kinematics of a lepton decay. This is achieved by maximising a probability defined in the kinematically allowed phase space region.

the charged leptons tend to go together given the scalar nature of the Higgs and the chirality of the neutrinos.

$H \to WW \to \ell \nu q\bar{q}$ is important at high mass, the latest analysis [45] was limited in the mass range 300 GeV $< m_H <$ 600 GeV. It is possibile to study this channel only at hight mass since for $m_H >$ 200 GeV the jet from the dominant background ($W+$ jets) are, on average, less energetic than the jets from the Higgs boson signal. An advantage of $H \to WW \to \ell \nu jj$ over channels with two final state neutrinos is the possibility of fully reconstructing the Higgs boson mass. This is done constraining the mass of $\ell\nu$ to be equal to the mass of the W.

After the discovery of a resonance at 125 GeV the current analysis [46] is focused in the low mass region using $H \to WW^{(*)} \to \ell\nu\ell\nu$. The high luminosity in 2012 results in a large Drell-Yan background to the same-flavour final states, due to the deterioration of the missing transverse momentum resolution. For this reason, and the fact that the $e^{\pm}\mu^{\mp}$ final state provides more than 85% of the sensitivity of the search, the same-flavour final states have not been used in the current analysis. Events are classified into two exclusive lepton channels depending on the flavour of the leading lepton ($e\mu$ and μe). To maximise the sensitivity to SM Higgs events, further selection criteria depending on the jet multiplicity are applied (0-jet, 1-jet, $\geq$ 2-jets). No narrow invariant mass peak can be reconstructed and transverse mass variable, m_T [47], is used to test for the presence of a signal for all jet multiplicities.

- $H \to ZZ^{(*)}$ can cover a wide mass range, and offers several possibilities with the Zs decaying to charged leptons, neutrinos or quarks. Above $M_H = 2M_Z$, final states involving only electrons and muons are the 'gold-plated' modes, leading to a narrow peak on top of a relatively smooth background. Their reach can go down to 120 GeV, except in the region close to $2 \times M_W$, where the Higgs decays almost exclusively to W bosons. For higher masses (above roughly 200 GeV) $H \to ZZ \to \ell\ell\nu\nu$ [48], $H \to ZZ \to \ell\ell q\bar{q}$ [49, 50] and, in principle, $H \to ZZ \to \ell\ell\tau\tau$, can increase the yields of $H \to 4\ell$ searches.

  Currently the analysis is focused in the low mass region using $H \to ZZ^{(*)} \to 4\ell$ channels selecting two pairs of isolated leptons, each of which is comprised of two leptons with the same flavour and opposite charge [51]. The largest background comes from continuum $(Z^{(*)}/\gamma^*)(Z^{(*)}/\gamma^*)$ production. For low masses there are also important background contributions from $Z+$jets and $t\bar{t}$ production, where charged lepton candidates arise either from decays of hadrons with b or c quark content or from misidentification of jets. Four different analysis sub-channels, $4e$, $2e2\mu$, $2\mu 2e$ and 4μ, arranged by the flavour of the leading lepton pair, are used.

Clearly one would like to combine the information from the various independent channels, on one hand to increase the overall sensitivity and on the other hand to provide a single measurement of the signal significance. A detailed statistical treatment for the combination of the most relevant ones in ATLAS ($H \to \gamma\gamma$, $H \to \tau^+\tau^-$, $H \to WW \to e\nu\mu\nu$ and $H \to ZZ^* \to 4\ell$) was studied and is described in ref. [38]. It follows a frequentist approach that includes systematic uncertainties by use of the *profile likelihood ratio*, outlined in appendix A.

1.7 Beyond the Standard Model

All the discussions up to now were done in the context of the Standard Model, usually assuming the existence of a single Higgs boson. Even if the SM is very successful in explaining basically all the data in particle physics experiments, it has some clear limitations. Going beyond particle experiments, the SM does not include gravity, has no candidate for dark matter – which should be four times more abundant than the ordinary one – and does not explain the baryon asymmetry in the universe.

From the theoretical point of view, the number of free parameters (18) is considered excessive and from the mass of the electron (~ 0.5 MeV) to the top-quark mass (~ 171 GeV) there are more than five orders of magnitude. Including the neutrinos, which are considered massless in the SM, the mass range goes to down to milli-electron-volts. The model offers no explanation for these parameters nor for the fact that $\mu^2 < 0$, in order to generate the spontaneous symmetry breaking. The mechanism clearly distinguishes strong and electroweak interactions and no real unification between them exist, as the evolution of the three SM coupling constants does not lead to a common crossing point at a high energy scale.

Moreover, there is the hierarchy problem that involves the Higgs boson. Unlike the other logarithmic divergences found in the SM when including higher order corrections, the Higgs mass has a quadratic one. The contributions from fermions and bosons at one-loop are represented in Fig. 1.16. Introducing a cut-off Λ, above which the Standard Model is not valid any more, the physical mass M_H becomes the difference between a 'bare mass' and an expression proportional to Λ^2. If this cut-off is placed at scales where the other three interactions should be unified ($\sim 10^{16}$ GeV), one must arrange for a cancellation of more than 10 digits to obtain $M_H < 1$ TeV. This very unnatural fine-tuning is viewed as a strong motivation for the appearance of new physics effects, likely in the TeVscale.

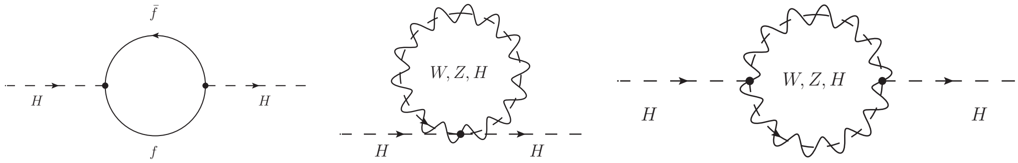

Figure 1.16: Feynman diagrams for the one-loop corrections to the Higgs boson mass.

The hierarchy problem is solved for instance in supersymmetric (SUSY) extensions of the SM. With the introduction of a bosonic (fermionic) partner for each fermion (boson), the quadratic divergences are automatically removed as the partners contribute with opposite signs. Moreover, SUSY models usually have a candidate for dark matter and provide a more natural explanation for electroweak symmetry breaking, as μ^2 is positive at a higher unification scale but becomes negative at the electroweak scale when loop corrections are considered.

The most celebrated of them is the Minimal Supersymmetric Standard Model (MSSM). In the general case, it has more than 100 free parameters, but some assumptions can reduce this number to about 10, on top of the SM ones. When it comes to the Higgs sector, the MSSM is an example of a Two Higgs Doublet Model (2HDM), with the phenomenology defined basically by the ratio of the vacuum expectation values of the two doublets ($\tan\beta$) and one mass. These models predict three neutral Higgses and two charged ones. The lightest neutral can be roughly indistinguishable from the SM one, having its mass limited to about 130 GeV in the MSSM. The other two neutrals might also be within the reach of the LHC, and the observation of another charged scalar heaviest than the one already discovered would be a clear proof of physics beyond the SM.

Detailed studies of the discovery potential of MSSM Higgses have been carried on both by ATLAS and CMS, and are described in refs. [39, 52]. In summary, at least one neutral particle should be found if present and large regions of the parameter space can be covered both for charged and neutral Higgs bosons with a few tens of fb^{-1}. Most of the accessible final states involve tau leptons and b-quarks, as the couplings to vector bosons are reduced proportionally to $\tan\beta$.

In many alternatives to the SM, including some MSSM scenarios, the Higgs decays mostly to particles that do not interact in the detector. To trigger on those events, associated production with top-pairs or vector bosons through Higgs-strahlung or VBF is required. The LHC also provides sensitivity to such cases beyond the LEP limits, and could exclude branching ratios (of $H \to$ invisible) below 90% for masses up to 250 GeV [53] if the Higgs couplings to W and Z bosons are similar to the SM ones.

Finally, one should consider the possibility that the Higgs does not exist. Some new dynamics must come up to explain electroweak symmetry breaking and restore unitarity in the VV scattering. Di-boson production can be the key to study its phenomenology. This time one has to exclude all the allowed mass range for a SM Higgs.

CHAPTER 2

The Large Hadron Collider

The Large Hadron Collider (LHC) [54] is the world's newest and most powerful tool for research in particle physics. It is a 26.7 km two-ring superconducting collider capable of accelerating counter-rotating proton beams to a center of mass energy ($\sqrt{s}$) of 14 TeV, and lead ions (Pb) to 2.8 TeV per nucleon.

The project started in the early '90s, when the scientific community begun to design a high energy physics collider able to deliver a center of mass energy one order of magnitude greater than the other already existing colliders (LEP and Tevatron). The main objective of this new machine would have been the investigation of the nature of electroweak symmetry breaking and the search for physics beyond Standard Model at TeV scale: this includes the search for the Higgs boson and the clarification of the issues related to Higgs boson mass scale.

The tunnel that previously hosted the LEP accelerator is now used by the LHC machine. It comprises eight straight sectors and eight arcs and lies between 45 m and 170 m below the surface. LEP operated from 1989 to 2000, colliding electrons and positrons at $\sim$ 90 GeV in its initial phase, reaching $\sqrt{s} = 209$ GeV in the end of its operations, aiming at the production of Z bosons and precise studies related to this particle. An upgraded machine reached $\sqrt{s} = 209$ GeV and was able to form W pairs and look for the Higgs boson. Synchrotron radiation was the limiting factor for the energy achievable at LEP and what drove the tunnel geometry: the acceleration in the long straight sections compensated the high radiation losses in the curved ones.

Center of mass energies achievable at the LHC are seven times higher than the previous record, detained by the Tevatron. This is only possible through several steps that take place in the CERN accelerator complex before the beam injection at the LHC. The chain is illustrated in Fig. 2.1. A hydrogen bottle is the beginning of the process, from where the protons are extracted. A linear accelerator (LINAC 2) bring their energy to 50 MeV and is followed by a circular booster (PSB) where the beams reach 1.4 GeV. The Proton Synchrotron (PS) and the Super Proton Synchrotron (SPS) are the last two steps, where the particles attain 26 GeV and then 450 GeV before being transferred to the LHC. The beams are injected in bunches with a length corresponding to 1.71 ns (reduced to 1.06 ns for collisions) and nominally spaced by 25 ns. Consequently, the bunch crossing occurs at a frequency of 40 MHz to induce the collisions.

Being a particle – particle collider (as opposed to particle – anti-particle), the LHC is composed of two separate beam-lines where the protons and ions are deflected by opposite magnetic fields to follow circular trajectories. A "two-in-one" magnet design was adopted to cope with restrictions in the tunnel diameter, with two coils sharing the same cooling infrastructure. Superconducting dipole magnets are the key elements of the machine, responsible for bending the beams with magnetic fields above 8 T. The

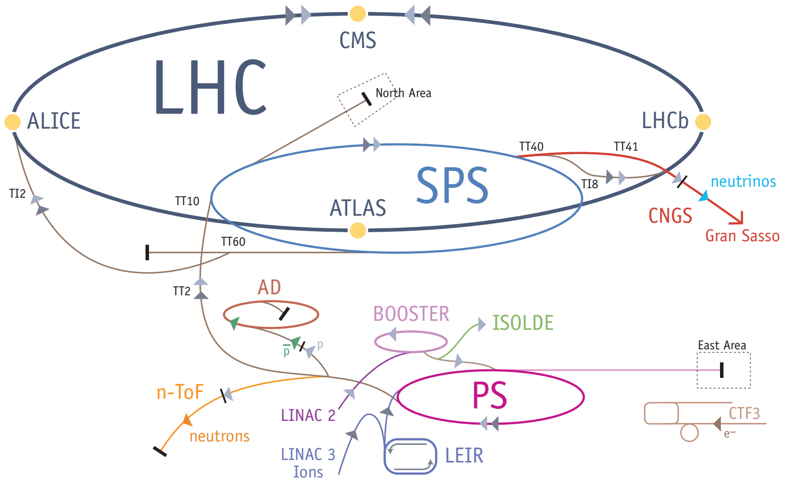

Figure 2.1: Illustration of the LHC injector complex. The LHC experiments are indicated with yellow circles.

1232 dipoles, and the 392 quadrupoles responsible for focusing the beam operate at temperatures below 2 K maintained by superfluid helium.

The acceleration is performed by radio-frequency (RF) cavities. A 400 MHz superconducting system increases the beam energy by 485 keV at each turn until it reaches 7 TeV. The limiting factor for the LHC is not the acceleration itself but the bending power of the dipole magnets.

2.1 Differences between electronic and hadronic collider

The main limitation to the energy of electron-positron collider as LEP is the loss due to synchrotron radiation. In fact, charged particles moving along a curve trajectory loose energy following the relation [55]:

$$\frac{dE}{dt} \propto \frac{E^4}{m^4 R} \tag{2.1}$$

where E and M are particle's energy and mass, while R is the trajectory's radius of curvature. This implies that at fixed energy and collider dimensions (radius), electrons loose $(m_p/m_e)^4 \sim 10^{12}$ times more energy than a proton beam with the same characteristics. The use of electrons would have been possible only in a synchrotron with a much larger radius or in a linear accelerator, options much more expensive than the one adopted.

A hadron collider brings some problems that are absent in leptonic colliders due to the proton's composite structure. Proton-proton collisions can be of two different types: soft collisions or hard collisions [1].

---

[1] A generic mixture of soft and hard collisions is called minimum bias event.

Soft collisions are distant collisions, with protons interacting as a whole object. These interactions have a small transferred momentum and the interaction's products have a small transverse momentum ($\langle p_T \rangle \simeq 500\,\text{MeV}$).

In hard collisions protons interact revealing their inner structure: the collision is studied in terms of QCD processes between different partons. In this type of interaction, the transferred momentum is large and there is a chance to generate new particles.

Furthermore, in hadron colliders the partonic center of mass energy is unknown, making kinematic calculation more difficult.

Another problem comes from the fact that the cross section for hard collisions, which are important for the discovery of new physics, is much smaller than the one for soft collisions: this creates the need for a high luminosity operating collider. In the LHC high luminosity regime, at every bunch crossing there are about 25 soft collisions that will sum themselves to each interaction with large transverse momentum. This soft-collision background is usually called pile-up.

2.2 Luminosity

A particle accelerator should aim at producing collisions at the maximum rate with the highest possible center of mass energy. The number of events per second generated in the collisions is given by:

$$N_{events} = L \times \sigma_{event} \tag{2.2}$$

where σ_{event} is the event cross section and L is the machine luminosity. The luminosity depends only on parameters of the beam through the equation:

$$L = \frac{N_b^2 n_b f_r \gamma_r}{4\pi \epsilon_n \beta^*} F \tag{2.3}$$

where (the nominal parameters for the LHC are given in parenthesis):

- N_b is the number of particles per bunch ($\sim 10^{10} - 10^{11}$),
- n_b is the number of bunches per beam (2808),
- f_r is the revolution frequency (11 245 Hz),
- γ_r the relativistic gamma factor (~ 7000),
- ϵ_n the normalized transverse beam emittance (3.75 μm), related to its size,
- β^* is the beta function at the collision point (0.55 m), related to the beam focusing,
- F is the geometric luminosity reduction factor if the beams do not collide head-on. A crossing angle of 285 μrad will be introduced to prevent collisions outside the nominal interaction points, leading to $F = 0.84$.

2.3 Startup and first physics run

The first beams circulated in the LHC by September 10, 2008 [28]. At that time, almost all the elements of the accelerator were only tested to reach a center of mass energy of 10 TeV. Nine days later an incident was caused by a faulty electrical connection between two magnets during powering tests of the main dipole circuit [56]. Helium leakage into the tunnel and serious mechanical damage delayed the operations by about a year.

Repairs and consolidation work allowed the accelerator to resume its program in the end of 2009. The first collisions were achieved in November 23 and the world energy record was set one week later, with 1.18 TeV beams colliding at $\sqrt{s} = 2.36$ TeV.

After a Christmas break, the LHC beams were ramped to 3.5 TeV and the research program started in March 30, 2010. During 2011 LHC collected $5\,\text{fb}^{-1}$ at $\sqrt{s} = 7\,\text{TeV}$. During 2012 LHC delivered $23\,\text{fb}^{-1}$ at $\sqrt{s} = 8\,\text{TeV}$. Figure 2.2 shows the evolution of the data taking. On December 17, 2012, after three years of data taking LHC completed the first proton run. In 2012 the luminosity has reached $7.7 \times 10^{33}\,\text{cm}^{-2}\text{s}^{-1}$, more than twice the maximum value obtained in 2011 ($3.5 \times 10^{33}\,\text{cm}^{-2}\text{s}^{-1}$). Running will resume in 2015 with increased collision energy of 13 TeV and another increase in luminosity.

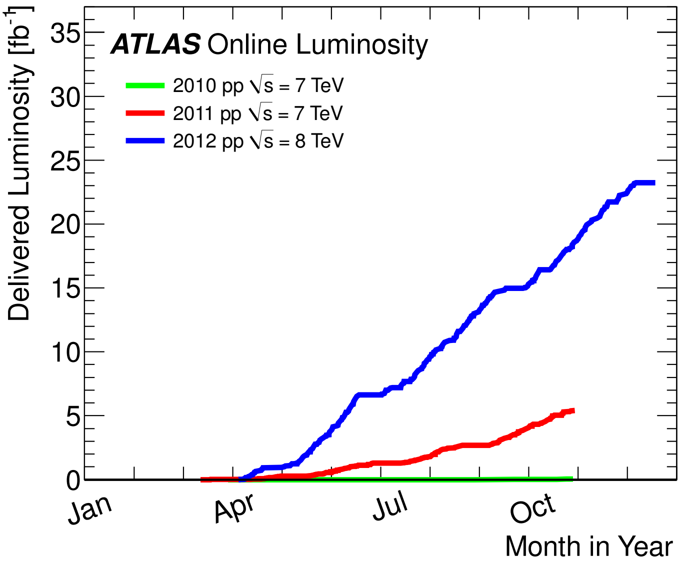

Figure 2.2: Cumulative luminosity versus day delivered to ATLAS during stable beams and for p-p collisions. This is shown for 2010 (green), 2011 (red) and 2012 (blue) running.

2.4 The LHC experiments and physics research

The LHC beams can collide in four different points, all instrumented with large experiments: ATLAS (A Toroidal LHC ApparatuS), CMS (Compact Muon Solenoid), ALICE (A Large Ion Collider Experiment) and LHCb.

ATLAS and CMS are general purpose detectors with broad physics programs. Studies of the Standard Model and searches for evidences of new physics are among their main objectives. Both were designed to operate at the highest luminosity achievable at the LHC. A more detailed description of ATLAS will be given in the next chapter.

ALICE is specialized in heavy-ion physics and is devoted to the characterization of quark-gluon plasma, a phase that should have existed in the early universe when extremely high temperature and/or densities were present. Although the other experiments also foresee studies with heavy ions, ALICE is the only one dedicated to the subject.

LHCb will focus on b-quark physics and precise CP violation measurements, addressing the question of apparent violations of the symmetry between matter and antimatter in the universe. It is designed to operate at a luminosity almost two orders of magnitude lower than the nominal one.

The study of the Standard Model and the search for new phenomena in proton-proton collisions involve the detection of very rare processes. The associated cross sections are many orders of magnitude below the total cross section, dominated by Quantum Chromodynamics effects. Their dependence with the center of mass energy is shown in Fig. 2.3. The figure highlights some of the interesting processes in the collisions, mentioned below:

- B-physics studies will probe the CP violation in systems involving the b-quark.
- Detection of electroweak bosons W and Z and precise measurement of the W boson mass constitute a powerful consistency test of the Standard Model.
- Studies with top quarks include precise measurements of its mass and production cross section, detection of single top events and searches for top – anti-top ($t\bar{t}$) resonances. The top is the heaviest known particle and plays a major role in constraining new physics phenomena. The LHC will be a top-factory with millions of particles produced per year.
- Higgs boson searches are the central goal of ATLAS and CMS and the main subject of this thesis. Its existence is behind the mechanism that originates the mass of the other particles in the Standard Model. The Higgs mass itself is a free parameter and will have to be determined.
- Physics beyond the Standard Model is expected in the energy regime probed by LHC collisions. Supersymmetric extensions of the SM foresee the production of dark matter that would escape the detection but induce large amounts of missing energy. Models based on extra-dimensions usually include heavy gauge bosons (W' and Z') with masses in the TeV range. A wide variety of phenomena and models will be tested at the LHC.

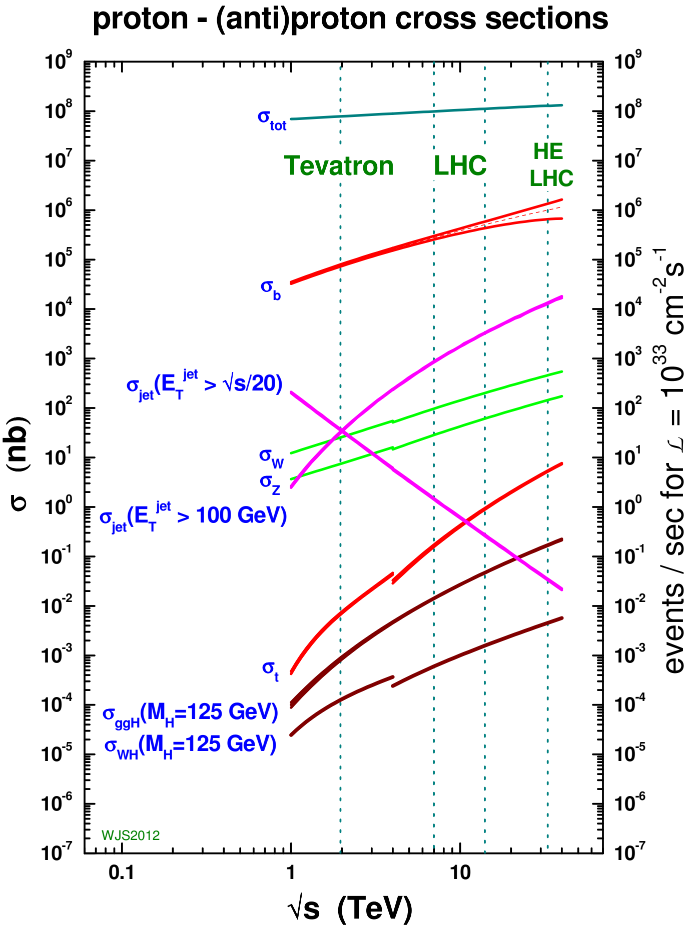

Figure 2.3: Cross sections of various physics processes in proton-proton (or proton anti-proton) collisions as a function of the center of mass energy $\sqrt{s}$. The scale on the right-hand side show the event rate with the design LHC luminosity. The vertical bands correspond to the center of mass energies at the Tevatron and the LHC.

CHAPTER 3

The ATLAS experiment

The ATLAS (A Toroidal LHC ApparatuS) collaboration is composed by more than 3000 physicists from 38 countries and 174 universities and laboratories. Together with CMS, ATLAS is a general purpose detector, designed to explore a wide range of physical processes and take advantage of the full LHC program.

The detection of rare processes produced in the LHC collisions imposes stringent demands on the capabilities of the experiment. To provide sensitivity to basically any evidence of new physics beyond the Standard Model, ATLAS had to meet the following requirements:

- Full azimuthal coverage and large geometrical acceptance.
- Excellent tracking capability with precise momentum determination over a wide range of momenta – from hundreds of MeV to a few TeV.
- Vertexing detectors close to the beam line, to identify b-quark jets and tau-leptons.
- Hermetical calorimetry for missing transverse energy measurements, and fine segmentation, for the measurement of photons, electrons and jets.
- Good muon identification and momentum measurement up to a few TeV.
- Fast triggering systems, to spot interesting events and reduce background levels for efficient storage.
- Radiation hardness to tolerate the large particle fluxes provided by the LHC without loss of performance or important ageing effects.

Those demands were achieved with an Inner Detector (ID) immersed in a 2 T solenoidal magnetic field, followed by electromagnetic and hadronic calorimeters, and a large Muon Spectrometer (MS) mounted inside air-core toroids. The configuration of the magnet systems has driven the design of the rest of the detector, illustrated in figure 3.1.

In what follows, the details of the sub-systems are given, including the trigger and software framework. But before, it is useful to present a few definitions and conventions which will be used throughout the text.

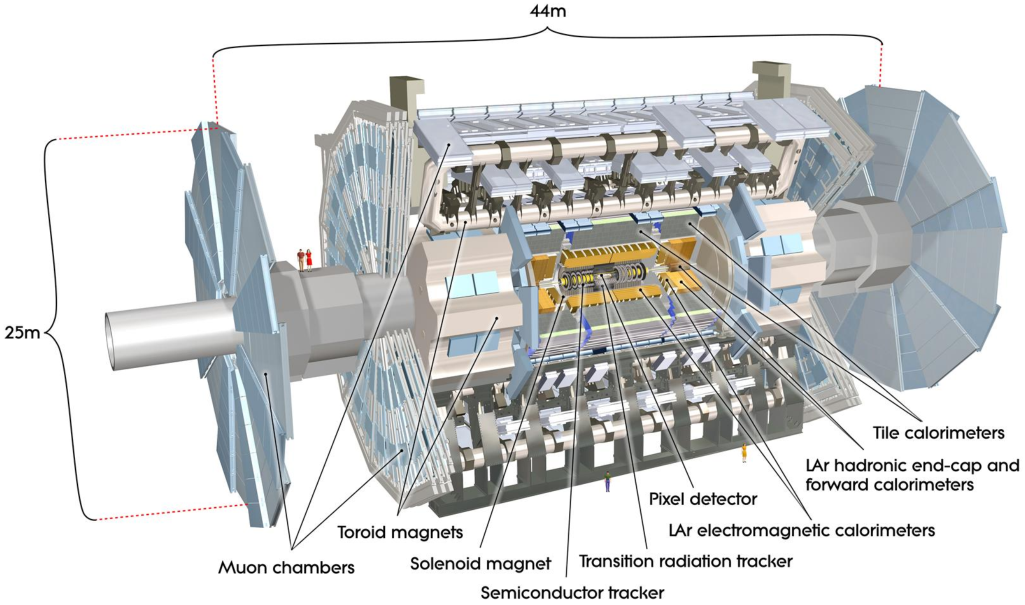

Figure 3.1: Cut-away view of the ATLAS detector, with the different sub-systems identified.

Geometry and coordinate system

ATLAS has cylindrical shape, with 25 m height, 44 m length and weights 7000 tonnes. The center of the detector corresponds to the interaction point (I.P.) and defines the origin of the coordinate system.

A right-handed Cartesian system, illustrated in Fig. 3.2, is used. The z-axis is defined by the beam direction, while the x-axis points towards the center of LHC and the y-axis points upwards in the vertical direction. A polar system is frequently used, and defined by the radial vector R, the azimuthal angle ϕ, and the polar angle θ. R starts at the origin of the system, ϕ is measured from the x-axis, and runs from $-\pi$ to π, while θ is comprised between 0 and π.

The transverse plane, perpendicular to the beam line, is the $x-y$ plane. Several quantities are expressed in this plane, such as the transverse momentum (p_T) and the transverse energy (E_T), and can be defined as:

$$p_T = P \sin(\theta) \tag{3.1}$$

A convenient way of expressing the polar angle is the pseudo-rapidity, η, defined by:

$$\eta = -\log\left(\tan\frac{\theta}{2}\right) \tag{3.2}$$

For highly relativistic particles, η is an approximation of the rapidity

$$Y = \frac{1}{2}\ln\left[(E + P_Z) / (E - P_Z)\right] \tag{3.3}$$

which transforms additively under boosts in the z direction. As a consequence of the last statement, differences in rapidity ΔY , and the shape of the rapidity distribution in particle collisions dN/dY are Lorentz invariants [57]. This shape is also flat in the central region up to a few units in rapidity. To determine y, one must know the energy or mass of the particle, while the pseudo-rapidity depends only on the polar angle of the track.

Boosts along the beam axis also do not affect the ϕ angle, and thus it is useful to measure distances in the azimuthal – pseudo-rapidity plane. The distance ΔR is defined as:

$$\Delta R = \sqrt{(\Delta\eta)^2 + (\Delta\phi)^2} \tag{3.4}$$

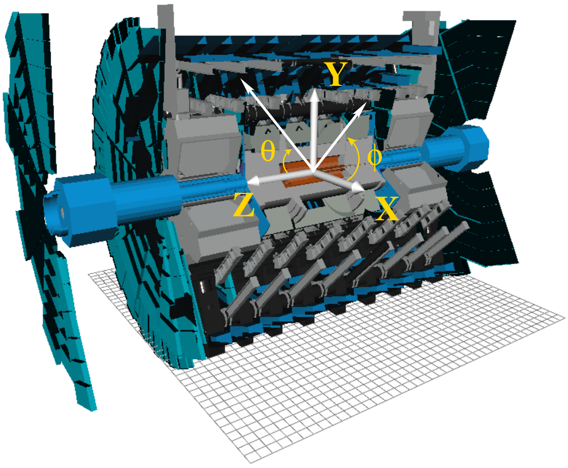

Figure 3.2: Illustration of the coordinate system used in ATLAS.

3.1 The Inner Detector

Precise tracking is achieved by the combination of high bending power and fine granularity position measurements for charged particles. The Inner Detector offers pattern recognition, momentum and vertex measurements, and electron identification capabilities.

Three independent and complementary systems help fulfilling these requirements. The inner part of the tracking volume is composed of precision silicon detectors – pixels and strips – while the outer part comprises straw-tube trackers with the capability to generate and detect transition radiation. The layout of the sub-system is illustrated in figure 3.3 and details can be found in ref. [58].

The high-radiation environment was a major consideration for the design of the Inner Detector sensors, on-detector electronics, mechanical structure and services. The silicon detectors are kept at low temperatures (approximately -5 to -10 C) to minimize the noise after radiation damage. Nonetheless, the innermost layer of the pixels needs to be replaced after three years of operation at full luminosity. The straw-tubes, on the contrary, can operate safely at room-temperature.

The material budget was also minimized, to avoid deterioration of the resolution of both tracking and calorimetry. Still, mainly due to the services and supports it varies

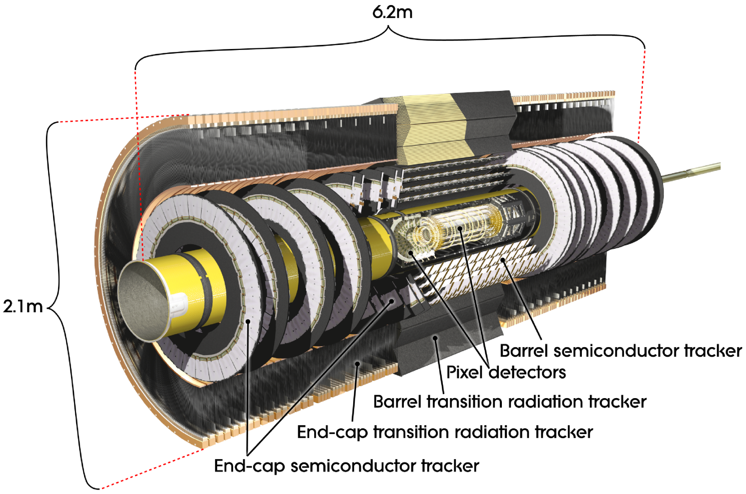

Figure 3.3: Cut-away view of the ATLAS Inner Detector.

from 0.5 to 2.5 radiation lengths (X_0) depending on η (Fig. 3.4). As a consequence, 40% of the photons convert into electron-pairs and electrons lose a great fraction of their energy through bremsstrahlung before reaching the electromagnetic calorimeter.

The system is surrounded by a central solenoid that generates a rather uniform axial magnetic field with a strength of 2 T in the center. The solenoid extends over a length of 5.3 m with a diameter of 2.5 m. The operating temperature of 4.5 K is maintained by a cryostat shared with the barrel electromagnetic calorimeter.

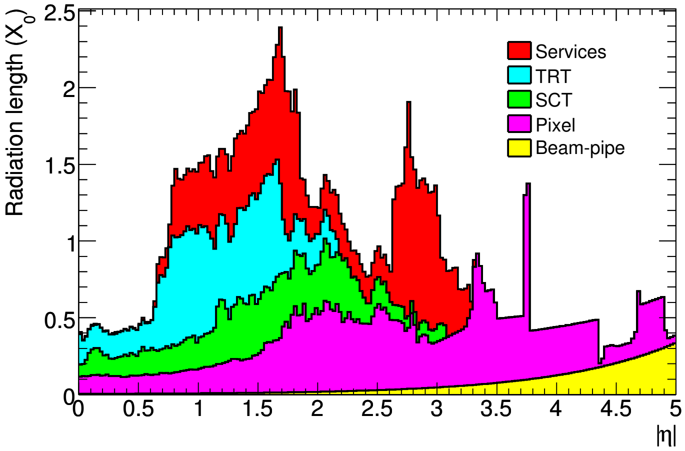

Figure 3.4: Material distribution at the exit of the Inner Detector envelope as a function of $|\eta|$ (averaged over ϕ).

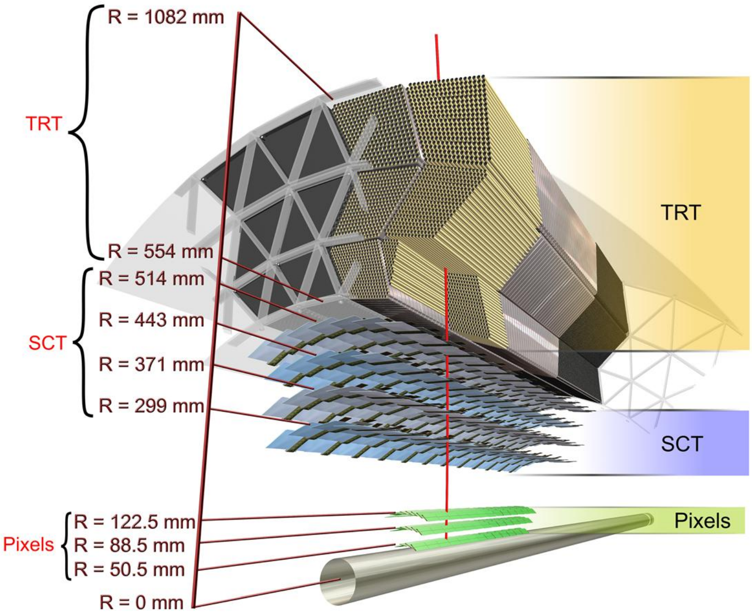

Figure 3.5: Illustration of the structural elements and sensors with their respective position, traversed by a track in the barrel region of the Inner Detector.

3.1.1 The pixel detectors and the silicon micro-strip trackers (SCT)

The precision tracking detectors (pixel and SCT) extend up to $|\eta| < 2.5$. They are arranged in concentric cylinders around the beam axis in the barrel, and disks perpendicular to this axis in the end-cap regions. Typically three pixel layers and four SCT strips are crossed by each track, as illustrated in Fig.3.5.

The pixel layers are positioned at radial distances of 50.5 mm, 88.5 mm and 122.5 mm in the barrel, and 49.5 mm, 58.0 mm and 65.0 mm in the end-caps. All pixel sensors are identical, segmented in $R-\phi$ and z, with intrinsic accuracies of 10 μm in $R-\phi$ and 115 μm in z (R) in the barrel (end-cap). Approximately 80.4 million readout channels are used. The high-precision space point measurements allow the reconstruction of short lived particles and the associated production vertices. This is of fundamental importance in the identification of b-quark jets.

Following the pixel detectors, eight layers of silicon strips are placed in 2-by-2 structures, providing four space point measurements for each track. The intrinsic accuracy per module is 17 μm in $R-\phi$ and 580 μm in z (R) in the barrel (end-cap), with a total of 6.3 million readout channels.

3.1.2 The transition radiation tracker

The outer part of the Inner Detector is composed of layers of gaseous straw tubes inserted in transition radiation material. With an average of 30 hits per charged particle track, the transition radiation tracker (TRT) provides continuous tracking and electron identification complementary to that of the calorimeter over a wide range of energies. Enhanced pattern recognition and significant improvement of the momentum resolution are achieved with this detector, which extends radially from 56 to 107 cm over $|\eta| < 2.0$.

The TRT only provides $R - \phi$ information in the barrel and $z - \phi$ in the end-cap, for which it has an intrinsic accuracy of 130 μm per straw. In the barrel region, straws with a diameter of 4 mm and 144 cm long are disposed parallel to the beam axis, with their wires divided around $\eta = 0$. In the end-cap region, the 37 cm long straws are arranged radially in wheels. The total number of TRT readout channels is approximately 351 000.

The tubes are filled with a non-flammable xenon-based gas mixture of 70% Xe, 20% CO_2 and 10% CF_4. This ensures high efficiency in the detection of ionization signals and transition radiation photons, produced in the polypropylene fibres that surround the straws. Typically, seven to ten high-threshold hits from transition radiation are expected for electrons with energies above 2 GeV. This capability is illustrated in figure 3.6.

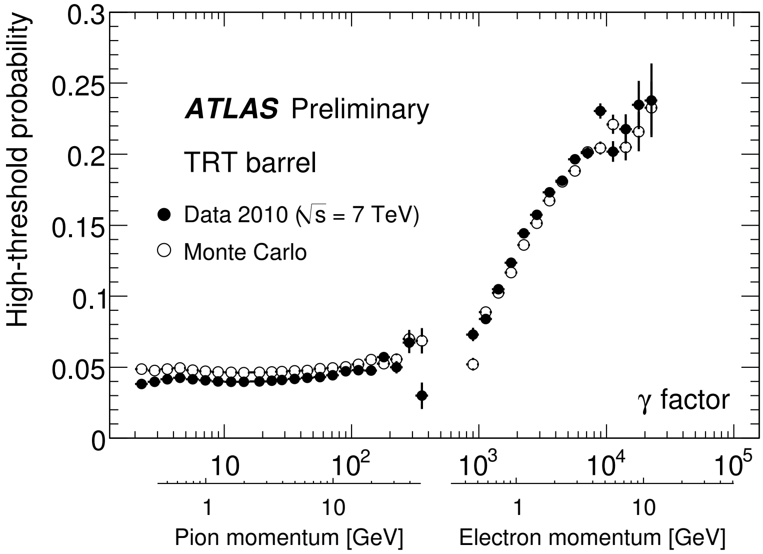

Figure 3.6: Probability of a transition radiation high-threshold hit in the TRT barrel as a function of the Lorentz Factor. Measurements from 2010 LHC collision events are compared to predictions from Monte Carlo simulations.

3.1.3 Inner Detector tracking performance

The Inner Detector offers robust pattern recognition and high performance tracking in both $R - \phi$ and z coordinates. Precision silicon trackers close to the beam line are complemented by straw tubes providing many space point measurements with a longer lever arm. As a result, a reconstruction efficiency above 99% is obtained for muons with transverse momenta above 5 GeV for all pseudo-rapidities, as shown in Fig. 3.7a. The efficiency for reconstructing pions and electrons around 5 GeV is expected to go down to $\sim 80\%$ at large rapidities, becoming larger and more uniform as a function of $|\eta|$ at higher momenta. Multiple scattering, hadronic interactions in the case of pions and bremsstrahlung effects in the case of electrons are behind such inefficiencies.

Overall, the momentum resolution can be approximated by the formula: $\sigma_{p_T}/Pt = 0.05\%\, p_T(\mathrm{GeV}) \oplus 1\%$. Low-$p_T$ tracking is limited by the amount of material in the detector, while for large pseudo-rapidities the absence of the TRT implies a degradation of the momentum resolution. The expected momentum resolution for muons as a function of η is given in Fig. 3.7b.

In addition, the impact parameter at the perigee, i.e. the point of closest approach with respect to the beam line, is determined accurately. The expected resolution on the modified longitudinal impact parameter ($z_0 \times \sin\theta$) is of a few hundred microns, while in the transverse plane (d_0) it goes down to 10 μm for high momentum tracks. Low momentum particles are more subject to multiple scattering effects, which limits the resolution. The results obtained with full simulations for pions of $p_T = 1$ GeV, 5 GeV and 100 GeV are shown in Fig. 3.8.

Although these results were evaluated for single particles, the performance is essentially unchanged in the presence of additional tracks [59]. The fine granularity of the silicon detectors ensures low occupancy rates ($< 4\%$) for up 100 collisions occurring per bunch crossing at the LHC, which corresponds to a luminosity of $4 \times 10^{34}\,\mathrm{cm}^{-2}\mathrm{s}^{-1} \times 10^{34}$. Only the momentum resolution may be worsen due to the high occupancy of the TRT (up to 60%), with degradations up to a factor of two.

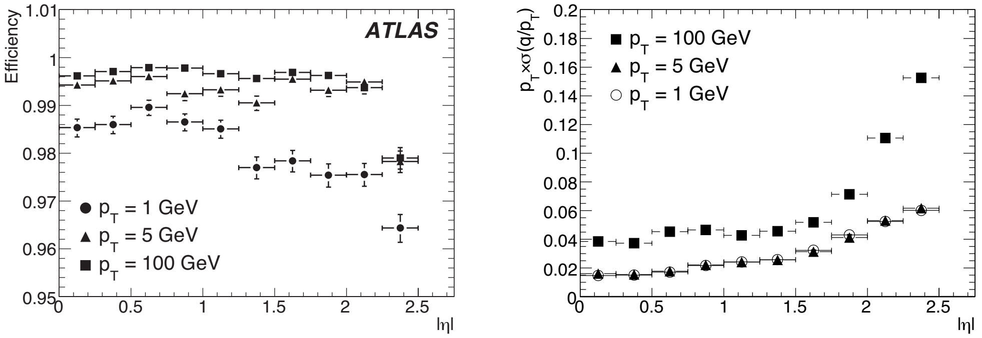

(a) **(b)**

Figure 3.7: Expected tracking performance in terms of (a) reconstruction efficiency and (b) relative transverse momentum resolution as a function of $|\eta|$ for muons of $p_T = 1\,\text{GeV}, 5\,\text{GeV}$ and $100\,\text{GeV}$.

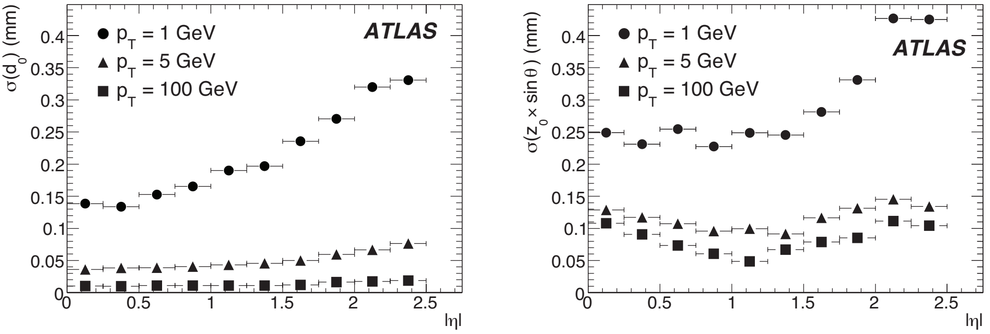

(a) **(b)**

Figure 3.8: Expected resolution on (a) transverse and (b) modified longitudinal impact parameters (d_0 and $z_0 \times \sin\theta$, respectively) as a function of $|\eta|$ for pions of $p_T = 1\,\text{GeV}, 5\,\text{GeV}$ and $100\,\text{GeV}$.

3.2 The Calorimeters

The calorimetric system is located between the Inner Detector and the Muon Spectrometer, covering the pseudo-rapidity range $|\eta| < 5$. Different techniques are used in the barrel and end-cap regions, according to the demands of a wide range of physics process and radiation environment. Measurements of electrons, photons and jets and information about missing transverse energy are provided, given the full azimuthal coverage and good hermeticity of the detectors.

In the region covered by the inner tracker, showers produced by electrons and photons are contained in the finely segmented liquid argon (LAr) electromagnetic calorimeters (EM), with excellent performance in terms of energy and position resolution. Liquid argon technology is also applied in the detection of hadronic activity in the end-cap and forward regions, instrumented by a Hadronic End-cap Calorimeter (HEC) and a Forward Calorimeter (FCal). Chosen for its intrinsic linear behaviour, its stability of response over time and its intrinsic radiation-hardness, the LAr detectors require an operating temperature around 88 K. The barrel EM calorimeter shares the cryostat with the central solenoid, eliminating two vacuum walls. The end-caps are hosted in their own cryostats, used for the EM, the HEC and the FCal.

Hadronic calorimetry is complemented by a scintillator-tile detector of easier assembling and lower cost, extending up to $|\eta| < 1.7$. A layout of the ATLAS calorimeters is presented in Fig. 3.9 and the segmentation of each part is summarized in table 3.1. Each sub-calorimeter is described in the following subsections and their performance is also discussed. The strategies for reconstructing photons are reviewed in 3.3.

An additional function of the calorimeters is to limit the rate of particles escaping to the muon system. The total depth of the EM calorimeter exceeds 22 radiation lengths (X_0) in the barrel and 24 in the end-cap. The hadronic part comprises 9.7 interaction lengths (λ) in the barrel and 10 in the end-caps. This ensures good resolution on high-energy jets and punch-through into the MS well below the irreducible level of prompt muons or the ones from pion and kaon decays. The material budget of the calorimeters as a function of pseudo-rapidity is presented in Fig. 3.10.

3.2.1 The electromagnetic calorimeter

The precision electromagnetic calorimeters are lead-liquid argon detectors with accordion shape absorbers and electrodes. This geometry, represented in figure 3.12, provides full azimuthal coverage without cracks, allows fast signal extraction and segmentation of the active layers in depth. In the barrel the accordion waves are parallel to the beam axis and their folding angle varies along the radius in order to keep the liquid argon gap as constant as possible. In the electromagnetic endcaps, the accordion waves run axially and the folding angle varies with radius, see figure 3.11.

The total calorimetric depth is approximately constant over η, although three layers are used in the region covered by the Inner Detector ($0 < |\eta| < 2.5$), and two both in the higher-η region ($2.5 < |\eta| < 3.2$) and in the overlap region between the barrel ($|\eta| < 1.475$) and the end-caps ($|\eta| > 1.375$). Geometrical limitations and simplicity of construction justify this layout.

Up to $|\eta| = 2.5$, accurate position measurements are obtained by finely segmenting the first layer, with narrow strips of 4 mm pitch. The cell granularity in the barrel is $\Delta\eta \times \Delta\phi = 0.003 \times 0.1$ and varies with η in the end-cap. The middle layer has a constant cell size of $\Delta\eta \times \Delta\phi = 0.025 \times 0.025$ and is the thickest of the three compartments, providing good positioning of photon clusters and precise energy measurement. A

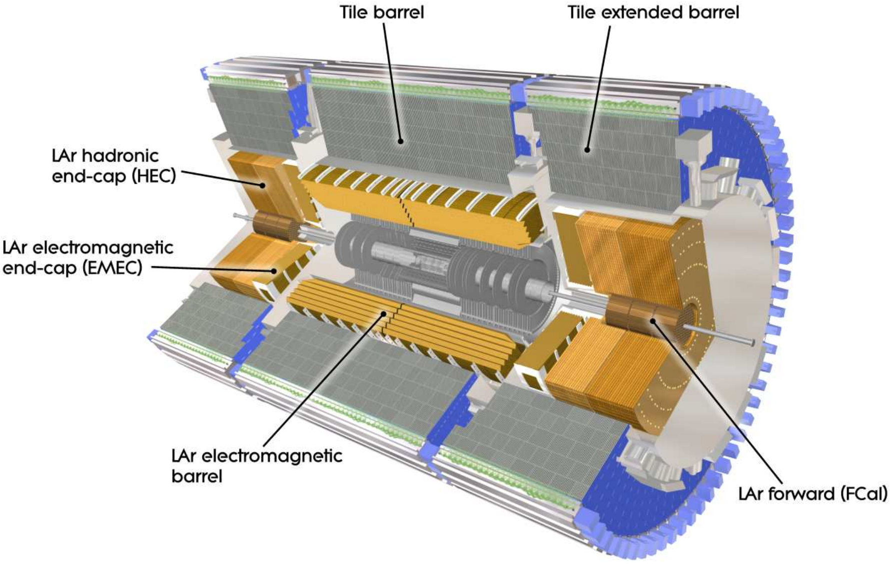

Figure 3.9: Cut-away view of the ATLAS calorimeter system.

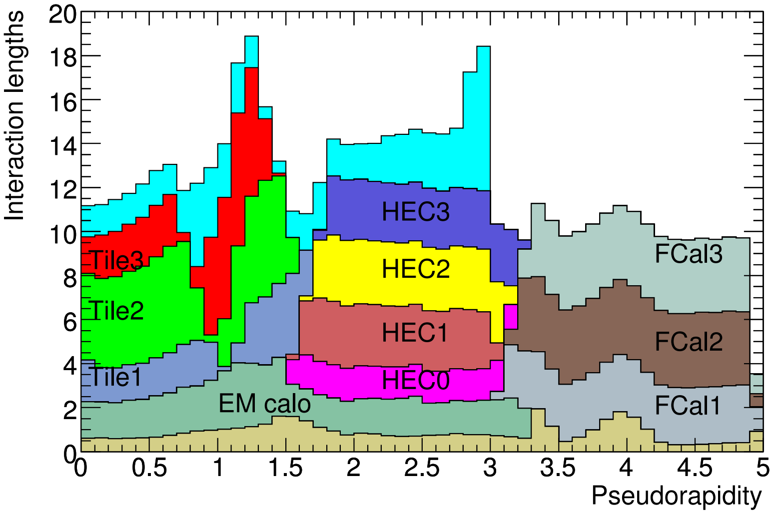

Figure 3.10: Cumulative amount of material, in units of interaction length, in front of and after the calorimeters as a function of $|\eta|$. Also shown for completeness is the total amount of material in front of the first active layer of the Muon Spectrometer (light blue). The peaks at $|\eta| \sim 1.3$ and $|\eta| \sim 3$ correspond to the TileCal extended barrel and a shielding disk, respectively. Details can be found in ref. [58].

back compartment with a granularity of $\Delta\eta \times \Delta\phi = 0.05 \times 0.025$ ensures the shower containment in the EM volume. The higher eta region ($2.5 < |\eta| < 3.2$) exhibits coarser

Calorimeter	**Coverage**		**Granularity ($\Delta\eta \times \Delta\phi$)**
EM calorimeter	**barrel**	**end-cap**	
Presampler	$\|\eta\| < 1.54$	$1.5 < \|\eta\| < 1.8$	0.025×0.1
Sampling 1	$\|\eta\| < 1.475$	$1.375 < \|\eta\| < 3.2$	0.003×0.1^{a} 0.025×0.025^{b} $0.003 - 0.025 \times 0.1^{c}$ 0.1×0.1^{d}
Sampling 2	$\|\eta\| < 1.475$	$1.375 < \|\eta\| < 3.2$	0.025×0.025 0.075×0.025^{b} 0.1×0.1^{d}
Sampling 3	$\|\eta\| < 1.35$	$1.5 < \|\eta\| < 2.5$	0.05×0.025
Tile calorimeter	**barrel**	**extended barrel**	
Sampling 1 Sampling 2	$\|\eta\| < 1.0$	$0.8 < \|\eta\| < 1.7$	0.1×0.1
Sampling 3			0.2×0.1
Hadronic end-cap calorimeter			
Samplings 1-4	$1.5 < \|\eta\| < 3.2$		0.1×0.1^{e} 0.2×0.2^{d}
Forward calorimeter			
Samplings 1-3	$3.1 < \|\eta\| < 4.9$		0.2×0.2

$^{a}|\eta| < 1.4$, $^{b}1.4 < |\eta| < 1.475$, $^{c}1.375 < |\eta| < 2.5$, $^{d}2.5 < |\eta| < 3.2$, $^{e}1.5 < |\eta| < 2.5$

Table 3.1: Pseudo-rapidity coverage, longitudinal segmentation and granularity of the ATLAS calorimeters. The full numbers can be found in ref. [60].

granularity, with the two layer segmented at $\Delta\eta \times \Delta\phi = 0.1 \times 0.1$.

Energy losses by particles crossing the material in front of the calorimeters introduce an uncertainty in the energy measurements. To overcome this difficulty, the EM is complemented by presamplers – thin layers of liquid argon – in the regions up to $|\eta| < 1.8$. The performance of the system is reviewed in section 3.2.4.

3.2.2 The hadronic calorimeters

Two different systems are used as hadronic calorimeters, the one in the end-caps using the radiation hard LAr technology and the barrel one made of scintillating tiles. Their main features are presented here, and their performance is compared in 3.2.4.

The hadronic end-cap calorimeter (HEC) is a parallel plate copper-liquid argon sampling calorimeter. It provides coverage for hadronic showers in the range $1.5 < |\eta| < 3.2$, sitting right behind the electromagnetic end-caps.

Radiation hardness and cost effectiveness drove the choice for this technology and the calorimeter geometry. The HEC is formed by two wheels divided into two segments in depth, with a total of four compartments per end-cap. Each wheel is built from 32 identical wedge-shaped modules, providing projective geometry in the ϕ direction but only "pseudo-projectivity" in η, as illustrated in figure 3.13. The size of the HEC cells is $\Delta\eta \times \Delta\phi = 0.1 \times 0.1$ up to $|\eta| < 2.5$ with twice those values in the rest of the coverage.

In the central region, hadronic activity is measured by the tile calorimeter (TileCal), placed directly outside the EM calorimeter envelope. Steel absorbers and scintillating

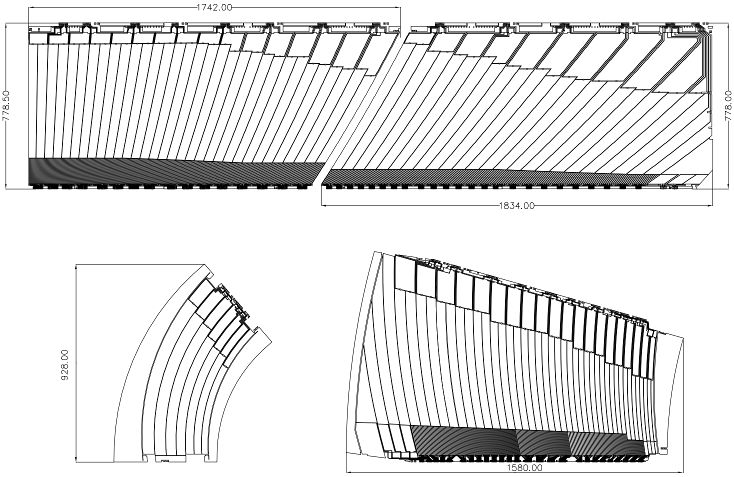

Figure 3.11: The fours types of electrodes of the electromagnetic calorimeter. The two top ones correspond to barrel electrodes: $|\eta| < 0.8$ (left) and $|\eta| > 0.8$ (right). The bottom left is an endcap inner wheel electrode and the bottom right is the outer wheel. Dimensions are in mm.

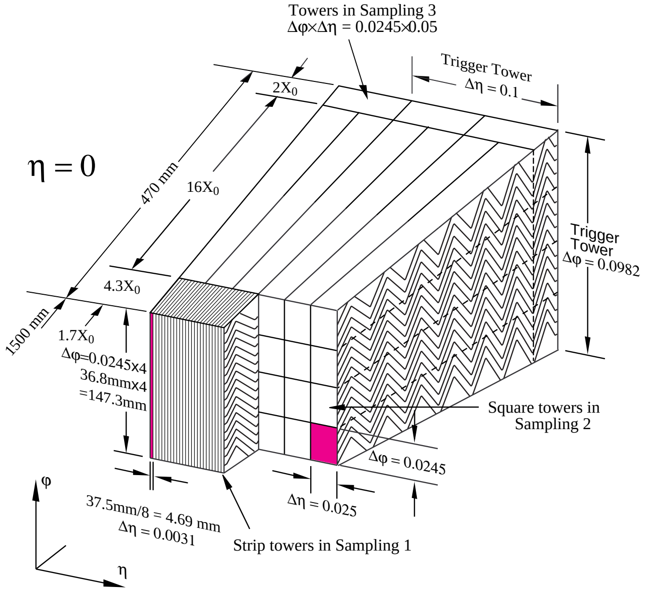

Figure 3.12: Sketch of a barrel module of the electromagnetic calorimeter.

tiles as active material are employed. The two sides of the scintillators are connected to wavelength shifting fibres, and read out by photomultiplier tubes.

The TileCal is divided into a 5.8 m long barrel, covering the region up to $|\eta| < 1.0$ and two extended barrels in the range $0.8 < |\eta| < 1.7$ with 2.6 m in length. It is segmented in depth in three layers, with approximately 1.5, 4.1 and 1.8 interaction lengths (λ) for the barrel and 1.5, 2.6, and 3.3 λ for the extended barrel. This provides maximum radial depth at a minimum cost, with an inner radius of 2.28 m and an outer radius of 4.25 m.

Cables and services from the detectors placed before the tile calorimeter occupy the 60 cm gap between the barrel and the extended barrel. In this region, scintillating tiles assembled in the so called Intermediate Tile Calorimeter complement the energy measurement.

The geometry of TileCal is sketched in figure 3.14, with the layers in depth noted as A, BC and D. The orientation of the scintillator tiles radially and normal to the beam line allows for full projective azimuthal coverage. On the other hand, the grouping of the readout fibres imply a "pseudo-projective" geometry in η. A particle crossing the calorimeter eventually leaves signal in more than one cell per layer, which have granularities of $\Delta\eta \times \Delta\phi = 0.1 \times 0.1$ in in the first two samplings and 0.2×0.1 in the third.

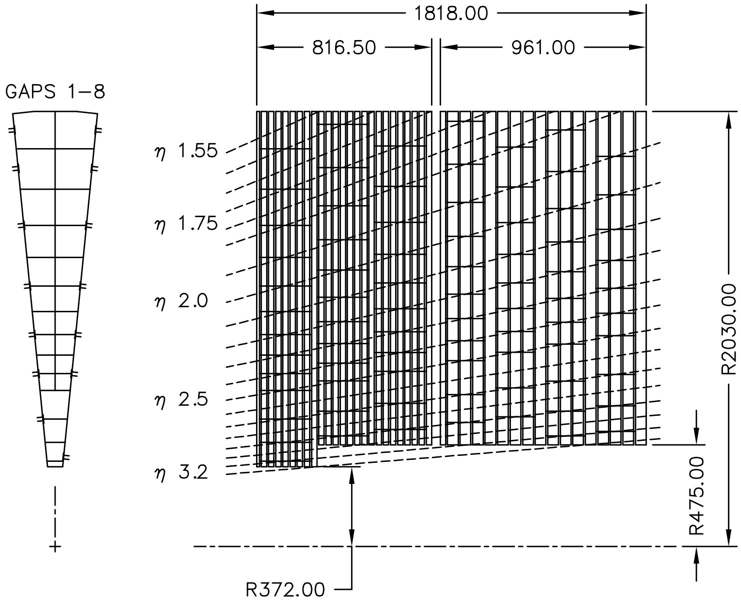

Figure 3.13: Schematic views of the hadronic end-cap calorimeter in $R - \phi$ (left) and $R - z$ (right). The semi-pointing layout of the readout electrodes is indicated by the dashed lines. Dimensions are in mm.

3.2.3 The forward calorimeter

The forward calorimeter (FCal) provides both electromagnetic and hadronic energy measurements, and extend the pseudo-rapidity coverage of the calorimetric system from $|\eta| = 3.1$ to $|\eta| = 4.9$. Although the system is not used for precision measurements, it provides valuable information for missing transverse energy determination and reconstruction of very forward jets.

Radiation tolerance is extremely important in this region, where high particle fluxes are expected. This has resulted in a design with very small liquid-argon gaps, separated by copper absorbers in the first compartment, and tungsten absorbers in the last two. Overall, the thickness of the FCal is of the order of 10 interaction lengths.

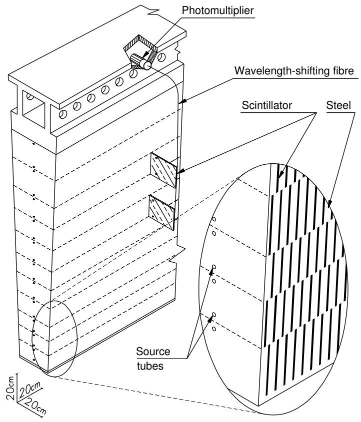

(a) Illustration of the components in a module of the tile calorimeter.

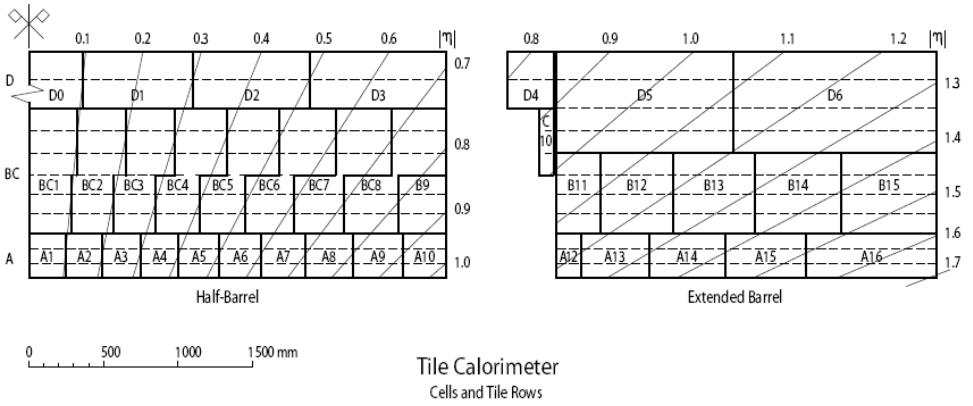

(b) $R-z$ view of the tile calorimeter. The diagonal lines indicate the semi-projective layout of the cells.

Figure 3.14: Schematic views of (a) a module and (b) the full tile calorimeter geometry in the $R-z$ plane.

3.2.4 Performance of the calorimeters

The energy resolution of each sub-calorimeter was evaluated with beams of electrons and pions before their insertion in the ATLAS detector. The experimental measurements, after noise subtraction, have been fitted with the expression:

$$\frac{\sigma(E)}{E} = \frac{a}{\sqrt{E/\mathrm{GeV}}} \oplus b, \tag{3.5}$$

where a is the stochastic term and b the constant term reflecting local non-uniformities in the response of the calorimeter. The design parameters, specified in ref. [61] were fulfilled, and the obtained performance is summarized in table 3.2. More detailed studies are presented in chapter4 using Monte Carlo simulation for electron, unconverted photons and converted photons, showing the behaviour of the sampling term (figures 4.25, 4.26, 4.27 and 4.41) and the constant term (figures 4.28, 4.29, 4.30 and 4.42) along $|\eta|$.

In what concerns the electronic noise, updated information was extracted during the cosmic-ray data taking periods, from 2007 to 2010. The noise was measured in intervals when no track was recorded in ATLAS. During LHC runs this is done in time windows when no collisions should happen. The results correspond to the expectations for both the LAr and Tile calorimeters and are shown in figures 3.15 and 3.16 respectively. No major impacts on jet reconstruction above $\sim 5\,\text{GeV}$ or electron identification above $\sim 0.5\,\text{GeV}$ are expected from these noise levels.

Calorimeter	**Particle**	**Energy Resolution**	
		a (% $\sqrt{\text{GeV}}$)	b (%)
Electromagnetic	electrons	10.0 ± 0.4	0.4 ± 0.1
Hadronic End-Cap	pions	70.6 ± 1.5	5.8 ± 0.2
Forward	electrons	28.5 ± 1.0	3.5 ± 0.1
	pions	94.2 ± 1.6	7.5 ± 0.4
Tile	pions	56.4 ± 0.4	5.5 ± 0.1

Table 3.2: Resolution of the different calorimeters for pions and electrons evaluated with test beam data, given by the stochastic term a and the constant term b as in equation 3.5. The constant term for the full electromagnetic calorimeter is expected to be around 1%.

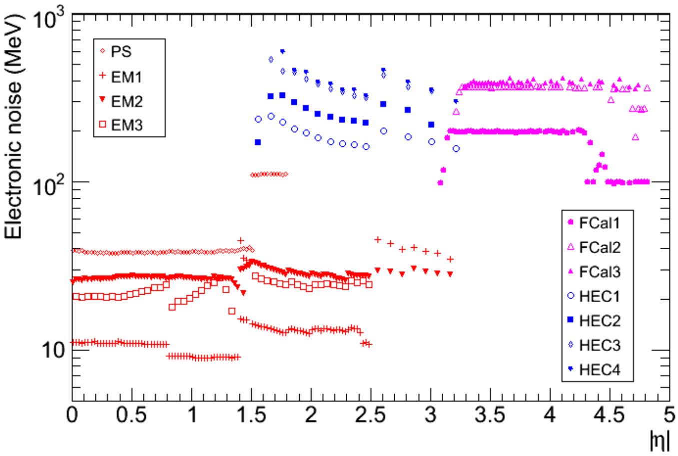

Figure 3.15: Electronic noise in the cells of the liquid argon calorimeters as a function of $|\eta|$.

3.3 Photon reconstruction and associated performance

The EM calorimeter was designed to provide good photon and electron identification over a broad energy range, from a few GeV up to $\sim 5\,\text{TeV}$. Isolated photon with large transverse momentum in the final state are distinguishing signatures for many physics analyses envisaged at the LHC.

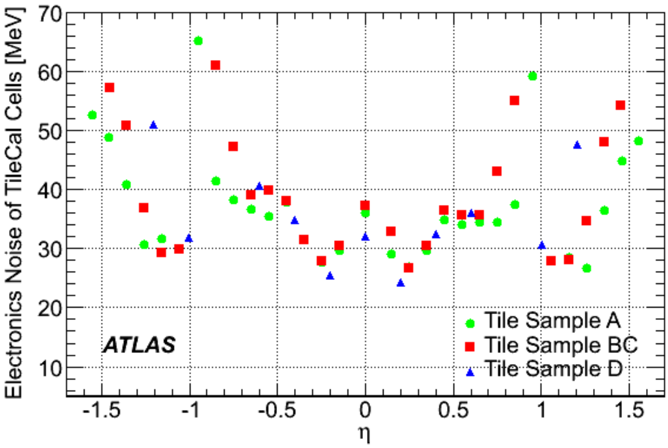

Figure 3.16: Electronic noise in the cells of the tile calorimeter as a function of η.

While the expected cross-section times branching ratio of the Higgs particle decaying into the two photon final state is relatively small, given its distinct signature, isolated high-p_T photons play a significant role in discovering the Higgs particle in the low mass region (see chapter 6). In addition, very high-p_T photons are also signatures of more exotic particles, such as the graviton which is expected to have mass larger than 500 GeV [62], Universal Extra Dimensions [63, 64] and dark matter [65]. These photons appear as single, isolated objects with most of their energy deposited in the electromagnetic compartment of the calorimeter. Thus the primary source for background to these photons, namely fake photons, result from jets with a large electromagnetic component, due to a high fraction of photons from neutral hadron decays, such as $\pi^0 \to \gamma\gamma$. Excellent jet rejection factors are therefore required with reconstruction efficiencies satisfying the needs of different physics channels. The strategies adopted to achieve this goal are briefly discussed here.

3.3.1 Photon conversion

Photons must pass through the ATLAS tracker before depositing their energy in the Liquid Argon Calorimeter. At photon energies above 1 GeV, the interaction of the photons with the tracker will be completely dominated by e^+e^- pair production in the presence of material, otherwise known as photon conversion. All other interactions between the photons and the tracker material, such as Compton or Rayleigh scattering, will have cross-sections which are orders of magnitude below that for the photon conversion, and may thus be safely ignored. The leading order Feynman diagrams for photon conversions in the presence of material are shown in Figure 3.17. The presence of the material is required in order for the conversion to satisfy both energy and momentum conservation.

For photon energies above 1 GeV the cross-section for the conversion process is almost completely independent of the energy of the incident photon, and may be given by the following equation [66]:

$$\sigma = \frac{7A}{9X_0N_A} \tag{3.6}$$

In this expression A is the atomic mass of the target given in g/mol, and $N_A =$

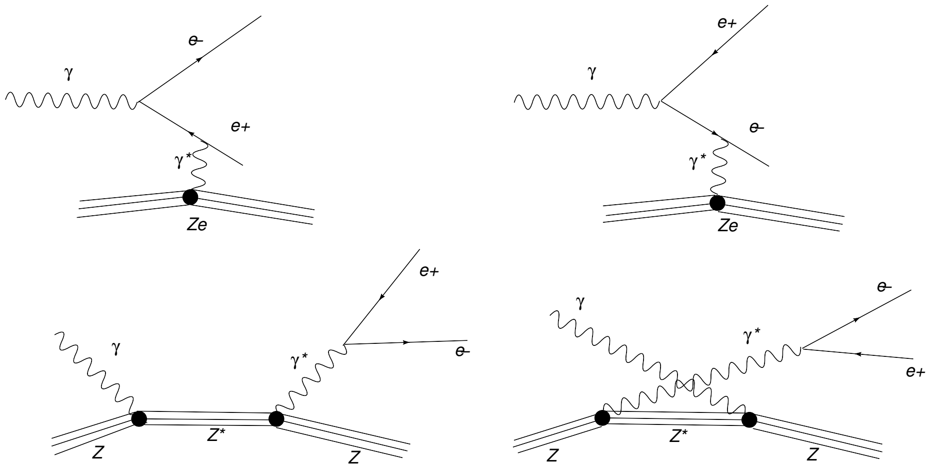

Figure 3.17: Leading-order Feynman diagrams for photon conversions.

6.022×10^{23} is Avogadro's number. X_0 is known as the radiation length of the material through which the photon passes.

The differential cross-section for photon conversions of energies of 1 GeV and above in terms of the quantity $x = (E_{\text{electron}}/E_{\text{photon}})$ is [67]:

$$\frac{d\sigma}{dx} = \frac{A}{X_0 N_A}\left(1 - \frac{4}{3}x(1-x)\right). \tag{3.7}$$

This cross-section is symmetric in x and $1 - x$, the electron and positron energies, and it implies that the momentum of the photon is not simply shared equally between the electron and the positron. Some fraction of the photon conversions will be highly asymmetric, and either the electron or the positron may be produced with a very low energy. If this energy falls below the threshold required to produce a reconstructable track in the ATLAS tracker, then the converted photon will be seen to have only one track, and will be difficult to distinguish from a single electron or positron. This problem is more serious at lower photon energies, as the proportion of conversions which are asymmetric enough to cause the loss of one of the two tracks increases as the photon energy decrease.

3.3.2 Sliding window algorithm

Photons are reconstructed using information from both the calorimeter and the Inner Detector. The standard algorithm starts from ensembles of cells (clusters), defined in the EM calorimeter, and then builds the identification variables based on information from both systems.

The sliding window algorithm [68, 69] is used to find and reconstruct electromagnetic clusters. This forms rectangular clusters with a fixed size, positioned so as to maximise the amount of energy within the cluster. The optimal cluster size depends on the particle type being reconstructed and the calorimeter region. These clusters are the starting point of the calibration and selection of electron and photon candidates. The algorithm looks for regions of approximately 0.1×0.1 in $\Delta\eta \times \Delta\phi$ where the deposits exceed 2.5 GeV and defines the cluster position such that the energy inside the window is maximized.

After the discrimination between electrons and photons (described below) the window size is redefined according to the region of the calorimeter and the particle being reconstructed. In the barrel, electrons need larger clusters than photons due to the bending in the magnetic field in the ϕ direction, which leads to soft photon radiation. In the end-cap, all the particles use the same window since the effect of the magnetic field is smaller. The window sizes were chosen as a compromise between the spread of the energy deposits and the noise (the inclusion of more cells increases the noise). The details can be found in ref. [69].

To distinguish between photons and electrons, a track-matching procedure follows cluster finding. Tracks are required to be within a rectangular window in $\Delta\eta \times \Delta\varphi$ of 0.05×0.10 of the cluster barycentre, and have a track momentum at least 10% of the cluster energy. If such a track is found, the object is assumed to be an electron candidate, its position and energy is calibrated under that assumption, and the calibrated object is stored in the "electron container". The electron reconstruction efficiency at this stage is roughly 93%. Clusters not matched to a track are classified as photons, and are stored in the "photon container". The reconstruction efficiency for photons which do not convert before the EM calorimeter is over 90%.

For photons that do convert in the inner tracker volume, the efficiency is significantly lower, and depends on the radius at which the photon converts. Conversions that occur late in the inner tracker are less likely to have a reconstructed track that is accurately matched to the calorimeter cluster, especially if the track is composed solely of TRT hits. Conversions that occur early in the ID volume, however, often produce a track that matches the cluster, and are reconstructed as an electron. The frequency of such conversions is driven by the amount of material, which depends strongly on η. A plot of the material profile for the inner tracker is shown in Fig. 3.4. In order to increase the container-level efficiency for converted photons, converted photons are recovered from the electron container by searching for electron candidates consistent with being converted photons.

3.3.3 Recovery from electrons

The recovery procedure begins with the track-cluster matching during the reconstruction of electron candidates. When a track is matched to a cluster, it is also checked to see if it is consistent with originating from a conversion vertex. Photons are massless particles, so their conversion products have zero opening angle. A special secondary-vertexing algorithm has been developed to exploit this feature, and is documented thoroughly in [52]. It searches for all pairs of tracks that have opposite signs, and then applies several selection criteria to reduce the combinatorial background, including cuts on: the angle between the two tracks; their separation distance at the point of their closest approach (which should be zero); and the separation of the tracks at the reconstructed vertex (which should be identical to the distance of closest approach, and also zero). After these selection criteria are applied, the combinatorial background is reduced by more than a factor of 100. Some final selection criteria on the quality of the vertex fit, on the invariant mass of the track pair, and on the p_T of the photon candidate are applied, increasing the total rejection to a factor of almost 400. Vertices which survive the selection above are matched to tracks associated with electron candidates, and used to identify possible photon conversions. Electron candidates with an associated vertex are copied from the electron container to the photon container, and can in principle be considered as either an electron or a photon at the analysis level. The total efficiency is over 80% at low R, where the track pairs typically have several precision silicon hits. At larger radii, the efficiency drops to less than 50%, and reaches zero at around $R = 800$ mm. The inefficiencies of the vertex-finding are due to several sources:

asymmetric-track conversions the fractional momentum carried away by one of the tracks in the electron-positron pair can range from 0 to 1, and is roughly flat for photons in the energy ranges considered in this analysis. Thus, some non-trivial number of photons that convert produce one hard and one soft track, where the soft track may not be reconstructed (or may not be matched to its partner by the vertex-finding algorithm).

merged-track conversions extremely energetic photons that convert can produce electron-positron pairs whose tracks do not separate sufficiently in the magnetic field, and are reconstructed as a single track.

late conversions photons that convert at large radii in the inner tracker produce tracks that are difficult to reconstruct, and whose track parameters may be mis-measured due to the lack of precision hits.

The default tracking algorithms, seeded by silicon hits, have poor efficiency for electrons from late conversions, and have zero efficiency for conversions that occur outside of the SCT. To improve the track-finding efficiency for late conversions, a tracking algorithm seeded by pattern-matched track segments in the TRT was developed [52]. This back-tracking algorithm restores good track-finding efficiency out to $R = 800$ mm (beyond which photons that convert can be safely treated as unconverted). To further reduce the total conversion-finding inefficiencies, the recovery algorithm also searches for electron candidates with tracks that are consistent with coming from a secondary vertex, but which are not matched with another track during vertex finding. The basic requirement for such tracks is that they not have a hit in the B-layer of the pixel detector. The lack of such a hit implies that the electron was not prompt, and may be due to a secondary (conversion) vertex. In this case, the vertex position is defined to be the first hit on the track.

After the inclusion of these “single-track” conversions, the total conversion reconstruction efficiency is improved to over 80% for most values of the conversion radius.

As photons may convert at any point in the tracker in the presence of material, the ability to reconstruct conversions will depend strongly on the type of tracking algorithm used. Due to the structure of the ATLAS tracker, photons which convert within 300 mm of the beam axis may be reconstructed with a high efficiency with standard (inside-out) Si-seeded tracking, while photons which convert further from the beam pipe may only be reconstructed using (outside-in) tracks, which begin with TRT seeds with or without associated Si hits

3.4 Photon identification

Photon identification is based on the lateral and longitudinal energy profiles of the shower in the calorimeter. The photon candidate is required to deposit only a small fraction of its energy in the hadronic calorimeter. The transverse shower shape in the second layer of the electromagnetic calorimeter needs to be consistent with that expected for a single EM shower. Finally, the high granularity first layer is used to discriminate photon showers from overlapping showers originating from photon pairs from neutral meson decays produced in jet fragmentation, which are the main background source.

More in detail, the variables used for the photon identification are:

R_{had} the ratio of the total transverse energy in the hadronic calorimeter (in a $\Delta\eta \times \Delta\phi$ region of 0.24×0.24 behind the photon cluster) to the transverse energy of the photon cluster.

R_{had1} : the ratio of the total transverse energy in the first sampling layer of the hadronic calorimeter (in a $\Delta\eta \times \Delta\phi$ region of 0.24×0.24 behind the photon cluster) to the transverse energy of the photon cluster.

w_2 This variable characterizes the lateral width of the shower in η, over a region of 3×5 cells in $\Delta\eta \times \Delta\phi$ around the center of the photon cluster. It is defined as:

$$w_2 = \sqrt{\frac{\sum E_i \eta_i^2}{\sum E_i} - \left[\frac{\sum E_i \eta_i}{\sum E_i}\right]^2} \tag{3.8}$$

where the subscript i indicates the cell index, ranging from 0 to 14.

R_η This variable measures the spread in η of the energy outside of the cluster. It is defined as:

$$R_\eta = \frac{E^{S2}_{3\times7}}{E^{S2}_{7\times7}} \tag{3.9}$$

where $E^{S2}_{x\times y}$ is the energy contained in $x \times y$ cells ($\eta \times \phi$) of the second layer, centred on the cluster used to define the photon.

R_ϕ This variable measures the spread in ϕ of the energy within (and outside of) the cluster. It is defined as:

$$R_\phi = \frac{E^{S2}_{3\times3}}{E^{S2}_{3\times7}} \tag{3.10}$$

where $E^{S2}_{x\times y}$ is defined as it is for R_η.

$F_{\textbf{side}}$ This variable measures the lateral spread in η of the shower. It is defined as:

$$F_{\text{side}} = \frac{E^{S1}_{7\times1} - E^{S1}_{3\times1}}{E^{S1}_{7\times1}} \tag{3.11}$$

where $E^{S1}_{x\times y}$ are the $x \times y$ ($\eta \times \phi$) strips surrounding the strip with the largest energy.

w_{s3} This variable measures the weighted shower width in η in the three strips centred on the strip with the largest energy. It is defined as:

$$w_{s3} = \sqrt{\frac{\sum E_i (i - i_{\text{max}})^2}{\sum E_i}} \tag{3.12}$$

where the index i corresponds to the strip number, and i_{max} is index of the strip with the largest energy.

$w_{s,tot}$ This variable is identical to w_{s3}, except it is measured over all strips in a region of $\Delta\eta \times \Delta\phi = 9.0625 \times 0.2(20 \times 2 \text{ strips})$.

ΔE : This variable attempts to quantify the degree to which there are two peaks present in the energy profile. It is defined as:

$$\Delta E = E^{S1}_{\mathrm{max2}} - E^{S1}_{\mathrm{min}} \tag{3.13}$$

where E^{S1}_{max2} is the energy of the strip that has the second-greatest energy, and E^{S1}_{min} is the energy of the strip with the least energy found between the strips with the greatest and second-greatest energies. For candidates without a distinguishable second peak, this value is close to zero, while candidates that have two peaks in the strips have some larger value.

$E_{\mathbf{ratio}}$: This variable looks at the size of the second maximum relative to the size of the first maximum. It is defined as:

$$E_{\mathrm{ratio}} = \frac{E^{S1}_{\mathrm{max1}} - E^{S1}_{\mathrm{max2}}}{E^{S1}_{\mathrm{max1}} + E^{S1}_{\mathrm{max2}}} \tag{3.14}$$

Groups of variables are used to introduce common criteria for physics analysis. Loose and tight definitions are described below:

loose selection applies cuts only on the variables using the second layer of the calorimeter and the hadronic calorimeter. The cuts were optimized to have the highest background rejection for a photon efficiency at least of 97%. They are identical for converted and unconverted photon.

tight selection applies cuts on all the above listed variables. They were optimized to have the highest rejection for an average efficiency e.g of about 85% for $p_T = 30\,\mathrm{GeV}$. Different cuts are used for converted and unconverted photons since the shower shapes are different for both types of photons (especially for R_ϕ, which has not a discriminating power against background in the case of converted photons).

3.4.1 Fudge factors

Discrepancies between data and Monte Carlo simulations in the distributions of the discriminating variables used to identify photons have been observed. These discrepancies are particularly pronounced for the variables describing the lateral electromagnetic shower shape variables (R_η, w_2, f_{side}). The sources of discrepancies are most probably due to an imperfect simulation of the shower's lateral development in the Monte Carlo.

The differences observed between data and MC simulation in the discriminating variables are measured comparing the shower shape distributions, and parametrized as simple shifts. These shifts (the "fudge factors") are computed as the difference between the means of a given variable in data and MC simulation. An alternative approach obtains the shifts by minimizing a χ^2 between the data and MC distributions. The fudge factors are then applied to the photons discriminating variables of the signal in MC simulation to obtain the corrected efficiency. Fudge factors are computed on top of different preselection and in several interval of $|\eta|$ and p_T.

These factors are applied to the shower shape variables to correct for differences between the data and the simulation in all the steps of the analyses.

An alternative approach to match distribution between data and simulation is the Smirnov transform. The shape differences are parametrized using the Smirnov transform, built in such a way that the transformed MC variables are distributed by construction as the input data PDF. The Smirnov transform function is computed from the data and MC cumulative distribution functions (CDF), exploiting the properties of the inverse transformation method or Smirnov transform[6].

3.5 Photon isolation

Prompt photons are expected to be well isolated from nearby hadronic activity, except for fragmentation photons which are accompanied by hadronic activity. In order to further separate prompt photons from their background of fake photons (mainly light mesons), photon candidates are required to be isolated from nearby hadronic activity. The activity surrounding the photon cluster can either be measured by the ID (track isolation) or by the calorimeter (calorimetric isolation). Calorimetric isolation has been widely used in previous isolated photon cross section measurements [72, 73], while track isolation has been recently introduced for the $H \to \gamma\gamma$ analysis in addition to the calorimetric isolation.

3.5.1 Calorimetric isolation

The calorimetric isolation is defined as the scalar sums of the transverse energy in all calorimeter cells (EM and hadronic) within a cone of some radius (typically $\Delta R = 0.4$) around the photon (or electron) axis. A rectangular core of cells (5×7 in $\eta \times \phi$) nearest to the photon is excluded from the sum, in an attempt to remove the photon energy from the sum. An illustration is shown in Fig. 3.18a .

The containment of an electromagnetic shower within the calorimeter is commonly characterized by the Molière radius: the radius of the circle (in the $\eta \times \phi$ plane) containing (on average) 90% of the shower energy. For the ATLAS EM calorimeter, the Molière radius is approximately 4.8 cm [74], which corresponds to 1.3 cells in the EM barrel. This means that over 90% of the photon energy should be contained in a grid of 3×3 cells, and over 95% of the energy should be contained by the 5×7 cells excluded from the isolation sum. This implies that the leakage of the photon energy should be limited to the few-percent level, but that the energy of the photon is never perfectly contained within the subtracted central core. In addition to contributions from the photon itself, two other effects play a large role in defining the isolation profile for isolated objects. The first is calorimeter noise at the cell level, which is centred at zero, with both positive and negative Gaussian fluctuations about the mean. The second is from physics not associated with the hard scattering process that produced the photon, e.g. from the underlying event and from pileup. Because the noise averages to zero, its only effect on the isolation profile is to induce a Gaussian smearing on the measured isolation, with a total width proportional to the radius of the isolation cone. Since the noise is random it is difficult to remove and no attempt is made to estimate its effect. The only correction applied to the measured isolation are the one for the leakage and the pileup.

The exclusion of the central core of cells can still leave a non-trivial fraction of the photon E_T left in the isolation cone, usually between 2% and 5% of the photon E_T

---

[6] more in detail the method is based on the probability integral transform [70] and on the inverse probability integral transform [71]. The first states that if X is a random variable with cumulative distribution function (CDF) F_X then the random variable $Y = F_X(X)$ is a random variable with uniform distribution on $[0, 1]$. On the contrary the second states that if Y is a random uniform variable in $[0, 1]$ then $X = F_X^{-1}(Y)$ is a random variable with CDF equal do F_X. Combining these two results it is possible to transform a random variable X with CDF equal to F_X to a random variable Y with CDF F_Y. Using the integral probability transform $U = F_X(X)$ is a random uniform variable on $[0, 1]$. Using the inverse probability integral transform $F_Y^{-1}(U)$ is a random variable with CDF equal to F_Y. Then $F_Y^{-1} \circ F_X$ maps the random variable X to the random variable Y.

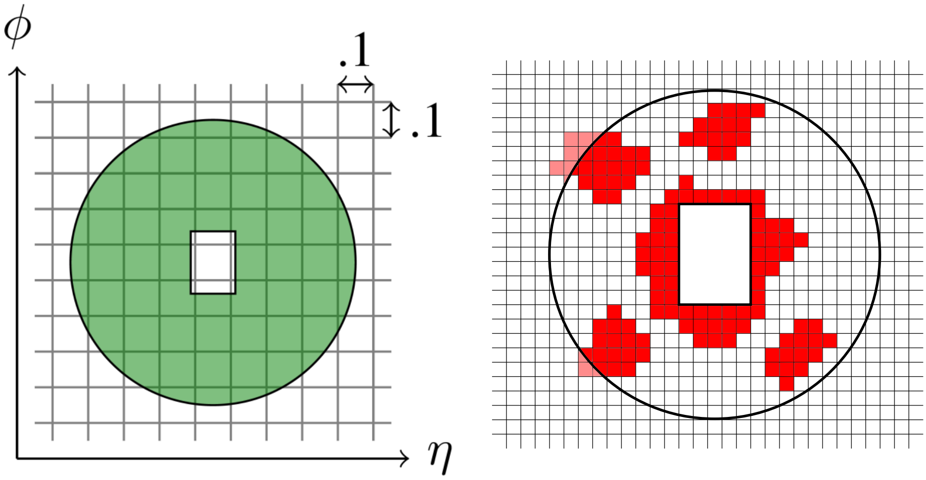

(a) using all the cell **(b)** using only cell associated to topo-clusters

Figure 3.18: An illustration of the calculation of the isolation variable in ATLAS. A circle is drawn around the photon in $\eta \times \phi$ space, and the energy from (a) all calorimeter cells (b) calorimeter cell associated to topocluster inside of that circle are summed. The energy in a central rectangle of the cone is excluded, in an attempt to remove the electron or photon shower.

(depending on η). For photons with large E_T, this residual leakage dominates the isolation profile. After this correction, the mean of the photon isolation distribution is independent of the true photon transverse energy.

The procedure used to correct for both the underlying event and pileup is based on ideas first presented in [75], and expanded on in [76]. The procedure estimates the ambient transverse energy density on an event-by-event basis, rather than applying an average correction to all events. This correction is computed by multiplying the ambient transverse energy density by the active area of the isolation cone. The ambient transverse energy density is given by the median of the distribution of the jet transverse energy divided by the jet area. The reconstruction of jets in a given event is done according to the k_T-algorithm [77, 78], with size parameter 0.5, which is run on three-dimensional noise suppressed topological clusters outside the cone. There is no explicit cut on the transverse energy of the jets, except that the total jet E_T must be positive. The topo cluster that seed the jet reconstruction are required to have one cell with a 4σ (or larger) deviation from the baseline noise rate. For a detailed definition of the topo clusters see [69].

The correction of UE and pileup based on topo-clusters leaves a residual dependence on the pileup due to low energy cells below the topo-cluster noise cut. An improvement was made in the beginning of 2012, defining the isolation summing the transverse energy of topo-clusters with positive energy whose barycenters fall into the isolation cone. The resulting variable is called here for simplicity topo-isolation[7]. This new isolation is used in the $H \rightarrow \gamma\gamma$ analysis described in chapter 6. The improved isolation reduces the difference between the isolation distribution of data and MC simulation from 800 MeV to 100 MeV. The new isolation is shown to be independent of the bunch crossing ID (BCID). Fig. 3.19 shows the correlation between the mean of the Crystal-Ball used to fit

---

[7] tecnically this is called `topoPosEMEtConeXX`, while the one using all the cell is called `EtConeXX` where `XX` is the size of the cone, usually `40`.

the isolation distribution and the BCID. The MC mean has been corrected with the shift described above. The right plot shows a very good stability with respect to pile-up using the topo-isolation.

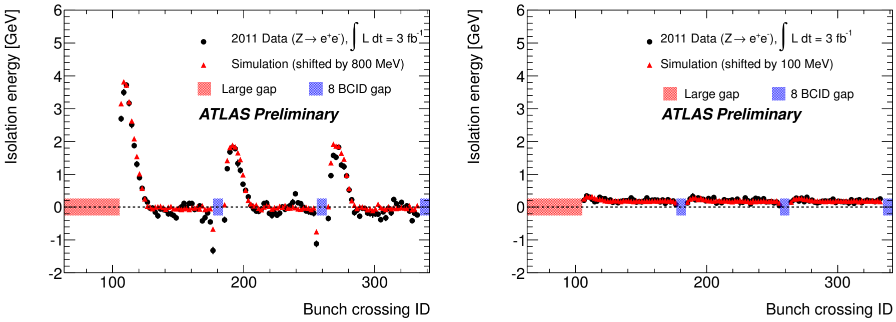

(a) `EtCone40` **(b)** `topoPosEMEtCone40`

Figure 3.19: Dependence of the isolation on the BCID considering (a) all the cell (`EtCone40`) or (b) only the one associated to a topocluster with noise suppression as in the topo-isolation (`topoPosEMEtCone40`). Only the first three sub-trains of the first train are shown. The MC BCID have been shifted by 104 to match the data configuration.

3.5.2 Track isolation

The track isolation is computed using tracks detected in the ID detector around the photon candidates, only charged particles can contribute the this quantity. In the $H \to \gamma\gamma$ analysis tracks are selected requiring:

- transverse momentum $p_T > 1\,\mathrm{GeV}$
- at least one hit in the first layer (if expected) of the ID and 9 hits in the silicon (pixel + SCT)
- transverse impact parameter $d_0 < 1.5\,\mathrm{mm}$
- longitudinal impact parameter ($z_0 \sin\theta$, with respect to reconstructed vertex) $<$ 15 mm

The track isolation is defined as the scalar sum of the transverse momenta of the tracks in a cone around the photon: $\sum_{\text{tracks}} p_T$.

3.6 The Muon Spectrometer

The Muon Spectrometer is the outermost part of the ATLAS detector, defining its overall dimensions. It is a combination of large superconducting air-core toroid magnets, instrumented with separate trigger and high-precision tracking chambers, represented in figure 3.20. High-resolution momentum measurements independently of the Inner Detector are provided for $|\eta| < 2.7$, and triggering capabilities up to $|\eta| < 2.4$.

The driving performance goal is a stand-alone transverse momentum resolution of approximately 11% for 1 TeV tracks, with minimum charge misidentification. The associated sagitta of 500 μm for such tracks requires a resolution of 50 μm, obtained with precise knowledge of the magnetic field and chamber positioning. A brief description of the different components of the muon system and the obtained performance are given in the following subsections. The reader is referred to [52, 58, 60, 79] for more information.

3.6.1 The toroid magnets

The toroidal configuration provides a field which is mostly orthogonal to the muon trajectories over a large volume and little material in the measurement regions, minimizing the degradation of resolution due to multiple scattering. Over the range of $|\eta| < 1.4$, magnetic bending is provided by the large barrel toroid. Eight coils are arranged symmetrically around the beam axis, extending radially from 9.4 m to 22 m, with a length of 25.3 m. For $1.6 < |\eta| < 2.7$, muon tracks are deflected by two smaller end-cap magnets inserted into both ends of the barrel system. The end-cap toroids are rotated in azimuth by an angle of 22.5 with respect to the barrel coils to provide for radial overlap, and to optimize the bending power in the transition region ($1.4 < |\eta| < 1.6$). Nevertheless, due to the finite number of coils, the field configuration is not perfectly toroidal. Small regions with degraded momentum resolution exist due to the low field integral, represented in figure 3.22.

A picture of the system during the ATLAS installation period is shown in figure 3.21. The magnets are cooled down to 4.5 K by liquid helium and operate at a nominal current of 20.5 kA. The chambers, on the other hand, can operate at room temperature, and four different technologies are used according to the requirements of precision, timing and radiation hardness. Each one is briefly described in the following subsection.

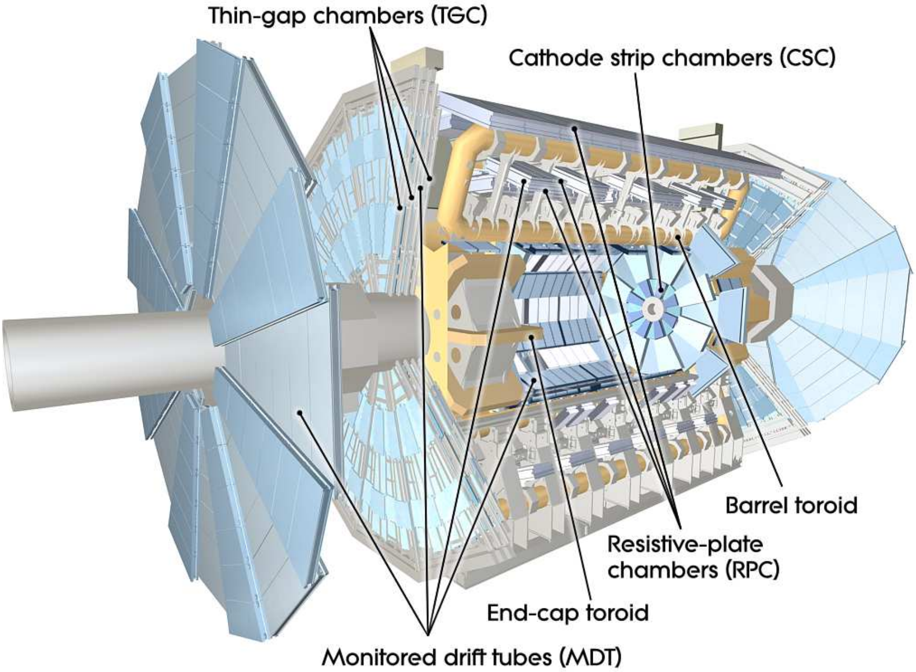

Figure 3.20: Cut-away view of the ATLAS muon system.

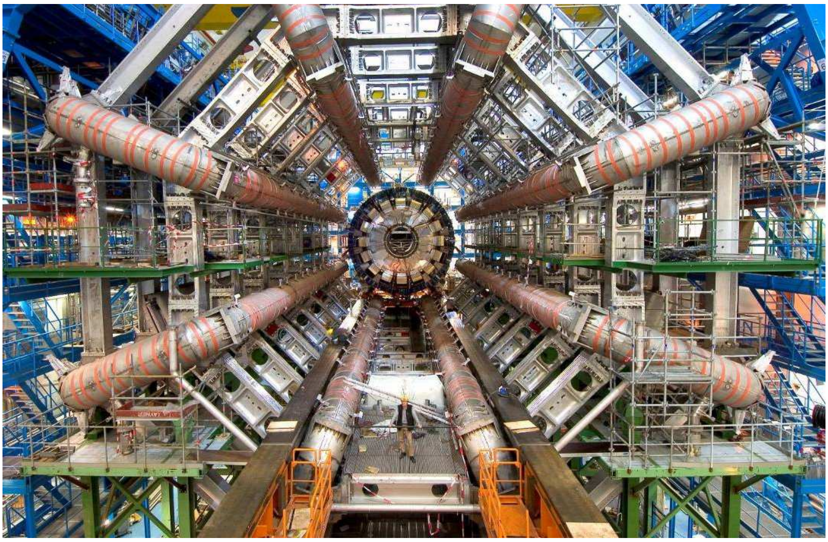

Figure 3.21: Picture of the barrel toroid magnet installed in the ATLAS cavern.

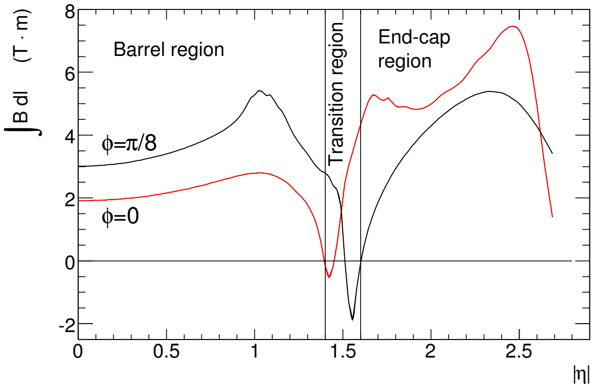

Figure 3.22: Predicted field integral as a function of $|\eta|$ inside the Muon Spectrometer.

3.6.2 Geometry and chamber types

The chamber geometry follows the eight-fold symmetry of the toroid magnets, as illustrated in figure 3.23. Each octant in the azimuthal direction is divided in a large and a small sector. The large chambers occupy the region between the barrel coils, while the small sectors are aligned with them. Overlaps in the boundaries of the sectors minimize gaps in detector coverage and also allow for the relative alignment of adjacent sectors using tracks recorded by both a large and a small chamber.

In the barrel region, tracks are measured in chambers arranged in three cylindrical layers around the beam axis, at radii of approximately 5 m, 7.5 m, and 10 m. In the transition and end-cap regions, the chambers are installed in planes perpendicular to the beam, also in three layers, located at distances of $|z| \approx 7.4$ m, 10.8 m, 14 m (transition region), and 21.5 m (end-cap) from the interaction point.

In the center of the detector ($\eta \approx 0$), a gap in chamber coverage has been left open to allow for services to the solenoid magnet, the calorimeters and the Inner Detector. The size of the gap varies from sector to sector depending on the service necessities, the biggest gaps of 1-2 m being located in the large sectors. This region extend up to $|\eta| = 0.08$ for large chambers and $|\eta| = 0.04$ for small sectors.

Precise momentum measurement is performed by determining the track coordinate in the bending plane. Monitored Drift Tubes (MDTs) were chosen for this task by their high measurement accuracy, predictability of mechanical deformations and simplicity of construction. In the forward region ($2.0 < |\eta| < 2.7$), the innermost layer is instead equipped with a radiation hard technology of Cathode Strip Chambers (CSCs), better suited for handling the expected particle fluxes. CSCs provide measurements of both coordinates and additionally good timing resolution. Fast triggering and second coordinate (ϕ) determination is provided by Resistive Plate Chambers (RPCs) in the barrel and Thin Gap Chambers (TGCs) in the end-caps. Both systems are able to separate beam crossings with intrinsic timing accuracies of a few nanoseconds and provide rough estimates of the track momentum. A summary of the expected resolution and number of elements of each technology is given in table 3.3. A brief description of the technologies follows.

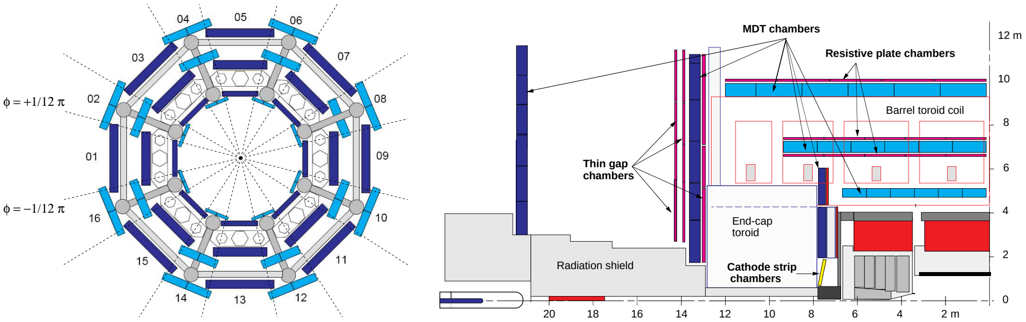

(a) $R-\phi$ view of the barrel Muon Spectrometer, illustrating large sectors (dark blue), small sectors (light blue) and the magnet coils (dark grey).

(b) $R-z$ view of the Muon Spectrometer showing the different technologies and stations.

Figure 3.23: Illustration of the muon system in $R-\phi$ and $R-z$ projections.

Type	Chamber resolution			Measurements/track		Number of	
	z/R	ϕ	time	barrel	end-cap	chambers	channels
MDT	35 μm	–	–	20	20	1150	354k
CSC	40 μm (R)	5 mm	7 ns	–	4	32	30.7k
RPC	10 mm (z)	10 mm	1.5 ns	6	–	606	373k
TGC	2-6 mm (R)	3-7 mm	4 ns	–	9	3588	318k

Table 3.3: Parameters of the four chamber technologies used in the muon system: expected resolutions (not including alignment effects), maximum number of measurements per track, number of chambers and channels.

Monitored drift tubes (MDTs)

MDT chambers have a projective design, covering a total area of 5500 m^2. Their are formed of six or eight layers of pressurized drift tubes, with diameters of 29.970 mm. Illustrations of a tube and a chamber can be seen on figures 3.24a and 3.24b. The tubes operate with Ar/CO$_2$ gas (93% / 7%) at 3 bar, selected for its excellent ageing properties. In the center of each tube, a 50 μm tungsten-rhenium wire is kept at 3080 V, generating a radial electric field.

The passage of a charged particle ionizes the gas, and the liberated electrons drift towards the anode wire under the influence of the electric field. In the vicinity of the wire, an avalanche process takes place, inducing measurable signals which are read out by the on-chamber electronics. An amplifier / shaper / discriminator chip including a charge analog-to-digital converter (ADC) feeds the pulses to a time-to-digital converter (TDC). The charge information is used for noise discrimination.

The arrival time of the signal can be interpreted as a drift-radius, using a calibration function to correct for the non-linear drift velocity in the gas mixture. Single hit resolutions of the order of 80 μm are achieved, with an efficiency around 96%. The chamber resolutions are of the order of 35 μm. To fulfill the requirements for high-precision momentum determination, they are equipped with an optical monitoring system to calculate their deformations. Four alignment rays are used on most part of the chambers and only one in the center of the smallest chambers.

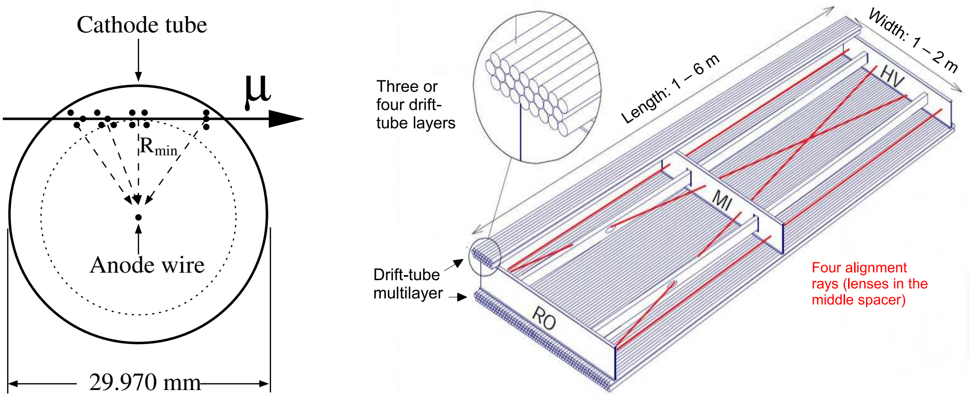

(a) Cross section of a MDT tube.

(b) Sketch of a MDT chamber. The alignment rays, shown in red, allow for the monitoring of chamber deformations.

Figure 3.24: Illustration of (a) a Monitored Drift Tube (MDT) and (b) the corresponding chamber.

Cathode Strip Chambers (CSCs)

The performance of MDTs is degraded at rates above 150 Hz/cm^2, which will be exceeded in the first layer of the forward region ($|\eta| > 2$). In this range up to $|\eta| < 2.7$, Cathode Strip Chambers provide high spatial and time resolutions with high-rate capability. CSCs are multiwire proportional chambers made of radial anode wires and cathode planes segmented into orthogonal strips. Strips in the plane perpendicular to the wires provide the precision coordinate (η) and the ones parallel to the wire give the second coordinate (ϕ) information.

Each chamber is composed by 4 layers with 5 mm gaps filled with Ar / CO_2 (80% / 20%). The wire plane is located at the center of each gap, with a wire pitch of 2.5 mm, equal to the anode-cathode spacing, as illustrated in figure 3.25. The wires are 30 μm in diameter and operate at 1900 V. This result in drift times of less than 40 ns, with an associated precision around 7 ns. The expected spatial resolutions are of the order of 40 μm in R and 5 mm in ϕ.

Resistive Plate Chambers (RPCs)

Three layers of Resistive Plate Chambers provide the trigger and second coordinate measurement in the barrel. Each station consists of two independent layers, each measuring η and ϕ, such that a track going through all three stations delivers six measurements per coordinate. The redundancy decreases fake rates from noise hits and increases the triggering efficiency.

RPCs are gaseous parallel-plate detectors, with a 2 mm gap created by insulating spacers between the electrodes. The gap is filled with a mixture of $C_2H_2F_4$ / Iso-C_4H_{10} / SF_6 (94.7/5/0.3), which allows relatively low operating voltage, non-flammability and low cost. The electric field between the plates of about 4.9 kV/mm creates avalanches in front of the anodes when an ionizing track crosses the chamber. Induced signals are read out via capacitive coupling to metallic strips, mounted on the outer faces of the resistive plates. Spatial resolution around 10 mm is expected for both coordinates, with timing resolutions below 2 ns.

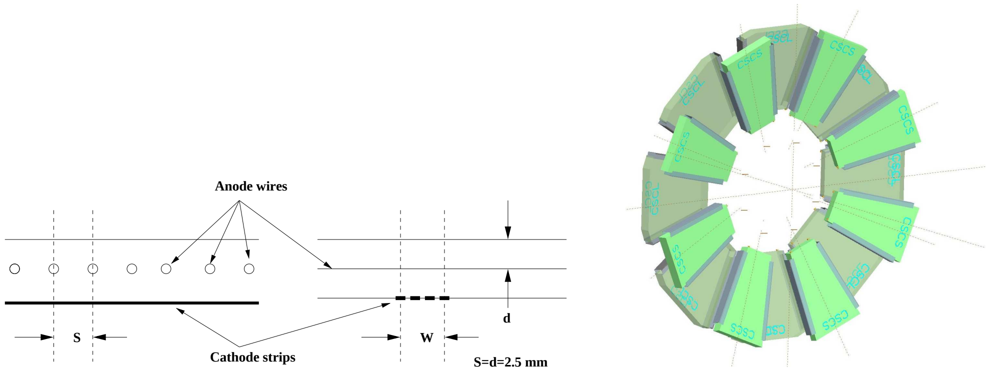

(a) Structure of the CSC cells looking down the wires. The wire pitch s is equal to the anode-cathode spacing $d = 2.5$ mm.

(b) Layout of a CSC end-cap with eight small and eight large chambers.

Figure 3.25: Illustration of (a) the structure and (b) the integration in the ATLAS detector of Cathode Strip Chambers (CSCs).

Thin Gap Chambers (TGCs)

TGCs have the same function as RPCs, providing trigger and second coordinate measurement in the end-cap. Each chamber is a multiwire proportional chamber filled with a highly quenching gas mixture of CO_2 and n-pentane. It operates in a quasi-saturated mode, preventing the occurrence of streamers in all operating conditions. Wire-to-cathode distance of 1.4 mm and wire-to-wire distance of 1.8 mm lead to very good time resolution.

Including the variation of the propagation time, signals arrive with 99% probability inside a time window of 25 ns. This corresponds exactly to the needs of the trigger system. The radial, bending coordinate is measured by the TGC wire groups, while the azimuthal coordinate is determined by the radial strips.

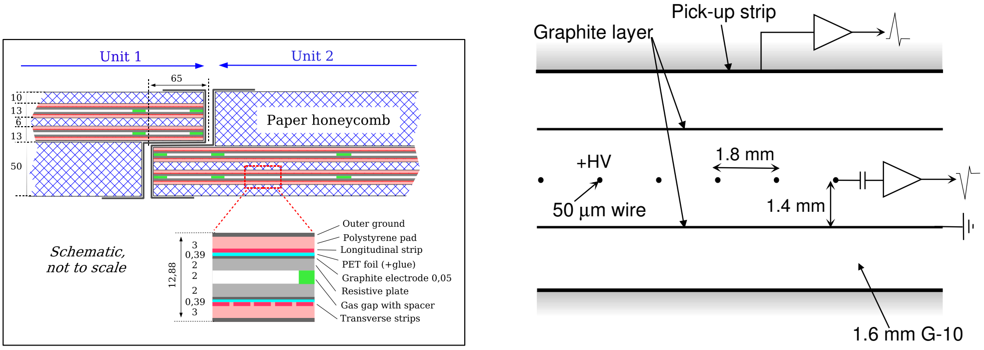

(a) **(b)**

Figure 3.26: Structure of (a) Resistive Plate Chambers (RPC) and (b) Thin Gap Chambers (TGC).

3.6.3 Alignment system

Although construction quality ensures a good precision for the chamber elements and the chambers as a whole, chamber positioning accuracy is limited to 5 mm, and additional deformations up to a few hundred microns due to thermal gradients and gravity are expected. This is two order of magnitude above the 50 μm resolution on sagitta measurements that are required for momentum determination to 10% at 1 TeV.

To reach this goal, a sophisticated optical alignment system was built to relate the position of each chamber to that of its neighbours within the same layer or tower continuously. In practice, the positions are measured and a new set of alignment constants are derived every 20 minutes. Given the present stability of the system, the measurements are only performed once per hour.

Three different technologies, described in [58] are applied for the more than 12 000 lines, based on optoelectronic image sensors that monitor an illuminated target. The different alignment lines are presented in figure 3.27. In the barrel, a row of MDT chambers are referenced to each other by praxial and axial systems, while the projective system links inner, middle and outer stations. Additional reference lines connect chambers with the barrel toroid, or small to large sectors. In the end-cap, polar lines and azimuthal lines linked to a grid of alignment bars are also used, extending the coverage to CSC chambers.

The global position determination of the barrel and end-cap muon-chamber systems with respect to each other and to the Inner Detector are complemented by track-based alignment algorithms. The latter ones exploit the nearly straight trajectories of high-p_T muons, or eventually might use dedicated runs without toroidal field. Individually, both optical and track-based alignment can only reach a precision a few hundred microns. The desired accuracy in the sagitta measurement of 50 μm or below can only be achieved with their combination.

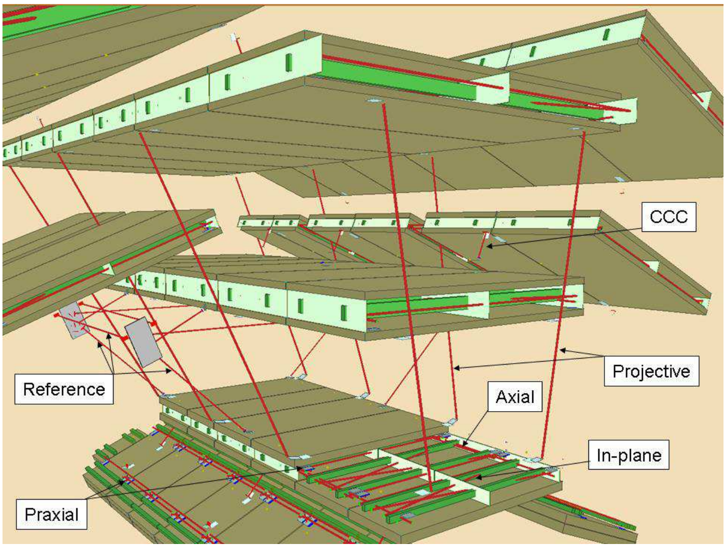

Figure 3.27: Layout of the optical-alignment lines (red) for three adjacent barrel sectors. The Chamber-to-Chamber Connector sensors (CCC) connect chambers in a small sector to those in an adjacent large sector.

3.7 The trigger, data acquisition and detector control systems

One of the main challenges of the LHC experiments is to record interesting events given the huge amount of data produced and the high collision rate. The proton-proton interaction rate at the design luminosity of 10^{34} cm^{-2}s^{-1} is approximately 1 GHz, while the event data recording, based on the available technology and resources, is limited to about 200 Hz. Therefore, a rejection factor above 10^6 must be achieved, with very efficient selection on physics processes of potential interest.

ATLAS has chosen a three level trigger system for this task, represented in figure 3.28. A hardware based Level-1 (L1) precedes a software based High-Level Trigger (HLT), that includes Level-2 (L2) and Event Filter (EF). Level-1 receives data from the muon system (RPCs and TGCs) and the calorimeters at the bunch crossing rate of 40 MHz, reducing the output to 75 kHz (upgradeable to 100 kHz). The L1 decision must reach the front-end electronics within 2.5 μs and it is based on signatures like high-p_T muons, electromagnetic clusters, jets, hadronic decays of τ-leptons, ETmiss and large total transverse energy.

The data corresponding to the regions of the detector where L1 decision has been taken are passed to Level-2. The L2 uses the information on these Regions-of-Interest (RoIs) and reduces the event rate below 3.5 kHz, with an average event processing time of approximately 40 ms. Special algorithms are run on this step that includes also tracking in the Inner Detector. Tracking and better information on energy deposition improve the threshold cuts and allow particle identification. One example is the distinction between photons and electrons.

The event filter uses the full granularity and precision of the detector to run some of the default reconstruction algorithms. The event rate is reduced to approximately 200 Hz, with an average event processing time around four seconds. Events selected in this stage are recorded and become available for offline analysis.

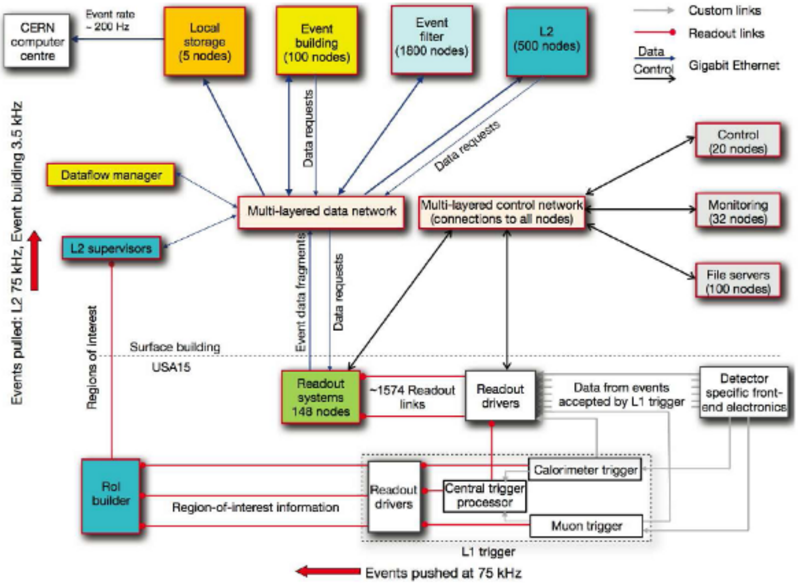

Figure 3.28: Block diagram of the ATLAS trigger and data acquisition. Details are given in ref. [58].

In parallel to the trigger, two independent, complementary and interacting systems are responsible for the data taking and control the experiment infrastructure: the data acquisition system (DAQ), and the Detector Control System (DCS).

The former is charged with controlling the hardware and software elements of the detectors and the elements associated with High-Level-Trigger and data storage. This enables diagnostic and error recovery, with the capability of removing or re-enabling individual parts without stopping the full acquisition.

The DCS, on the other hand, ensures coherent and safe operation. It handles the control of the detector equipment and related infrastructure, monitoring the operational parameters such as temperature and power-supply voltages. Both systems are capable of taking corrective actions and additionally provide a human interface for the full control of ATLAS and its sub-detectors.

3.8 The ATLAS software framework

A common and robust analysis framework is a major requirement to deal with the huge amount of data produced by a large experiment like ATLAS. Moreover, combining the effort of different communities in a world-wide experiment with a few thousand collaborators requires the enforcement of a rather rigid structure for software development and the use of standard data formats. All that must be achieved combining flexibility and functionalities for common tasks.

A standard framework called ATHENA [80] is used by ATLAS for simulation, reconstruction and physics analyses. It is an implementation of the component-based architecture Gaudi, initially developed by the LHCb collaboration. Major design principles are the clear separation of data and algorithms, and between transient (in-memory) and persistent (in-file) data. All levels of processing of ATLAS data, from high-level trigger to event simulation, reconstruction and analysis, take place within the Athena framework. ATHENA is responsible for handling the configuration and execution of several C++ packages through python scripts called *jobOptions*. It takes care of the execution order, data flow and storage (persistification). Some basic design principles under which ATHENA is developed are:

- Use of abstract software interfaces, making easy to handle groups of components.
- Clear separation between data and algorithms. Clients of the data should not be exposed to the machinery of the algorithms that created it. In this way, changes are transparent to the client.
- Classification of data with respect to their lifetime. Persistent data are stored on disk while transient data reside on memory.

In practice, the framework is composed by a multitude of components that take care of different tasks in the simulation, reconstruction and analysis chain. Some of them are described below. This subset correspond to the components typically used in analyses, and their definition will be useful for the next chapter. A simplified scheme of their relations in the ATHENA framework is presented in figure 3.29.

Algorithm application building block, visible and controlled by the framework, performing a well-defined configurable operation. Runs once per event, calling *tools* and *services*, reading and usually producing data.

Service globally available software, for common tasks such as data access and message printing.

Tool lightweight piece of code to execute a specific task once or multiple times per event. Shared and owned by *algorithms* or *services*.

Data object object-oriented representation of particles (muon, electron) or detector information (cells).

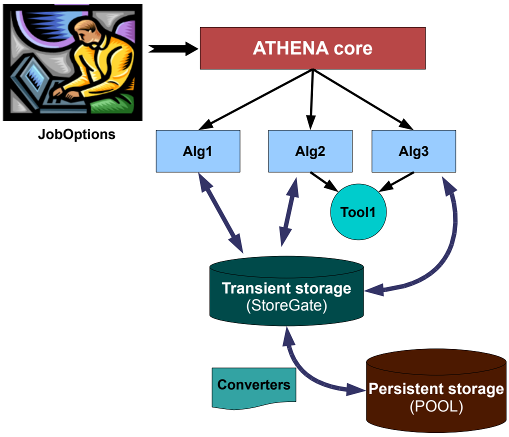

Figure 3.29: Simplified scheme of the ATHENA framework and relations between components.

3.8.1 Data management and data formats

The yearly data volume of $\mathcal{O}(10\text{ PB})$ is used by data processing and analysis activities spread around the world. High degree of decentralisation and sharing of computing resources was promoted and met with the Grid paradigm. A three level Tier structure was implemented, in order to use all the available resources efficiently:

- One Tier-0 (CERN) is responsible for the primary event processing, storage of the RAW data and distribution of the data to Tier-1s.
- Approximately 10 Tier-1 facilities archive a copy of the RAW data, provide the reprocessing capacity, access to the various processed versions and allow scheduled analysis of the processed data by physics analysis groups.
- Several Tier-2 centers store analysis data and provide resources for calibration, simulation and analysis.

Some details about the several data formats handled in the framework, and foreseen in the ATLAS Event Data Model are given below. They correspond to different steps in the event processing and filtering, meeting the capabilities of the data storage centers and the needs of the end-users to perform physics analyses. The following types are available:

- **RAW** data: contains the output of the ATLAS detector, produced by real or simulated events after the High-Level Trigger. It comes in the "bytestream" format as they are delivered from the detector, rather than object-oriented format. The size of each event is approximately 1.6 MB.

- **Event Summary Data (ESD)**: holds the output of the reconstruction process. Both detector information and combined reconstruction objects like muons, electrons and jets are stored at this stage. An object-oriented format is adopted, and the typical event size is 1 MB.

- **Analysis Object Data (AOD)**: a subset of the ESD, with the physical objects used in analysis and few detector objects to allow track-refitting, isolation studies and others. Also stored in object oriented format, the nominal event size is of the order of 100 KB.

- **Derived Physics Data (DPD):** contains a small subset derived from the AOD / ESD, specific for an analysis or performance group. More than one derivation is possible, in which the data is reduced by removing unnecessary containers, selecting objects and dropping information from those objects. User-data can be added in the process, and in the final stage of derivation a flat ROOT tuple can be produced.

- **TAG**: event-level meta-data containing a minimum set of information for fast event selection. Can be either ROOT [81] files or databases which are replicated and can be accessed online. Advanced queries can be made and ROOT files, histograms and tables can be produced. The event size is $\mathcal{O}(1\text{ kB})$.

The availability of Event Summary Data is reduced, being restricted to basic studies on detector performance, specially in the initial phase of the experiment. Physics analyses are performed using Analysis Object Data and Derived Physics Data. Lightweight data formats like TAGs are used for efficient event selection. Tools for their production are provided in the context of the Physics Analysis Tools working group [82].

Coherent development, integration and operation of the distributed database and data management software and infrastructure are essential for this scheme. A complex system of replicated databases is used to control technical aspects of the detector construction, installation and survey, together with the detector geometry, data acquisition conditions, offline processing configuration and data management services.

This whole structure was successfully exercised in the commissioning phase and initial collision data taking. However, the first tests of the framework and Event Data Model were done with simulated data, with the chain described in the following.

3.8.2 The simulation chain

The same data formats described above are used when dealing with simulated data. Instead of starting from signals measured in the detector, the input now is a list of the four momenta of final-state particles, as given by an event generator. The response of the ATLAS detector is simulated by `GEANT4` [83] using a detailed model of the detector geometry and the underlying physics. Each particle is propagated through the detector, generating hits which are then digitized, reproducing the RAW data coming from ATLAS. Reconstruction is done using the same algorithms than run in collision events, including the trigger. The output files contain information about the generated and reconstructed particles and can be analysed using the offline software.

This chain is very CPU-time consuming and the need for great quantities of Monte Carlo in some studies obliges the use of fast simulation. `Atlfast` or its second generation version `Atlfast II` are adopted in such cases. Although less precise than the full simulation, they still contain a realistic model of the detector and physics processes. These chains are illustrated in Fig. 3.30, and detailed descriptions can be found in ref. [80].

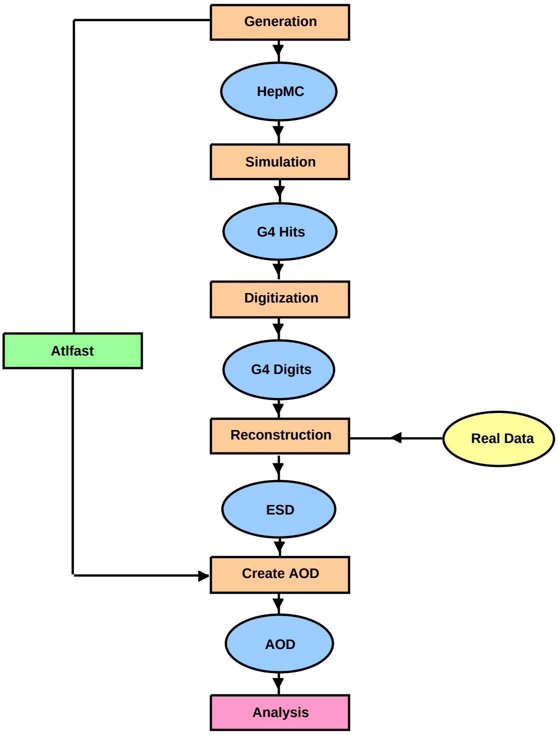

Figure 3.30: Schematic representation of the generation / simulation / reconstruction chain for Monte Carlo and real data in ATLAS. Extracted from ref. [84].

3.8.3 Proof

Most of the work done during my PhD was done using data in ROOT tuple format produced from AOD. The advantage is that only the ROOT framework is need instead of the whole ATHENA framework.

The ROOT framework provides PROOF (Parallel ROOT Facility), an extension to process a large sets of ROOT files in parallel on clusters of computers or many-core machines. The parallelism introduced by PROOF is the easiest one, the so called "embarrassingly parallelism", essentially it processes every events with many processes without dependency between the parallel tasks. With a physics terminology the parallelism is at event-level. For this reason it is easy to adapt a non-parallel analysis to the Proof framework. All the details about the features of Proof are available on [85]. In this section the performance of such tool are evaluated using a cluster of machines at the Physics Department of the University of Milan.

The cluster is made by 8 machines, with Intel Xeon CPU E5645 @ 2.40 GHz processors, everyone with 24 cores and 47 GB of RAM. The cluster reads the data from a GPFS (General Parallel File System) [86] filesystem. The total size of the filesystem 1.1 PB and it is shared between seven storage systems (six DotHill and one Hitachi). The disk configuration is RAID6. It is difficult to quantity the reading speed because this filesystem is used at the same time by several other services and many users from the Tier2, Tier3 and Grid. The hardware limit should be $< 600\,\mathrm{MB\,s^{-1}}$.

The system has been stressed with an utility provided by the Proof framework. The first test doesn't do any I/O operation, so the performance is CPU-bounded. This benchmark consists in creating 16 histograms filled with (30 000 × # cores) random numbers. The test is repeated varying the number of active cores and for every case it is repeated four times and the mean is considered. Figure 3.31 shows the process rate varying the number of active cores. The performance increase linearity with a small overhead. This is effect is visible on the right plot in the figure showing the process rate divided by the number of active cores: without overhead the behaviour should be flat.

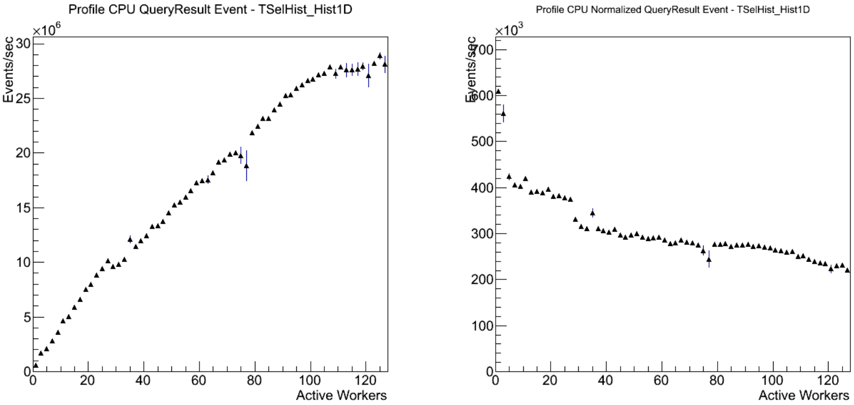

Figure 3.31: Performance of the CPU-bounded stress test on the proof cluster in Milan. The plot on the left shows the process rate varying the number of used cores. The plot on the right is similar but it is normalized to the number of used cores.

The previous test is very different from a typical physical analysis where large I/O is needed. An I/O-intensive test based on reading data from ROOT tuples previously created has been performed. The result is very different and the performance saturates around 400 MB s^{-1} when only 35 cores are used, see Fig. 3.32. The same test has been performed using proof cluster located in other institutes, the first at LPNHE, the second in Lion. Both of these cluster have 80 cores and the performance are identical: they reach the saturation around 300 MB s^{-1} using 30 cores.

The present performance is limited by the hardware, but respect to the single-core case the improvement is of the order of $\sim$ 15.

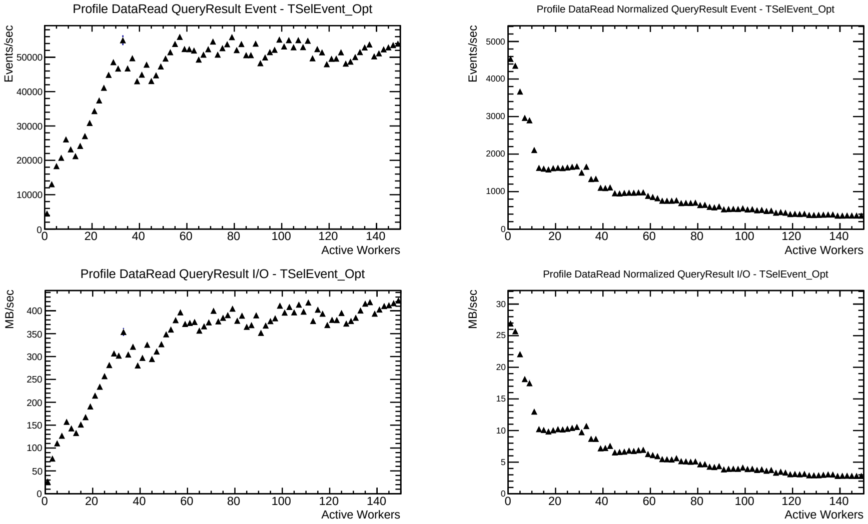

Figure 3.32: Performance of the I/O-bounded stress test on the proof cluster in Milan. The plots on the left shows the process rate (in event/sec on the top and MB on the bottom) varying the number of used cores. The plots on the right is similar but it is normalized to the number of used cores.

CHAPTER 4

Electron and photon energy calibration

Energy is one of the most important physics quantities measured by the detector and it is the one calorimeters are designed for. A description of the ATLAS electromagnetic calorimeter can be found in section 3.2.1.

In general the calibration of electrons and photons can be divided in three steps:

- The LAr calorimeter calibration converts the raw electronics signal read out by each cell into a deposited energy. Sometimes it is called “current to energy” calibration or “µA → MeV” calibration [87, 88].
- The Monte Carlo based calibration applies corrections at the cluster level for energy losses (dead material, leakage,. . .), corrections for energy modulation in η and ϕ and a special correction for transition region at $|\eta| = 0$ and $|\eta| = 0.8$ because of the discontinuity of the calorimeter geometry. This calibration starts from the energies of the cells inside a sliding-window cluster associated to a reconstructed particle and returns the energy of the cluster.
- The in-situ calibration [89, 90] uses physics events recorded by the ATLAS detector (mainly $Z \to ee$) to intercalibrate the different regions of the calorimeters and to determine the energy scale factors to match the real data with the MC simulation.

This chapter describes the MC based calibration for the barrel and the endcap, for electrons and photons. In the following only this step of the calibration chain is called “calibration”. The energy before this step is called “uncalibrated” or “raw”.

Two different techniques have been studied and optimized. The first calibration (called “standard”) is used since years and it is the default calibration used by all the analyses. It is described in detail in this chapter. The second one was recently developed using multivariate techniques to improve the resolution of the invariant mass of $H \to \gamma\gamma$, but it can be used also for other channels and it is described in the next chapter. The standard MC calibration is tuned using simulated electrons and photons from few GeV to 1 TeV and so it is suitable for all the analyses in ATLAS.

Both calibrations cover the region $|\eta| < 2.5$ except the crack region between the EM barrel and endcap, defined as $1.425 < |\eta| < 1.55$, where a special and simpler calibration is used.

After an introduction on the general idea behind the calibration in section 4.1, the input variables are described in section 4.2. In section 4.3 the optimization of the calibration is described. The performances are presented in section 4.4 and some final considerations about the standard calibration are in section 4.5. A correction for converted photons using the radius of conversion as additional input is described in section 4.6.

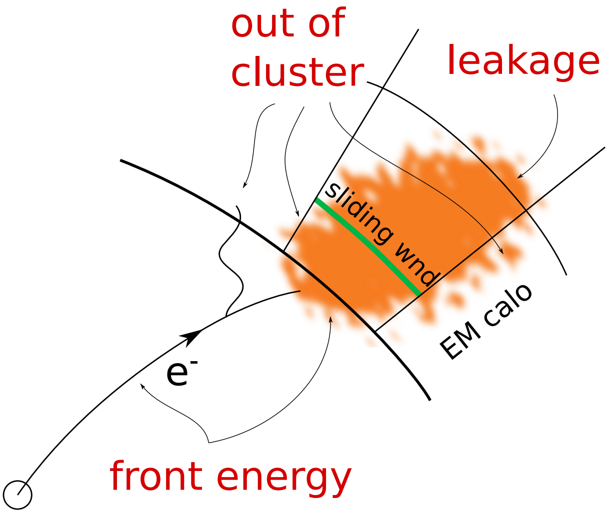

Figure 4.1: Sketch of the various component of the energy loss affecting the linearity and the resolution of the final energy measurement.

4.1 Introduction

Several effects deteriorate the total energy resolution and bias the measured value of the total energy, in particular:

- the energy loss due to the amount of material in front of the calorimeter, usually called the "front" component,
- the energy loss due to dead material inside the calorimeter, usually called the "sampling" or the "accordion" component,
- the energy loss laterally outside of the reconstructed cluster, usually called "out of cluster",
- the energy loss longitudinally behind the electromagnetic calorimeter, usually called "leakage".

These components are illustrated in figure 4.1 and an example of the decomposition is shown in Fig. 4.2 for 50 GeV electrons. Without the calibration, the simple sum of the energy in the cells of the cluster associated to an electron of 100 GeV with respect to the true energy is shown in Fig. 4.3. To see the correlation, on the same figure the distribution of the material in front of the calorimeter is shown.

The goal of the calibration is to estimate this energy loss using measurable quantities. Some of them are described in the next section.

4.2 Standard variables

Few variables are used in the standard calibration and all of them are measured by the electromagnetic calorimeter. All the variables are functions of:

- the pseudorapidity $|\eta|$ of the cluster in the calorimeter reference assuming the calorimeter to be symmetric,

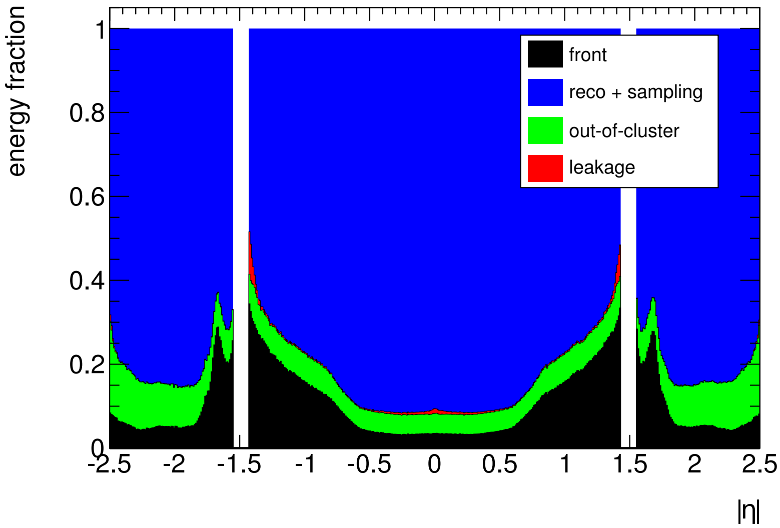

Figure 4.2: Energy decomposition for 50 GeV electrons.

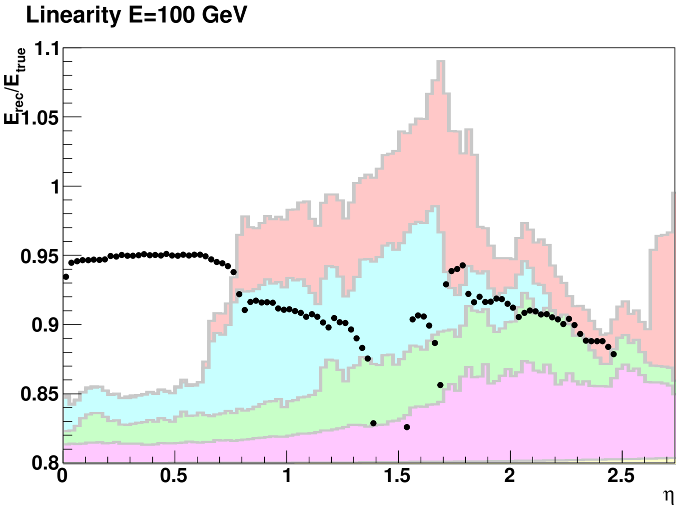

Figure 4.3: Linearity of the raw energy (sum of the energies in the four layers with respect to the true energy) versus the pseudorapidity (point) for 100 GeV electrons. On the background the distribution of the material in front of the calorimeter.

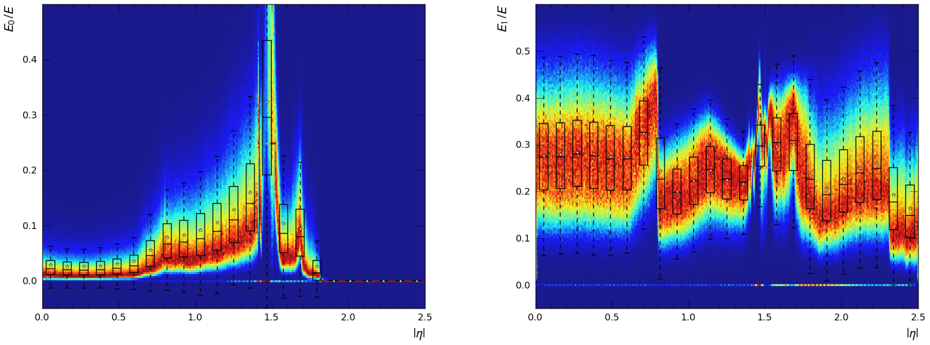

(a) presampler **(b)** strips

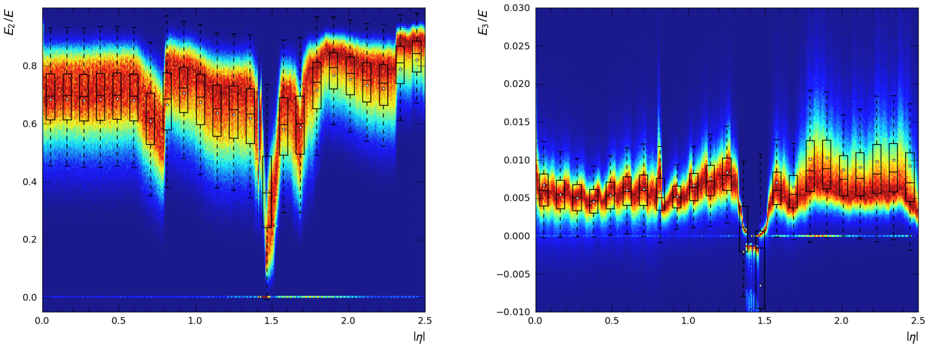

(c) middle **(d)** back

Figure 4.4: Fraction of the energy deposited in the four layers with respect to the total calibrated energy: (a) presampler, (b) strips, (c) middle, (d) back for electrons with true transverse energy between 7 and 800 GeV. The coloured histogram on the background are normalized in such a way that the maxima for every vertical slice have the same value. A box plot [91] is superimposed to the histogram: the edges of the box represent the first and the third quartile, the horizontal line inside the box corresponds to the median. The two ticks represent the 1st and the 99th percentile. The "star" markers represent the mean.

- the reconstructed energies in the active part of the four layers of the calorimeter: presampler (E_0^{clLAr}), strips (E_1^{clLAr}), middle (E_2^{clLAr}) and back (E_3^{clLAr}).

The distribution of the energies of the three layers are shown in Fig. 4.4 considering electrons with true transverse energy between 7 and 800 GeV. Most of the energy is collected by the middle layer ($\sim$ 70%), 30% is deposited in the strips layer and a small fraction (< 1 %) in the back. The fraction in the presampler is variable between 10 % and 20 % and Fig. 4.4a shows a clear correlation between the fraction of the energy in the presampler and the amount of material before the accordion (compare with Fig.3.4 for the material in the inner detector and Fig. 4.6 for the total material before the accordion). It is important also to notice that the width of the distribution increases with the amount of material.

The reconstructed energies in the active material of the four layers (E_i^{clLAr}) are used to define some basic quantities used in the standard calibration:

longitudinal shower depth (or longitudinal barycentre) defined as a weighted mean of longitudinal position of the three layers:

$$X = \frac{\sum_{i=1}^{3} E_i^{\mathrm{clLAr}} X_i}{\sum_{i=1}^{3} E_i^{\mathrm{clLAr}}} \tag{4.1}$$

where X_i is the depth of the longitudinal centre of each compartment computed from the centre of ATLAS expressed in radiation length. X_i are functions of $|\eta|$. This values are computed in two ways: for the barrel they come from a parametrization, for the endcap they are fixed values for every cell computed with a specific simulation scanning the endcap with Geantino particles[1]. Figure 4.5 shows the values of X_i at various η, X_0 is set to 0 in the endcap.

In the formula (4.1) the index of the summation starts from 1, so the presampler energy is not used in this definition. This convention was used because the presampler energy is very noisy and very small, so it can add only a small information,

presampler fraction defined as the fraction of the measured energy in the presampler with respect to the total energy measured inside the cluster:

$$f_0 = \frac{E_0^{\mathrm{clLAr}}}{\sum_{i=0}^{3} E_i^{\mathrm{clLAr}}} \tag{4.2}$$

it is useful for its high correlation with the energy lost in front of the calorimeter.

cell index defined as an integer identifying a cell in the middle layer:

$$\text{cell index} = \left\lfloor \frac{|\eta|}{0.025} \right\rfloor \tag{4.3}$$

depending on the calibration type η is defined in different ways. 0.025 is the pseudorapidity width of one middle cell (see table 3.1).

---

[1] Geantino is a virtual particle used for simulations which do not interact with materials and undertake transportation processes only.

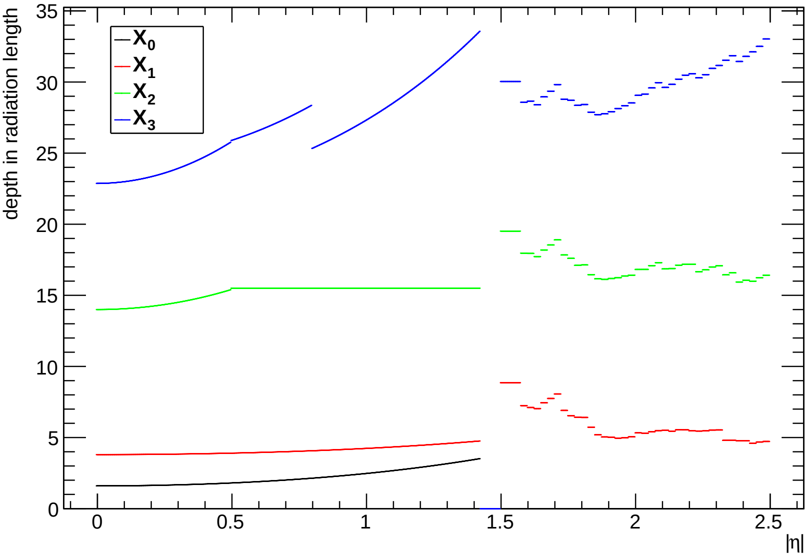

Figure 4.5: depth in radiation length of the four layers of the calorimeter used in the calibration. The presampler depth is shown only for the barrel, even if it ends at $|\eta| = 1.8$; it is not used in the computation of X, see (4.1).

4.3 Calibration optimization

The standard calibration (sometimes called “CalibHits” calibration) uses as input only the variables described in the previous section. Three optimizations have been developed for three different particle definitions: electrons, unconverted photons and converted photons. Converted photons with a radius of conversion greater than 800 mm are considered as unconverted since conversions reconstructed in the final part of the TRT detector are not reliable. For the optimization the true radius of conversion is used. As in the case for the radius of conversion, in general true variables are favourite instead of the reconstructed ones. The advantage of this convention is that the calibration can be used also if the reconstruction algorithm changes, for example if the radius of conversion reconstruction changes. The drawback is that there can be biases between true and reconstructed variables.

The main idea of the standard calibration is to estimate separately the four sources of energy loss (front, sampling, out of cluster, leakage), described at the beginning of the chapter, to compute the energy of the particle. For this reason dedicated Monte Carlo simulation (CalibHits) containing the information about the energy loss into all the parts of the detector are needed, considering active material (as the liquid argon), but also inactive material (as the absorbers) or dead material (as the cryostat, the solenoid) and the inner detector. Information from the inner detector are not used for this calibration. From this simulations all the energy losses are grouped into the four groups described before.

The energy loss decomposition has some benefits also for the computation of the missing transverse momentum E_T^{miss} defined as the negative vector sum of the transverse momenta of all the visible particles in the event: $-\sum \vec{E}_T^{(i)}$. In particular it allows to remove the out-of-clusters contribution from the calibration for electron entering the E_T^{miss} computation avoiding double energy counting. In fact, the E_T^{miss} is calculated using a sophisticate algorithm in which each contribution is calibrated according to the physics objects which it belongs to and taking into account also the energy deposits outside physics objects [92]. This last term covers the out-of-cluster energy which, therefore, is no longer needed in the electron calibration.

In the region instrumented with the presampler ($|\eta| < 1.8$) the energy of the particle is estimated using:

$$\begin{aligned} E_{e,\gamma} = {} & \underbrace{a(E^{Acc}_{tot},|\eta|) + b(E^{Acc}_{tot},|\eta|) \times E^{\mathrm{clLAr}}_{ps} + c(E^{Acc}_{tot},|\eta|) \times (E^{\mathrm{clLAr}}_{ps})^2}_{\text{Energy in front}} \\ & + \underbrace{\frac{s^{Acc}_{cl}(X,\eta)}{f_{out}(X,|\eta|)} \times \left(\sum_{i=1,3} E^{\mathrm{clLAr}}_{i}\right)}_{\text{Energy in the Accordion}} \times \underbrace{(1+f_{leak}(X,|\eta|))}_{\text{Longitudinal leakage}} \times \underbrace{F(|\eta|,\phi)}_{\text{Energy modulation}} \end{aligned} \tag{4.4a}$$

where:

- $E_{e,\gamma}$ is the electron/photon energy to be estimated,
- $a(E^{Acc}_{tot},|\eta|)$, $b(E^{Acc}_{tot},|\eta|)$ and $c(E^{Acc}_{tot},|\eta|)$ are parameters determined as a function of the energy deposited in the accordion (E^{Acc}_{tot}) and $|\eta|$. The coefficients a and b are commonly named *offset* and *slope*. For the barrel the parametrization is limited to the first two terms ($c = 0$),

- E_{ps}^{clLAr} is the part of the cluster energy measured in the presampler cluster corrected for the fraction deposited in the passive materials,
- X is the longitudinal barycentre of the shower (shower depth) defined by equation (4.1) where: E_i^{clLAr} are the energies deposited in the cluster in the active medium of the presampler and the three compartments of the calorimeter (strip, middle, back), and X_i is the depth, expressed in radiation length, of the longitudinal centre of each compartment computed from the centre of ATLAS. X_i are functions of $|\eta|$,
- $s_{cl}^{Acc}(X,|\eta|)$ is a correction factor to the accordion sampling fraction in the cluster. It is parametrized as a function of X and $|\eta|$,
- $f_{out}(X,|\eta|)$ is the correction for the energy deposited in the calorimeter outside the cluster (lateral leakage). It is parametrized as a function of X and $|\eta|$,
- $f_{leak}(X,|\eta|)$ is the longitudinal leakage correction. It is parametrized as a function of $|\eta|$ and X,
- $F(|\eta|,\phi)$ is the energy correction depending from the impact point inside a cell (*energy modulation*).

In the region $|\eta| \geq 1.8$, not instrumented with the presampler, the energy deposited in front of the calorimeter is parametrized as a function of the shower longitudinal barycentre X (4.1) computed with the information given by the three calorimeter layers only:

$$
\begin{aligned}
E_{e,\gamma} = {} & \underbrace{a(E_{tot}^{Acc},|\eta|) + b(E_{tot}^{Acc},|\eta|) \times X + c(E_{tot}^{Acc},|\eta|) \times X^2}_{\text{Energy in front}} \\
& + \underbrace{\frac{s_{cl}^{Acc}(X,\eta)}{f_{out}(X,|\eta|)} \times \left(\sum_{i=1,3} E_i^{\mathrm{clLAr}} \right)}_{\text{Energy in the Accordion}} \times \underbrace{(1 + f_{leak}(X,|\eta|))}_{\text{Longitudinal leakage}} \times \underbrace{F(|\eta|,\phi)}_{\text{Energy modulation}}
\end{aligned}
\tag{4.4b}
$$

4.3.1 Samples and selections

For the standard calibration MC simulations with single particle at 16 fixed energies (5 GeV, 7.5 GeV, 10 GeV, 15 GeV, 25 GeV, 35 GeV, 50 GeV, 60 GeV, 75 GeV, 90 GeV, 100 GeV, 200 GeV, 300 GeV, 500 GeV, 700 GeV, 1000 GeV) have been used. Most of the samples contain 800k events, at high energy the statistics is lower (200k for the 1 TeV sample) for a total of 15M events for electrons and 13M for photons.

Some selections are applied both for electrons and photons:

- tight selection based on shower shapes,
- only 1 reconstructed cluster in the events.

Because of the second requirement this calibration in fact is calibrating only the electromagnetic shower and not the full particle. The difference is only when from one particle more than one cluster is reconstructed, for example for converted photons when the conversion is very asymmetric and for electron in the presence of hard bremsstrahlung.

4.3.2 Front energy

The energy lost in front of the calorimeter, or simply the “front energy”, is the most difficult energy loss to estimate and it is the only one depending on the raw-energy. It is defined as the sum of all the energy deposits into active and passive material located before the calorimeter. This quantity is strongly correlated with the amount of material traversed by the particle, so with its direction in η and ϕ. The distribution of the material up to the active calorimeter is in Fig. 4.6, the one at the edge of the inner detector is in Fig. 3.4. In region $|\eta| < 0.6$ the material is small (less than $2X_0$) and quite constant. In the second part of the barrel the material increases to the maximum of $5X_0$ just before the transition region between the barrel and the endcap. Only the region $|\eta| < 2.5$ is taken into account for the calibration.

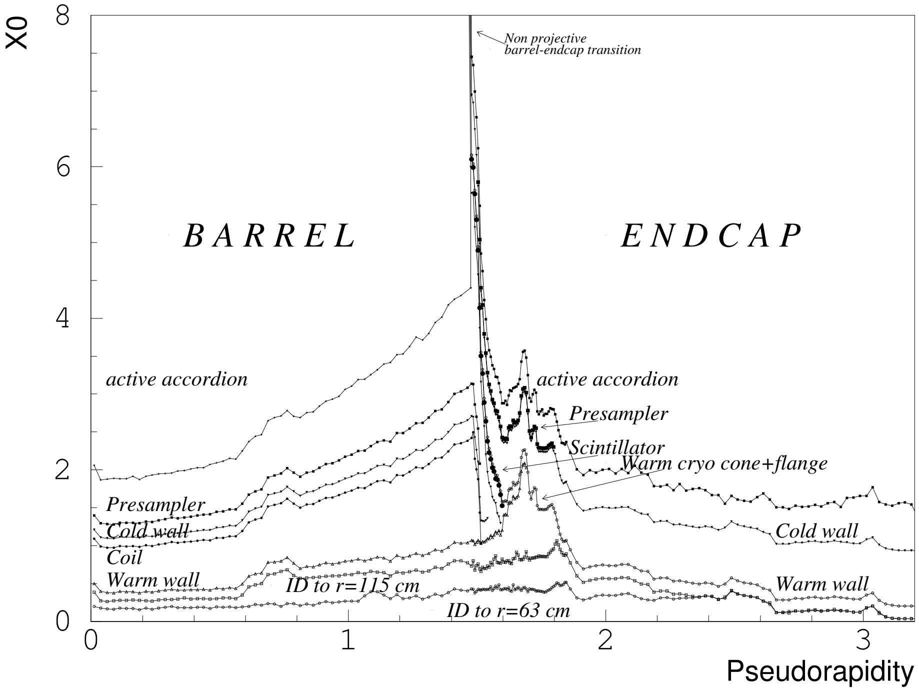

Figure 4.6: Breakdown of dead material (in X_0) up to the active EM calorimeter, as function of $|\eta|$.

The front energy is parametrized as in equation (4.4a) for $|\eta| < 1.8$ and as in equation (4.4b) for $1.8 < |\eta| < 2.5$. The coefficients a, b, and c are parametrized with various functions:

$$a(E_{tot}^{Acc},|\eta|) = \begin{cases} a_1(|\eta|) + a_2(|\eta|)E_{tot}^{Acc} + a_3(|\eta|)\left(E_{tot}^{Acc}\right)^2 & |\eta| < 1.425 \\ a_1(|\eta|) + a_2(|\eta|)E_{tot}^{Acc} + a_3(|\eta|)\sqrt{E_{tot}^{Acc}} & 1.55 < |\eta| < 1.8 \\ a_1(|\eta|) + a_2(|\eta|)E_{tot}^{Acc} + a_3(|\eta|)\left(E_{tot}^{Acc}\right)^2 & 1.8 < |\eta| < 2.5 \end{cases} \tag{4.5a}$$

$$b(E_{tot}^{Acc}, |\eta|) = \begin{cases} b_1(|\eta|) \left(\log(E_{tot}^{Acc})\right)^{b_2(|\eta|)} + b_3(|\eta|)\sqrt{E_{tot}^{Acc}} \left(E_{tot}^{Acc}\right)^2 & |\eta| < 1.425 \\ b_1(|\eta|) + b_2 \left(\log(E_{tot}^{Acc})\right)^{b_2(|\eta|)} + b_3(|\eta|)\sqrt{E_{tot}^{Acc}} & 1.55 < |\eta| < 1.8 \\ b_1(|\eta|) + b_2(|\eta|)E_{tot}^{Acc} + b_3(|\eta|) \left(E_{tot}^{Acc}\right)^2 & 1.8 < |\eta| < 2.5 \end{cases} \tag{4.5b}$$

$$c(E_{tot}^{Acc}, |\eta|) = \begin{cases} 0 & |\eta| < 1.425 \\ c_1(|\eta|) + c_2(|\eta|)E_{tot}^{Acc} + c_2(|\eta|)/(E_{tot}^{Acc})^2 & 1.55 < |\eta| < 1.8 \\ c_1(|\eta|) + c_2(|\eta|)E_{tot}^{Acc} + c_3(|\eta|) \left(E_{tot}^{Acc}\right)^2 & 1.8 < |\eta| < 2.5 \end{cases} \tag{4.5c}$$

these functions have no a physics meaning. The three $|\eta|$ regions correspond to: barrel, endcap with presampler and endcap without presampler.

To estimate all the coefficients various fits are needed: the procedure is complicated by the fact that almost all the distributions are asymmetric. The following steps are followed for every cell in pseudorapidity.

1. For every dataset (every one with a fixed true energy) the core of the distribution of the energy deposited inside the accordion is fitted with a gaussian fit (see Fig. 4.7 for an example). In this way the mean of the gaussian is the peak of the accordion energy distribution and it is used as E_{tot}^{Acc} in formulas (4.5a), (4.5b) and (4.5c). During the reconstruction the accordion energy is the energy corrected for all the effects except for the energy lost in front (sampling, out of cluster).

2. For every dataset the distribution of the energy lost in front versus the energy in the presampler (or the longitudinal barycentre for $|\eta| > 1.8$ is considered (Fig. 4.8 and Fig. 4.9). The distribution is divided in 15 slices with different values of presampler energy (or shower depth for $|\eta| > 1.8$). For every slice the distribution of the energy lost in front is fitted with a gaussian fit to find the peak position (see Fig. 4.10 as an example). Some criteria are defined to quantify the goodness of the fit as the reduced-χ^2, the number of fitted bins and the distance between the mean of the gaussian and the mean of the whole distribution. Using these criteria some fits are discarded, others are replaced with the mean of the distribution. The points corresponding to the 15 peaks are fitted with the first line of (4.4a) or (4.4b) (see blue points in Fig. 4.8 and 4.9) .

3. At this point a set of E_{tot}^{Acc}, a, b and c coefficients are determined for every true energy and for every $|\eta|$ bin. They are fitted using the parametrizations in (4.5a), (4.5b) and (4.5c) as shown in Fig. 4.11 obtaining coefficients a_i, b_i and c_i.

The dependency of the energy lost in front of the accordion with respect to the front energy varies along $|\eta|$, for this reason a linear function is used up to $|\eta| = 1.8$. Some example with electrons at different pseudorapidity and true energy are shown in Fig. 4.12.

4.3.3 Accordion sampling fraction

The electromagnetic calorimeter is a sampling calorimeter, this means that a large fraction of the energy is lost in the absorber material. A factor (~ 5) is already applied to the raw

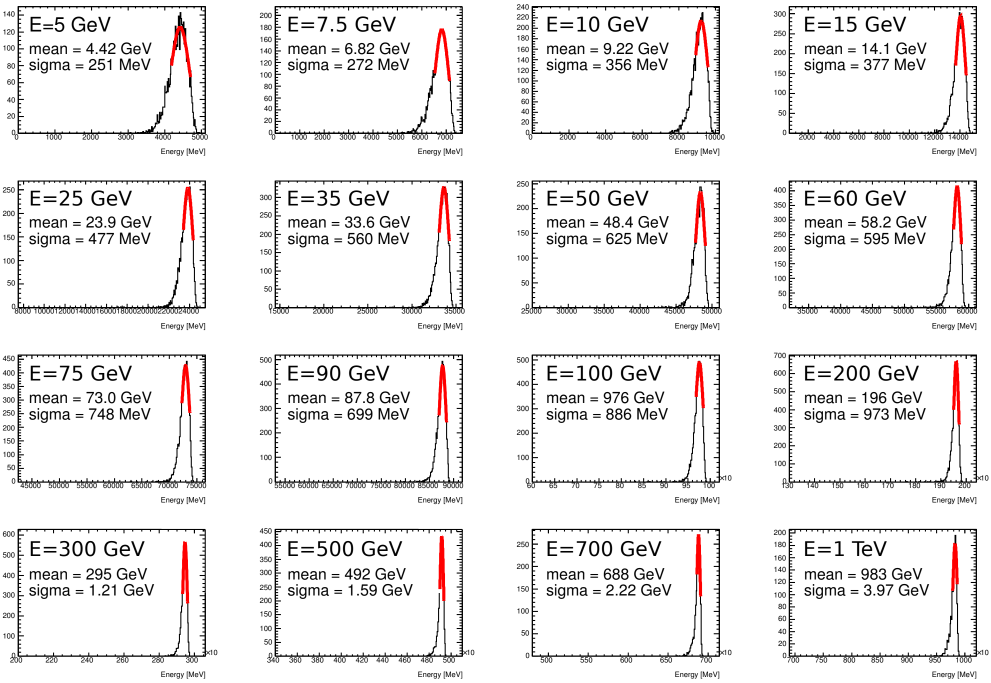

Figure 4.7: accordion energies for all the 16 electron samples from 5 GeV to 1 TeV with $0.25 < |\eta| < 0.275$. The mean and the width of the truncated iterative gaussian fit are reported.

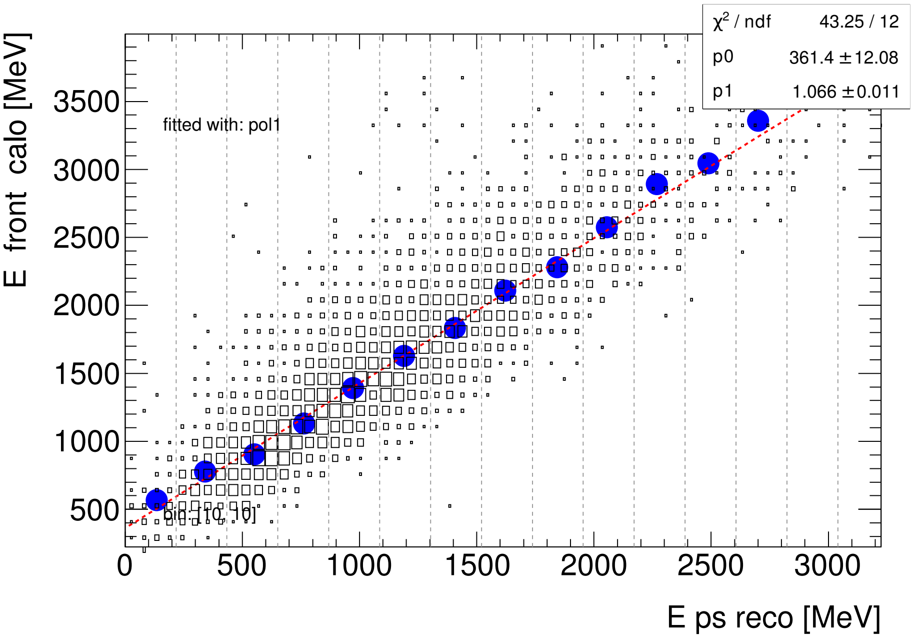

Figure 4.8: energy lost before the accordion versus the energy in the presampler for 50 GeV electron with $0.25 < |\eta| < 0.275$. The vertical dotted lines divided the range of the presampler energy in 15 bins. The vertical position of the blue points are from 15 fits as in Fig. 4.10, the horizontal position is the mean of the presampler energy in each bin. The dotted line is the fit of the blue points.

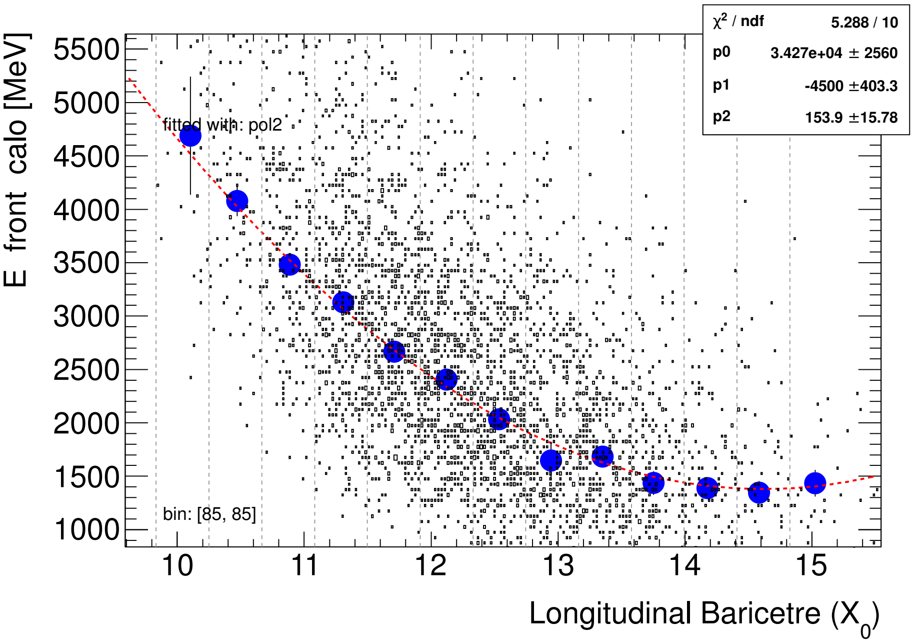

Figure 4.9: energy lost before the accordion versus the longitudinal barycentre for 50 GeV electron with $2.125 < |\eta| < 2.15$. The vertical dotted lines divided the range of the presampler energy in 15 bins. The vertical position of the blue points are from 15 fits, the horizontal position is the mean of the longitudinal depth in each bin. The dotted line is the fit of the blue points.

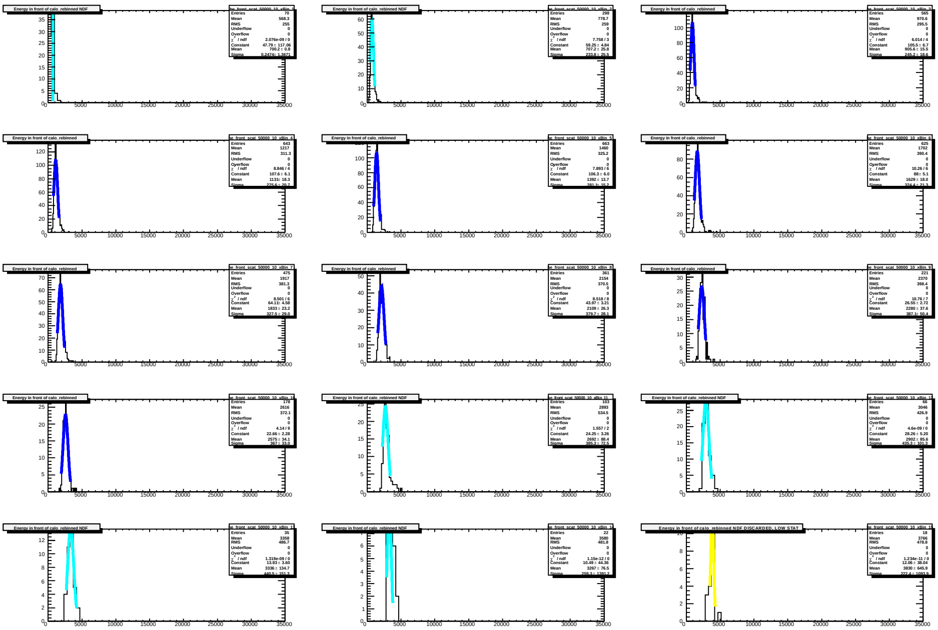

Figure 4.10: distribution of the energy lost before the accordion for 15 slice in the presampler energy for 50 GeV electron with $0.25 < |\eta| < 0.275$ (see previous figure 4.8). Yellow fit are discarded, light blue fit are not used and the mean of the distribution is used instead.

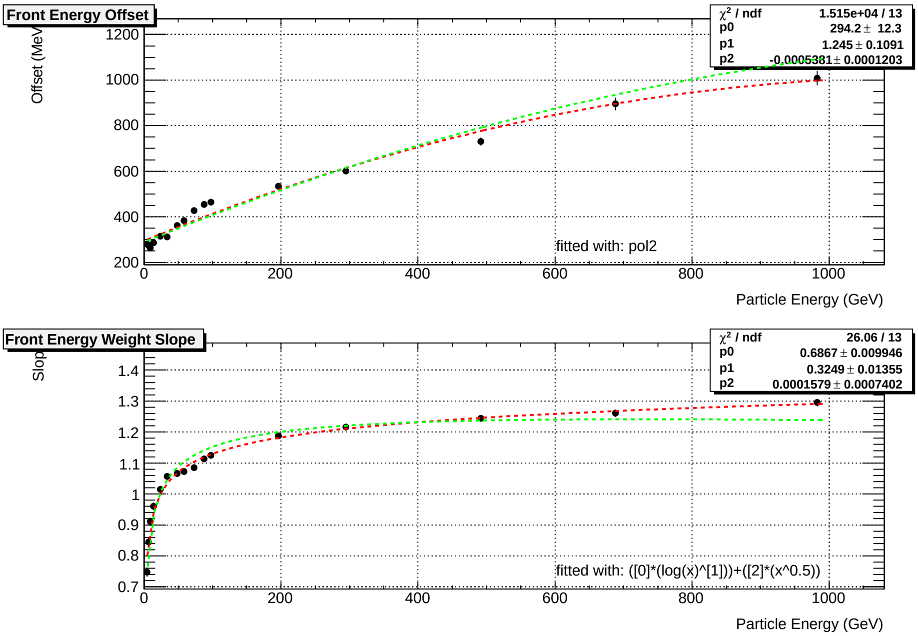

Figure 4.11: Fit of the offset parameter a and of the slope b versus the corrected energy in the accordion for electron with $0.25 < |\eta| < 0.275$. The red curve is the one described in section 4.3.2, the green one is from the procedure described in section 4.5.

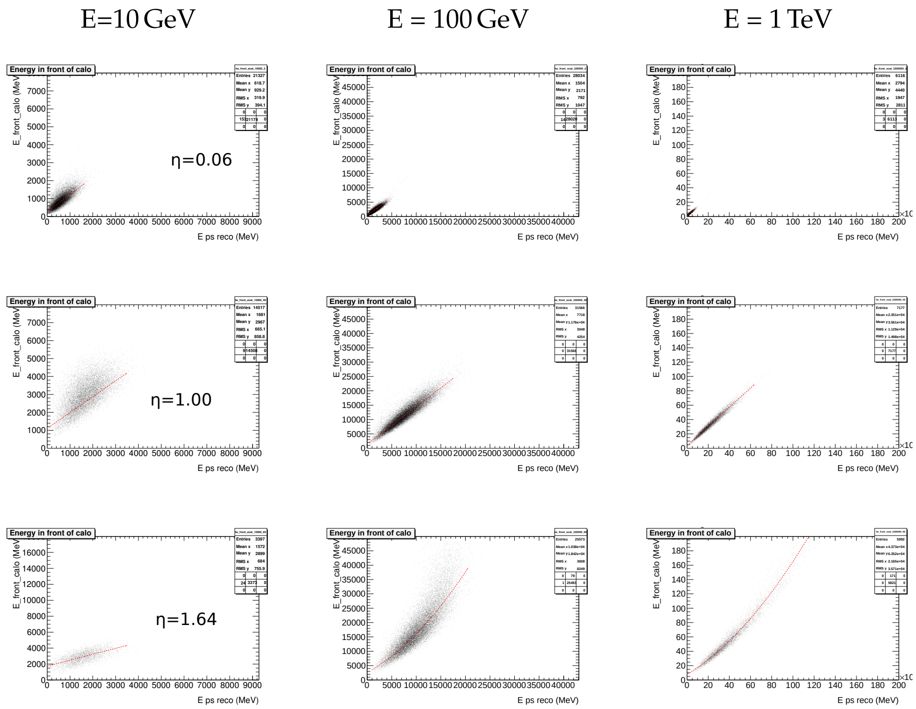

Figure 4.12: Distribution of the energy lost in front of the accordion versus the presampler energy for various true energy and η direction. The fit in red are done using the procedure described in the text.

energy to take into account this effect. In this calibration this effect is finely corrected with the factor s_{cl}^{Acc} depending on the longitudinal barycentre X and $|\eta|$ parametrized as:

$$s_{cl}^{Acc} = s_1 + s_2 X + s_3 X^2 \tag{4.6}$$

This parametrization is different for every cluster size. As an example in figure 4.13 the behaviour of the sampling fraction for electron with $0.25 < |\eta| < 0.275$ at different energies. The fitted points correspond to a profile of the distribution using the mean. Since no energy dependency is observed the parametrization is not energy dependent. The correction is very small and only at low X little deviations from 1 are observed.

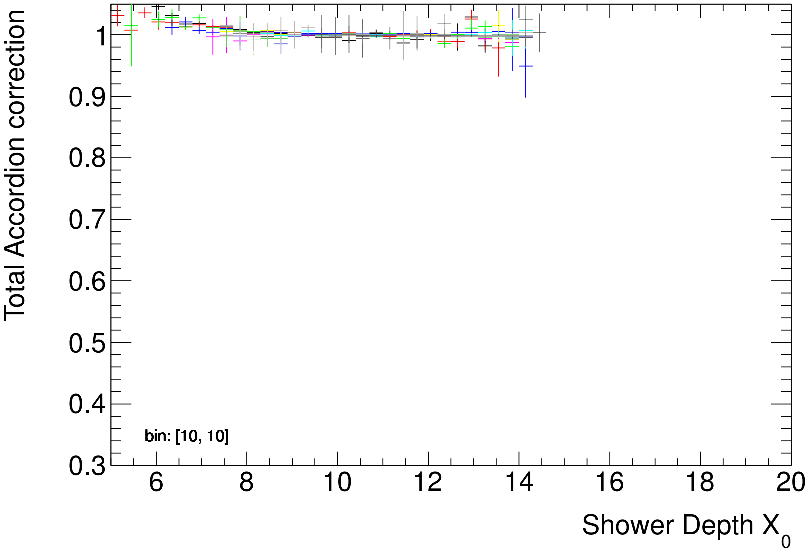

Figure 4.13: sampling fraction for electron with $0.25 < |\eta| < 0.275$ versus the longitudinal barycentre using 3×7 cluster window, different colours correspond to different energies.

4.3.4 Out of cluster

The out of cluster energy correspond to the energy deposited outside the reconstructed cluster and since it corrects for the fact that the cluster has a finite dimension in $\eta \times \phi$ it depends on the cluster size.

To get the out of cluster parametrization, the energy deposited outside the cluster versus longitudinal barycentre is considered (Fig. 4.14) using all the energies. The distribution is divided in 15 slices. For every slice a fit with a Landau distribution is performed to find the peak of the distribution (see Fig. 4.15 as an example). Some criteria are defined to quantify the goodness of the fit as the reduced-χ^2, the number of fitted bins and the difference between the most probable value of the Landau distribution and the mean of the whole distribution. Some fits are discarded, others are replaced with the mean of the distribution. The points corresponding to the 15 peaks are fitted with

$$\begin{aligned}\text{percentage of out of cluster energy} &= \frac{1}{100}\left(\frac{1}{f_{out}}-1\right) = \\ &= \begin{cases} f_1 + f_2 X + f_3 X^2 & |\eta| < 1.425 \\ f_1 + f_2 X + f_3/X & 1.55 < |\eta| < 2.5 \end{cases}\end{aligned} \tag{4.7}$$

As shown on Fig. 4.16 no energy dependence is observed and so the parametrization is energy independent.

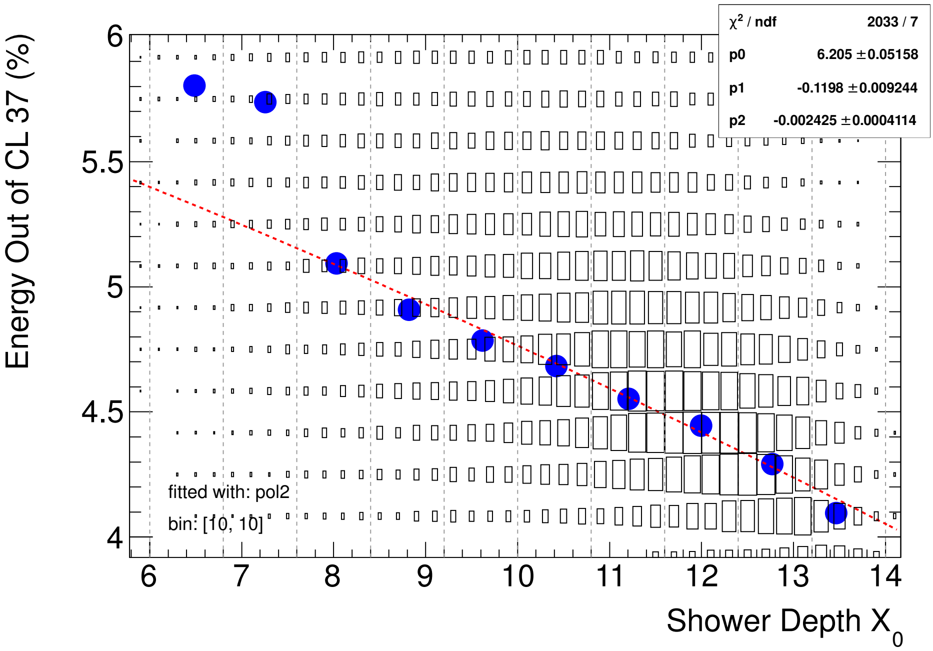

Figure 4.14: percentage of out of cluster energy fraction with respect to the longitudinal barycentre X for electron with $0.25 < |\eta| < 0.275$ using 3×7 cluster window using all the energies. The vertical dotted lines divided the range of X in 15 bins. The vertical position of the blue points are from 15 fits as in Fig. 4.15, the horizontal position is the mean of X in each bin. The dotted line is the fit of the blue points using (4.7).

4.3.5 Longitudinal leakage

The longitudinal leakage is the less important correction, it corrects for the fraction of energy leaking the electromagnetic calorimeter into the hadronic calorimeter. The hadronic calorimeter is not used, but a parametrization function of the longitudinal barycentre is used:

$$f_{leak}/100 = g_0 + g_1 X + g_2 \exp(X) \tag{4.8}$$

As an example in Fig. 4.17 the distribution of the percentage leakage is shown for various energy for electron with $0.25 < |\eta| < 0.275$, no energy dependency is observed so the correction is energy independent.

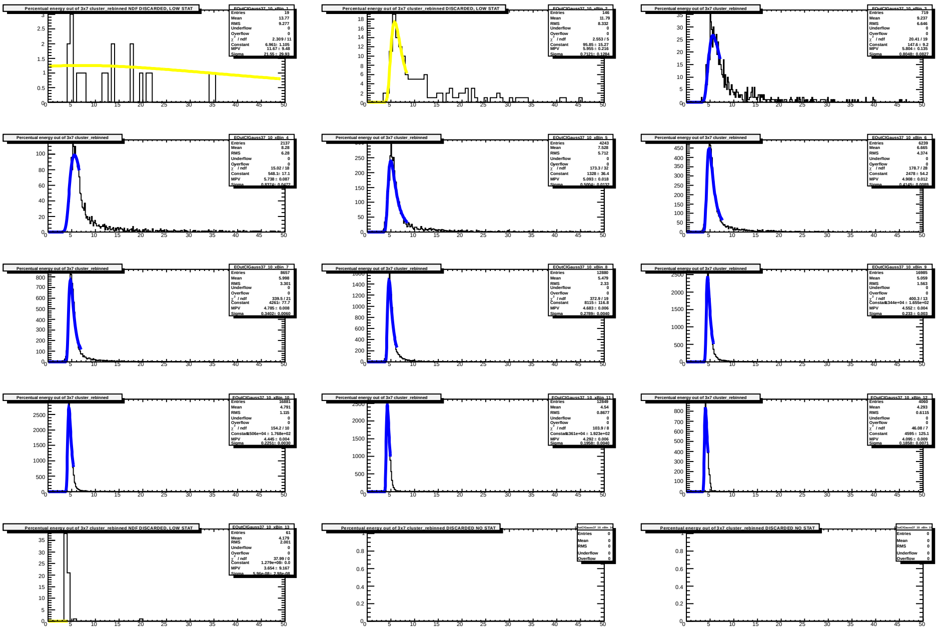

Figure 4.15: distribution of the out of cluster energy for 15 slice in the longitudinal barycentre for 50 GeV electron with $0.25 < |\eta| < 0.275$ (see previous figure 4.14). Yellow fit are discarded, light blue fit are not used and the mean of the distribution is used instead.

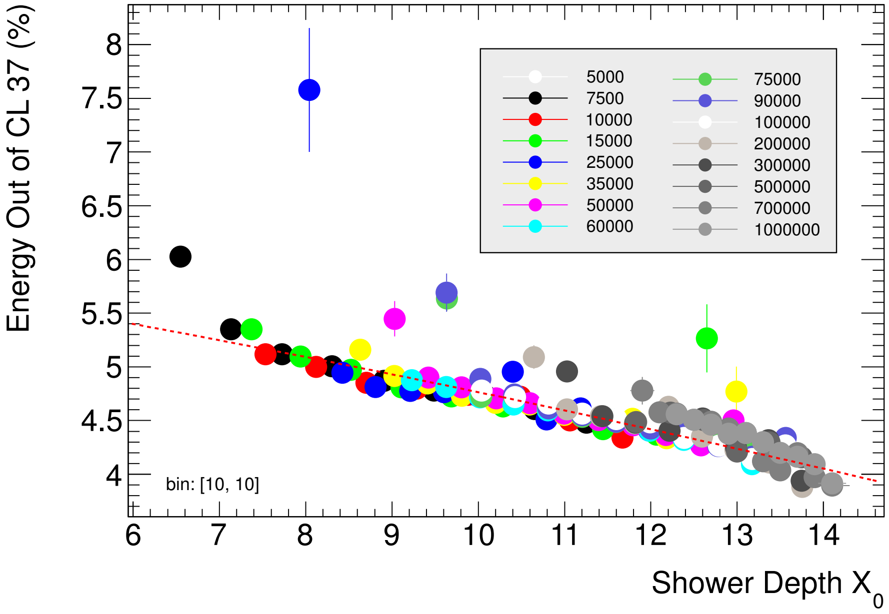

Figure 4.16: percentage of out of cluster energy fraction with respect to the longitudinal barycentre X for electron with $0.25 < |\eta| < 0.275$ for various energies (different colours). The points are from Landau fits of the bidimensional distribution dividing it in 15 vertical slices as described in the text.

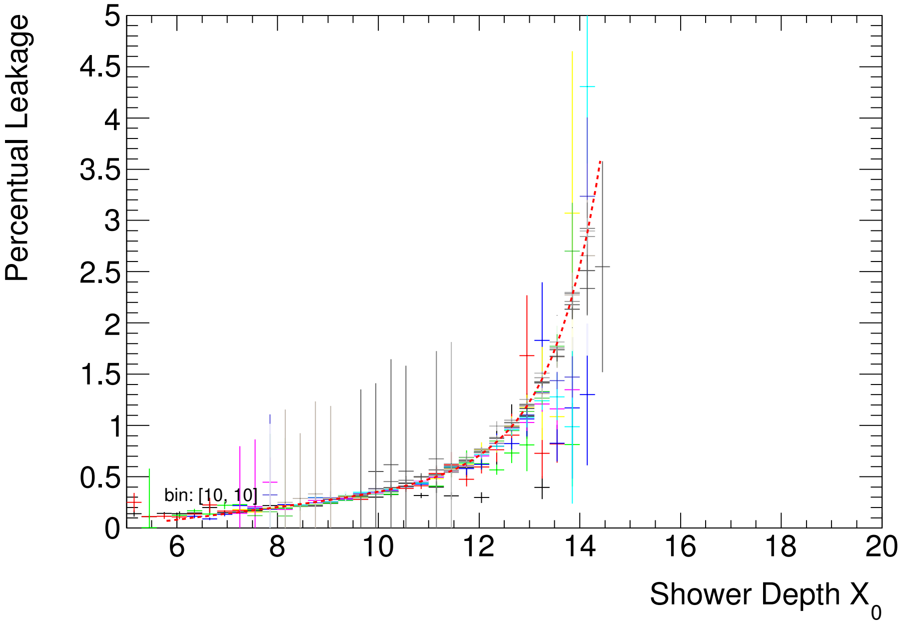

Figure 4.17: percentage of longitudinal leakage function of the longitudinal barycentre X for electron with $0.25 < |\eta| < 0.275$ for various energies (different colours). The point are from a profile of the distribution using the mean. The dotted red line is the fit using formula (4.8) summing all the energies.

4.4 Performance of the standard calibration

There are many quantities useful to study the performance and the quality of a calibration. The two main aspects are the linearity (how the difference between the calibrated energy and the true energy varies with the energy) and the resolution (the width of the distribution of the reconstructed energy). The most useful distribution is E/E_{true} where the numerator is the reconstructed energy and the denominator is the true energy of the particle (an example in Fig. 4.18). The main problem arises from the fact that this distribution is not symmetric and has tails at low values. For historical reasons this distribution is fitted with a truncated Gaussian with an iterative method, in such a way that at the end the fit range are between -1σ and 2.5σ where σ is the width of the last but one iteration with respect to the mean of the last but one iteration. In this way only the core of the distribution is fitted and the tails are ignored. The linearity is defined as the mean of the Gaussian and the relative resolution is the width of the Gaussian.

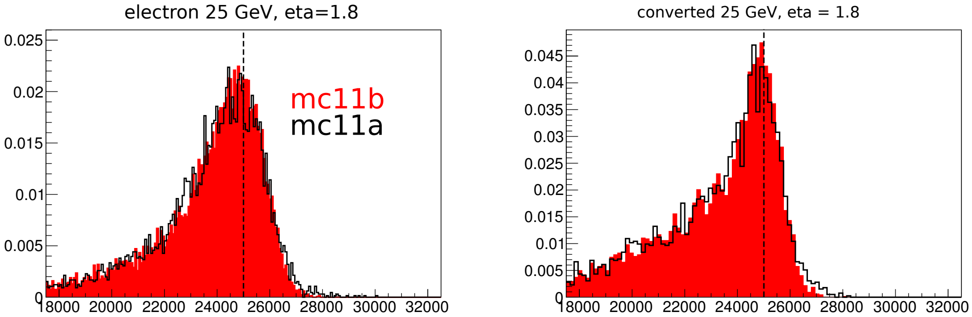

(a) electrons **(b)** converted photons

Figure 4.18: distribution of E/E_{true} for (a) electron and (b) converted photons of 25 GeV and $|\eta|$ around 1.8.

The performances are evaluate on single particle with pileup (mc11a) and without pileup (mc11b) for electrons, converted and unconverted photons. The definition of converted photons is the same used in the optimization of the standard calibration (radius of conversion less than 800 mm). Particles are required to pass the tight selection cut, but no requirements have been done on the number of reconstructed clusters.

In the following the linearity is plotted versus the pseudorapidity for electron (Fig. 4.19), unconverted (Fig. 4.21) and converted photons (Fig. 4.20). Very low energies are shown only for the endcap since they don't pass the cut at the reconstruction level on the transverse energy $E_T = E/\cosh\eta$. Usually the linearity is inside the $\pm 0.5\%$ band around the unity for energies greater than 25 GeV in the barrel and 50 GeV in the endcap. The most problematic region are the one around $|\eta| \sim 1.6$ and at the end of the accordion at $|\eta| \sim 2.5$. The unconverted photons are the best calibrated particles because the energy lost in front is negligible, the worst calibrated particles are the converted photons. It is also important to remember that the linearity is estimated as the mean of a gaussian fit and so it can be affected by problems regarding the fit procedure or the peak definition itself in particular at low energy where the E/E_{true} distribution becomes very wide. The effect of the pileup is visible, deteriorating the linearity.

The resolution defined as the with of the truncated Gaussian iterative fit is shown in figure 4.22 for electrons, 4.23 converted and 4.24 unconverted photons. From the plots it

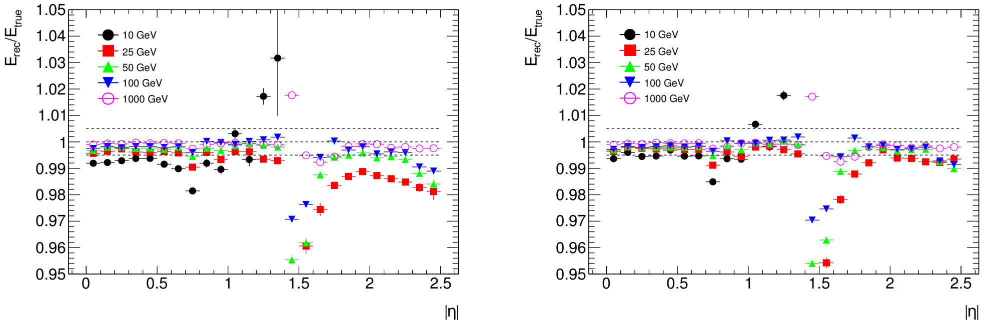

(a) mc11a **(b)** mc11b

Figure 4.19: linearity for electron (a) with and (b) without pileup.

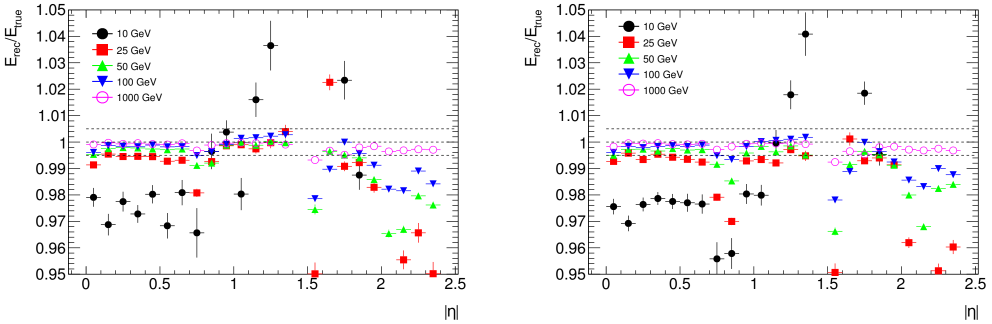

(a) mc11a **(b)** mc11b

Figure 4.20: linearity for converted photons (a) with and (b) without pileup.

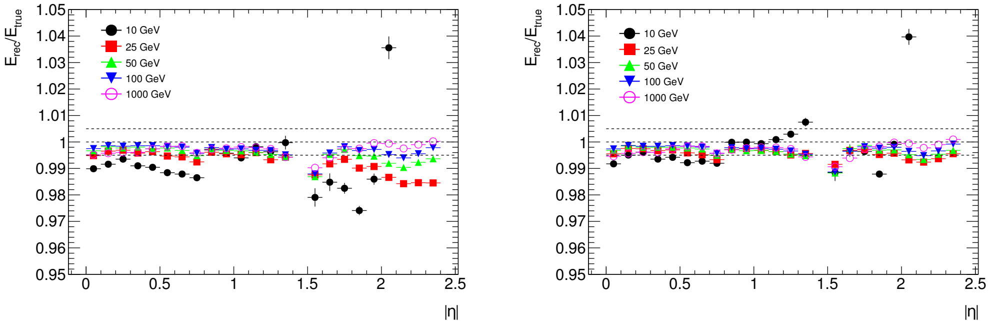

(a) mc11a **(b)** mc11b

Figure 4.21: linearity for unconverted photons (a) with and (b) without pileup.

is clear that the resolution is mainly function of the material in front of the calorimeter. As for the linearity the best resolution is for unconverted photons, the worse for converted photons. Since the pileup with respect to the calibration is a random process it increases the resolution.

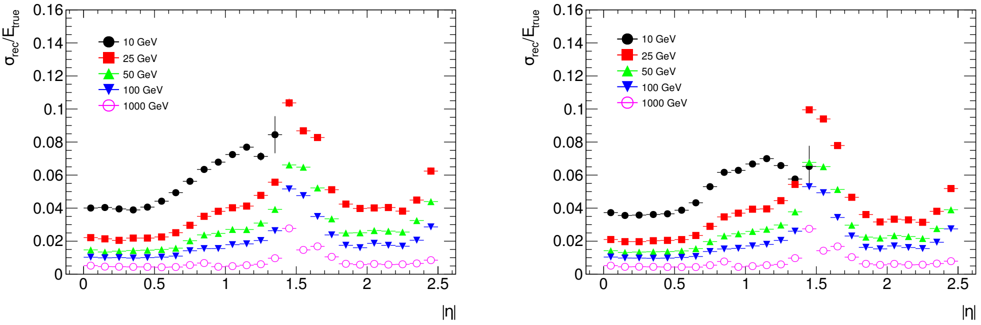

(a) mc11a **(b)** mc11b

Figure 4.22: resolution for electron (a) with and (b) without pileup.

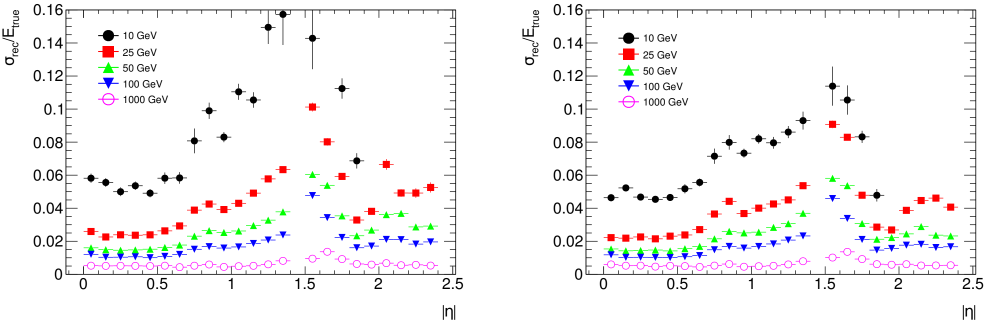

(a) mc11a **(b)** mc11b

Figure 4.23: resolution for converted photons (a) with and (b) without pileup.

From the dependency of the resolution with the energy it is possible to extract the sampling A, the noise B and the constant term C of the calorimeter with the usual formula:

$$\frac{\sigma_E}{E} = \frac{A}{\sqrt{E}} \oplus \frac{B}{E} \oplus C. \tag{4.9}$$

The fit is done fixing the noise term to the one from a direct measure of the electronic chain, the values are in table 4.1. The sampling term is shown in figure 4.25 for electrons, 4.26 for converted photons and 4.27 for unconverted photons. The constant term is shown in figure 4.28 for electrons, 4.29 for converted photons and 4.30 for unconverted photons.

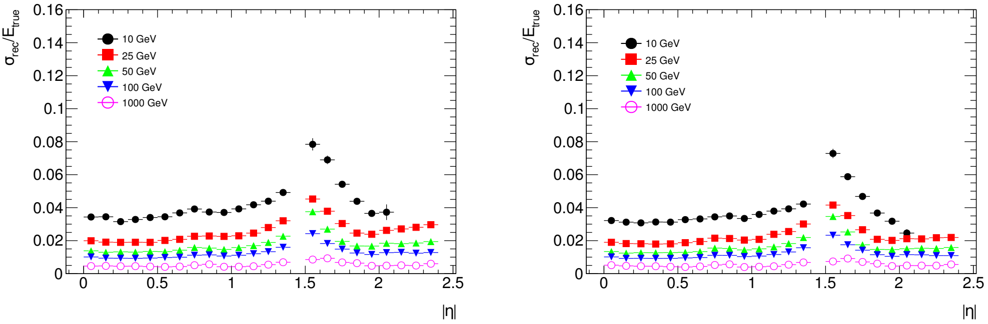

(a) mc11a

(b) mc11b

Figure 4.24: resolution for unconverted photons (a) with and (b) without pileup.

$\|\eta\|$	noise term [GeV]		
	3×7	5×5	3×5
0.0–0.1	0.27	0.3	0.23
0.1–0.2	0.27	0.3	0.23
0.2–0.3	0.27	0.3	0.23
0.3–0.4	0.27	0.3	0.23
0.4–0.5	0.27	0.29	0.23
0.5–0.6	0.26	0.28	0.22
0.6–0.7	0.25	0.27	0.21
0.7–0.8	0.23	0.25	0.19
0.8–0.9	0.21	0.22	0.17
0.9–1.0	0.19	0.2	0.16
1.0–1.1	0.17	0.18	0.14
1.1–1.2	0.16	0.17	0.13
1.2–1.3	0.15	0.16	0.13
1.3–1.4	0.14	0.14	0.12
1.4–1.5	0.27	0.3	0.23
1.5–1.6	0.23	0.25	0.2
1.6–1.7	0.17	0.2	0.16
1.7–1.8	0.15	0.15	0.13
1.8–1.9	0.13	0.13	0.1
1.9–2.0	0.1	0.1	0.08
2.0–2.1	0.07	0.07	0.07
2.1–2.2	0.06	0.06	0.05
2.2–2.3	0.05	0.05	0.04
2.3–2.4	0.04	0.04	0.03
2.4–2.5	0.03	0.03	0.02

Table 4.1: noise term used in the fit for the sampling and constant term for the three sliding window sizes.

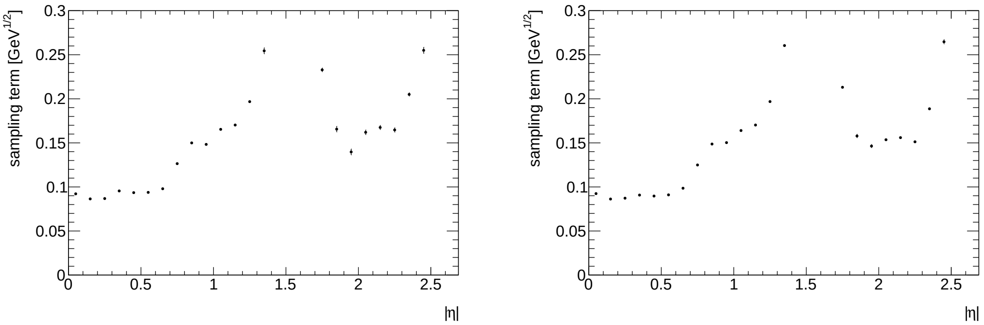

(a) mc11a **(b)** mc11b

Figure 4.25: sampling term for electron (a) with and (b) without pileup.

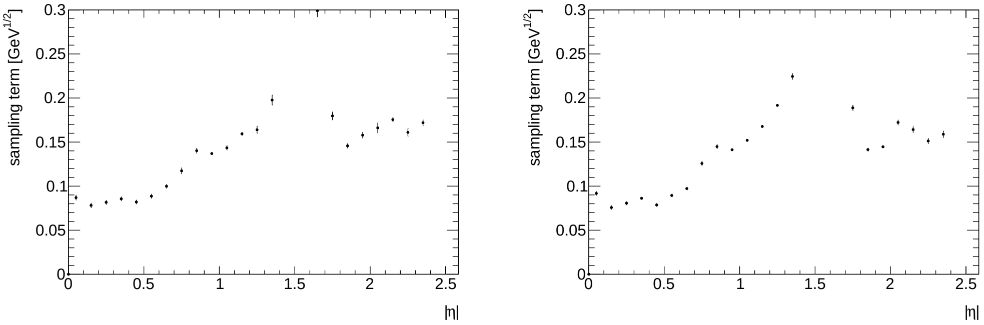

(a) mc11a **(b)** mc11b

Figure 4.26: sampling term for converted photons (a) with and (b) without pileup.

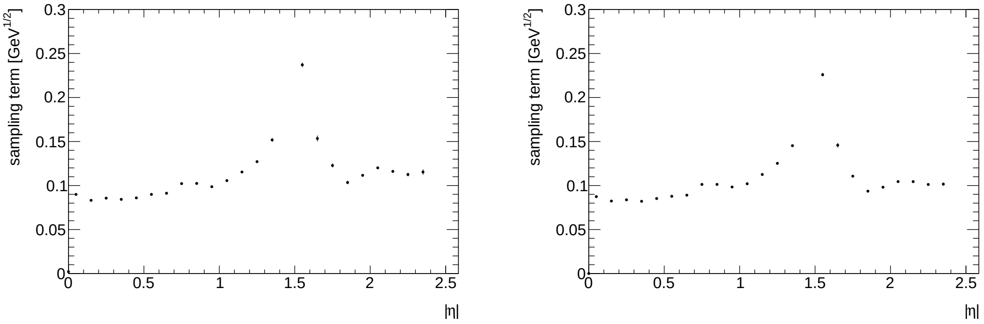

(a) mc11a **(b)** mc11b

Figure 4.27: sampling term for unconverted photons (a) with and (b) without pileup.

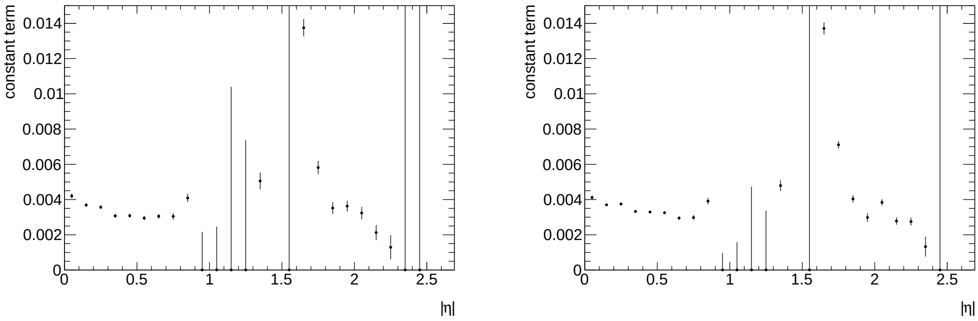

(a) mc11a **(b)** mc11b

Figure 4.28: constant term for electron (a) with and (b) without pileup.

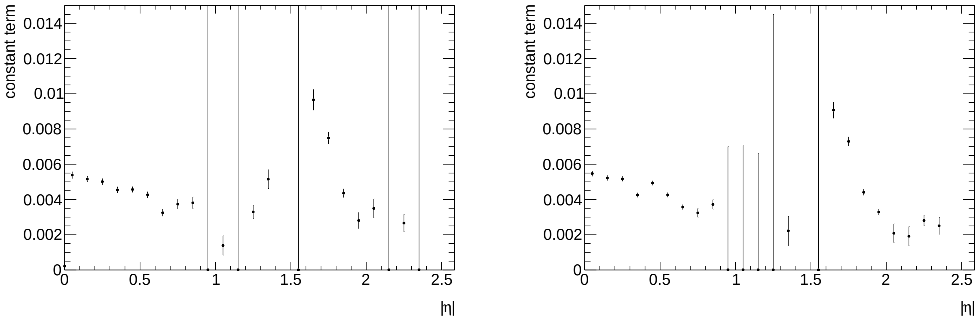

(a) mc11a **(b)** mc11b

Figure 4.29: constant term for converted photons (a) with and (b) without pileup.

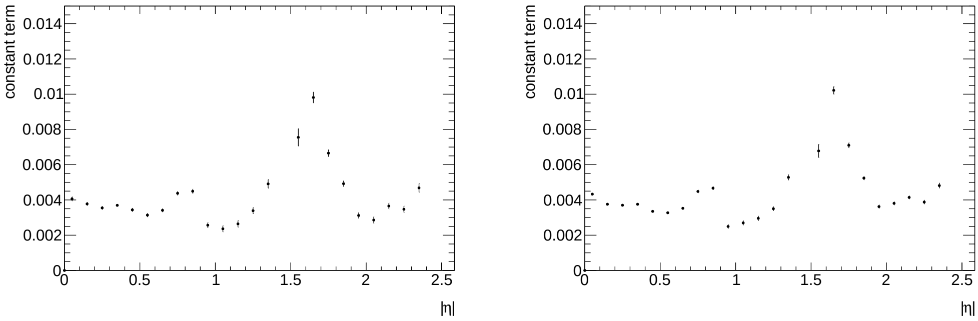

(a) mc11a **(b)** mc11b

Figure 4.30: constant term for unconverted photons (a) with and (b) without pileup.

4.5 Improvements and considerations about the standard calibration

The standard calibration presented in this chapter is based on several parametrizations of various components of the energy loss. Mainly because of the huge number of needed fits it is quite difficult to maintain mainly and to improve. Considering three different particle calibrations (electrons, unconverted photons and converted photons) the number of fits for a complete calibration is:

$$\begin{aligned}
3\times &\quad \text{\# of particles}\\
2.5/0.025\times &\quad \text{\# of } |\eta| \text{ bins}\\
[16\times(15+1)+3 &\quad \text{\# of fits for the front correction}\\
+3 &\quad \text{\# of fits for the sampling correction}\\
+3\times(15+1) &\quad \text{\# of fits for the out of cluster correction}\\
+1] &\quad \text{\# of fits for the leakage correction}\\
&\quad \simeq 90\,000
\end{aligned}$$

All of these fits are important for a correct calibration, some automatic check are implemented testing the goodness of the fits but essentially all of them have to be checked. One improvement has been the usage of linear fit when possible to improve the robustness of the fit, because in this case an algebraic method is used instead of a minimization method. In addition also the removal of outliers has been helpful to improve the stability of fits.

For the front energy parametrization a new method has been tried, but no big improvements have been observed. Instead of using two steps (see section 4.3.2), the first to derive a, b and c, the second to derive all the a_i, b_i, c_i only one step was used using a multidimensional fit, fitting the parameters a_i, b_i and c_i directly. The derived a, b and c parameter are the green lines in Fig. 4.11.

Another variation of the method was to change the way the cells are grouped. In the standard calibration every cell is calibrated independently from the neighbour ones. It was tried to optimize the coefficients for one cell using the particle hitting also the neighbour cells (first neighbours or second neighbours). This methods gives more stable coefficients along $|\eta|$ but it doesn't work well where the variation of the amount of material is fast. No improvement in performance have been observed.

Since the huge number of fit it is impossible to introduce new dependencies. In fact the only correction depending by two parameters (the energy and the presampler energy / longitudinal barycentre) is the front correction and it contributes to the total count with $\sim 70\,000$ fits. For this reason the only way to introduce a new dependency without changing completely the method is to factorize the new dependence or, in other words, to introduce the correction on the top of the standard calibration. This method has been used by the correction described in the next section, taking into account the radius of conversion for converted photons.

4.6 Correction for converted photons

Using the standard calibration method the only way to improve the performances is to add additional information. Some other improvements have been developed (more robust fit techniques, more consistent definition of the quantities) but the observed improvements are only on the stability of the optimization and not on the performance. A special correction has been developed to improve the performance of the worst category: converted photons.

There are many information that are not used in the standard calibration: the one that seems to give more information for this category is the radius of conversion R. A correlation between this quantity and the energy loss is expected, see Fig. 4.32:

- the front energy is negatively correlated with the radius of conversion because if the radius is big it means that the two electrons from the conversion have less space to traverse before the calorimeter and so less material and less chance to start a shower,
- the out of cluster is negatively correlated because if the radius is small the two electrons have more space to open.

The standard calibration is already able to partially take into account the R dependence since R is correlated with the longitudinal barycentre already included in the standard calibration. This effect is shown in figure 4.31 where the front energy and the out of cluster energy estimated by the tool are plotted for two extreme cases: $0 < R < 100$ and $700 < R < 800$.

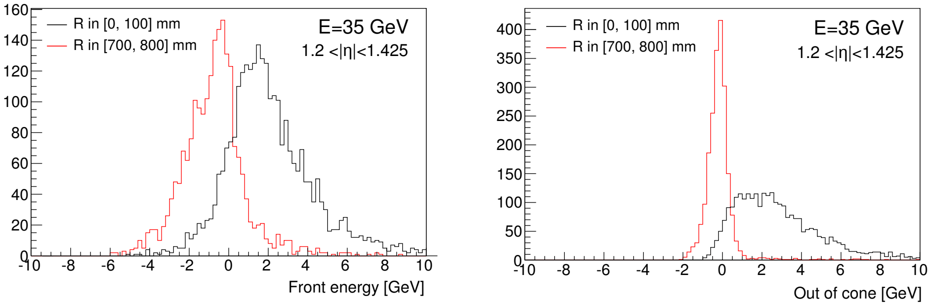

(a) front **(b)** out of cluster

Figure 4.31: Distribution of (a) the estimated front energy and (b) out of cluster energy by the standard calibration for converted photons of 35 GeV and $1.2 < |\eta| < 1.425$. The black distribution is for converted photons with $0 < R < 100$, the red for $700 < R < 800$.

4.6.1 Perfect calibration procedure

Since this correction wants to be generic, a preliminary correction is needed to decouple the effect of the R correlation with the energy correction and other effects. In particular the correction should not correct for the non-linearity of the standard calibration as in figure 4.20 but only for the effect due to the radius of conversion. For this reason the distributions of E/E_{true} used in the following are scaled by the inverse of the linearity in such a way that the peak of the distribution is perfectly centred at 1. For this reason the resulting distribution is called "perfect".

4.6.2 Recalibration procedure

To provide in a fast way an improvement a correction on top of the standard calibration has been developed using as input the radius of conversion R, the pseudorapidity η

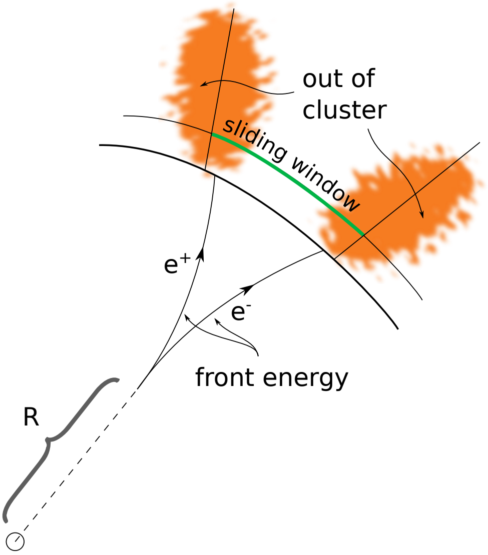

Figure 4.32: Sketch of the energy loss dependency on the radius of conversion for converted photons.

and the calibrated energy as in the previous section. As in the standard calibration the detector is supposed to be symmetric between positive and negative η. A tool is provided to apply the correction directly on the available data format, so no reprocessing of the data is needed.

The tool was optimized looking at the correlation of the calibrated energy, using the standard calibration, with the true radius of conversion. As before the choice to use the true radius of conversion instead of the reconstructed one is driven by the fact that in this way the correction is independent of the reconstruction algorithm. In figure 4.33 the correlation of the E/E_{true} distribution with R is shown stacking several distributions corresponding to different ranges of R.

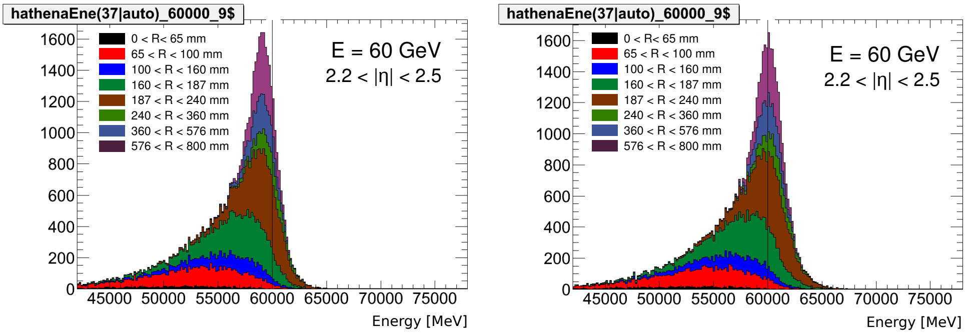

(a) standard calibration **(b)** "perfect" calibration

Figure 4.33: E/E_{true} distribution for eight R-categories stacked, using (a)the standard calibration and (b) the "perfect" calibration for converted photons of 60 GeV and $2.2 < |\eta| < 2.5$.

For this optimization the distribution of E/E_{true} is divided in R_{true} intervals and for every category the distribution is fitted with the usual iterative truncated Gaussian fit. The mean of this fit is used to scale the distribution in such a way to have the peak well centred at 1.

The first step is to define the R_{true} intervals, this is not trivial because the R_{true} distribution depends on the material distribution of the inner detector and therefore on $|\eta|$ (see Fig. 4.34c and 4.34d). For this reason the definition of the R_{true} intervals is different for every range in $|\eta|$. The categories are defined in such a way to uniform the statistics inside every interval. The procedure is illustrated in figure 4.34 and the categories are listed in table 4.2.

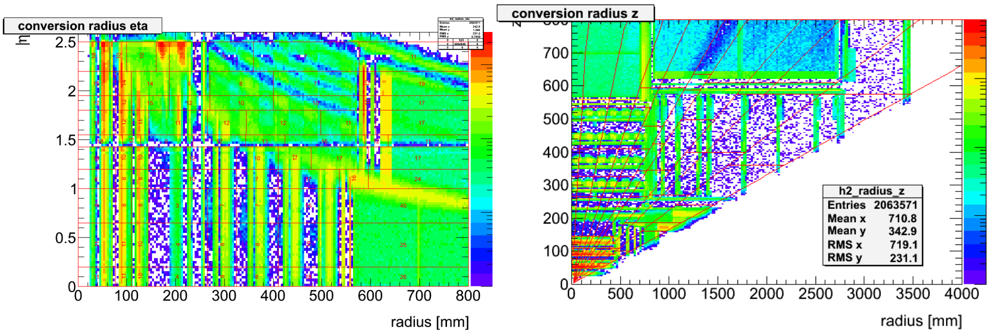

(a) $|\eta|$ vs R **(b)** z vs R

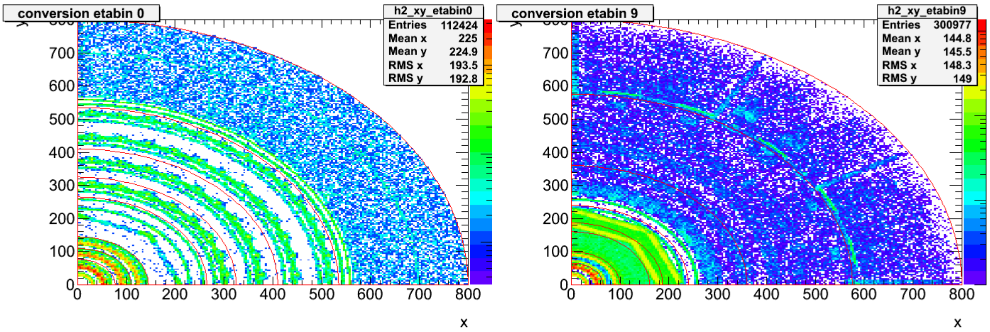

(c) x vs y for $0 < |\eta| < 0.2$ **(d)** x vs y for $2.2 < |\eta| < 2.5$

Figure 4.34: Position of the conversion point projected on $|\eta|$ vs R (a) and z vs R (b). The number in the first plots are the relative fraction of entries for every bin (delimited by the red line) normalized in such a way that the sum over an $|\eta|$ slice (horizontal row) is equal to 1. In (c) and (d) the distribution of the $x - y$ position of the conversion sliced for two different $|\eta|$ ranges. The colour scale of the plots is logarithmic.

The linearity is evaluated for every $|\eta| \otimes E_{\text{true}} \otimes R_{\text{true}}$ category using the E/E_{true} "perfect" distribution using the iterative truncated Gaussian fit previously described. The peak position usually is not at 1, meaning that a correction equal to the inverse of the linearity has to be applied. The linearity is parametrized for every $|\eta| \otimes E_{\text{true}}$ bins function of the true R_{true}, some example are in Fig. 4.35, and it is fitted with:

$$A + BR_{\text{true}} + C\sqrt{R_{\text{true}}} \tag{4.10}$$

	R [mm]								
$0 < \|\eta\| < 0.2$	0	77	110	145	265	325	410	535	800
$0.2 < \|\eta\| < 0.65$	0	77	110	145	265	325	410	535	800
$0.65 < \|\eta\| < 1.0$	0	77	110	145	265	325	410	535	800
$1.0 < \|\eta\| < 1.2$	0	77	110	145	325	410	535	595	800
$1.2 < \|\eta\| < 1.425$	0	77	110	145	325	410	478	595	800
$1.425 < \|\eta\| < 1.55$	0	92	128	236	344	420	588	636	800
$1.55 < \|\eta\| < 1.8$	0	77	110	145	265	345	498	610	800
$1.8 < \|\eta\| < 1.95$	0	77	110	187	270	400	576	610	800
$1.95 < \|\eta\| < 2.2$	0	77	110	187	270	400	576	610	800
$2.2 < \|\eta\| < 2.5$	0	65	100	160	187	240	360	576	800

Table 4.2: Definition of the $|\eta| \times R$ categories used in the correction for the converted photons. Every $|\eta|$ bin is divided in eight R bins.

As expected the correction is bigger at low R_{true} since the energy lost in front and the out-of-cluster are larger. It is interesting to notice that the linearity for high R_{true} is bigger than 1. This is because the standard calibration provide an optimization averaged over the R_{true} distribution.

The coefficients in the previous formula depend on the true energy and on the pseudorapidity direction so in order to remove the energy dependency they are fitted versus E_{true} with the following formulas:

$$\begin{aligned}
A &= A_1 + A_2/E_{\text{true}} + A_3/E^2_{\text{true}} \\
B &= B_1 + B_2/E_{\text{true}} + B_3/E^2_{\text{true}} \\
C &= C_1 + C_2/E_{\text{true}} + C_3/E^2_{\text{true}}
\end{aligned} \tag{4.11}$$

Some example are in figure 4.36. The coefficients A_i, B_i and C_i depend only on the $|\eta|$ region and they are used by the correction tool. To check the goodness of the fit chain the procedure is backpropagated: parameter A, B and C are evaluated with the previous formula (4.11) and the result is used with (4.10) to estimated the linearity. The result are the dotted curves in Fig.4.35. This curves are very close to the ones from a direct fit with (4.10) (solid curves in the figure).

An example of the effect of the correction is shown in figure 4.37. The correction is able to shift the distribution corresponding to low R in such a way that they are well centred with a linearity close to 1. Since the distribution with low R are wider when moving them to the core of the distribution they increase as a side effect the total with of the core of the inclusive distribution. This fact is important when evaluating the performance. On the other way the left tail is drastically reduced and the distribution is more symmetric. Figure 4.38 shows an example of the effect of the correction on the linearity for all the R-categories.

4.6.3 Performance of the correction

The linearity and the resolution are computed as in section 4.4 using an iterative truncated Gaussian fit of the E/E_{true} distribution and considering the mean and the width of the function. Using the correction described in this section the linearity is shown in figure 4.39, the resolution in Fig. 4.40. Since the main goal of the tool is to improve the resolution, the

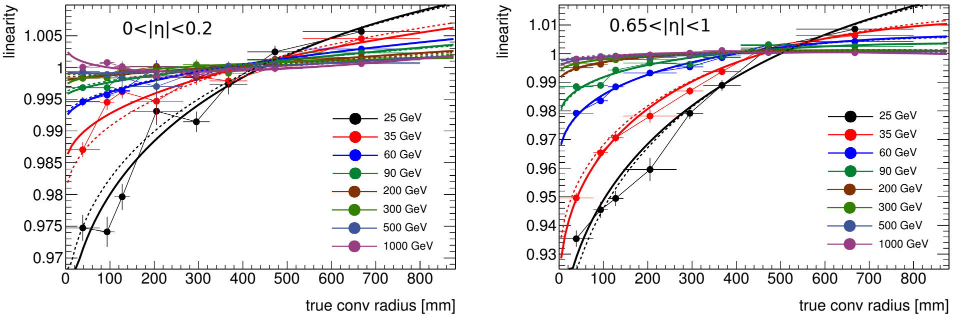

(a) $0 < |\eta| < 0.2$ **(b)** $0.65 < |\eta| < 1$

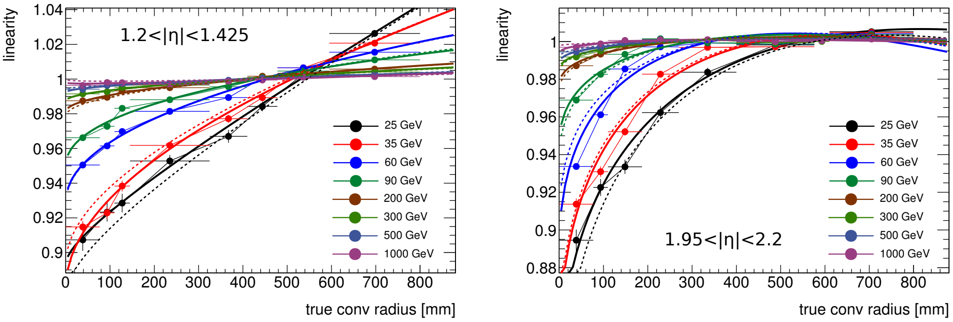

(c) $1.2 < |\eta| < 1.425$ **(d)** $1.95 < |\eta| < 2.2$

Figure 4.35: Linearity (as the mean from an iterative truncated Gaussian fit of the E/E_{true} "perfect" distribution) for converted photons for various $|\eta|$ regions (different subplot) and different true energies (different colours) versus the true R. The solid line is a fit of the points while the dotted line is the same function used in the fit but using the coefficients from figure 4.36.

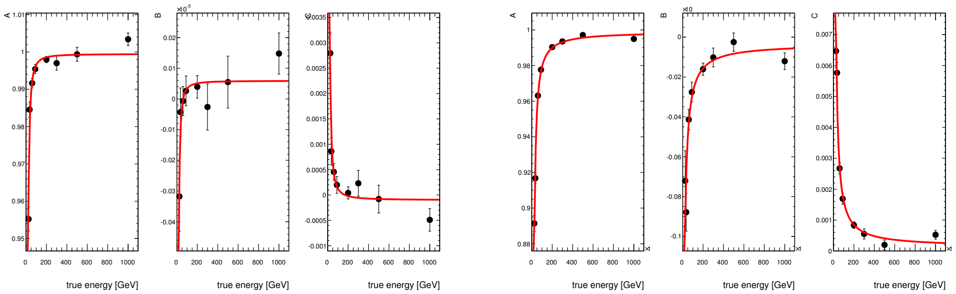

(a) $0 < |\eta| < 0.2$ **(b)** $0.65 < |\eta| < 1$

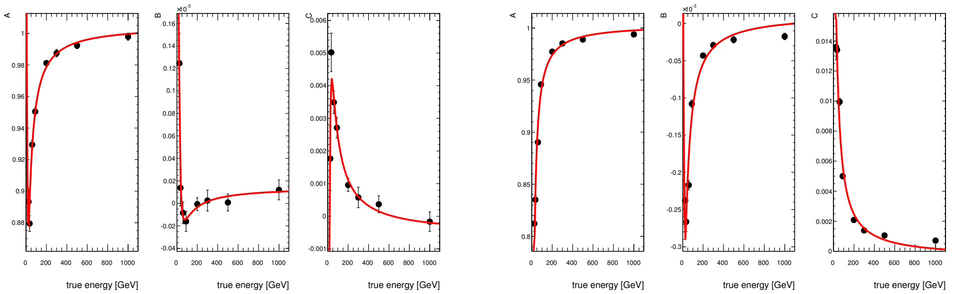

(c) $1.2 < |\eta| < 1.425$ **(d)** $1.95 < |\eta| < 2.2$

Figure 4.36: Coefficients A, B and C fitted versus the true energy for four $|\eta|$ regions.

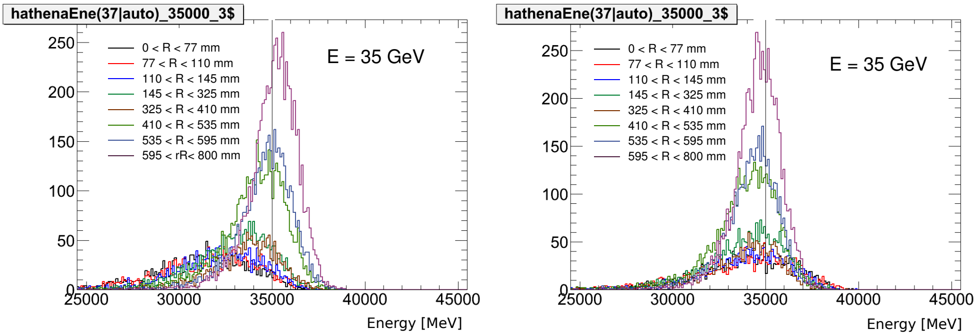

(a) before the correction **(b)** after the correction

Figure 4.37: Distribution of E/E_{true} for eight conversion radius ranges (a) before and (b) after the correction for converted photons of 35 GeV and and $1 < |\eta| < 1.2$.

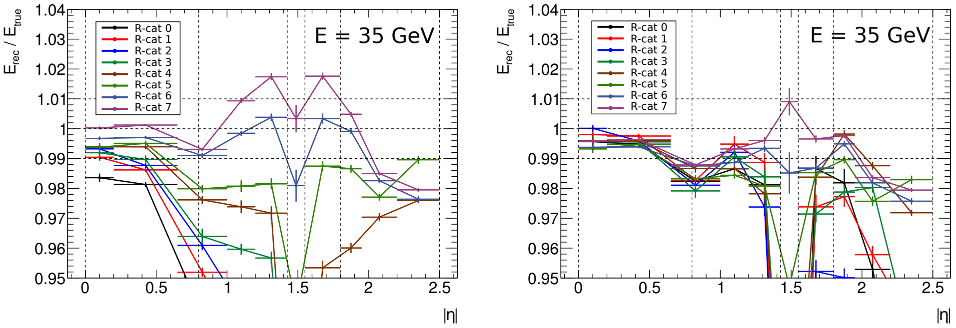

(a) before the correction **(b)** after the correction

Figure 4.38: Linearity for converted photons (a) before and (b) after the correction for the eight R-categories along $|\eta|$ for converted photons of 35 GeV.

linearity is only slightly affected and only in the endcap. Depending on the energy and on the pseudorapidity region the observed improvement on the resolution is between 1% and 5%. Larger improvement are for low energies and for the endcap.

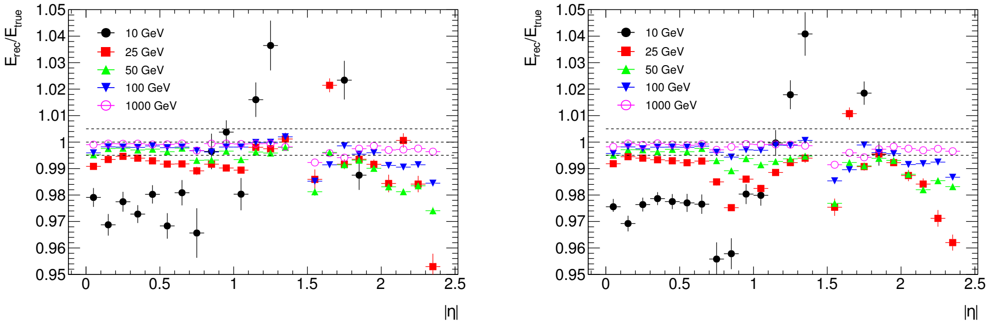

(a) mc11a **(b)** mc11b

Figure 4.39: linearity for converted photons (a) with and (b) without pileup using the correction for the radius of conversion.

As before the sampling (Fig. 4.41) and the constant (Fig. 4.42) term are computed keeping fixed the noise term to previous measurement.

The improvement on the resolution with the conversion tool seems to be quite small with respect to the effect that is visible in figure 4.37. This is because the effect of the conversion tool is to move the events with low radius of conversion from the tail of the E/E_{true} to the core of the distribution. The problem is that these distributions moved from the tail to the core are very wide and so the core distribution is not improved. For this reason the width of the Gaussian from the iterative truncated fit is not a good estimator of the resolution because it is not taking into account the tails where the effect of the correction is important. The RMS of whole distribution is shown in figure 4.43 with improvement up to 10%. The fraction of events in the low tail, defined as the region $[-\infty, 0.95]$, is shown in figure 4.44 with reduction up to 35%. More comparison with

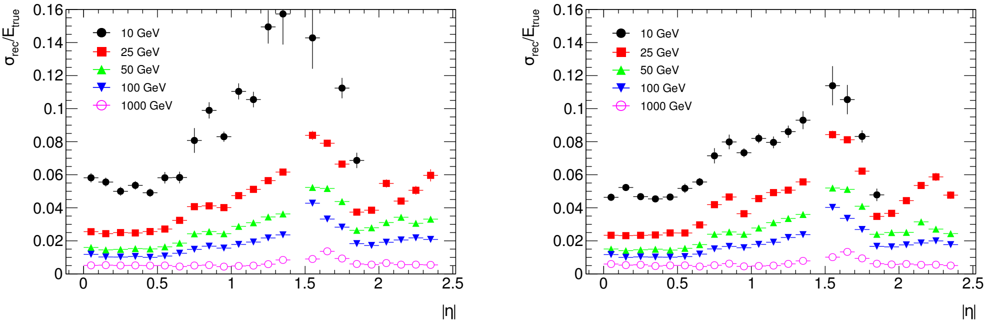

(a) mc11a

(b) mc11b

Figure 4.40: resolution for converted photons (a) with and (b) without pileup using the correction for the radius of conversion.

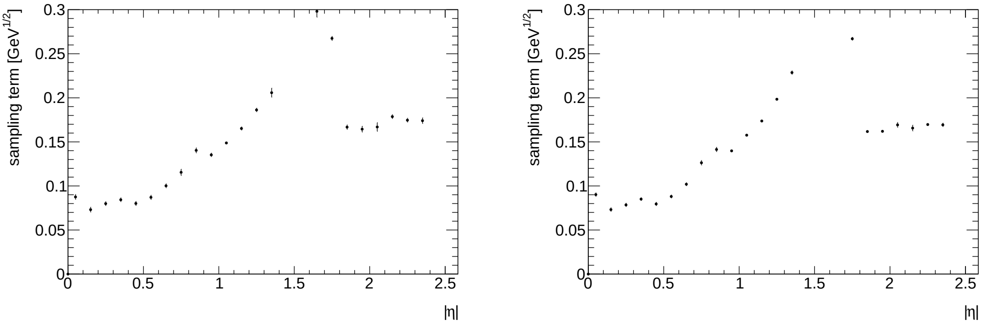

(a) mc11a

(b) mc11b

Figure 4.41: sampling term for converted photons (a) with and (b) without pileup using the correction for the radius of conversion.

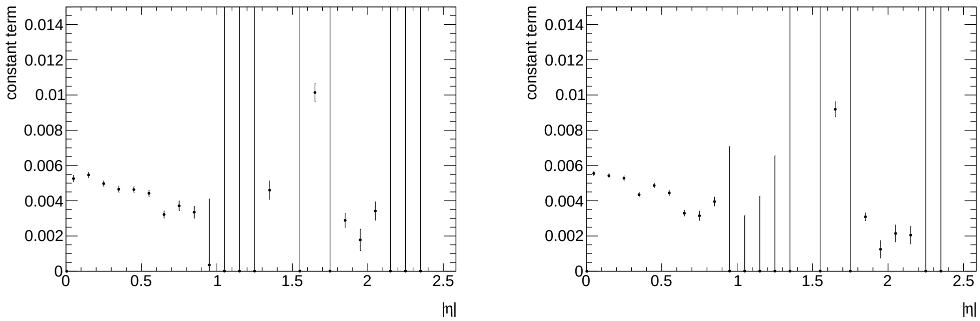

(a) mc11a

(b) mc11b

Figure 4.42: constant term for converted photons (a) with and (b) without pileup using the correction for the radius of conversion.

other estimators are presented in the next chapter when introducing the multivariate calibration.

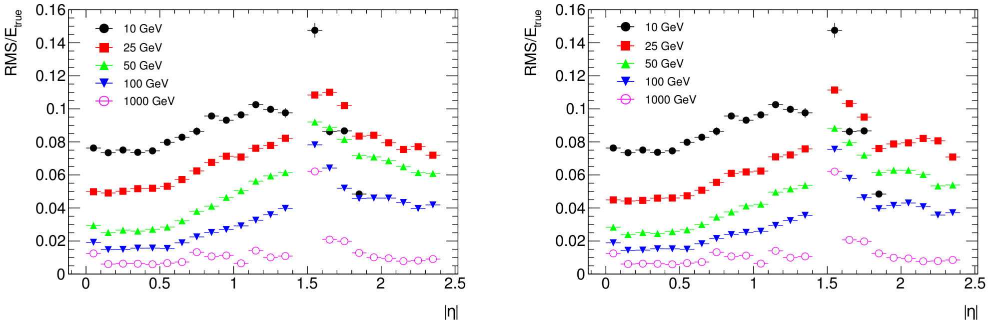

(a) without the radius correction

(b) with the radius correction

Figure 4.43: RMS for converted photons (a) without and (b) with the tool without pileup.

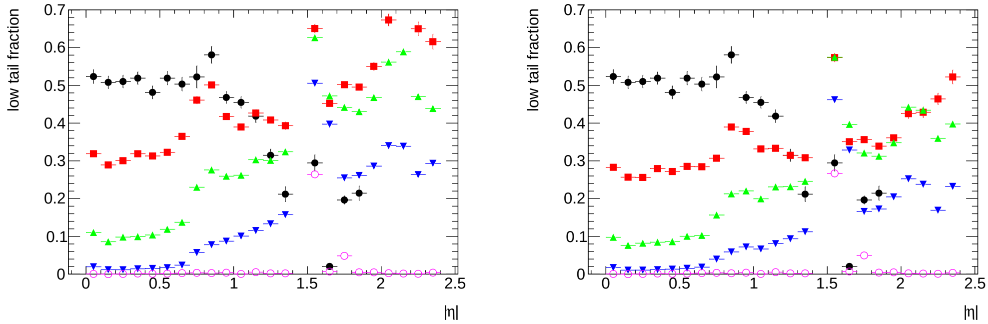

(a) without the radius correction

(b) with the radius correction

Figure 4.44: fraction of event in the low tail for converted photons (a) without and (b) with the tool without pileup.

CHAPTER 5

Multivariate calibration

5.1 Introduction

As discussed in the previous chapter the standard calibration is a powerful tool but it is difficult to exploit due to the huge number of involved parameters and in particular it is difficult to take into account additional inputs. A new approach based on multivariate analysis (MVA) methods has been developed and it is presented in this chapter. The MVA energy calibration is a completely different calibration procedure and can replace the standard calibration described in the previous chapter.

The main reason to move to a MVA calibration is that it is easy to introduce an arbitrary number of variables. It has been shown that to improve the standard calibration new variables have to be considered, for example in section 4.6 the dependence with the radius of conversion has been evaluated and a correction on the top of the standard calibration has been developed.

After an introduction of MVA methods and some technical details of the implementation the sample used for the optimization of the calibration are described in section 5.2. The output and the inputs of the calibration are described in sections 5.3 and 5.4. A final correction of the MVA calibration is in section 5.5. Detailed performance are quantified in section 5.6.

It is implemented using the Toolkit for Multivariate Analysis (TMVA) framework [93]. The tool provides a ROOT-integrated machine learning environment for the processing and parallel evaluation of multivariate classification and regression techniques. TMVA is specifically designed to the needs of high-energy physics (HEP) applications[1]. In the package several multivariate methods are available, the more suitable for the energy calibration are the artificial neural network (ANN) and the boosted decision tree (BDT). Due to the "brute force" nature of the BDT algorithm, it works "out of the box" and no special configuration are needed. It is able to take into account different input configurations without any special tuning. For this reason after some preliminary tests the BDT algorithm (with gradient boosting, BDTG) has been used for this study. The technical details of the algorithm are explain in appendix B.

The use of an MVA tool has several advantages due to the fact that a lot of steps are done automatically by the TMVA framework:

- it is easier to maintain since most of the work is done by the TMVA package and most of the user code is only a configuration of the algorithms,

---

[1] in particular it is suitable for an energy calibration, in fact the TMVA manual says:"A typical [...] problem in High-Energy Physics is for example the estimation of the energy of a (hadronic) calorimeter cluster from the cluster's electromagnetic cell energies".

- it is easier to develop new features, for example it is easy to introduce new variables as input,
- thanks to the multivariate nature of the algorithms it is possible to take into account the correlation between the input variables. For example in the standard calibration all the corrections use one variable as input (the longitudinal barycentre) except the correction for the energy lost in front of the accordion which is using two variables (for example the presampler energy fraction and the raw energy) but it treats them in a separate way, without exploiting the information inside the correlation of the variables,
- the code was developed to run on batch queues over hundreds of nodes, so even if the algorithms used are slower with respect to the fits used by the standard calibration at the end the MVA training is faster than the optimization of the standard calibration.

5.1.1 MVA regression

MVA algorithms can be used for two tasks:

categorization to classify the input in subsets, e.g. data and background,

regression is the process that estimates the parameter values of a function, which predicts the value of a response variable (or vector) in terms of the values of other variables (the input variables).

The energy calibration is a regression problem. Some algorithms are suitable only for categorization, other only for regression and some are suitable for both. An MVA algorithm can be thought as a black box (Fig.5.1) with some inputs and usually one output. The goal is to match the output with the target variables, for example in the MVA calibration the target variable could be the true energy of the particle.

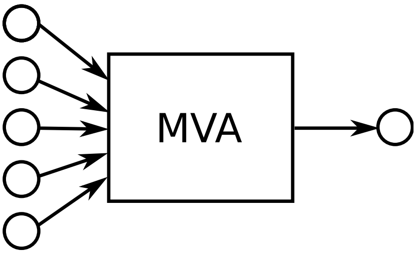

Figure 5.1: Sketch of an MVA algorithm with various input variables and one output variable.

A typical MVA classification or regression analysis consists of two independent phases: the training phase, where the multivariate methods are trained, tested and evaluated, and an application phase, where the chosen methods are applied to the concrete classification or regression problem they have been trained for. Usually the sample is divided in two subsamples of equal size, one is the training sample and consists of a set of training examples and it is used to train the algorithm, the other (the test sample) is used to test the performance. As in supervised learning, each example is a pair consisting of an input object (typically a set of variables) and a desired output value. During the training the algorithm is tuned automatically to predict the correct output value for any valid input object. This requires the learning algorithm to generalize from the training data to unseen situations. In TMVA the optimized configuration of an algorithm after the training is stored in a set of weights, saved in an xml file. During the testing phase the goodness of the optimized algorithm is evaluated using the test sample. It is important that the testing and the training sample are independent to avoid bias.

5.2 Sample and selection

Because of the method used in the training of MVA algorithm, it is not possible to use single particles at fixed energies because the training sample would not be representative of all the possible outputs. As an example, if the 16 samples with single particles at fixed energies used for the optimization of the standard calibration (see section 4.3.1) were used for the training of the MVA the output of the MVA would be one of the 16 energies, but this would be correct only on this particular kind of datasets. Such a trained algorithm would continue to return one of these 16 energies also on data. For this reason a different set of samples has been used. These new samples contain simulated single particles (electrons or photons) with true transverse momentum p_T^{true} flat distributed. The first sample contains particles at low energy with 7 GeV $< p_T^{\text{true}} <$ 80 GeV with 3.5M event, the second with 80 GeV $< p_T^{\text{true}} <$ 800 GeV and 1.5M events. Figure reffig:distMVA shows the distribution of p_T^{true} for the whole sample. For this Monte Carlo the CalibrationHit simulation is not available and so it is not possible to decompose the energy losses into the various components as in the standard calibration.

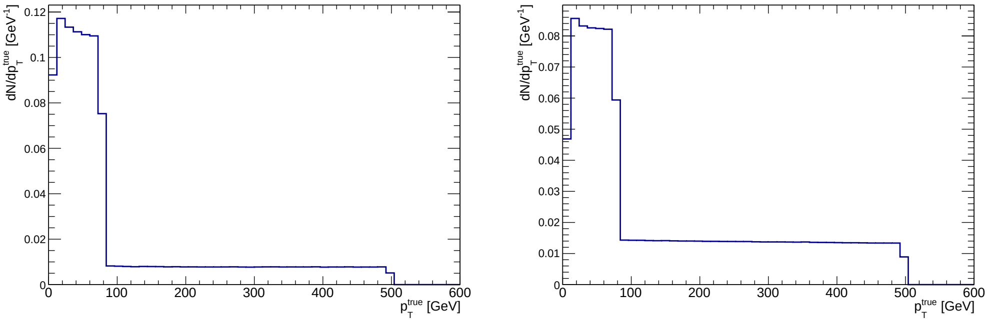

(a) electron **(b)** photon

Figure 5.2: Distribution of p_T^{true} for (a) electron and (b) photon samples used in the MVA calibration.

The following selection are applied on the training sample:

- loose identification cuts. Requiring tight identification doesn't change the results,
- matching between the generated particle and the reconstructed object (truth matching) is required. This is because it is important to avoid particles reconstructed with the wrong identification. The mismatching for electron is shown in figure 5.3 and it is very small, of the order of 5×10^{-3}.

The main difference with the standard calibration selection is that there is no requirement on the number of reconstructed clusters per event.

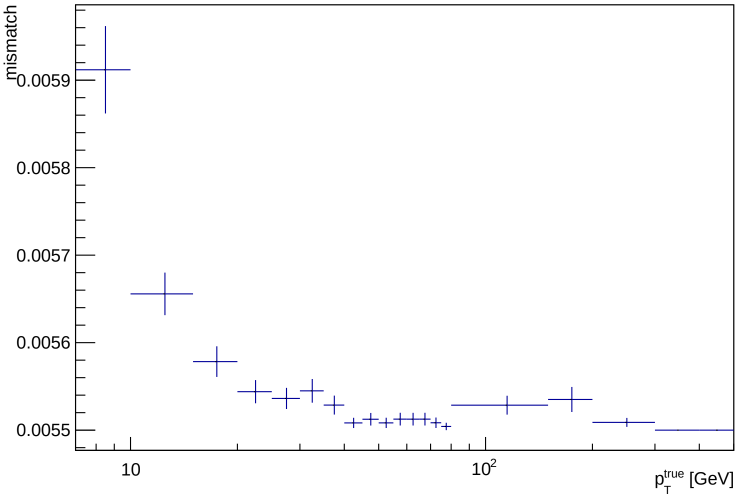

Figure 5.3: mismatch for electron versus the true p_T.

5.3 Target variable

The goal of the calibration is to estimate the true energy of the particle from the quantity measured by the detector. The MVA target must be a variable from which it is possible to compute the calibrated energy. The targets that have been considered for the training are:

true energy $E_{\mathbf{true}}$: the MVA estimates directly the energy of the particle,

correction factor to the raw energy : $E_{\text{true}}/E_{\text{raw}}$, the MVA estimates a factor close to $1 \div 1.2$ (see figure 4.3),

correction to the standard calibrated energy : $E_{\text{true}}/E_{\text{std}}$, the MVA estimates a factor very close to 1.

One feature of multivariate algorithms is that they work better if the target is uniform with respect to the input. The E_{true} target is not uniform because it spans the whole range of the energy of the electromagnetic particles reconstructed by the calorimeter, considering the training sample it is between 7 GeV and 500 GeV. On the other hand the correction to the raw energy and the correction to the energy calibrated with the standard calibration are very uniform since the target is a number close to unity. One problem with the correction of the energy calibrated with the standard calibration is that the correlations of the target with the inputs are very complex since the target is a quantity computed with very complex formulas that can smear and fold the correlation. For this reason and for the reason that the MVA calibration should be a replacement of the standard calibration, the correction factor to the raw energy is used.

5.4 Inputs and binning

Since the MVA algorithms give the possibility to use an arbitrary number of variables, many variables have been considered as input variable, in addition to those already used by the standard calibration (see section 4.2). Thanks to the flexibility to the TMVA framework it is easy to test many variables and various configurations. A list of the input variable follows, not all of them will be used for the final version. It is important to know how much these variables are correlated to the correction of the raw-energy (the target). If the dependence of $E_{\text{raw}}/E_{\text{true}}$ is not a flat function of one variable it means that variable can be used as input by the calibration to improve the resolution. It is also important to see if the calibration is able to use this correlation. For this reason, for the most important variables, the correlation with the truncated mean (defined in section 5.6.1) of the distribution $E_{\text{raw}}/E_{\text{true}}$ is shown before the calibration, after the standard calibration and after the MVA calibration as defined in section 5.6.

Variables used both for electron and photons:

total accordion energy defined as in the standard calibration as the sum of the uncalibrated energies of the accordion layers (strips, middle and back),

fraction of presampler energy as in the standard calibration, but defined with respect to the accordion total energy: $E_0/\sum_{i=1}^{3}$,

fraction of energies in the accordion layer $E_j/\sum_{i=1}^{3}$ for $j = 1, 2, 3$

pseudorapidity in the Atlas frame taking into account all the misalignment of the detector and with (0,0,0) at the center of the detector considering or not the symmetry of the detector. This variable is important because the material in front of the accordion varies with this pseudorapidity definition,

pseudorapidity in the calorimeter frame it is the pseudorapidity without any misalignment in such a way that the first cell is exactly between 0 and 0.025, the second between 0.025 and 0.050, . . . This variable is important because it is possible to distinguish every cell and correct for the modulations,

pseudorapidity sign to distinguish the two side of the calorimeter,

azimuthal directory φ

cell index an integer number between 0 an 99 defined as the integer part of the division of the pseudorapidity in the calorimeter frame with the width of one middle cell ($\Delta\eta = 0.025$),

longitudinal barycentre as in the standard calibration but defined with different X_i, see equation 4.1,

shower shapes described in section 3.4, in particular the one sensitive to the width in η and ϕ of the electromagnetic shower,

η modulation defined as the pseudorapidity modulus the width of one cell of the middle layer ($\Delta\eta = 0.025$). This variable is important to correct for modulation in the reconstructed energy due to the fact that the response of one cell vary with respect to the position where the particle hit it,

φ modulation for the cell as the η modulation defined as the azimuthal angle modulus the with of the middle layer ($\Delta\varphi = 0.025$),

φ modulation for the electrodes similar to the previous variable but using the periodicity of the electrodes. It is defined as φ (in the calorimeter frame) modulus $\pi/512$ in the barrel and $\pi/384$ in the endcap,

material before the accordion traversed by the track. This is an important variable and it has been implemented specifically for the MVA calibration. For electron it is defined as the total amount of material traversed by the track, associated to the electron, from the origin to the surface of the accordion. For converted photons the material is integrated from the conversion point using the electron from the conversion with larger transverse momentum. The amount of material is estimated summing the material of all the geometric elements traversed by the track from a simplified ATLAS geometry. Figure 5.7 shows a map of the material variable for electrons.

The following variables are defined only for electron:

z_0 defined as the z coordinate at the beginning of the electron track multiplied by the sign of η,

track pseudorapidity is the pseudorapidity measured only with the inner detector for electrons,

q/p defined as the ratio of the momentum measured at the beginning and at the end of the electron track.

These variables are defined only for converted photons:

radius of the conversion R as for the correction described in section 4.5,

z **position of the conversion** , since the endcap is a rotated version of the barrel, the coordinate corresponding to R in the barrel is z in the endcap,

p_T **of the electrons from the conversion** p_{T1} and p_{T2},

p_T **of the conversion** is the vectorial sum of the transverse momenta of the two electrons from the conversion: $|\vec{p}_{T1} + \vec{p}_{T2}|$,

conversion E_T/p_T defined as the raw accordion transverse momentum divided by the sum of the momentum of the two electrons,

conversion p_T **ratio** defined as the ratio between the most energetic electron from the conversion and the p_T of the conversion transverse momentum,

SiSi tracks is a boolean variable defining the quality of the electron tracks from the photon conversion. It is true if both tracks have at least two hits in the silicon (pixel or SCT detectors).

The behaviour of electrons and photons is different depending on the interested part of the detector and the energy range. In fact these variables are used as input, but to help the training algorithm several categories are defined and they are trained separately. The raw-p_T and the $|\eta|$ of the cluster are used to divide the sample in categories. The subdivision in $|\eta|$ is driven by the distribution of the material and by the geometry of the calorimeter, in particular special $|\eta|$ bins are introduced around the transition region at $|\eta| = 0$ and just after the crack. The boundaries of all the categories are listed in table 5.1. The subdivision in raw-p_T is driven by the statistics of the training sample (see figure 5.2), the values are listed in table 5.2.

Considering the categories one by one the p_T-true spectrum is distorted at the edges by migration between the categories (see Fig. 5.10). This can create some undesirable

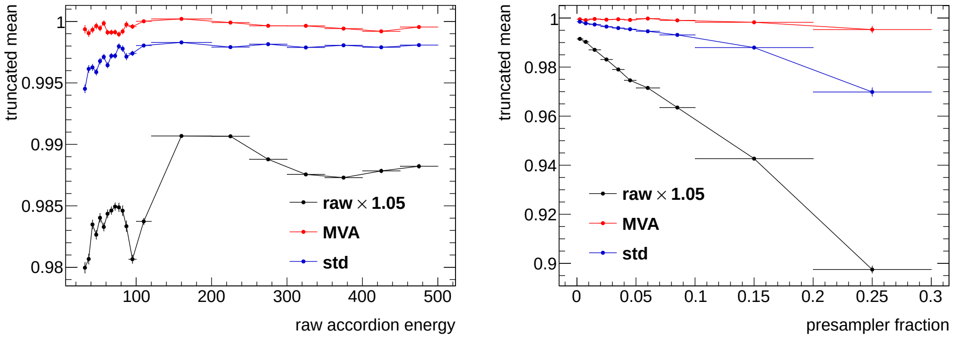

(a) raw accordion energy **(b)** fraction of energy in the presampler

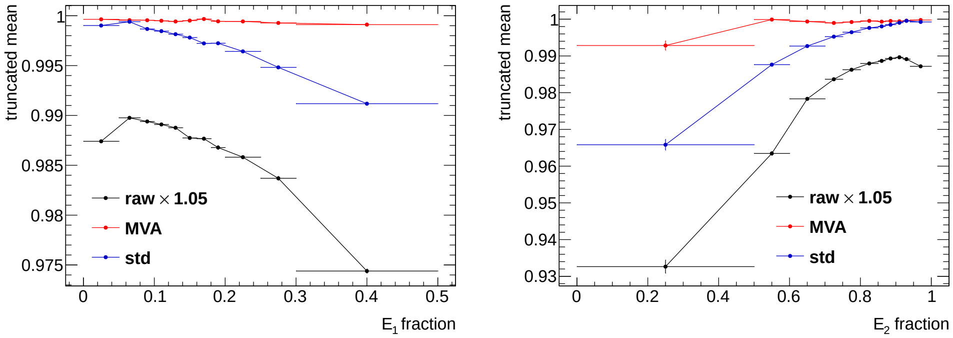

(c) fraction of energy in the strips **(d)** fraction of energy in the middle

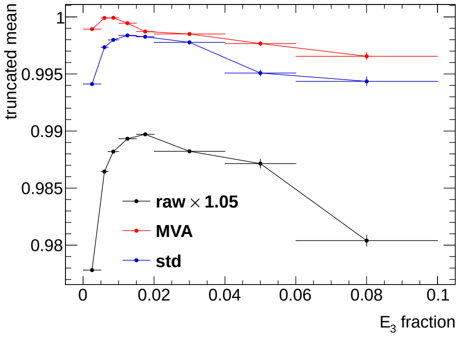

(e) fraction of energy in the back

Figure 5.4: The correlation between several variables and the truncated mean of the E/E_{true} before the calibration (black), after the standard calibration (blue) and after the MVA calibration described in section 5.6 (red) for unconverted photons. The point for the raw-energy are scaled by a factor 1.05. If not specified the whole test sample is used $7\,\mathrm{GeV} < E_{T,\mathrm{true}} < 500\,\mathrm{GeV}$ and $0 < |\eta| < 2.5$.

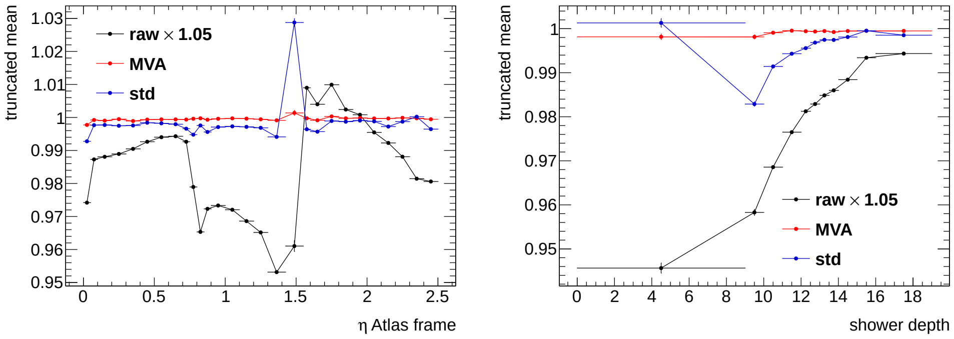

(f) pseudorapidity in the Atlas frame

(g) shower depth

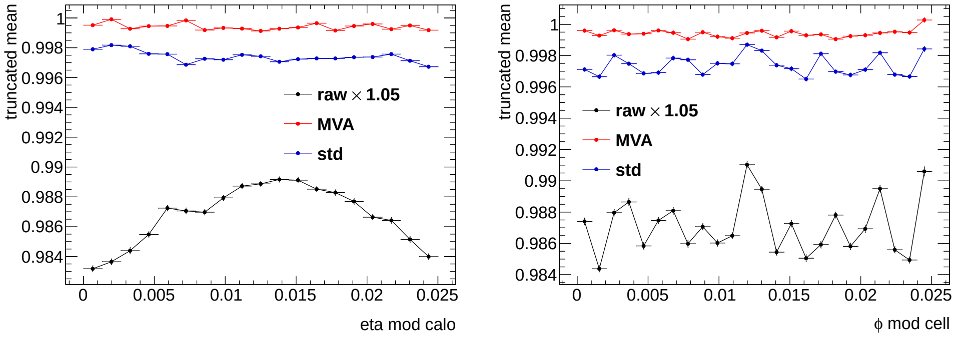

(h) η modulation

(i) ϕ cell modulation

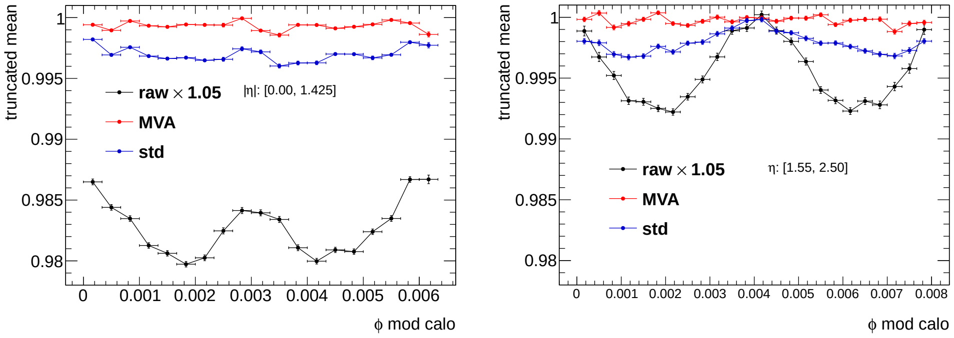

(j) ϕ electrode modulation (barrel)

(k) ϕ electrode modulation (endcap)

Continued Figure 5.4: The correlation between several variables and the truncated mean of the E/E_{true} before the calibration (black), after the standard calibration (blue) and after the MVA calibration described in section 5.6 (red) for unconverted photons. The point for the raw-energy are scaled by a factor 1.05. If not specified the whole test sample is used $7\,\text{GeV} < E_{T,\text{true}} < 500\,\text{GeV}$ and $0 < |\eta| < 2.5$.

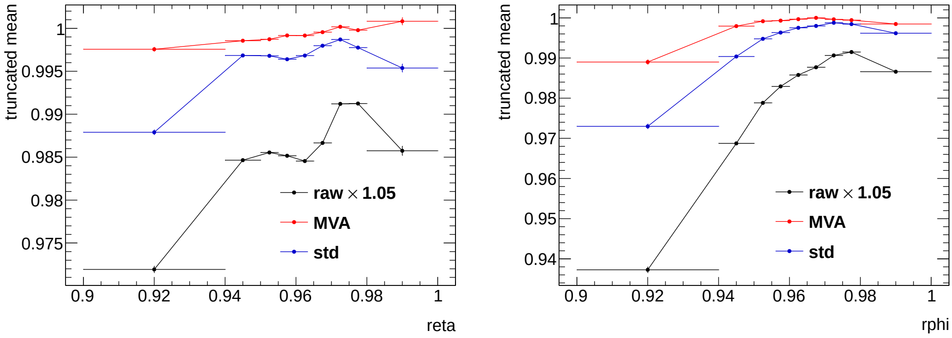

(l) R_η **(m)** R_ϕ

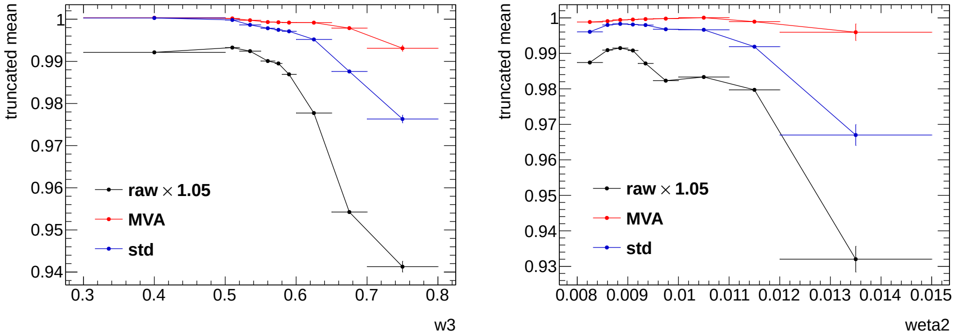

(n) w_3 **(o)** $w_{\eta 2}$

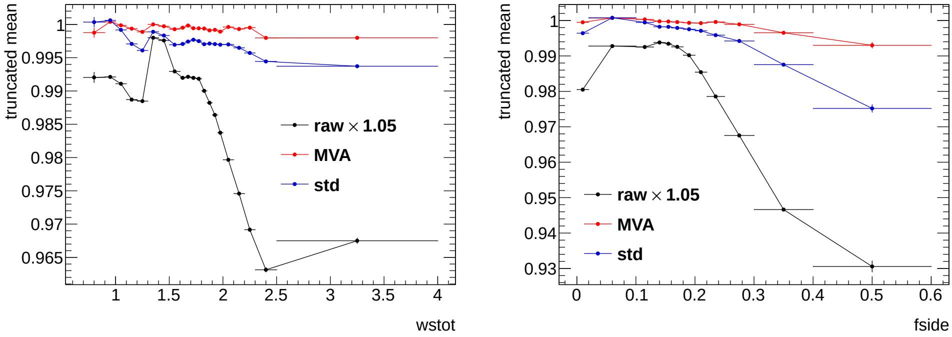

(p) w_{stot} **(q)** f_{side}

Continued Figure 5.4: The correlation between several variables and the truncated mean of the E/E_{true} before the calibration (black), after the standard calibration (blue) and after the MVA calibration described in section 5.6 (red) for unconverted photons. The point for the raw-energy are scaled by a factor 1.05. If not specified the whole test sample is used $7\,\text{GeV} < E_{T,\text{true}} < 500\,\text{GeV}$ and $0 < |\eta| < 2.5$.

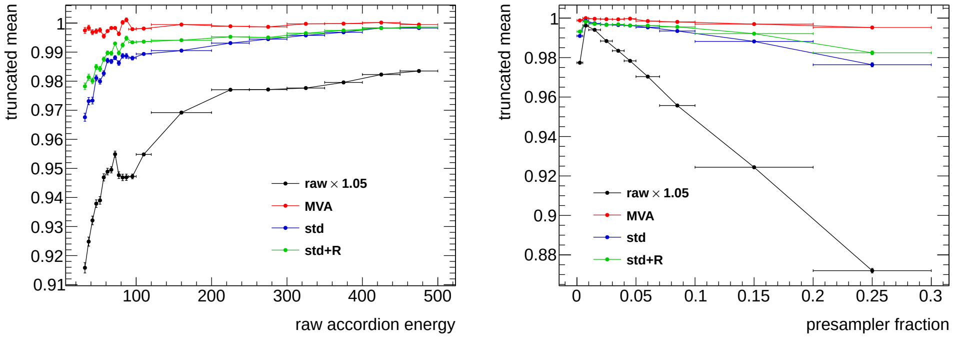

(a) raw accordion energy **(b)** fraction of energy in the presampler

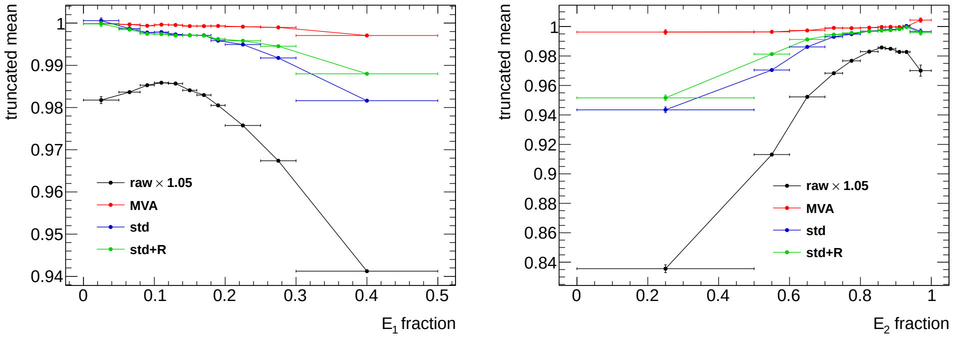

(c) fraction of energy in the strips **(d)** fraction of energy in the middle

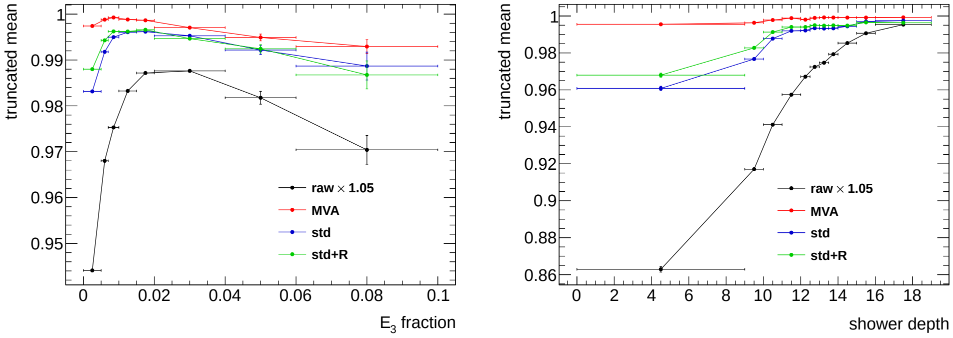

(e) fraction of energy in the back **(f)** shower depth

Figure 5.5: The correlation between several variables and the truncated mean of the E/E_{true} before the calibration (black), after the standard calibration (blue), after the standard calibration corrected using the radius of conversion (green) and after the MVA calibration described in section 5.6 (red) for converted photons. The point for the raw-energy are scaled by a factor 1.05. If not specified the whole test sample is used $7\,\text{GeV} < E_{T,\text{true}} < 500\,\text{GeV}$ and $0 < |\eta| < 2.5$.

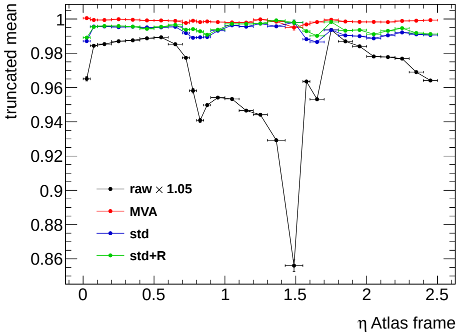

(g) pseudorapidity in the Atlas frame

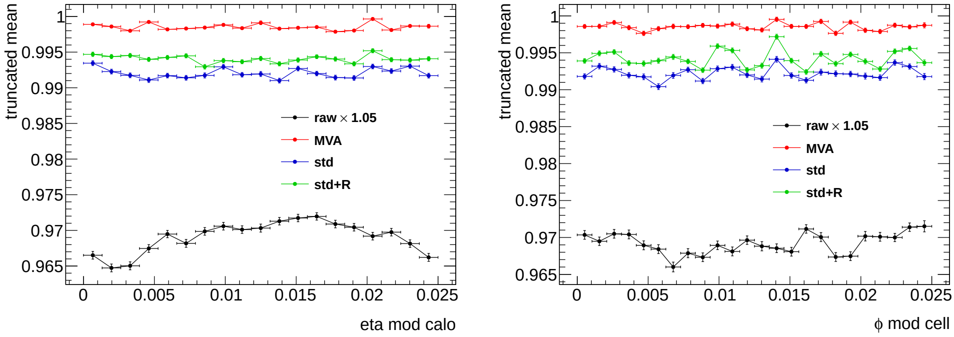

(h) η modulation **(i)** ϕ cell modulation

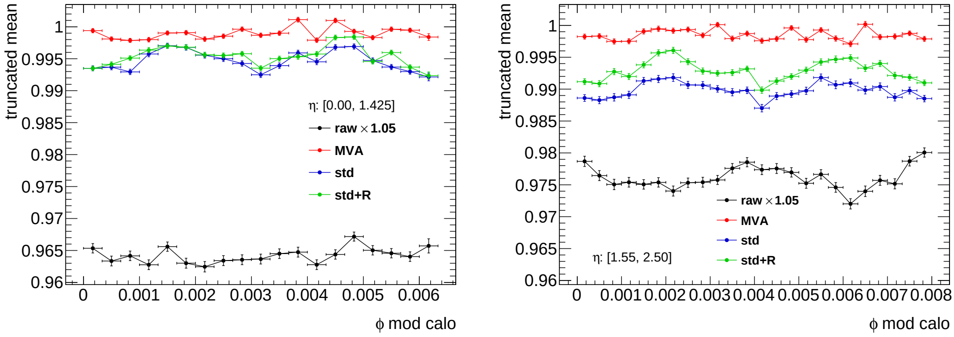

(j) ϕ electrode modulation (barrel) **(k)** ϕ electrode modulation (endcap)

Continued Figure 5.5: The correlation between several variables and the truncated mean of the E/E_{true} before the calibration (black), after the standard calibration (blue), after the standard calibration corrected using the radius of conversion (green) and after the MVA calibration described in section 5.6 (red) for converted photons. The point for the raw-energy are scaled by a factor 1.05. If not specified the whole test sample is used $7\,\text{GeV} < E_{T,\text{true}} < 500\,\text{GeV}$ and $0 < |\eta| < 2.5$.

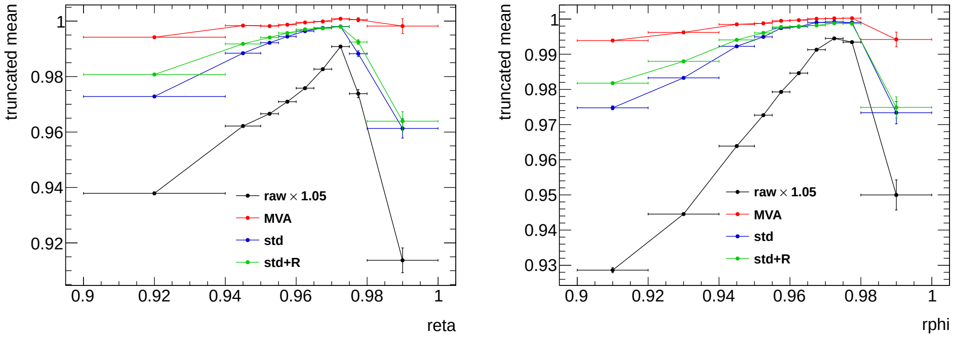

(l) R_η **(m)** R_ϕ

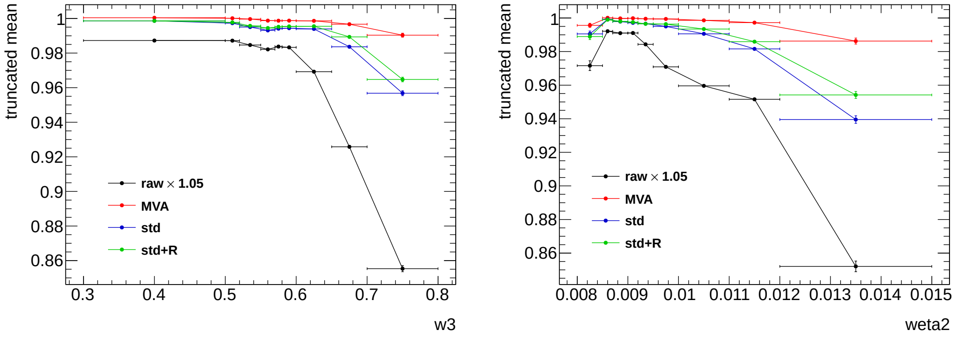

(n) w_3 **(o)** w_{η_2}

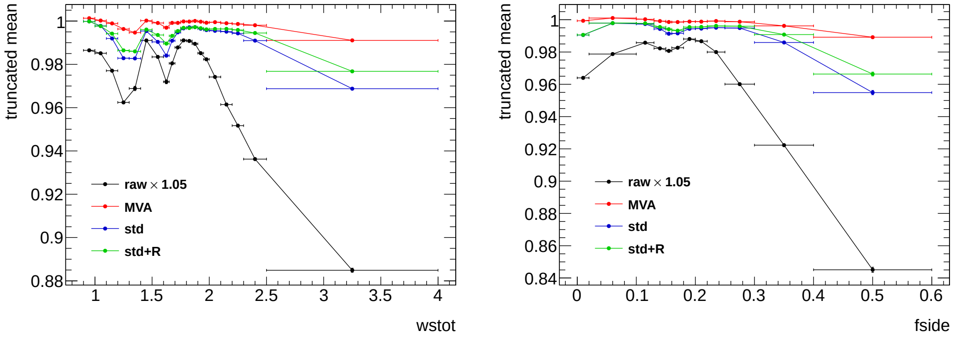

(p) w_{stot} **(q)** f_{side}

Continued Figure 5.5: The correlation between several variables and the truncated mean of the E/E_{true} before the calibration (black), after the standard calibration (blue), after the standard calibration corrected using the radius of conversion (green) and after the MVA calibration described in section 5.6 (red) for converted photons. The point for the raw-energy are scaled by a factor 1.05. If not specified the whole test sample is used $7\,\text{GeV} < E_{T,\text{true}} < 500\,\text{GeV}$ and $0 < |\eta| < 2.5$.

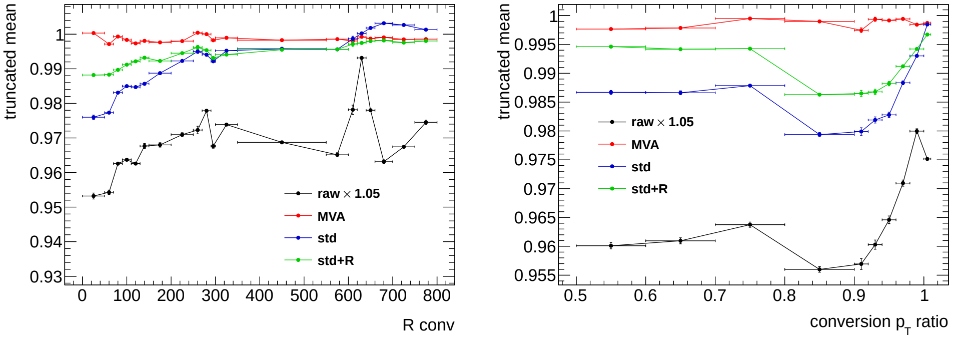

(r) radius of conversion

(s) conversion p_T ratio

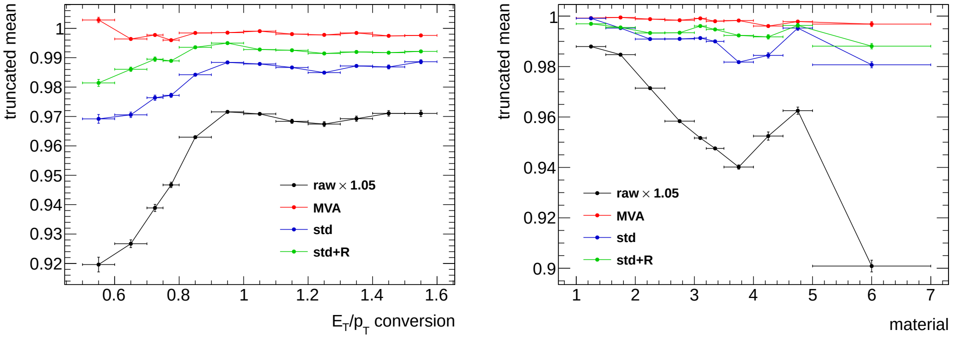

(t) E_T/p_T conversion

(u) material

Continued Figure 5.5: The correlation between several variables and the truncated mean of the E/E_{true} before the calibration (black), after the standard calibration (blue), after the standard calibration corrected using the radius of conversion (green) and after the MVA calibration described in section 5.6 (red) for converted photons. The point for the raw-energy are scaled by a factor 1.05. If not specified the whole test sample is used $7\,\text{GeV} < E_{T,\text{true}} < 500\,\text{GeV}$ and $0 < |\eta| < 2.5$.

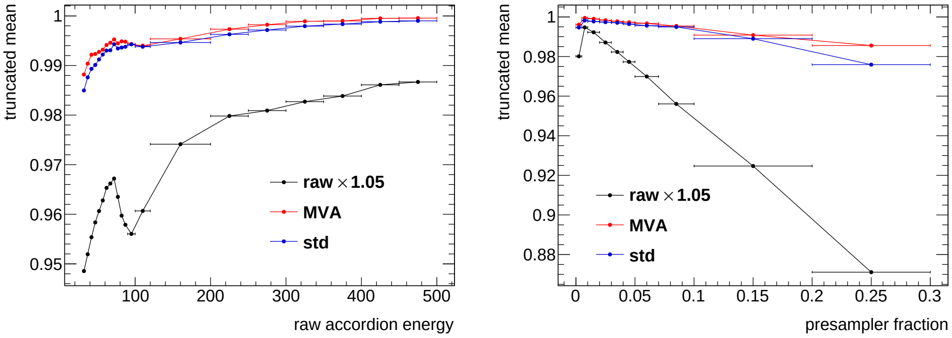

(a) raw accordion energy **(b)** fraction of energy in the presampler

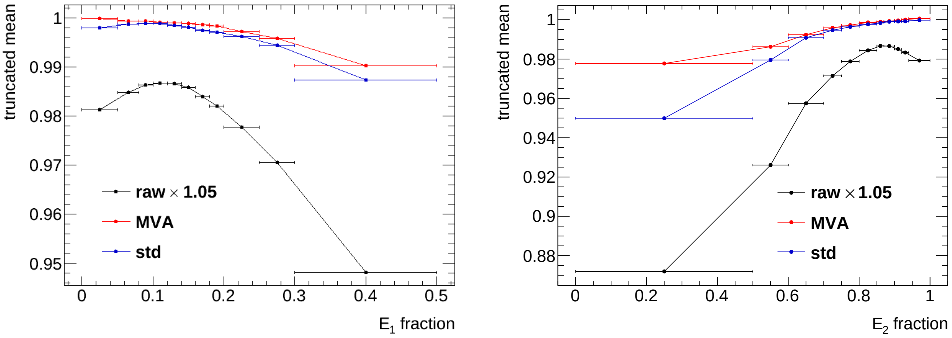

(c) fraction of energy in the strips **(d)** fraction of energy in the middle

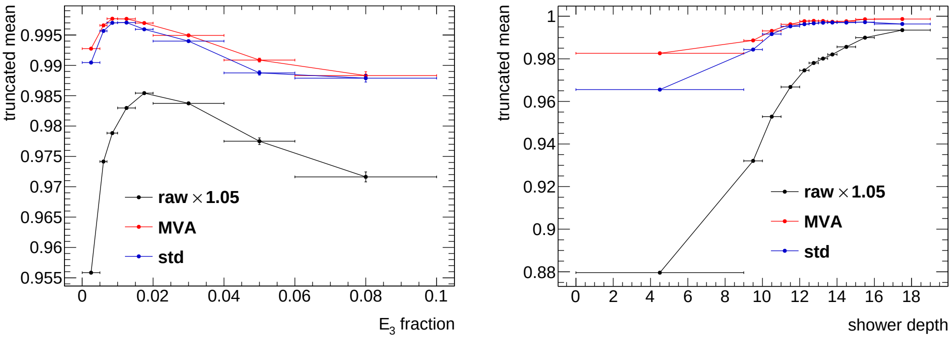

(e) fraction of energy in the back **(f)** shower depth

Figure 5.6: The correlation between several variables and the truncated mean of the E/E_{true} before the calibration (black), after the standard calibration (blue) and after the MVA calibration described in section 5.6 (red) for electrons. The point for the raw-energy are scaled by a factor 1.05. If not specified the whole test sample is used $7\,\text{GeV} < E_{T,\text{true}} < 500\,\text{GeV}$ and $0 < |\eta| < 2.5$.

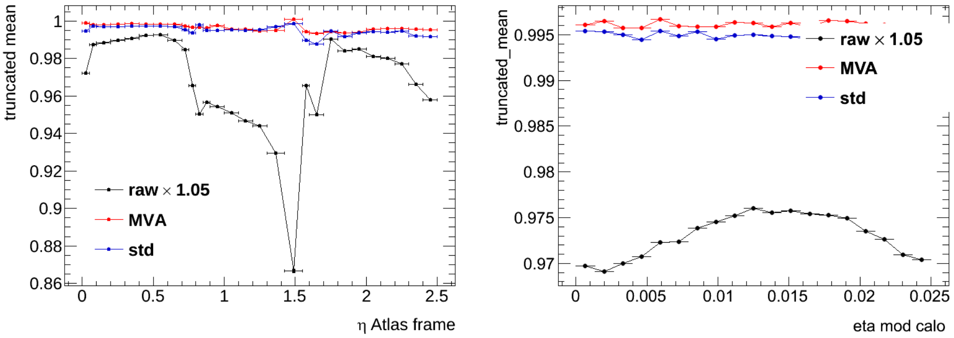

(g) pseudorapidity in the Atlas frame

(h) η modulation

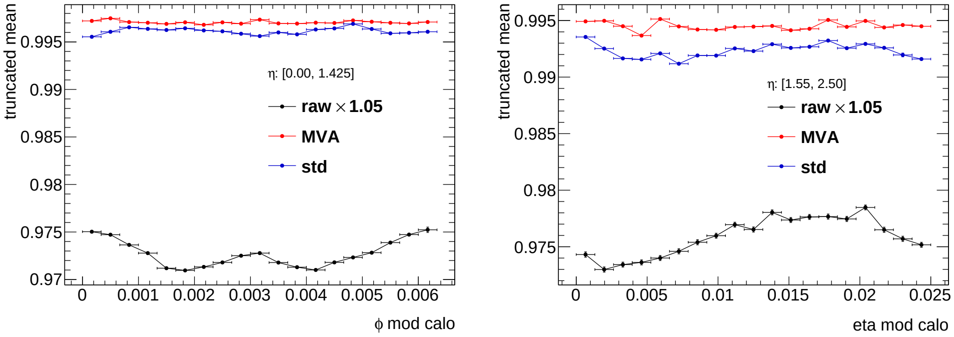

(i) ϕ electrode modulation (barrel)

(j) ϕ electrode modulation (endcap)

Continued Figure 5.6: The correlation between several variables and the truncated mean of the E/E_{true} before the calibration (black), after the standard calibration (blue) and after the MVA calibration described in section 5.6 (red) for electrons. The point for the raw-energy are scaled by a factor 1.05. If not specified the whole test sample is used $7\,\text{GeV} < E_{T,\text{true}} < 500\,\text{GeV}$ and $0 < |\eta| < 2.5$.

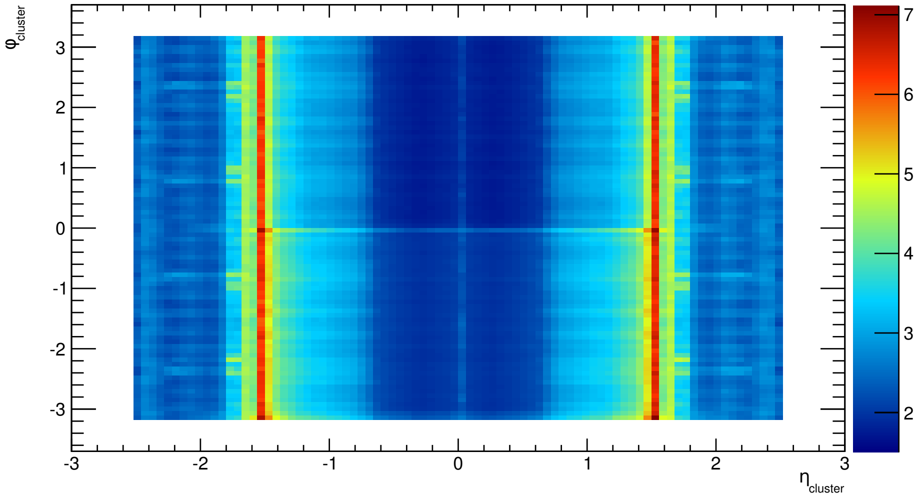

Figure 5.7: Profile of the energy distribution as function of η and ϕ of the cluster for electron with $7 < p_T^{\mathrm{true}} < 500\,\mathrm{GeV}$. The unit on the colour scale is the number of radiation length X_0.

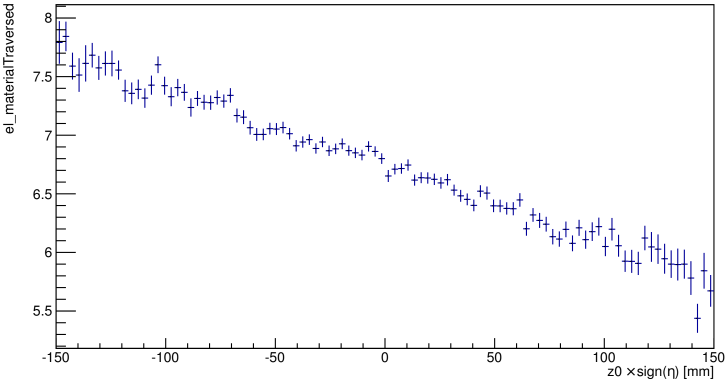

Figure 5.8: Correlation with the $z_0 \times \operatorname{sgn} \eta$ and the material for a slice in pseudorapidity $1.52 < |\eta| < 1.55$

barrel	0	0.05	0.65	0.8	1.0	1.2	1.37
endcap	1.52	1.55	1.74	1.82	2.0	2.2	2.47

Table 5.1: $|\eta|$ subdivision used by the MVA calibration

0	20	40	60	80	140	200	∞

Table 5.2: raw-p_T in GeV subdivision used by the MVA calibration

effect around the discontinuity regions, in particular near the largest one at 80 GeV of p_T^{true} where the population density of the training sample changes. This effect is visible when plotting the linearity function of p_T^{true} as in figure 5.16 (electron), 5.24 (converted photons) or 5.20 (unconverted photons), but it is not present when considering the raw-p_T as in figure 5.6a (electrons), 5.5a (converted photons) or 5.4a (unconverted photons).

As in the standard calibration photons are divided in converted and unconverted with the usual convention that if a conversion is reconstructed with $R > 800$ mm the photon is considered as unconverted. In some optimizations converted photons are divided in two categories: SiSi converted photons are converted photons when the tracks associated with the electrons from the conversion have at least one hit in the silicon detector (pixel or SCT) and non-SiSi converted photon for the opposite case. SiSi converted photons have smaller radius of conversion (see Fig. 5.9) and thanks to the silicon detector some input variables related to the conversion are more reliable and can be used as inputs.

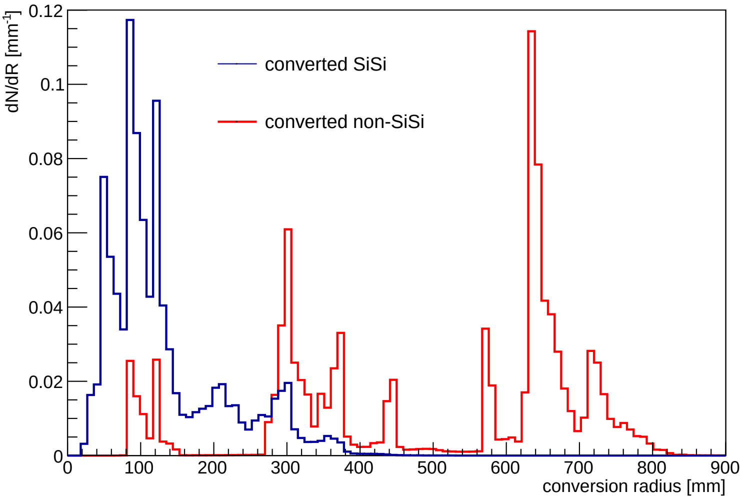

Figure 5.9: Distribution of the radius of conversion for converted SiSi photon and converted non-SiSi photon without the requirement $R < 800$ mm.

5.5 Shifting

It has been observed that the BDT tends to optimize a quantity close to the mean of the distribution. The reason is that for every step of the training the minimized quantity is

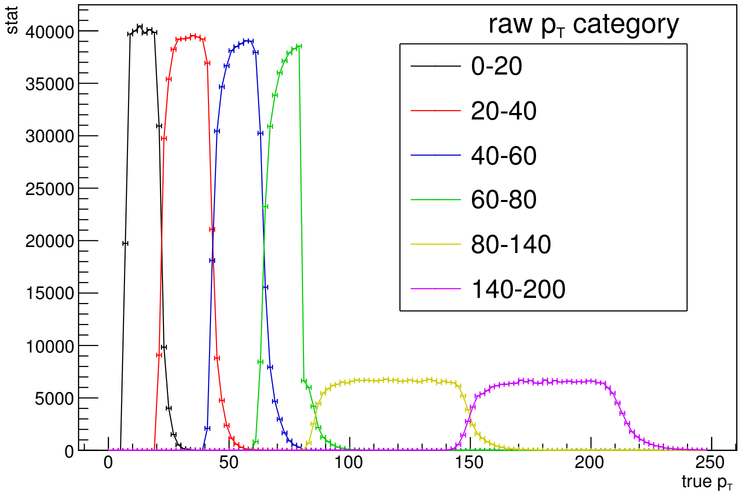

Figure 5.10: Distribution of the true-p_T for different raw-p_T categories.

the mean quadratic error computed with respect to the mean:

$$\frac{1}{N}\sum(y-\hat{y})^2 \tag{5.1}$$

where y is the regression target of each event in the node and $\hat{y}$ is its mean value over all events in the node (see appendix B). This feature is in contrast with the standard calibration where the peak of the distribution E/E_{true} is centred at 1. Even if usually the output distributions from the MVA is more symmetric than the one from the standard calibration, the mean is significantly distant from the peak in particular at low energy. In this case the usage of an external package as TMVA is a limitation because the mean quadratic error is the only available estimator for regression problems.

To overcome this difficulties some methods have been tried:

- remove from the training sample the events in the left tail with $E_{\text{raw}}/E_{\text{true}} \ll 1$. This solves almost completely the problem but when evaluating the performance of such an optimization without this cut the events in the left tail are not well calibrated,
- weight the events in a different way using the ratio $E_{\text{raw}}/E_{\text{true}}$ in such a way that event in the left tail are less important during the training. Various weighting function have been tried (linear cost, exponential cost) but the difference between the mean and the peak of the final distribution is not completely fixed. The weighting function should not decrease too much the weight of the tails to avoid the problem of the previous method,
- shift the final distribution in such a way to have the peak centred at one. This is the simplest approach, but it is also an ad-hoc approach and it needs a manual implementation. Since one problem of the standard calibration is the robustness of the fitting procedure in this case the peak position is defined without the truncated iterative gaussian fit used for the standard calibration. The quantity used to define

the peak position is the mean of the events inside the smallest interval containing 10% of the statistics. Also other estimators have been tried, for example changing the mean to the median, or moving the window from 10% to 20% but the result is very stable at the level of 0.1%, much smaller than the usual error with a gaussian fit.

Two examples are in figure 5.11, showing the distribution of $E_{\mathrm{MVA}}/E_{\mathrm{true}}$ for electrons before the shifting procedure for one very asymmetric distribution (low energy) and one very symmetric (high energy). In this figure various estimators are shown. In particular the mean and the median are well centred at 1 and the same quantities computed using the events in the smallest window containing 10% of the events are well centred at the peak position.

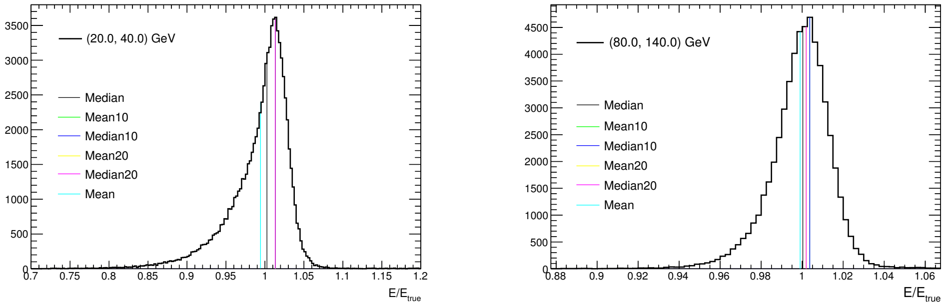

(a) 20 GeV $<$ raw-E_T $<$ 40 GeV and $1.82 < |\eta| < 2.00$ **(b)** 80 GeV $<$ raw-E_T $<$ 140 GeV and $0.80 < |\eta| < 1.00$

Figure 5.11: Distribution of $E_{\mathrm{MVA}}/E_{\mathrm{true}}$ for electrons before the application of the shifting procedure: (a) low energy, (b) high energy. The mean and the median estimators are superimposed. The ranges on the x-axes are different.

The peak position for electron using the mean of the event inside the smallest range containing 10% of the statistics is shown in figure 5.12, for converted photons in figure 5.13 and for unconverted photons in figure 5.14. As expected bigger shifts are needed for electrons and converted photons at low energy and in pseudorapidity regions with more material.

5.6 Performance

The performance is evaluated comparing the standard calibration, the standard calibration corrected for the radius of conversion (for converted photons) and the MVA calibration.

The performance is quoted in terms of linearity and resolution. In the standard calibration section (4.4) they were estimated from an iterative gaussian fit of the core of the distribution, but in the section about the correction with the radius of conversion (4.6.3) it has been shown that neglecting the tails is not the optimal way to quote the performance. For the MVA calibration new performance estimators have been introduced.

Several factors in addition to the performance have driven the final selection of the best MVA calibration:

- the robustness, for example against different samples,

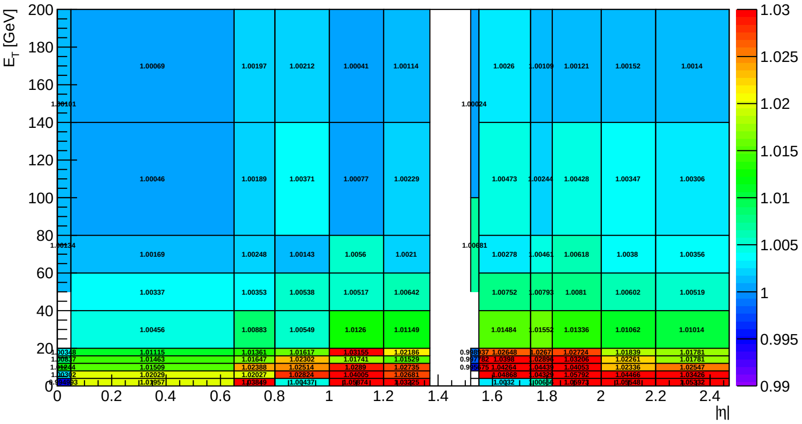

Figure 5.12: Peak position of the $E_{\mathrm{MVA}}\,/\,E_{\mathrm{true}}$ distribution for electrons using the mean of the event inside the smallest range containing 10% of the statistics.

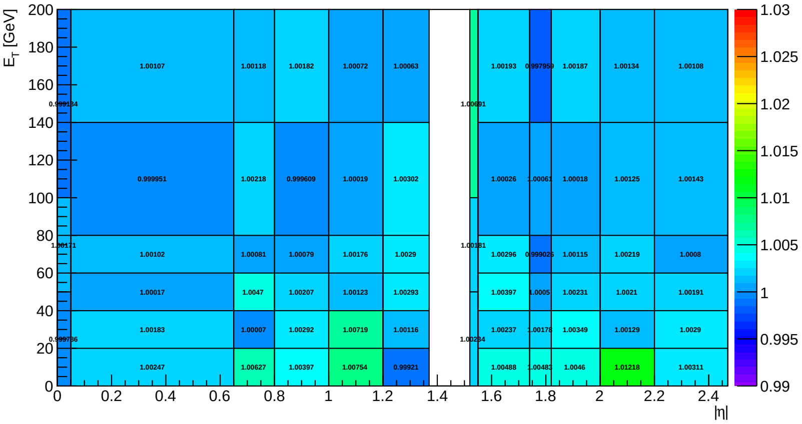

Figure 5.13: Peak position of the $E_{\mathrm{MVA}}\,/\,E_{\mathrm{true}}$ distribution for converted photons using the mean of the event inside the smallest range containing 10% of the statistics.

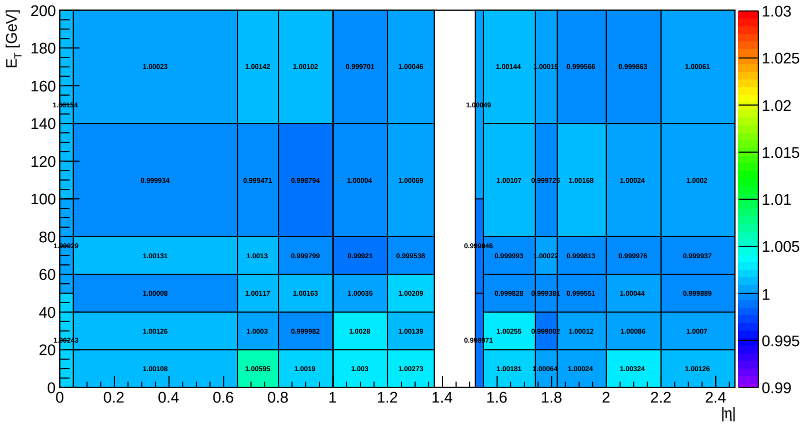

Figure 5.14: Peak position of the $E_{\mathrm{MVA}}/E_{\mathrm{true}}$ distribution for unconverted photons using the mean of the event inside the smallest range containing 10% of the statistics.

- the degree of understanding of the input variables on data. For example the shower shape variables are not completely understood on data, in particular for photons, so it can be dangerous to use an optimization trained using these variables,
- since the scale factors applied to match the energy between data and MC for photons are the same ones as from electron it is good to have a similar optimization for electrons and photons.

These criteria tend to choose a calibration using few input variables, while the improvement of the performance are driven by the usage of many variables. Since this is the first time such a calibration is developed the used variables have been limited to (see section 5.4 for the descriptions):

- fraction of presampler energy,
- cell index,
- total accordion energy,
- pseudorapidity in the Atlas frame,
- longitudinal barycentre,
- η cell modulation,
- φ electrodes modulation,
- conversion E_T/p_T (only for converted photons with two reconstructed in the silicon detectors),
- conversion p_T ratio (only for converted photons),
- radius of conversion (only for converted photons with conversion $p_T > 3\,\mathrm{GeV}$.

The final version is trained with 95% of the events in the sample and the output is shifted with the procedure described in 5.5. In the following this final version is labelled as “MVA”.

5.6.1 Estimators

The new estimators are chosen in order to not neglect the contribution of the tails of the E/E_{true} distribution and at the same time they are not biased by the presence of outliers. The estimator are called "truncated" estimator in the sense that they use only a fraction of the distribution truncating the event very far away from the core. In particular only events inside the smallest window containing 90 % of the total population are used. The width of this window could be an estimator of the width of the distribution. Two estimators are defined and used in the following:

truncated mean : the mean computed using the events in the smallest window containing 90 % of the events,

truncated RMS : the root mean square computed using the events in the smallest window containing 90 % of the events.

In addition these estimators do not need any fit, but only algebraic computation.

5.6.2 Linearity and resolution

Electron

Three optimizations are compared with the standard calibration: the MVA described in the previous section, a similar one but using 50% of the sample to training and one MVA using the material crossed by every particle as additional input. The distribution of E/E_{true} integrated over the p_T^{true} spectrum of the single particle sample is shown in figure 5.15. The linearity of this distribution, defined using the truncated mean, is shown in Fig. 5.16, the resolution as truncated RMS function of p_T^{true} in Fig. 5.17 and in Fig. 5.18 function of $|\eta|$. Looking at the performance function of η and p_T the major improvement are at high energy and around $|\eta| = 1.6$. The resolution is improved up to a factor 15% at high energy in the endcap, and up to a factor 30% in the region around $|\eta| = 1.6$ at high energy. The MVA calibration has a decrease in performance around $p_T \sim 80\,\text{GeV}$, this is due to the discontinuity in the p_T distribution of the training sample (see Fig. 5.2). The improvement using the material as additional input variable is small and visible only in some regions.

Unconverted photons

For unconverted photon, defined with the usual convention that photon with $R > 800\,\text{mm}$ are considered as unconverted, only the MVA and the standard calibration are compared. The distribution of E/E_{true} integrated over the p_T^{true} spectrum of the single particle sample is shown in figure 5.19. The linearity as truncated mean is shown in Fig. 5.20. In figure 5.20a the little effect of the sample transition at 80 GeV is visible. The resolution defined as truncated RMS is shown in Fig. 5.21 function of p_T^{true} and in fig 5.22 function of $|\eta|$. Improvement are concentrated at high energy and high pseudorapidity up to 30%.

Converted photons

For converted photons the MVA is compared with the standard calibration and the standard calibration corrected for the residual dependence with the radius of conversion. Figure 5.23 shows the E/E_{true} distribution integrated over the p_T^{true} spectrum of the single particle sample. The linearity as truncated mean is shown in Fig. 5.24. As for unconverted photons figure 5.24a shows the little effect of the sample transition at 80 GeV.

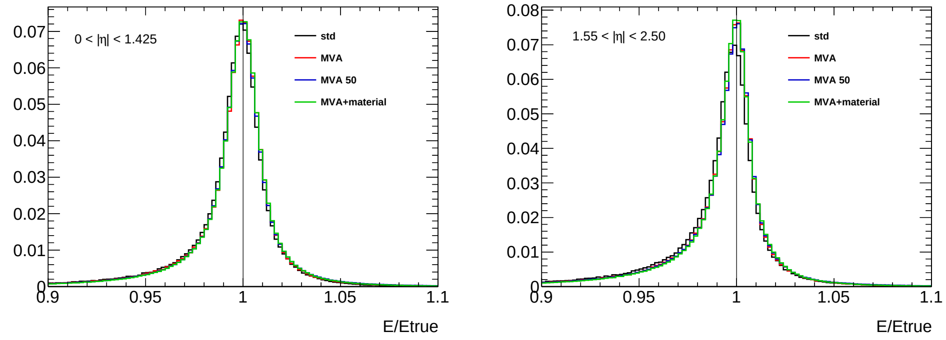

(a) barrel **(b)** endcap

Figure 5.15: E/E_{true} integrated over the p_T^{true} spectrum of the single particle sample for (a) barrel and (b) endcap for electron.

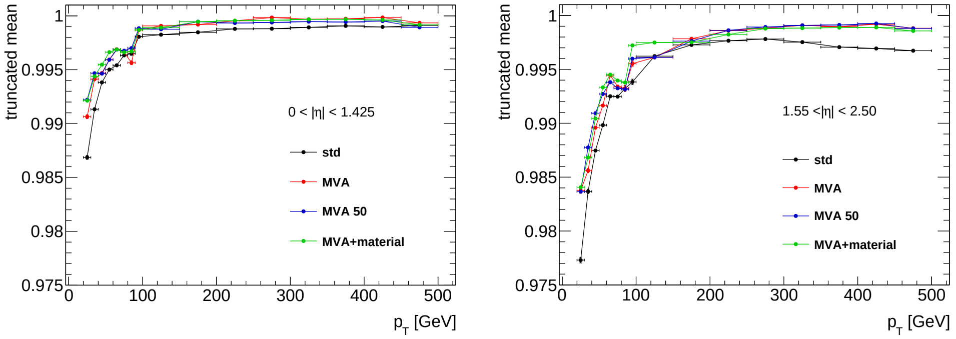

(a) barrel **(b)** endcap

Figure 5.16: Linearity defined as the truncated mean of the E/E_{true} distribution function of p_T^{true} for (a) barrel and (b) endcap for electrons.

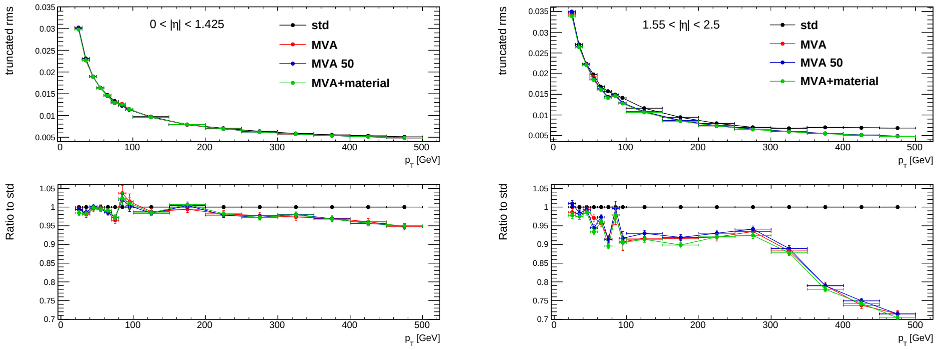

(a) barrel **(b)** endcap

Figure 5.17: Resolution defined as the truncated RMS of the E/E_{true} distribution function of p_T^{true} for (a) barrel and (b) endcap for electrons.

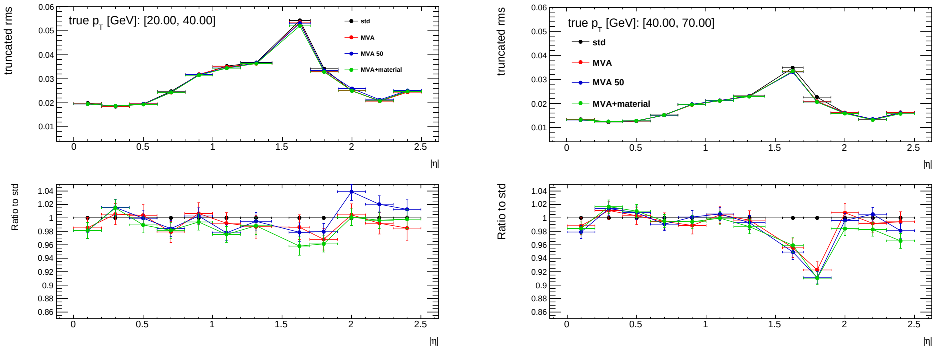

(a) 20 GeV $< p_T^{\text{true}} <$ 40 GeV **(b)** 40 GeV $< p_T^{\text{true}} <$ 70 GeV

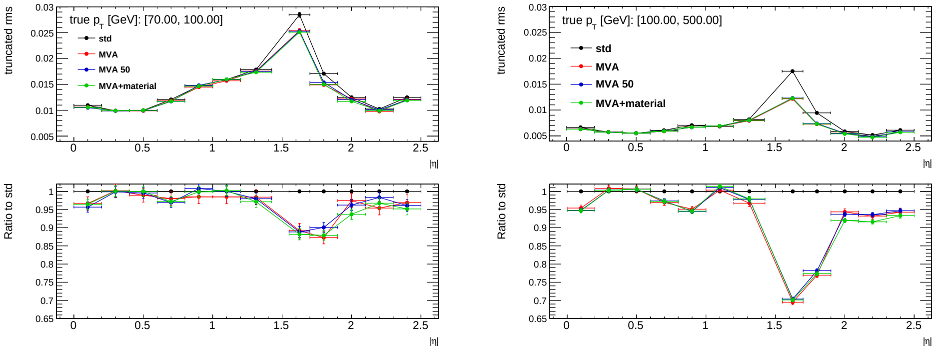

(c) 70 GeV $< p_T^{\text{true}} <$ 100 GeV **(d)** 100 GeV $< p_T^{\text{true}} <$ 500 GeV

Figure 5.18: Resolution defined as the truncated RMS of the E/E_{true} distribution function of η for various ranges of p_T^{true} for electrons. The boxes at the bottom show the improvement with respect to the standard calibration.

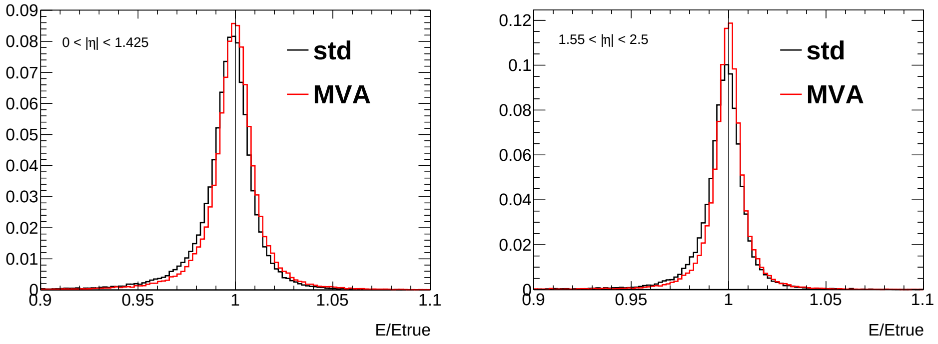

(a) barrel **(b)** endcap

Figure 5.19: E/E_{true} integrated over the p_T^{true} spectrum of the single particle sample for (a) barrel and (b) endcap for unconverted photons.

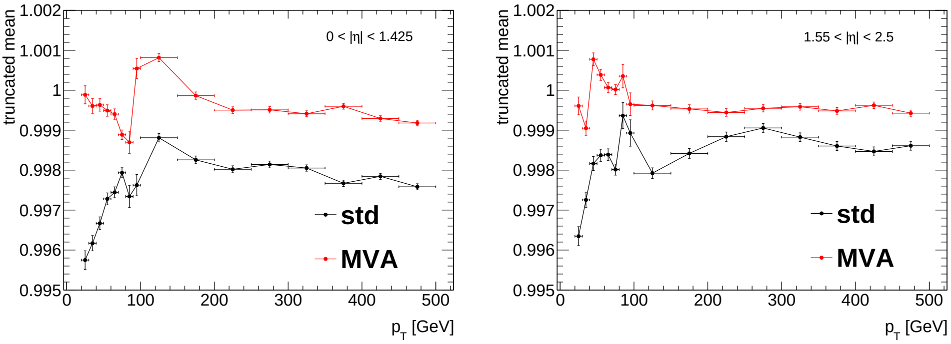

(a) barrel **(b)** endcap

Figure 5.20: Linearity defined as the truncated mean of the E/E_{true} distribution function of p_T^{true} for (a) barrel and (b) endcap for unconverted photons.

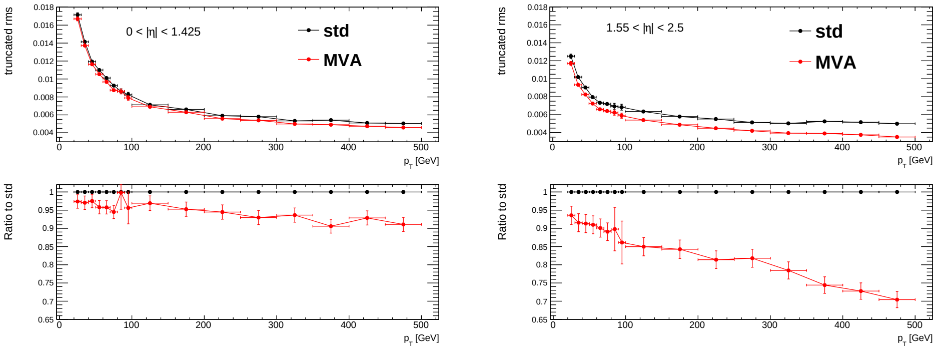

(a) barrel **(b)** endcap

Figure 5.21: Resolution defined as the truncated RMS of the E/E_{true} distribution function of p_T^{true} for (a) barrel and (b) endcap for unconverted photons.

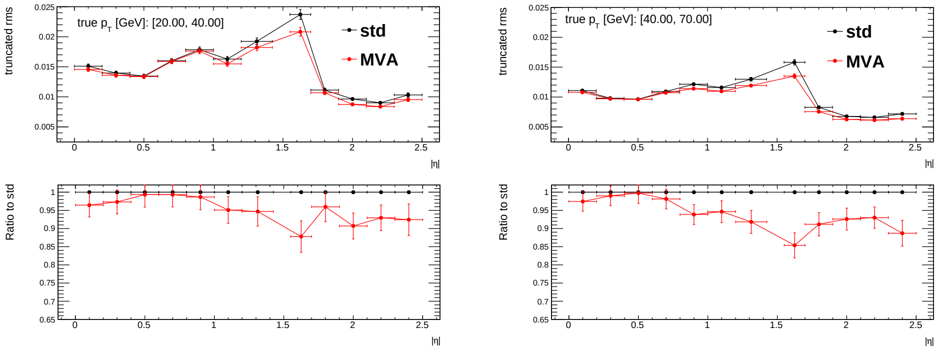

(a) 20 GeV $< p_T^{\text{true}} <$ 40 GeV

(b) 40 GeV $< p_T^{\text{true}} <$ 70 GeV

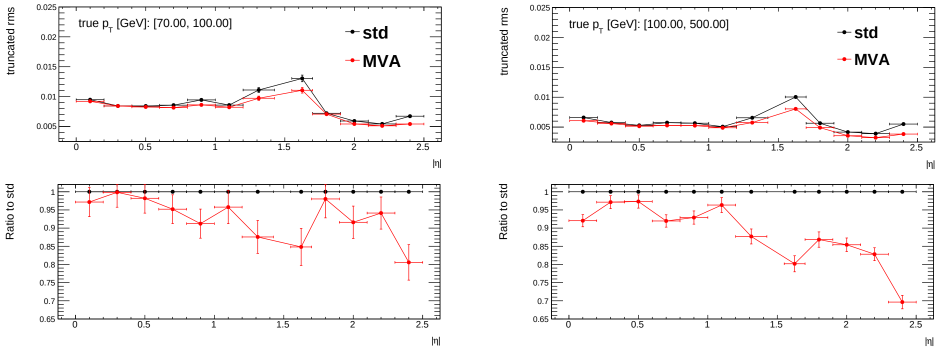

(c) 70 GeV $< p_T^{\text{true}} <$ 100 GeV

(d) 100 GeV $< p_T^{\text{true}} <$ 500 GeV

Figure 5.22: Resolution defined as the truncated RMS of the E/E_{true} distribution function of η for various ranges of p_T^{true} for unconverted photons. The boxes at the bottom show the improvement with respect to the standard calibration.

The resolution defined as truncated RMS is shown in Fig. 5.25 function of p_T^{true} and in fig 5.26 function of $|\eta|$. For converted photons the improvement seems to be more uniform with respect to $|\eta|$ and p_T^{true}

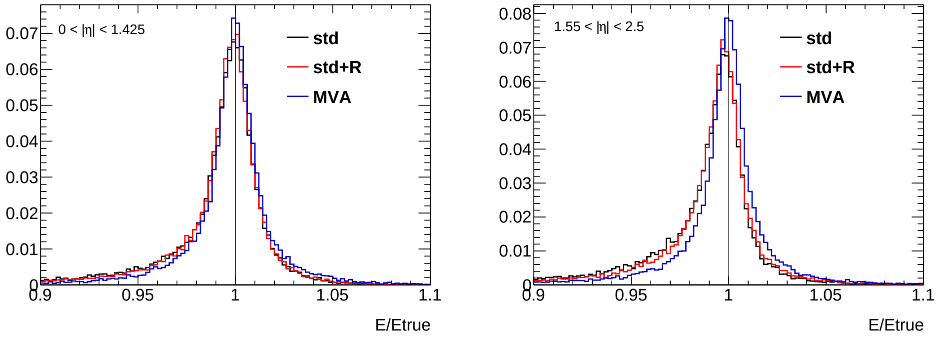

(a) barrel **(b)** endcap

Figure 5.23: E/E_{true} integrated over the p_T^{true} spectrum of the single particle sample for (a) barrel and (b) endcap for converted photons.

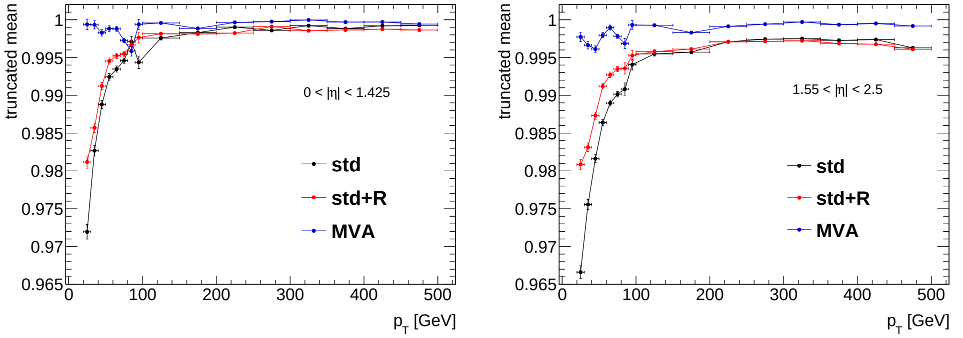

(a) barrel **(b)** endcap

Figure 5.24: Linearity defined as the truncated mean of the E/E_{true} distribution function of p_T^{true} for (a) barrel and (b) endcap for converted photons.

5.6.3 Linearity and resolution using photons from Higgs decay

Since the calibration has been developed for the $H \to \gamma\gamma$ analysis the performance have been evaluated also on an Higgs sample, in particular a simulated Monte Carlo decay of an Higgs boson with a mass $M_H = 125\,\text{GeV}$ produced through the gluon-gluon fusion mechanism has been used. The training has not been redone on the Higgs sample, but the optimization trained on single particles has been applied to the Higgs sample. There are two reasons to follow this procedure:

- the Higgs sample is too small for a proper training (only $1M$ of photon pass the Higgs selection),

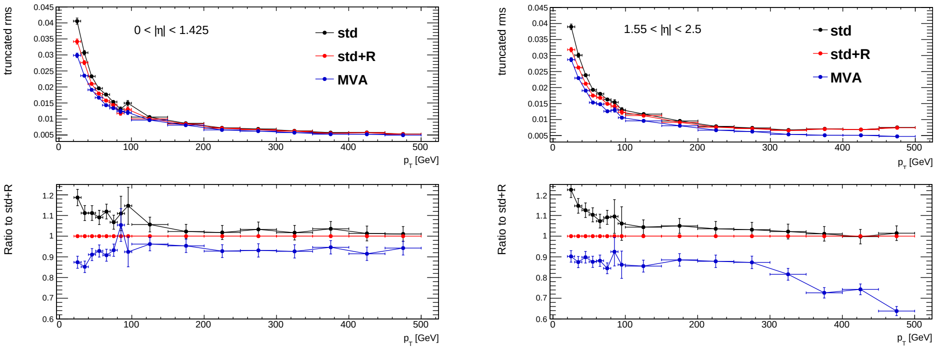

(a) barrel **(b)** endcap

Figure 5.25: Resolution defined as the truncated RMS of the E/E_{true} distribution function of p_T^{true} for (a) barrel and (b) endcap for converted photons. The boxes at the bottom show the improvement with respect to the standard calibration corrected with the radius of conversion.

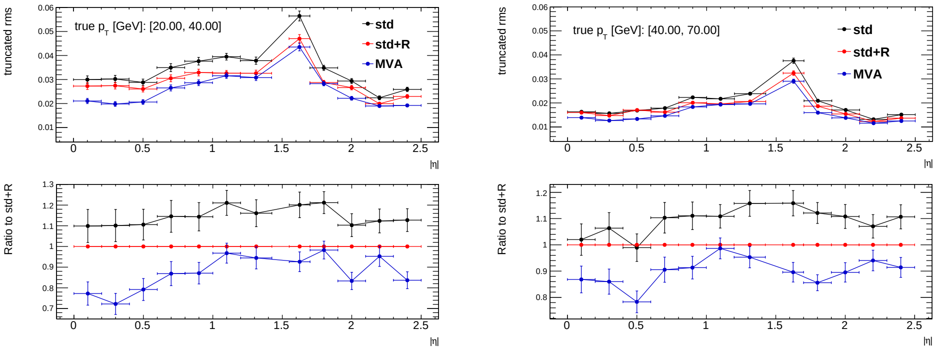

(a) 20 GeV $< p_T^{\text{true}} <$ 40 GeV **(b)** 40 GeV $< p_T^{\text{true}} <$ 70 GeV

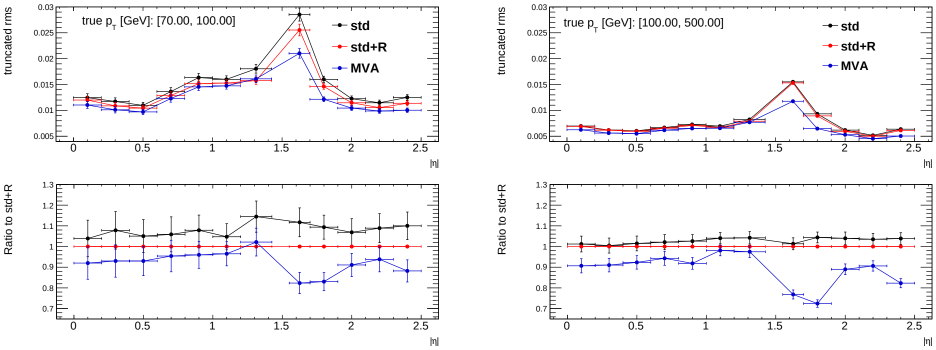

(c) 70 GeV $< p_T^{\text{true}} <$ 100 GeV **(d)** 100 GeV $< p_T^{\text{true}} <$ 500 GeV

Figure 5.26: Resolution defined as the truncated RMS of the E/E_{true} distribution function of η for various ranges of p_T^{true} for converted photons. The boxes at the bottom show the improvement with respect to the standard calibration corrected with the radius of conversion.

- it is a cross check of the robustness of the calibration.

The performance is evaluated as before with this new sample, but at the same time they are compared with the single particle sample. To do that it is important to take into account the p_T^{true} distribution of the photons from the Higgs decay, since it is very different from the distribution of the p_T^{true} of the single particle sample: it is peaked around 60 GeV and it ends around 120 GeV. To match the p_T^{true} distribution, in order to compare the single particle sample with the Higgs sample a reweighing procedure is applied on single particle, the effect of the procedure is shown in Fig. 5.27.

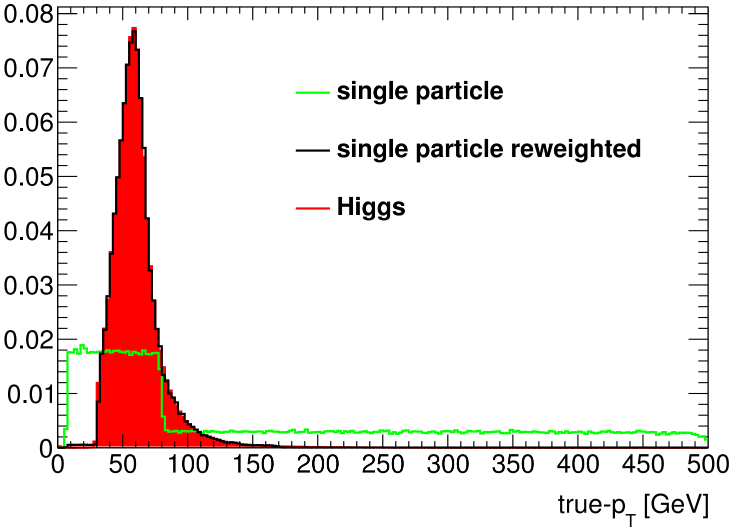

Figure 5.27: Reweighing of the single particle sample to match the photon p_T^{true} distribution from the Higgs decay.

The E/E_{true} distribution is shown in figure 5.28 for barrel and endcap. The distribution computed on the Higgs sample with the MVA is narrower than the one computed with the standard calibration, but for unknown reason the performance of the standard calibration evaluated on the training sample weighted with the Higgs spectrum is better. This is confirmed by the resolution in figures 5.29 and 5.30. By the way considering only the Higgs sample the resolution of the MVA calibration is better by a factor between 2% and 10% than the standard one.

For converted photon the comparison is with the standard calibration corrected with the radius of conversion. Figure 5.31 shows the distribution of E/E_{true} for barrel and endcap. Figures 5.32 and 5.33 show improvement in the resolution by a factor up to 10% with respect to the standard calibration corrected with the conversion radius evaluated on the Higgs sample.

The effect on the invariant mass distribution will be shown in the next chapter dedicated to the analysis of the decay of the Higgs boson into a couple of photons.

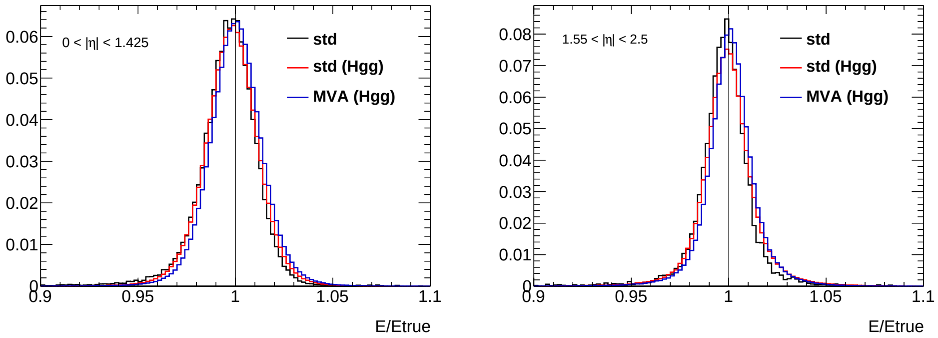

(a) barrel **(b)** endcap

Figure 5.28: E/E_{true} integrated over the p_T^{true} spectrum for (a) barrel and (b) endcap for unconverted photon passing the Higgs cutflow (Hgg) and unconverted photons from the test sample weighted with the Higgs p_T^{true} distribution.

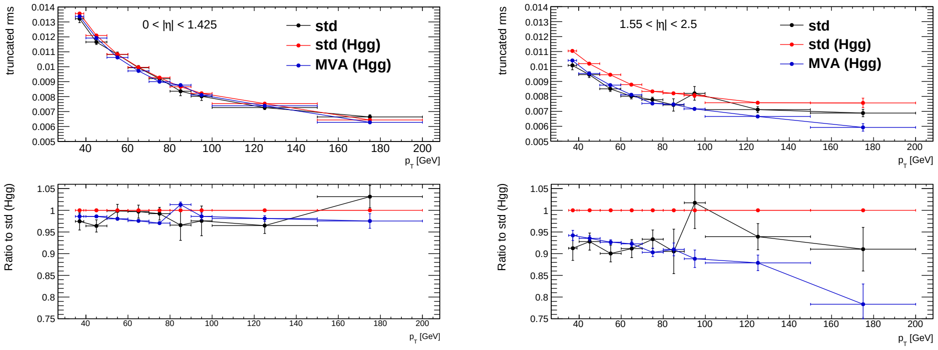

(a) barrel **(b)** endcap

Figure 5.29: Resolution defined as the truncated RMS of the E/E_{true} distribution function of p_T^{true} for (a) barrel and (b) endcap for unconverted photon passing the Higgs cutflow (Hgg) and unconverted photons from the test sample weighted with the Higgs p_T^{true} distribution.

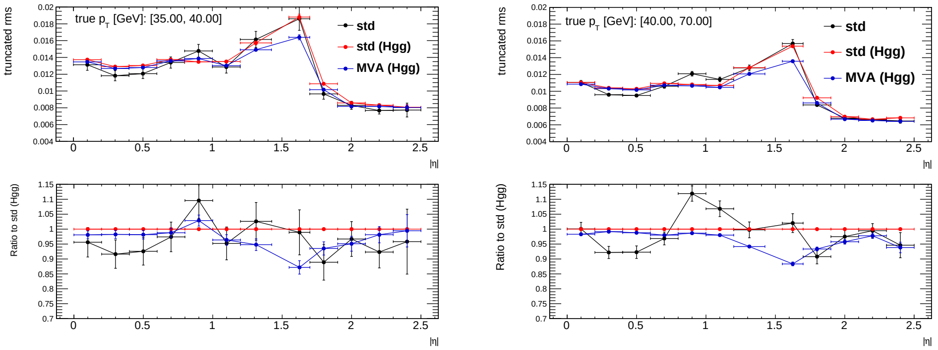

(a) 20 GeV $< p_T^{\text{true}} <$ 40 GeV **(b)** 40 GeV $< p_T^{\text{true}} <$ 70 GeV

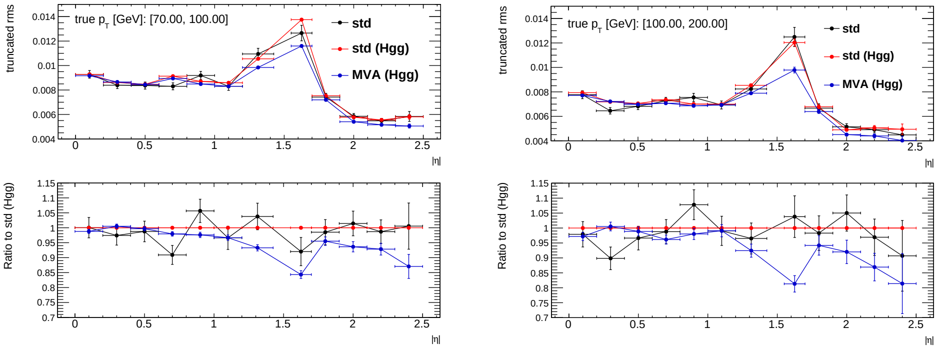

(c) 70 GeV $< p_T^{\text{true}} <$ 100 GeV **(d)** 100 GeV $< p_T^{\text{true}} <$ 500 GeV

Figure 5.30: Resolution defined as the truncated RMS of the E/E_{true} distribution function of η for various ranges of p_T^{true} for unconverted photon passing the Higgs cutflow (Hgg) and unconverted photons from the test sample weighted with the Higgs p_T^{true} distribution. The boxes at the bottom show the improvement with respect to the standard calibration.

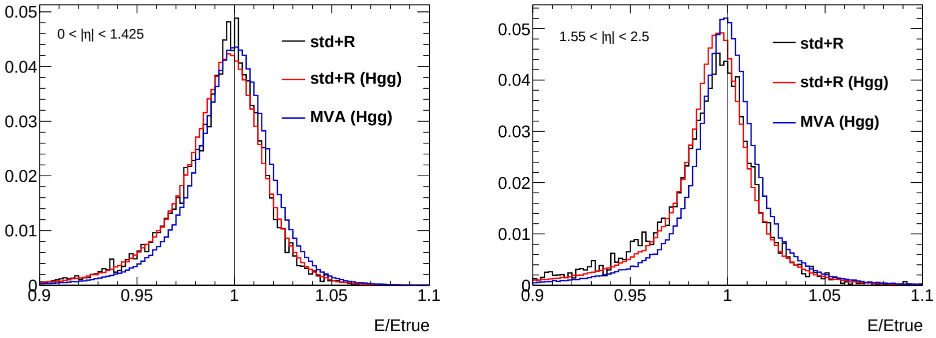

(a) barrel **(b)** endcap

Figure 5.31: E/E_{true} integrated over the p_T^{true} spectrum for (a) barrel and (b) endcap for converted photon passing the Higgs cutflow (Hgg) and converted photons from the test sample weighted with the Higgs p_T^{true} distribution.

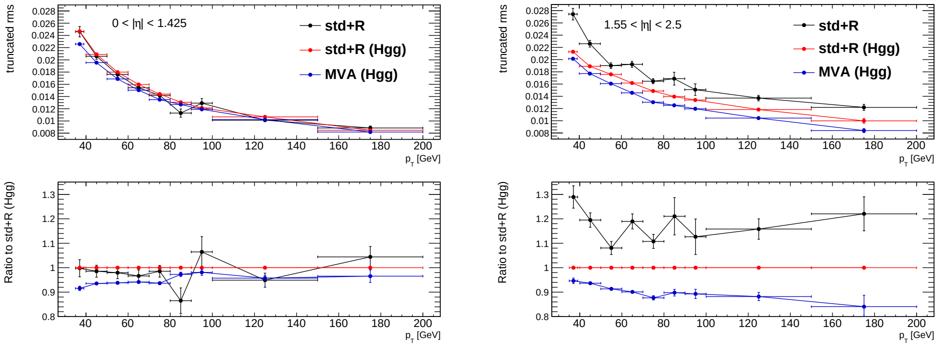

(a) barrel **(b)** endcap

Figure 5.32: Resolution defined as the truncated RMS of the E/E_{true} distribution function of p_T^{true} for (a) barrel and (b) endcap for converted photon passing the Higgs cutflow (Hgg) and converted photons from the test sample weighted with the Higgs p_T^{true} distribution.

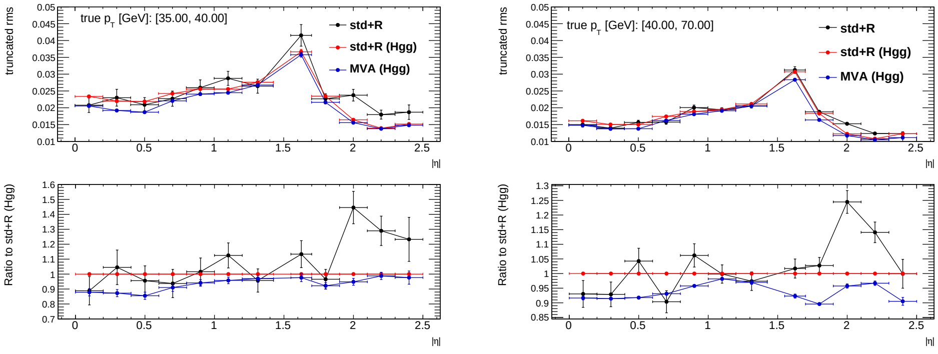

(a) 20 GeV $< p_T^{\text{true}} <$ 40 GeV **(b)** 40 GeV $< p_T^{\text{true}} <$ 70 GeV

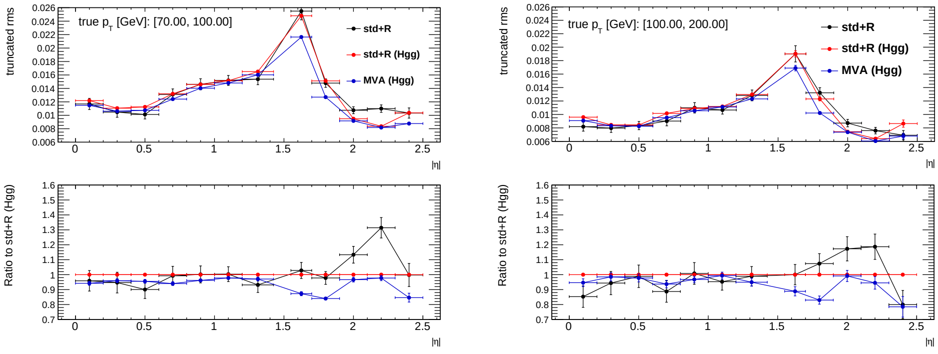

(c) 70 GeV $< p_T^{\text{true}} <$ 100 GeV **(d)** 100 GeV $< p_T^{\text{true}} <$ 500 GeV

Figure 5.33: Resolution defined as the truncated RMS of the E/E_{true} distribution function of η for various ranges of p_T^{true} for converted photon passing the Higgs cutflow (Hgg) and converted photons from the test sample weighted with the Higgs p_T^{true} distribution. The boxes at the bottom show the improvement with respect to the standard calibration.

CHAPTER 6

$H \to \gamma\gamma$ analysis

In this chapter the analysis of the decay of the Higgs boson into a couple of photons with the ATLAS detector is described. This analysis is based on the result presented at the CERN Council in December 2012 [8].

The analysed proton-proton collision datasets correspond to an integrated luminosities of $4.8\,\mathrm{fb}^{-1}$ collected at $\sqrt{s} = 7\,\mathrm{TeV}$ in 2011 and $13.0\,\mathrm{fb}^{-1}$ collected at $\sqrt{s} = 8\,\mathrm{TeV}$ in 2012. The results confirm the observation of a new boson which was previously reported by the ATLAS [30] and CMS [29] collaborations with the combination of several decay channels, and, for the first time, establish the observation in the diphoton channel alone.

First the analysis is presented, with the selection in section 6.1, the invariant mass reconstruction in section 6.2 and the categorization in section 6.3. Then the modelization of signal the background are in section 6.4 and the improvement with the MVA calibration is discussed in section 6.4.2. In section 6.5 the decomposition of the background is illustrated, in particular using the 4×4 matrix method. After a list of the systematic uncertainties in section 6.6 the results are summarized in section 6.7 showing the quantification of the observed excess, the mass measurement and the strength relative to the various production modes.

6.1 Data selection

The selection of the data is presented in its steps: trigger selection, offline photon preselection and offline event selection.

6.1.1 Trigger

The trigger used for this analysis is a diphoton trigger with thresholds on the transverse energy of the leading (highest E_T) and subleading photons. The thresholds are different for the two datasets: 20 GeV is required on both clusters for the $\sqrt{s} = 7\,\mathrm{TeV}$ run, while for the $\sqrt{s} = 8\,\mathrm{TeV}$ data sample, the thresholds are increased to 35 GeV for the leading and 25 GeV on the subleading. These triggers are the first unprescaled triggers suitable for this analysis. In addition the trigger uses clusters of energy in the EM calorimeter. At the final trigger level these EM clusters are required to match loose criteria similar to the one used in the offline selection. The triggers have been chosen to be fully efficient on the signal (99% for signal events fulfilling the final event selection). The performance of the loose triggers as a function of the number of primary vertices is constant up to a number of primary vertices of at least 28.

Data quality requirements are applied to ensure good performance from the inner detector, electromagnetic and hadronic calorimeter (the Good Run List). The obtained data sample corresponds to a total integrated luminosity of 4.8 fb^{-1} at $\sqrt{s} = 7$ TeV collected in 2011, and 13.0 fb^{-1} at 8 TeV collision data, which is the full dataset recorded up to the LHC technical stop of September 17, 2012. The data were recorded with instantaneous luminosity varying between $1 \times 10^{32}\,\mathrm{cm}^{-2}\mathrm{s}^{-1}$ and $7.8 \times 10^{33}\,\mathrm{cm}^{-2}\mathrm{s}^{-1}$. One of the most important differences between the two datasets is the pileup condition: the mean number of interactions per bunch crossing is 9.1 in the data sample acquired at 7 TeV during 2011, and of 20.0 for the data at 8 TeV taken up to September 17, 2012 (see Fig. 6.1). The simulations used in the analysis are corrected to reflect the distribution of interactions per bunch crossing and the spread of the z position of the primary vertex observed in data.

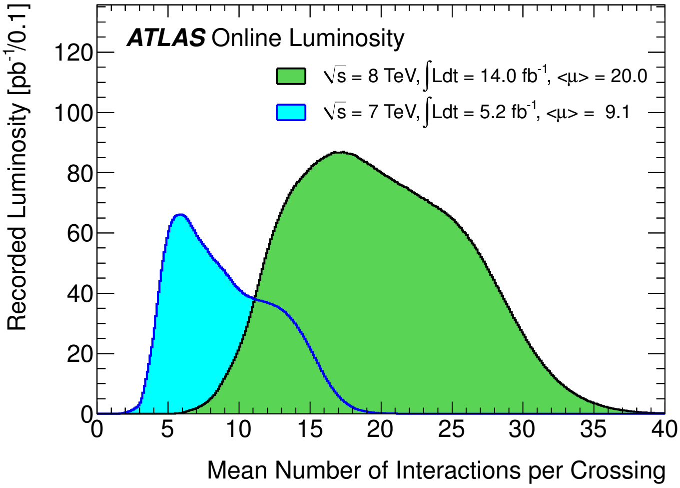

Figure 6.1: Mean number of interactions per crossing for the 2011 and 2012 data, between April 4th and September 17th.

6.1.2 Photon preselection

Two-photons events candidates are selected applying kinematics and quality cuts:

- the leading photon candidate is required to have $E_T > 40$ GeV, and the subleading photon candidate $E_T > 30$ GeV,
- only photons inside the EM calorimeter acceptance ($|\eta| < 2.37$) are considered, excluding the transition region between the barrel and the endcap ($1.37 < |\eta| < 1.52$),
- photon candidates are required to pass the loose identification criteria. In the MC simulation, the cuts are applied after the correction of the shower shape using the fudge factor (FF) method (see section 3.4.1).

6.1.3 Event selection

After having preselected the photons only the two most energetic are considered:

- In order to reject candidates from non-collision backgrounds at least one primary vertex must be reconstructed in the event,

- The preselected photon candidates are required to pass the tight identification criteria. For the $\sqrt{s} = 7\,\text{TeV}$ data a neural network based selection tuned to achieve similar jet rejection as the cut-based used in the previous analysis [6] but with higher efficiency, is used. For the $\sqrt{s} = 8\,\text{TeV}$ data, due to the necessity of ensuring a reliable photon performance for data recorded very recently, a cut-based selection is used. As for the loose cut FF are applied on MC simulation. The photon identification efficiency for the tight criteria averaged on η ranges between 85% and above 95% for the p_T range considered for a Higgs boson with mass as low as $m_H = 120\,\text{GeV}$,

- the two selected photons must be isolated in the calorimeter through the use of criteria based on both the inner tracker and the calorimeter (see section 3.5). The first is the scalar sum of the transverse momenta of all tracks with $p_T > 1\,\text{GeV}$ in a cone of $\Delta R = \sqrt{\Delta\eta^2 + \Delta\phi^2} < 0.2$ around each photon, and is required to be less than 2.6 GeV. Only tracks consistent with originating from the diphoton production vertex (see section 6.2) are used, and tracks associated to converted photon candidates are excluded. The second variable is the transverse energy sum of positive-energy topological clusters deposited in the calorimeter around each photon in a cone of $\Delta R = 0.4$, and is required to be less than 6 GeV. Topological clusters are three-dimensional clusters of variable size, built by associating calorimeter cells on the basis of the signal-to-noise ratio [94]. The energy sum excludes deposits in the core region which are expected to originate from the photon itself, and corrections for the small estimated energy leakage outside this region are applied. The effects of the underlying event and of additional minimum bias interactions occurring in the same or neighbouring bunch crossings are corrected on an event-by-event basis using the energy density measured from observed soft jets (see section 3.5).

With this selection, 23 788 diphoton candidates are observed in the diphoton invariant mass range between 100 and 160 GeV in the $\sqrt{s} = 7\,\text{TeV}$ data sample. In the same mass range, 77 411 events are selected in the $\sqrt{s} = 8\,\text{TeV}$ data sample.

6.2 Pointing and invariant mass

The invariant mass of the photon candidate pair is computed using the transverse energies of the two photons, their pseudorapidity and azimuthal directions:

$$m_{\gamma\gamma} = \sqrt{E_{T1}E_{T2}(\cosh\Delta\eta - \cos\Delta\varphi)} \tag{6.1}$$

Many corrections are applied on the quantity in this formula. The photon energies are measured in the calorimeter as described in chapter 4 using the correction for converted photon described in section 4.6. The effect of the multivariate calibration described in chapter 5 is discussed in section 6.4.2. In addition the photon energy is corrected on data with scale factor to take into account the energy differences between data and MC simulation. The calibration is refined by applying η-dependent correction factors, which are of the order of $\pm 1\%$ determined comparing the $Z \to ee$ peak between data and MC simulation. The simulation is corrected to reflect the energy resolution observed using $Z \to ee$ events in data, which requires an energy smearing of about 1% in the calorimeter barrel region and between 1.2% and up to 2.1% in the calorimeter endcaps.

In addition to the energies, the angle between the photons is required for the computation of the diphoton invariant mass. This angle is determined from the interaction vertex position and the photon impact points in the calorimeter. The resolution of the angle measurement is dominated by the resolution of the primary vertex z position.

The directions of the photons are determined as following: φ is determined from the second calorimeter layer, and η from the straight line connecting the primary vertex to the impact point in the first layer of the EM calorimeter. For the mass measurement the η direction of the photons is refined using the position of the primary vertex. For this reason the selection of the primary vertex is important to improve the resolution of the invariant mass. The selection of the vertex is also important for the selection of the jets associated with the hard interaction and the track isolation.

Several variables are used to select the vertex associated with the Higgs production, the most important is the pointing variable, the direction of photons measured by EM calorimeter thanks to its longitudinal segmentation. In particular the direction for unconverted photons is determined using the barycentre of the cluster measured in the first and the second layer of the accordion. For converted photons having tracks it is determined from the conversion point measured by the inner detector and the position in the first layer of the accordion. For each of the two photons in the event, the intersection between the flight line and the beam line gives the estimate of the z-coordinate of the photon origin. Then, a weighted average of the two gives the estimate, with its uncertainty. Finally, a MVA is used to combine this estimate with other observables, to select the best vertex among the reconstructed ones. The variables used to select the vertex associated to the Higgs boson production are:

- distance between the z position measured by the inner detector and by the pointing procedure taking into account the resolution of the pointing:

$$\frac{z_{\mathrm{ID}} - z_{\mathrm{pointing}}}{\sigma_{\mathrm{pointing}}} \tag{6.2}$$

- the sum of the squared momentum of all the tracks associated to a vertex: $\sum_{\mathrm{tracks}} p_T^2$,
- the scalar sum of the momentum of all the tracks associated to a vertex: $\sum_{\mathrm{tracks}} p_T$,
- the difference between the diphoton azimuthal direction and the azimuthal direction of the vector sum of the momenta of the tracks associated to a vertex.

For the $\sqrt{s} = 7\,\mathrm{TeV}$ dataset the first two variables have been combined using a likelihood ratio and the vertex with higher ratio have been selected. For the $\sqrt{s} = 8\,\mathrm{TeV}$ dataset the procedure have been updated using all the four variables with a multi layer perceptron (MLP). Figure 6.2 shows the efficiency to select a vertex close to the Higgs production as a function of the number of reconstructed primary vertices. With respect to the the likelihood method the improvement of the MLP method on the inclusive mass resolution is 0.7% on the RMS at $\sqrt{s} = 8\,\mathrm{TeV}$.

The vertex selection was checked on data using $Z \to ee$ events removing the electron tracks and verifying the efficiency of finding the correct vertex previously associated to the tracks. The efficiencies in the MC samples $H \to \gamma\gamma$ and $Z \to ee$ after the reweighing agree to better than 1%. The reweighing is needed to match the di-electron and diphoton p_T spectra and the fraction of events with zero, one or two photons (or electrons) in the barrel.

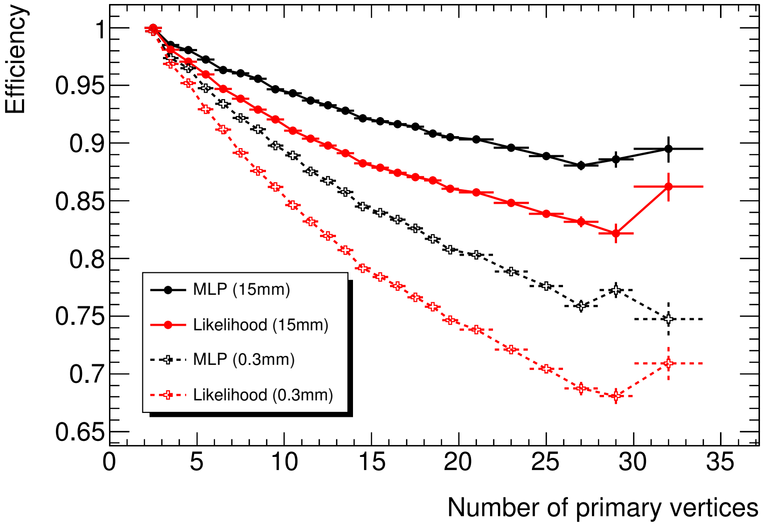

Figure 6.2: Efficiency to select a primary vertex close to the position of the Higgs production along the z-axis inside a window of 15 mm or 0.3 mm as a function of the number of reconstructed vertices.

6.3 Event categorization

To improve the analysis the selected events are divided in various categories. Some categories are designed to improve the discovery sensitivity, other to be sensitive to specific production modes. They differ in signal/background ratio, resolution of the invariant mass and by the presence of additional final particles. Five categories (called EPS categories[1] from now on) are defined using the pseudorapidity of the two photons and the conversion status (see Fig. 6.3):

unconverted central both photon candidates are reconstructed as unconverted photons and have $|\eta| < 0.75$,

unconverted rest both photon candidates are reconstructed as unconverted photons and at least one candidate has $|\eta| > 0.75$,

converted central at least one photon candidate is reconstructed as converted photon and both photon candidates have $|\eta| < 0.75$,

converted rest at least one photon candidate is reconstructed as a converted photon and both photon candidates have $|\eta| < 1.3$ or $|\eta| > 1.75$, but at least one photon candidate has $\eta > 0.75$,

converted transition at least one photon candidate is reconstructed as a converted photon and at least one photon candidate is in the range $1.3 < |\eta| < 1.37$ or $1.52 < |\eta| < 1.75$. This category cover at the same time part of the barrel and part of the endcap.

---

[1] The name is from the 2011 European Physical Society conference.

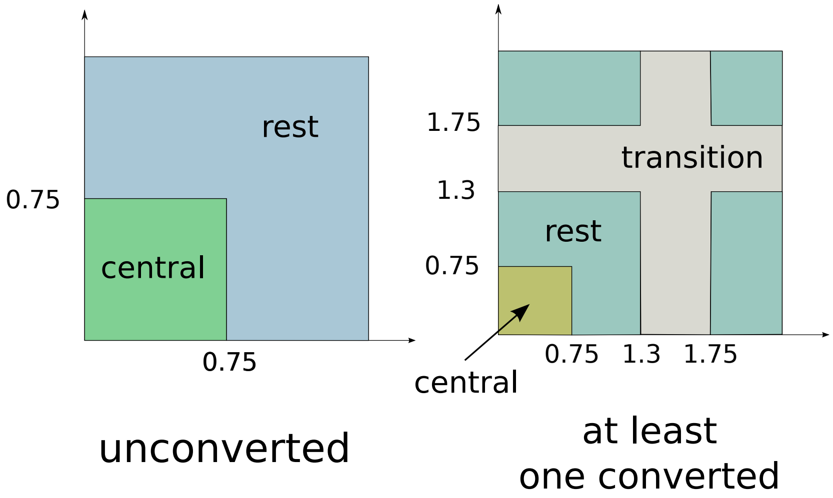

Figure 6.3: EPS categorization using $|\eta|$ and the conversion status.

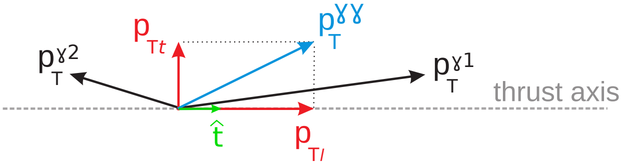

Figure 6.4: Illustration of the p_{Tt} quantity.

A further categorization is introduced using the p_{Tt} variable defined as the orthogonal projection of the diphoton momentum on the thrust axis $\hat{t}$ defined as the direction of the vectorial difference between the transverse momenta of the photons (see Fig. 6.4):

$$\hat{t} = \frac{\vec{p}_{T,1} - \vec{p}_{T,2}}{|\vec{p}_{T,1} - \vec{p}_{T,2}|} \tag{6.3}$$

$$\vec{p}_T^{\gamma\gamma} = \vec{p}_{T,1} + \vec{p}_{T,2} \tag{6.4}$$

$$\vec{p}_{Tt} = \vec{p}_T^{\gamma\gamma} - (p_T^{\gamma\gamma} \cdot \hat{t}) \cdot \hat{t} \tag{6.5}$$

$$p_{Tt} = \left|\vec{p}_T^{\gamma\gamma} \times \hat{t}\right| . \tag{6.6}$$

All the EPS categories, except for the converted transition, are split in low-p_{Tt} ($<$ 60 GeV) categories and high-p_{Tt} ($>$ 60 GeV) categories. The p_{Tt} quantity is strongly correlated with the diphoton transverse momentum, but it has a better detector resolution and retains a monotonically falling diphoton invariant mass distribution. Fig. 6.5 displays the distributions of p_{Tt} for data and Monte Carlo signal processes for the inclusive event selection. Different p_{Tt} categories have different signal/background ratio, in particular the gluon-gluon fusion p_{Tt} distribution is very similar to the one of the background, but the other signal processes show on average larger p_{Tt} values than the data.

Other categories are designed to increase the sensitivity to Higgs boson production via vector-boson fusion (VBF) and associated production with vector bosons (WH, ZH). This requires the reconstruction of jets as well as electrons and muons. The selection of jets and leptons is described in the next section. Three categories have been introduced:

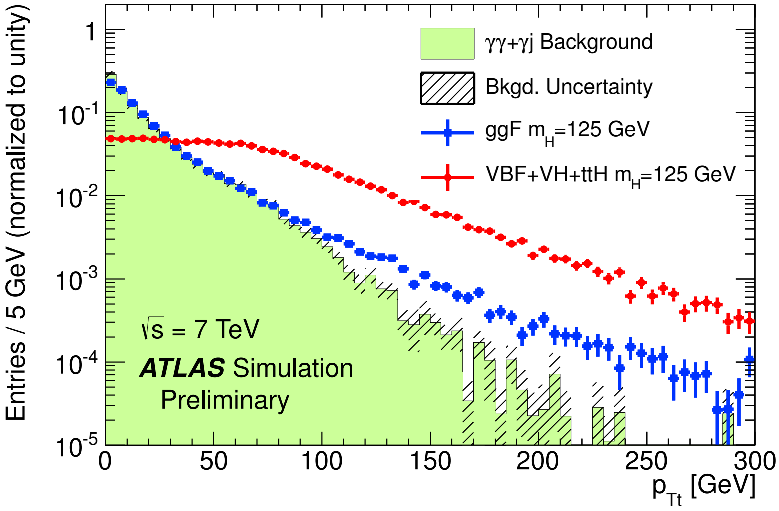

Figure 6.5: Normalized distribution of p_{Tt} in simulated events with Higgs boson production at $m_H = 125$ Gev and in background events. The signal distribution is shown separately for gluon fusion (blue), and vector-boson fusion together with associated production (red).

VBF (or high-mass two-jet) events are characterised by two forward jets with little hadronic activity between the two jets. The high-mass two-jet category, designed to have high selection efficiency for VBF production, collects events containing two jets with invariant mass greater than 400 GeV and a pseudorapidity separation larger than 2.8. In addition, the azimuthal angle difference $\Delta\phi$ between the diphoton and the dijet systems is required to be larger than 2.6,

VH (or low-mass two-jet) events where the vector boson decays hadronically by identifying two jets with dijet invariant mass in the range of 60–110 GeV and a pseudorapidity separation between the two jets of less than 3.5. In addition, the diphoton transverse momentum orthogonal to the diphoton thrust axis in the transverse plane (p_{Tt}) is required to be larger than 60 GeV,

one lepton events where the vector boson decays leptonically by identifying either an electron or a muon candidate in the event. One electron with $p_T > 15$ GeV or one muon with $p_T > 10$ GeV are required.

The category of each event is tested in the following order: one lepton, low-mass two-jet and VBF. The events failing this categorization are categorized using the 9 category $p_{Tt} \otimes |\eta| \otimes$ conversion status. Since only partial information about jets and leptons are stored in the 2011 dataset used in this analysis the lepton category and the low-mass two-jet were used only for the 2012 dataset. Events from 2011 are then divided in 10 categories, events from 2012 in 12 categories.

Table 6.1 and table 6.2 list the number of observed events and the expected number of signal events for $m_H = 126.5$ GeV, for each category in the mass range 100–160 GeV, based on SM predictions at 8 TeV, for $\sqrt{s} = 7$ TeV and $\sqrt{s} = 8$ TeV respectively.

$\sqrt{s}$	7 TeV						
Category	N_D	N_S	ggH [%]	VBF [%]	WH [%]	ZH [%]	ttH [%]
Unconv. central, low p_{Tt}	2054	10.4	92.9	4.0	1.8	1.0	0.2
Uncon. central, high p_{Tt}	97	1.5	66.5	15.7	9.9	5.7	2.4
Unconv. rest, low p_{Tt}	7129	21.6	92.8	3.9	2	1.1	0.2
Unconv. rest, high p_{Tt}	444	2.7	65.4	16.1	10.8	6.1	1.8
Conv. central, low p_{Tt}	1493	6.7	92.8	4.0	1.9	1.0	0.2
Conv. central, high p_{Tt}	77	1.0	66.6	15.3	10	5.7	2.5
Conv. rest, low p_{Tt}	8313	21.0	92.8	3.8	2.0	1.1	0.2
Conv. rest, high p_{Tt}	501	2.7	65.3	16.0	11.0	5.9	1.8
Conv. transition	3591	9.5	89.4	5.2	3.3	1.7	0.3
High Mass two-jet	89	2.2	22.5	76.7	0.4	0.2	0.1
All categories (inclusive)	23788	79.3	87.8	7.3	2.9	1.6	0.4

Table 6.1: Number of events in the data (N_D) at 7 TeV and expected number of expected signal events (N_S) for $m_H = 126.5\,\mathrm{GeV}$, for each category in the mass range 100–160 GeV, based on SM predictions at 7 TeV. The statistical uncertainty on N_S is less than 1%. The breakdown of expected signal events in the $gg \to H$, VBF, WH, ZH, ttH processes is detailed.

$\sqrt{s}$	8 TeV							
Category	N_D	N_S	ggH [%]	VBF [%]	WH [%]	ZH [%]	ttH [%]	FWHM [GeV]
Unconv. central, low p_{Tt}	6797	32	93	4.2	1.4	0.9	0.2	3.45
Unconv. central, high p_{Tt}	319	4.7	76	15.2	3.9	2.9	1.7	3.22
Unconv. rest, low p_{Tt}	26802	69	93	4.2	1.7	1.1	0.2	3.75
Unconv. rest, high p_{Tt}	1538	9.7	76	15.1	4.5	3.3	1.2	3.59
Conv. central, low p_{Tt}	4480	21	93	4.2	1.4	0.9	0.2	3.86
Conv. central, high p_{Tt}	199	3.1	77	14.5	4.1	2.8	1.7	3.51
Conv. rest, low p_{Tt}	24107	60	93	4.1	1.7	1.1	0.2	4.32
Conv. rest, high p_{Tt}	1324	8.3	75	15.1	4.9	3.4	1.3	4.00
Conv. transition	10891	28	90	5.6	2.3	1.5	0.3	5.57
High Mass two-jet	345	7.6	31	68.2	0.3	0.2	0.1	3.65
Low Mass two-jet	477	4.7	60	5.1	20.7	12.1	1.6	3.45
One-lepton	151	2.0	3.2	0.4	62.5	15.8	18.0	3.85
All categories (inclusive)	77430	249	88	7.4	2.8	1.6	0.5	3.87

Table 6.2: Number of events in the data (N_D) at 8 TeV and expected number of expected signal events (N_S) for $m_H = 126.5\,\mathrm{GeV}$, for each category in the mass range 100–160 GeV, based on SM predictions at 8 TeV. The mass resolution Full Width at Half Maximum (FWHM) is also given. The statistical uncertainties on N_S and FWHM are less than 1%. The breakdown of expected signal events in the $gg \to H$, VBF, WH, ZH, ttH processes is detailed.

6.3.1 Jet and lepton selection

Electron candidates are reconstructed from clusters of energy deposits in the electromagnetic calorimeter associated with a track reconstructed in the inner detector. The following cuts are applied on electron candidates:

- a transverse momentum greater than 15 GeV,
- $|\eta| < 2.47$, excluding the region around the transition between the barrel and endcap calorimeters ($1.37 < |\eta| < 1.52$),
- identification criteria based on electromagnetic shower shapes with somewhat looser requirements than in case of photons

Muon candidates are reconstructed from tracks in the inner detector and the muon spectrometer, and in the forward region ($2.5 < |\eta| < 2.7$) from the muon spectrometer alone. A transverse momentum larger than 10 GeV is required.

Both electron and muon candidates are required to be isolated in the tracker and calorimeter with algorithms similar to the photon isolation requirements. The track-isolation is required to be less than 3 GeV in a cone of $\Delta R = 0.2$ and the calorimetric isolation is required to be less than 5 GeV in a cone $\Delta R = 0.4$.

Jets are reconstructed from three-dimensional clusters of energy in the electromagnetic and hadronic calorimeters using the anti-k_t algorithm [95] with a distance parameter of $R = 0.4$. Jets are selected with:

- transverse momentum greater than 25 GeV (30 GeV) for $|\eta| < 2.5$ ($2.5 < |\eta| < 4.5$),
- jets within $|\eta| < 2.5$ must fulfill a requirement, based on tracking information, that they originate from the diphoton production vertex. A jet vertex fraction (JVF) is calculated for each vertex using tracks matching the jet and is defined as the ratio of the p_T sum of the matched charged particles associated to the selected vertex and the p_T sum of all matched particles. The JVF fraction is required to be greater than 0.5.

To prevent potential double-counting of objects in the detector, the reconstructed objects are required to have a minimal spatial separation. The two leading photons are always kept. Electrons within a cone of $\Delta R(e, \gamma) = \sqrt{\Delta\eta^2 + \Delta\varphi^2} < 0.4$, jets within $\Delta R(j, e) < 0.2$ or $\Delta R(j, \gamma) < 0.4$, and muons within a cone of $\Delta R(\mu, j) < 0.4$ or $\Delta R(\mu, \gamma) < 0.4$ are removed in this order. Finally, events for which the φ or θ angular difference between the electron and the muon is lower than 0.005 are rejected from the one-lepton tagged category.

6.4 Signal and background model

For the statistical analysis the signal and background models are needed to quantify the agreement of the data with the background-only hypothesis and the signal+background hypothesis. The signal model is derived from MC simulation, while the background model is from a fit to the data. Figure 6.6a shows the diphoton invariant mass spectrum combining the $\sqrt{s} = 7$ TeV and $\sqrt{s} = 8$ TeV datasets with the result of a fit to the data of the signal+background model fixing the signal mass to $m_H = 126.5$ GeV. Figure 6.6b is similar but the events are weighted using a weight based on the expected significance of every categories.

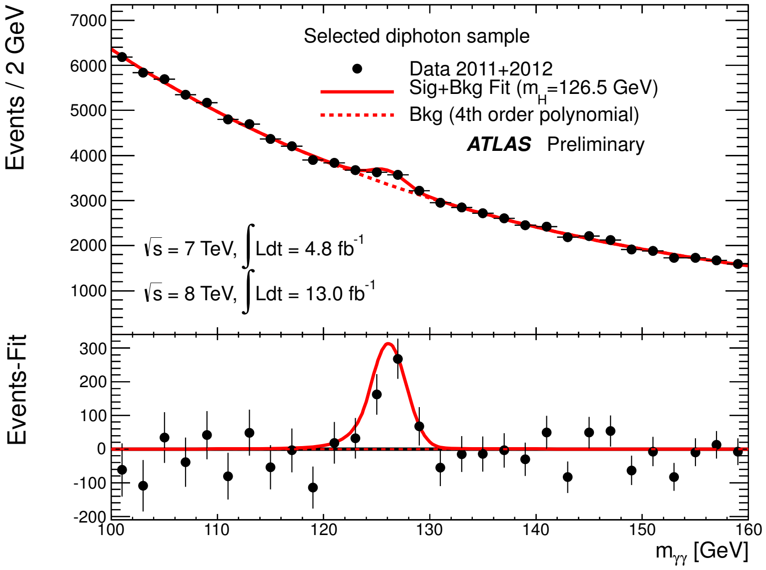

(a) unweighted

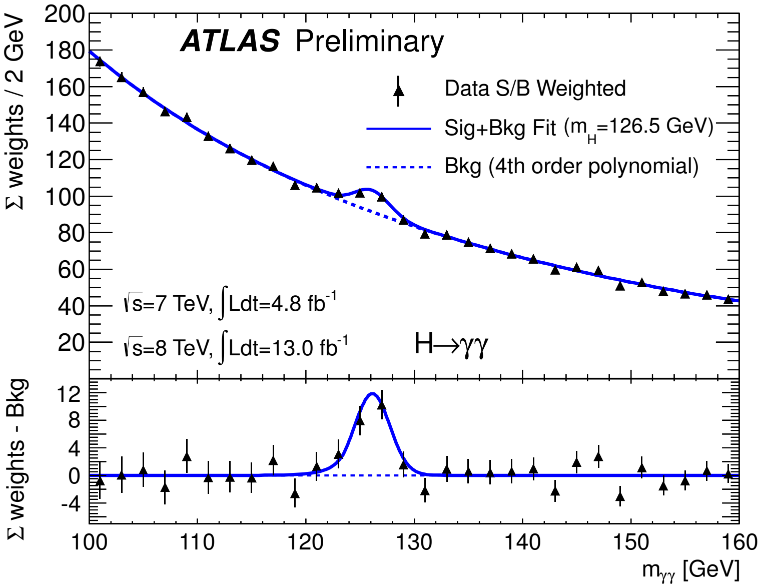

(b) weighted

Figure 6.6: Invariant mass distribution of diphoton candidates for the combined $\sqrt{s} = 7\,\text{TeV}$ and $\sqrt{s} = 8\,\text{TeV}$ data samples. The result of a fit to the data of the sum of a signal component fixed to $m_H = 126.5\,\text{GeV}$ and a background component is superimposed. The weighted distribution uses weights defined to be $\log(1 + S_i/B_i)$, where S_i is the expected number of signal events in a mass window that contains 90% of the signal events, and B_i is the integral of a background-only fit in the same window in the ith-category. The bottom insets display the residuals of the data with respect to the fitted background component.

6.4.1 Signal modelling

Signal MC samples are generated in steps of 5 GeV for hypothesised Higgs boson mass in the range of 100–150 GeV and passed through a full ATLAS detector simulation based on the GEANT4 program [83]. Pile-up effects are simulated by overlaying each MC event with a number of additional simulated inelastic pp collisions. The number of extra interactions is adjusted according to the measured multiplicity in each data-taking period.

The Higgs boson signal produced through the gluon fusion (ggF) and vector boson fusion (VBF) processes is simulated with the next-to-leading order POWHEG [96] generator interfaced to PYTHIA [97] for showering and hadronisation. Higgs boson production in association with a vector boson (VH) or a top quark pair (ttH) is simulated with PYTHIA. The Higgs boson production cross sections are computed at up to next-to-next-to-leading order (NNLO) [35, 98–101] in QCD for the gluon fusion process. The cross sections for the VBF process are calculated with full NLO QCD and EW corrections [102–104], and approximate NNLO QCD corrections are applied [105]. The W/ZH processes are calculated at NLO [106] and at NNLO [107], and NLO EW radiative corrections [108] are applied. The full NLO QCD corrections for $t\bar{t}H$ are calculated [109–112]. The theoretical uncertainty on the Higgs boson production cross section mainly comes from the renormalisation and factorisation scale variations and parton distribution functions (PDF) uncertainties [113–116]. The Higgs boson decay branching fractions are taken from Refs. [98, 117, 118] and their uncertainties are compiled in Refs. [119, 120].

The probability density function (PDF) of the reconstructed invariant mass $m_{\gamma\gamma}$ used for the signal parametrization is modelled from the signal MC samples by the sum of a Crystal Ball function (CB) (for the bulk of events) and a small, wider Gaussian component (to model the far outliers in the distribution). The CB function consists of a Gaussian core portion and a power-law low-end tail, below a certain threshold:

$$f(m_{\gamma\gamma}|\alpha_{\text{CB}}, n_{\text{CB}}, \mu_{\text{CB}}, \sigma_{\text{CB}}) = N \begin{cases} \exp(-t^2/2), & \text{for } t > -\alpha \\ A \cdot (B - t)^{-n_{\text{CB}}}, & \text{for } t \leqslant -\alpha \end{cases} \tag{6.7}$$

where $t = (m_{\gamma\gamma} - \mu_{\text{CB}})/\sigma_{\text{CB}}$, N is a normalization parameter, m_H is the hypothesized Higgs boson mass, σ represents the diphoton invariant mass resolution, n_{CB} is fixed to 10 and α_{CB} parametrize the non-Gaussian tail. A and B constants are chosen to have the function continuous and differentiable:

$$\begin{aligned} A &= \left(\frac{n_{\text{CB}}}{|\alpha_{\text{CB}}|}\right)^n \exp\left(-\frac{|\alpha_{\text{CB}}|^2}{2}\right) \\ B &= \frac{n_{\text{CB}}}{|\alpha_{\text{CB}}|} - |\alpha_{\text{CB}}| \end{aligned} \tag{6.8}$$

The mean of the Gaussian added to the CB is fixed to μ_{CB} and its width is equal to $k_{\text{GA}}\sigma_{\text{CB}}$.

The parameters of this function, as well as the signal yield, are parametrised as a function of hypothesised Higgs boson mass, and a simultaneous fit to signal MC samples at different mass is performed to interpolate the signal shape and yield to the intermediate mass values where MC samples are not available.

6.4.2 Effect of the MVA calibration on the invariant mass

The multivariate calibration described in chapter 5 is tested on this analysis and its effect is evaluated on the invariant mass distribution using a MC simulation with the Higgs boson produced at $m_H = 125$ GeV through the gluon-gluon mechanism. Figure 6.7 shows the inclusive distribution and the improvement on the truncated RMS used to estimate the resolution, as described in section 5.6.1. The improvement with respect to the calibration corrected for the radius of conversion is 3.3% and 6.4% with respect to the standard calibration without corrections.

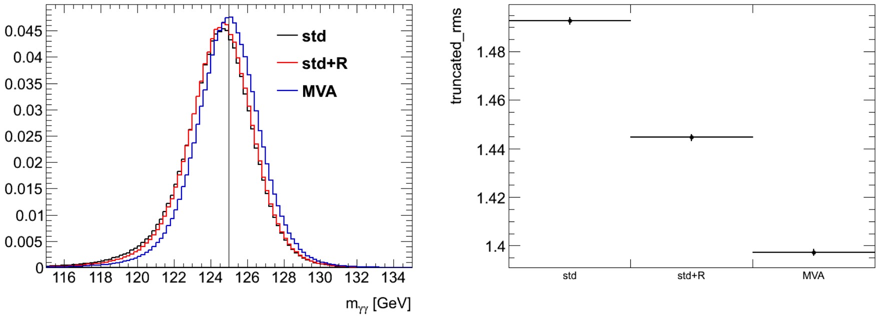

(a) invariant mass **(b)** truncated RMS

Figure 6.7: (a) Inclusive $m_{\gamma\gamma}$ distribution from ggH and (b) truncated RMS for the standard calibration (std), standard calibration corrected for the radius of conversion (std+R) and the MVA calibration.

Since the EPS categories are the ones which depend more on the resolution they are used to investigate where the MVA improvement are larger. Fig. 6.8 shows the invariant mass for the EPS categories. In figure 6.9 the linearity is evaluated using the truncated mean and the resolution using the truncated RMS in 6.10 for the EPS categories. The mass peak is much closer to the true value and the improvement on the truncated RMS ranges from 1% for converted central to 5% for the converted rest.

As in the standard analysis the invariant mass distribution is fitted with a Crystal Ball function plus a Gaussian as described in section 6.4.1. The parameters of this model are described as functions of the true mass m_H with a global fit using 9 MC samples with different Higgs masses between 110 GeV and 150 GeV. The most probable value of the Crystal Ball (equal to the Guassian one) μ_{CB}, the width of the Crystal Ball σ_{CB} and the α_{CB} parameter of the Crystal Ball are parametrised with linear functions of the true mass. The fraction of Crystal Ball f_{CB} and the width of the Gaussian k_{GA} with respect to σ_{CM} are constant. The main difference using the MVA calibration are in the position of the peak of the Crystal Ball and in the resolution. The peak position is very close to the true value (Fig. 6.11a), with maximum variation of 100 MeV, while using the standard calibration the peak is shifted by 200-600 MeV. The perfect position of the peak is not very important for the analysis because thanks to the signal parametrization the shift between the true mass and the peak position is known. By the way this shift is known only from MC simulation, so small shift are desirables. As before the resolution is improved in particular for converted photons. The α_{CB} (Fig. 6.11c) is usually larger with the MVA, meaning that the Crystall Ball has a more Gaussian behaviour. This is confirmed by the fraction of the Crystall Ball (Fig. 6.11e), in particular for the unconverted central category it was necessary to limit the fraction of Crystall Ball to be a least 90%; without this limit the fit converges to a pure Gaussian without the Crystall Ball component.

Despite of the performance improvement of the MVA calibration, the study of the systematics uncertainties on the energy scale using this new calibration is not completed, even if no large difference with the one computed from the standard calibration is

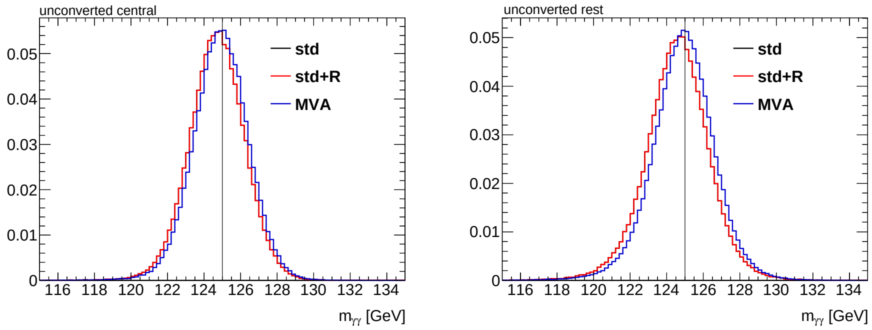

(a) unconverted central **(b)** unconverted rest

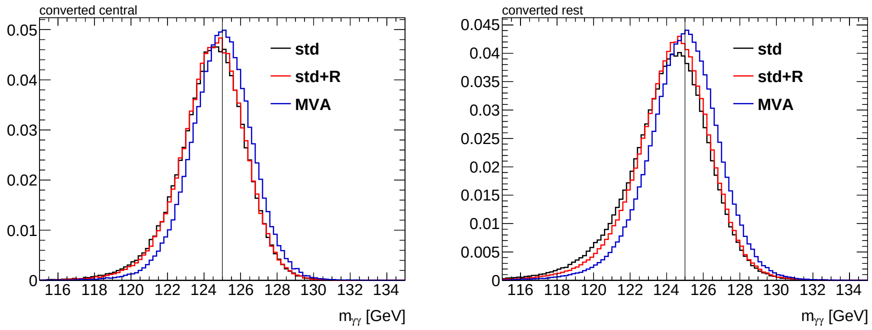

(c) converted central **(d)** converted rest

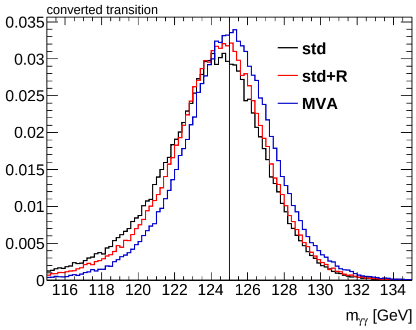

(e) converted transition

Figure 6.8: Distribution of $m_{\gamma\gamma}$ for the EPS categories using the standard calibration (std), standard calibration corrected for the radius of conversion (std+R) and the MVA calibration.

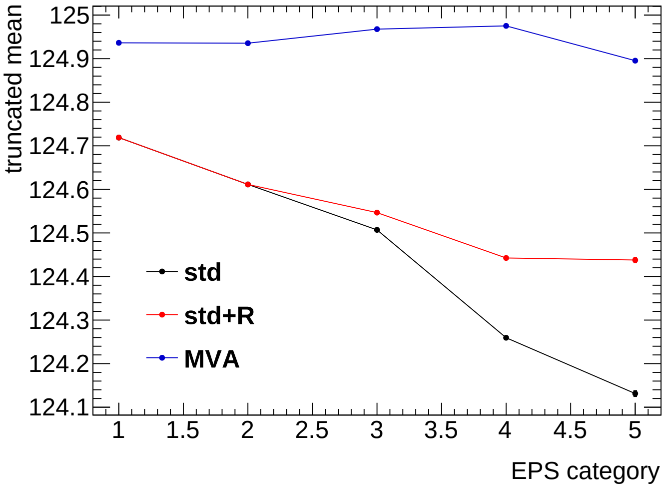

Figure 6.9: Truncated mean for of the $m_{\gamma\gamma}$ distribution using the standard calibration (std), standard calibration corrected for the radius of conversion (std+R) and the MVA calibration. The x-axis labels the EPS categories: unconverted central (1), unconverted rest (2), converted central (3), converted rest (4), converted transition (5).

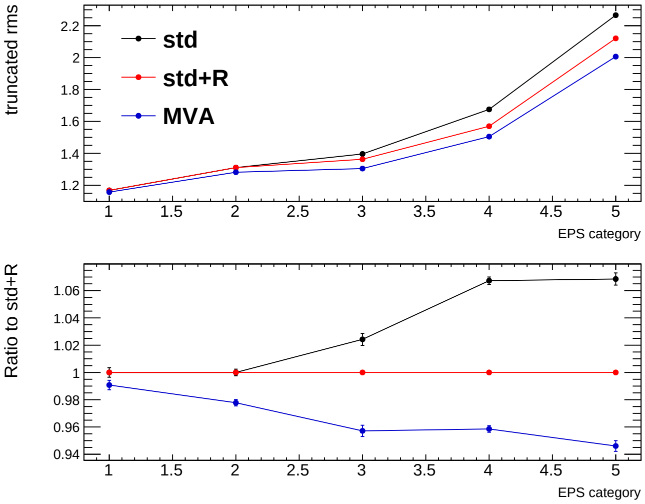

Figure 6.10: Truncated RMS for of the $m_{\gamma\gamma}$ distribution using the standard calibration (std), standard calibration corrected for the radius of conversion (std+R) and the MVA calibration. The x-axis labels the EPS categories: unconverted central (1), unconverted rest (2), converted central (3), converted rest (4), converted transition (5). The bottom plot shows the improvement as a ratio with respect to the standard calibration corrected for the radius of conversion.

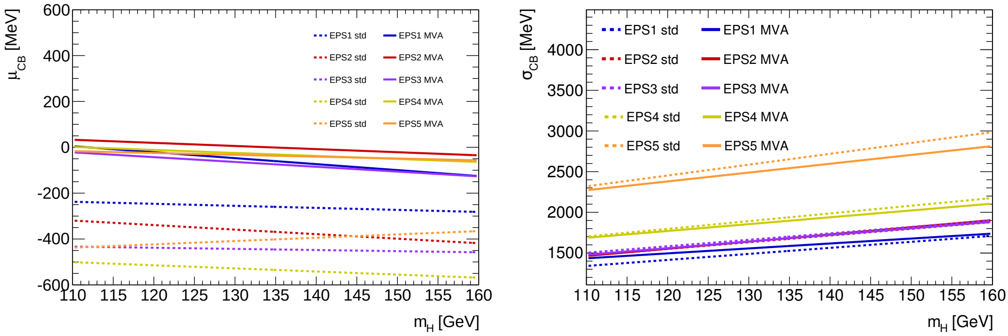

(a) μ_{CB} **(b)** σ_{CB}

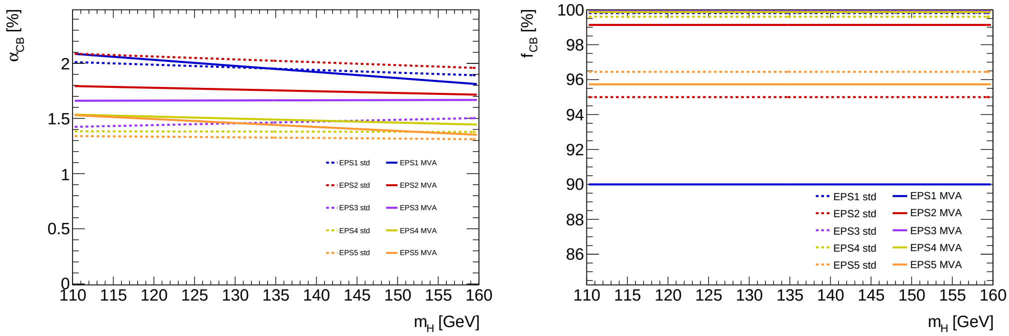

(c) α_{CB} **(d)** f_{CB}

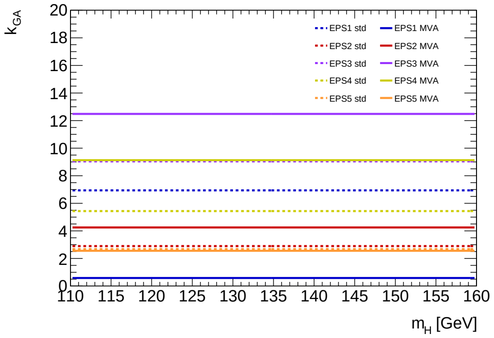

(e) k_{GA}

Figure 6.11: Global parametrization for the gluon-gluon signal. The parameters describing the signal model are parametrized as function of the true mass m_H. Dotted line are for the standard calibration, solid line using the MVA calibration. f_{CB} is forced to be $\geq 90\%$.

expected. For this reason the MVA calibration is not used for the Higgs analysis yet and its usage is postponed to 2013 analyses.

6.4.3 Background modelling

The model of background events is crucial to the robustness of the analysis since the signal to background ratio in the $H \to \gamma\gamma$ is relatively small. For statistical analysis of the measured diphoton spectrum, the background is parametrized by an analytic function for each category, where the normalization and the shape are obtained from fits to the data diphoton invariant mass distribution in the 100-160 GeV diphoton invariant mass range. Different parametrizations are chosen for the different event categories to achieve a good compromise between limiting the size of a potential bias introduced by the chosen parametrization and retaining good statistical power. Depending on the category, an exponential function, a fourth-order Bernstein polynomial [121] or the exponential of a second-order polynomial is used. The inclusive data sample background is modelled by a fourth-order Bernstein polynomial. The shape of the background is obtained from data, but the functional forms of the parametrizations used to perform the fits are selected before looking at data.

Potential biases from the choice of background parametrization are estimated using three different sets of high statistics background-only MC models. The prompt diphoton background is obtained from the three generators RESBOS [122], DIPHOX [123] and SHERPA [124], while the same reducible background is used for all three models, based on SHERPA for the gamma-jet component and on PYTHIA6 [97] for the jet-jet background. The Drell-Yan component is also taken into account. SHERPA and PYTHIA are particle-level generator with full fragmentation and hadronisation. RESBOS and DIPHOX are parton-level generator, therefore a full detector simulation and reconstruction is not possible. All experimental effects are thus introduced through effective parametrizations. The relative amount of diphoton, photon-jet and di-jet backgrounds are taken from data-driven estimation, as described in section 6.5.

The potential bias for a given parametrization is estimated by performing a maximum likelihood fit in the mass range of 100–160 GeV using the sum of a signal and the background parametrization to all three sets of background-only simulation models for each category. The signal shape is taken to follow the expectation for an SM Higgs in terms of shape, with a mass between 110 GeV and 150 GeV, and with the normalization floating. The categories mainly affected by background parametrization bias are the high-statistics categories, which also have a lower signal to background ratio. Parametrizations that exhibit problems with fit convergence are discarded. Parametrizations for which the estimated potential bias is smaller than 20% of the uncertainty on the fitted signal yield, or where the bias is smaller than 10% of the number of expected signal events for each of the background models are selected for further studies. Among these selected parametrizations, the parametrization with the best expected sensitivity at $m_H = 125$ GeV is selected as the background parametrization. For categories with low statistics, an exponential function is found to have sufficiently small bias, while polynomials and exponentials of polynomials, respectively, are needed for limiting the potential bias to stay within the predefined requirements for the higher-statistics categories.

The systematic uncertainty on the background model is defined as the largest absolute signal component fitted anywhere in the full mass range studied with a SHERPA sample.

6.5 Background decomposition

The main backgrounds to the $H \to \gamma\gamma$ are: the irriducible diphoton from QCD, the associated production of a photons with jets and processes with several jets in the final state. The last two contribute to the background when one or two jets fragmenting into neutral mesons (mainly π^0) are misidentified as photons. The background component are called $\gamma\gamma$, γj and jj. Another minor background component is due to the misidentification of electrons as photons, which mostly arises when electrons are also reconstructed as converted photons. The tail of the $Z \to ee$ mass peak, which is just below the mass region of interest, is the source for this background. Its electrons have an isolation profile similar to that of signal photons. This background has been estimated with a data driven method using the misidentification rates measured by using $Z \to ee$ data events reconstructed as dielectron and e-γ pairs. For the $\sqrt{s} = 7\,\text{TeV}$ data, the Drell-Yan background in the mass region (100 - 160) GeV is estimated to be $N_{DY}^{\gamma\gamma} = 325 \pm 3(stat) \pm 30(syst)$. For the $\sqrt{s} = 8\,\text{TeV}$ data, the Drell-Yan background in the region (100 - 160) GeV is estimated to be $N_{DY}^{\gamma\gamma} = 270 \pm 4(stat) \pm 24(syst)$. The lower level of Drell-Yan background in the $\sqrt{s} = 8\,\text{TeV}$ data is due to the improvements in the reconstruction of converted photons, in particular conversion candidates with tracks reconstructed in inactive regions of the innermost pixel layer are rejected to reduce the contamination from misidentified electrons.

Four different methods have been developed to decompose observed data into its main background components ($\gamma\gamma$, γj and jj): 1×2D, 2D Template Fit, 2×2D and 4×4-matrix. To discriminate between the background sources all the methods rely on the definition of control regions using a relaxed version of the tight identification cuts and the calorimetric isolation E_T^{iso}. In the following section the "4 × 4 matrix" method is described.

In Table 6.3 the results of the background decompositions are listed. The estimations were also performed in bins of $m_{\gamma\gamma}$. The differential spectra obtained with different methods are shown in Figure 6.12.

Component	1×2D	2D Template Fit	2×2D	4×4-matrix
$\gamma\gamma + DY$	$61556 \pm 281^{+3703}_{-2852}$	55674 ± 2888	58690^{+1670}_{-2000}	$63526 \pm 305^{+1694}_{-1184}$
γj	$9658 \pm 38^{+1862}_{-2822}$	15518 ± 3165	16560^{+2150}_{-1330}	$9675 \pm 72^{+834}_{-1265}$
$j\gamma$	$3921 \pm 15^{+1961}_{-1961}$	2735 ± 327		$2336 \pm 50^{+369}_{-387}$
jj	$2295 \pm 32^{+278}_{-422}$	183^{+3079}_{-183}	2240^{+230}_{-1000}	$1849 \pm 17^{+242}_{-296}$
$\gamma\gamma$ Purity	$(79^{+5}_{-4})\%$	$(75^{+3}_{-4})\%$	$(76 \pm 3)\%$	$82.1 \pm 0.4^{+2.2}_{-1.5}\%$

Table 6.3: 8 TeV diphoton sample composition estimated from four different methods. The first error denotes the statistical uncertainty, the second the systematic uncertainty. In the 2x2D and 1x2D sideband methods, the number of events is constrained to the number of candidates observed in the identified-isolated photon pairs sample. This is not the case in the 2D template fit, where the number of events is constrained to the number of identified photon pair candidates before applying the isolation cut. The 4×4-matrix method conserves the number of events both before and after the isolation requirement.

The study of the sample composition demonstrates a good understanding of the diphoton selection efficiency with good agreement with theoretical predictions, even if these predictions are affected by a large uncertainty. As described in section 6.4.3 the background is parametrized with only one component an then the Higgs boson

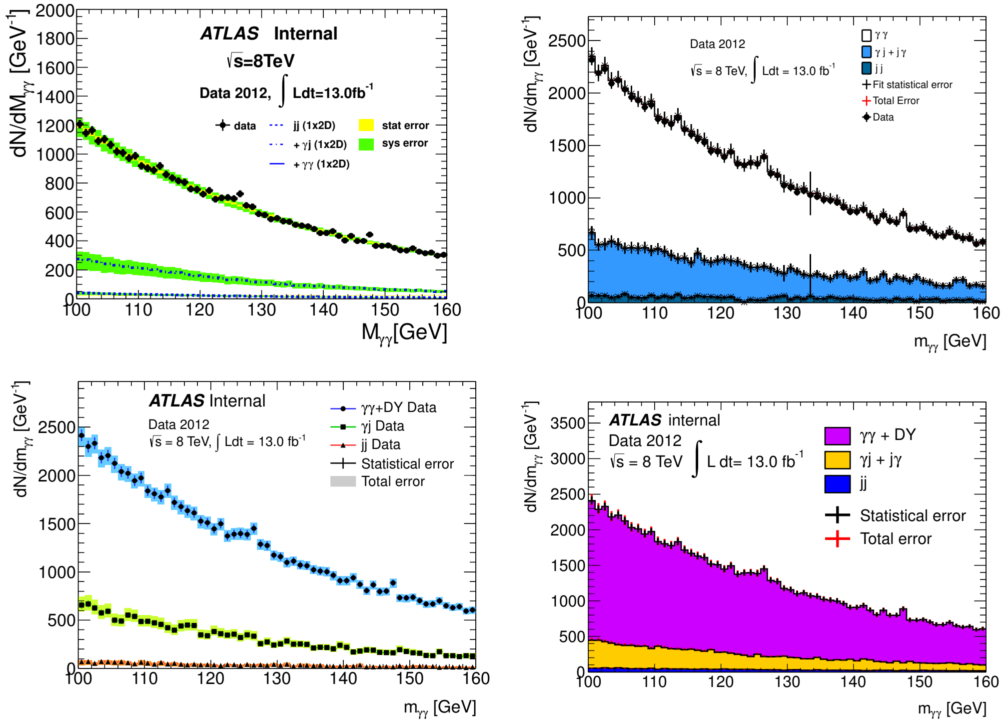

Figure 6.12: 8 TeV diphoton sample composition as a function of the invariant mass. The results obtained with the different methods are shown in the following order: 1x2D sideband method, 2D template fit, 2x2D sideband method and 4 × 4 matrix method. The results of the different methods are compatible with each other. The DY background is estimated as part of the $\gamma\gamma$ component. The numbers per bin are divided by the bin size.

search analysis and its properties measurement do not rely on the determination of the background composition.

6.5.1 4×4 matrix method

Since, as the other methods, the 4×4 matrix method relies on isolation control region the used sample is the set of events passing the analysis selection except the isolation cut. Each event, with both photon candidates satisfying the identification criteria, is classified according to whether the photons pass (P) or fail (F) the isolation requirement, resulting in four different categories called: PP, PF, FP, FF. This classification information is translated into four event weights $W_{\gamma\gamma}, W_{\gamma j}, W_{j\gamma}, W_{jj}$, which describe how likely the event is to belong to each of the four final states, $\gamma\gamma$, γj, $j\gamma$ and jj (the difference between γj and $j\gamma$ is that in the first case the γ is the leading candidate).

This translation is done through a 4×4 probability matrix which has been filled using the efficiency of the isolation cut on prompt and fake photons. The main advantages of this method with respect to the others is that it is applied event-by-event, so for example it is easy to decompose the distribution of any observable (e.g. $m_{\gamma\gamma}$, p_{Tt}, …). Once the weights have been computed for all the events, the number of events corresponding to each background component can be obtained through sums of weights. The connection between the pass/fail outcome and the weights is:

$$N = \begin{pmatrix} N_{PP} \\ N_{PF} \\ N_{FP} \\ N_{FF} \end{pmatrix} = \mathbf{E} \begin{pmatrix} W_{\gamma\gamma} \\ W_{\gamma j} \\ W_{j\gamma} \\ W_{jj} \end{pmatrix} = \mathbf{E}W \tag{6.9}$$

Using the event-by-event approach, N is a boolean vector (e.g. for an event where both candidates are isolated it is $(1,0,0,0)$). $\mathbf{E}$ is a 4×4 matrix, whose coefficients give the probability that a given final state produces a certain pass/fail status using the efficiencies and the fake rates. Since the efficiency and the fake rates depends on $|\eta|$ and p_T of the candidates the matrix is computed event-by-event. If there were no correlation between the isolation transverse energies of the two candidates, it would have the form:

$$\mathbf{E} = \begin{pmatrix} \varepsilon_1\varepsilon_2 & \varepsilon_1 f_2 & f_1\varepsilon_2 & f_1 f_2 \\ \varepsilon_1(1-\varepsilon_2) & \varepsilon_1(1-f_2) & f_1(1-\varepsilon_2) & f_1(1-f_2) \\ (1-\varepsilon_1)\varepsilon_2 & (1-\varepsilon_1)f_2 & (1-f_1)\varepsilon_2 & (1-f_1)f_2 \\ (1-\varepsilon_1)(1-\varepsilon_2) & (1-\varepsilon_1)(1-f_2) & (1-f_1)(1-\varepsilon_2) & (1-f_1)(1-f_2) \end{pmatrix} \tag{6.10}$$

where ε_i and f_i ($i = 1,2$ for the leading/sub-leading candidate) are the probabilities that a signal or a fake photon respectively pass the isolation cut:

$$\varepsilon = \Pr(\underbrace{\text{pass isolation}}_{P} \,|\, \underbrace{\text{true photon}}_{\gamma}) \qquad f = \Pr(\underbrace{\text{pass isolation}}_{P} \,|\, \underbrace{\text{true jet}}_{j})$$

As an example combining (6.10) and (6.9):

$$N_{PP} = \varepsilon_1\varepsilon_2 W_{\gamma\gamma} + \varepsilon_1 f_2 W_{\gamma j} + f_1\varepsilon_2 W_{j\gamma} + f_1 f_2 W_{jj}$$

Due to the correlation between the isolation E_T^{iso} of the two candidates (especially when both are fake photons), the matrix coefficients in equation (6.10) must be corrected introducing conditional efficiencies and fake rates, depending on the pass/fail status of the other (called "tag") candidate in the candidate pair. For example:

$$f_1 f_2 \rightarrow \frac{1}{2}\left[f_1 f_2^{(P_1)} + f_1^{(P_2)} f_2\right]$$

or:

$$f_1(1-f_2) \rightarrow \frac{1}{2}\left[f_1(1-f_2^{(P_1)}) + f_1^{(F_2)}(1-f_2)\right]$$

where:

$$f_2^{(P_1)} = \Pr(P_2|j_2, P_1) \qquad f_1^{(P_2)} = \Pr(P_1|j_1, P_2) \qquad f_1^{(F_2)} = \Pr(P_1|j_1, F_2)$$

The efficiencies ε and fake rates f are extracted from collision data, as a function of $|\eta|$ and p_T, and for all possible conditions of the "tag" photon, as described in the following.

First, a control region is defined by all photon candidates failing the standard tight selection used in the analysis, but passing a looser selection called loose′, defined in a similar way to the tight one, but without applying some of the strips shower shape cuts. The choice of cuts to be relaxed is a compromise between having a little photon leakage into the control region and avoiding variables too correlated with E_T^{iso}. This sample, called non-tight ($\tilde{T}$), is enriched in fake photons, although a small component of prompt photons is present. Another control region is defined by an anti-isolation ($\tilde{I}$) criterion: $7\,\text{GeV} < E_T^{\text{iso}} < 25\,\text{GeV}$, in order to ensure that it be essentially free of prompt photons.

Then, the photon candidates in the complete sample are counted according to their conditions, i.e. whether they pass the tight identification selection (T) or the non-tight selection ($\tilde{T}$), and whether they are isolated (I) or anti-isolated ($\tilde{I}$). Some basic assumptions are needed:

- the ratio α of prompt photons going into $\tilde{T}$ and T is independent of isolation status:

$$\alpha = \frac{n_\gamma^{\tilde{T}}}{n_\gamma^{T}} = \frac{n_\gamma^{\tilde{T}I}}{n_\gamma^{TI}} = \frac{n_\gamma^{\tilde{T}\tilde{I}}}{n_\gamma^{T\tilde{I}}} \tag{6.11}$$

  (α being expected to be small, but actually it is not negligible)

- the ratio β of fake photons going into T and $\tilde{T}$ is independent of isolation status:

$$\beta = \frac{n_j^{T}}{n_j^{\tilde{T}}} = \frac{n_j^{TI}}{n_j^{\tilde{T}I}} = \frac{n_j^{T\tilde{I}}}{n_j^{\tilde{T}\tilde{I}}} \tag{6.12}$$

- the $\tilde{I}$-region is chosen to be enough anti-isolated, that there are no prompt photons in it: therefore $0 = n_\gamma^{\tilde{I}} = n_\gamma^{T\tilde{I}} = n_\gamma^{\tilde{T}\tilde{I}}$, and β can be computed from data: $\beta = n^{T\tilde{I}}/n^{\tilde{T}\tilde{I}}$

From these counts the prompt and fake photon yields n_γ^X, n_j^X may be evaluated for any region X. The relation:

$$n_\gamma^T = n^T - n_j^T = n^T - \beta n_j^{\tilde{T}} = n^T - \beta\left(n^{\tilde{T}} - n_\gamma^{\tilde{T}}\right) = n^T - \beta\left(n^{\tilde{T}} - \alpha n_\gamma^T\right) \tag{6.13}$$

can be solved for n_γ^T, and a similar one for n_γ^{TI}, giving:

$$n_\gamma^T = \frac{n^T - \beta n^{\tilde{T}}}{1-\alpha\beta} \qquad n_\gamma^{TI} = \frac{n^{TI} - \beta n^{\tilde{T}I}}{1-\alpha\beta} \tag{6.14}$$

Then, $n_j^X = n^X - n_\gamma^X$, therefore:

$$n_j^T = \frac{\beta}{1-\alpha\beta}\left(n^{\tilde{T}} - \alpha n^T\right) \qquad n_j^{TI} = \frac{\beta}{1-\alpha\beta}\left(n^{\tilde{T}I} - \alpha n^{TI}\right) \tag{6.15}$$

Finally, the ε, f-coefficients are evaluated as:

$$\varepsilon = \frac{n_\gamma^{TI}}{n_\gamma^T} = \frac{n^{TI} - \beta n^{\tilde{T}I}}{n^T - \beta n^{\tilde{T}}} \tag{6.16}$$

$$f = \frac{n_j^{TI}}{n_j^T} = \frac{n^{\tilde{T}I} - \alpha n^{TI}}{n^{\tilde{T}} - \alpha n^T} \tag{6.17}$$

Notice that, while ε is completely data-driven, f needs α as an external input from MC simulation, in particular it is extracted from a Sherpa sample. The values of α range from $\alpha \sim 0.05$ for $p_T \approx 100$ GeV to $\alpha \sim 0.1$ for $p_T \simeq 20$ GeV, and show an increase up to $\alpha \sim 0.14$ in the region $|\eta| > 1.81$.

The diphoton signal yield in the selected diphoton sample can be computed as a sum of weights running over all events with both photons satisfying the tight selection:

$$N_{\gamma\gamma} = \sum_k w^{(k)} \pm \sqrt{\sum_k \left[w^{(k)}\right]^2} \tag{6.18}$$

where the weight $w^{(k)}$ for the k-th event is:

$$w^{(k)} = W_{\gamma\gamma}^{(k)}\, \varepsilon_1^{(k)} \varepsilon_2^{(k)} \tag{6.19}$$

and the sum over k is carried out on the events in a given bin of invariant mass. Similar expressions hold for $N_{\gamma j}$, $N_{j\gamma}$, N_{jj}.

The main sources of systematic errors are:

- the definition of the non-tight control sample: estimated by changing the number of released strips cuts from 4 (default) to 2 or 5,
- the statistics used to compute the E_T^{iso} distributions, and hence the precision of the matrix coefficients: quantified by increasing and decreasing the ε, f parameters by their statistical errors, and recomputing the signal yield: the variations are then added in quadrature,
- the choice of the $7 < E_T^{\text{iso}} < 25$ GeV to normalize the non-tight sample before subtraction: estimated by moving the lower boundary to 6 GeV and 10 GeV, and the upper boundary to 20 GeV and 35 GeV.

6.6 Systematic uncertainties

All systematics are treated as fully correlated between 7 and 8 TeV data except for the uncertainty on the luminosity. The uncertainties can affect either the signal yield (section 6.1), the signal resolution (section 6.2) or the migration of events in between categories (section 6.3). Finally additional systematics are derived for the mass measurement (section 6.4). The systematics from the background modeling (the spurious signal) has already been described in section 6.4.3.

6.6.1 Systematic uncertainties on the signal yield

The systematics affecting the signal yield (see table 6.4) comes from the uncertainty on the luminosity, on the efficiencies (trigger, identification, isolation, kinematics), on the theoretical error on the production cross section and the branching ratio. The largest experimental systematic uncertainty comes from the identification efficiency uncertainty.

Systematic uncertainties	$\sqrt{s} = 7\,\text{TeV}$ [%]	$\sqrt{s} = 8\,\text{TeV}$ [%]
Luminosity	3.9	3.6
Trigger efficiency	1	0.5
Photon identification efficiency	8.4	5.3
Isolation efficiency	0.4	1
Photon energy scale	0.3	0.4
Higgs cross section (perturbative)	$gg \to H$: $^{+12}_{-8}$ VBF: ± 0.3 WH: $^{+0.2}_{-0.8}$ ZH: $^{+1.4}_{-1.6}$ $t\bar{t}H$: $^{+3}_{-9}$	$gg \to H$: $^{+7}_{-8}$ VBF: ± 0.2 WH: $^{+0.2}_{-0.6}$ ZH: $^{+1.6}_{-1.5}$ $t\bar{t}H$: $^{+4}_{-9}$
$gg \to H$ contribution to the two-jets cat.	± 25	high-mass: ± 25 low-mass: ± 30
Higgs cross section (PDF+α_S)	gg: $^{+8}_{-7}$, VBF: $^{+2.5}_{-2.1}$, VH: ± 3.5, $t\bar{t}H$: ± 9	gg: $^{+8}_{-7}$, VBF: $^{+2.6}_{-2.8}$, VH: ± 3.5, $t\bar{t}H$: ± 8
Branching fraction	$5.9(110\,\text{GeV}) \div 2.1(150\,\text{GeV})$	

Table 6.4: Systematic uncertainties affecting the signal yield.

6.6.2 Systematic uncertainties on the signal resolution

The systematics affecting the signal resolution (see table 6.5) used in the signal parametrization come from the calorimeter energy resolution uncertainty (due to the uncertainty on the constant term), extrapolation of the electron calibration to photons due to the simulation of the material upstream of the calorimeter, possible pile-up mis-modelling. The uncertainty associated with the primary vertex selection is negligible (smaller than 0.2%) and it is neglected. The resulting relative uncertainty on the mass resolution is 14%, which is applied to both the Crystal Ball width and the wide Gaussian width in a correlated way.

Systematic uncertainties	$\sqrt{s} = 7\,\text{TeV}$	$\sqrt{s} = 8\,\text{TeV}$
Energy resolution uncertainty	12 %	12 %
Extrapolation from the electron calibration	6%	6%
Pile-up mis-modelling	4%	1.5%

Table 6.5: Systematic uncertainties affecting the signal resolution.

6.6.3 Migration of signal events between categories

Since the analysis divides the events in several categories described in section 6.3 the number of events in each category is affected by the uncertainties on the variables used to define such categories. The main are from the mismodelling of the p_{Tt} of the signal, the jet energy scale, migration between converted and unconverted photons due to material and pileup, the JVF cut, underlying event, lepton identification and efficiency. Different effects affect different categories in different way (see table 6.6).

Systematic unc.	$\sqrt{s} = 7\,\text{TeV}$	$\sqrt{s} = 8\,\text{TeV}$
underlying event	6% ÷ 30% depending on the production	
pileup	3% (unconv.)	2% (unconv.)
	2% (conv.)	2% (conv.)
	2% (VBF)	12% (VBF)
jet enegy scale	18% (VH), 4% (others)	
p_{Tt}	1.3% (low-p_{Tt})	
	10% (high-p_{Tt})	
	8.6% (VBF)	
	11% (VH)	
	0.45% (lepton)	
mat. mismodelling	4% (unconverted), 3.5% (converted)	
JVF cut	18% (VH), 12% (VBF)	
e rec. and identif.		2% (lepton)
e energy scale		$<$ 1% (lepton)
μ reconstruction		$<$ 1% (lepton)
tracker resolution		$<$ 1% (lepton)
μ resolution		2% (lepton)

Table 6.6: Systematic uncertainties affecting the migration between categories. Inside the parenthesis the name of the affected category.

6.6.4 Systematic uncertainties on mass measurement

Many effects can bias the mass peak position (see table 6.7 for a full list): effect from the uncertainty on the presampler scale (5% in the barrel, 10% in the end-caps), uncertainty on the material effects on photons, extrapolation of the electron energy scale to photons. These systematic uncertainties amount to a total effect of 0.45% (550 MeV) for an invariant mass $\sim$ 125 GeV. In addition for this analysis more uncertainties have been introduced: non-linearities of the EM calorimeter electronics, corrections for lateral energy leakage out of the cluster, effects from the uncertainties on the resolution, migration between converted and unconverted (see Fig. 6.13), relative calibration of the first and second sampling (E_1/E_2) of the electromagnetic calorimeter, angle measurement and calorimeter and tracker misalignment, background modelling. These additional uncertainties on the mass measurement, treated as uncorrelated, amount to a total of 0.25% (350 MeV). The total systematic uncertainty on the mass determination from both category dependent and overall uncertainties is estimated to be 0.5% (650 MeV).

6.7 Results

The statistical procedures used to test the background-only hypothesis and to set exclusion limits and the procedure do exclude the background hypothesis and set a discovery significance are described in detail in appendix A. The results are quantified by the compatibility probability between the observed data and the models described in 6.4 based on SM Higgs boson signal and a background description from the data. Here the

Systematic uncertainties	
presampler scale	0.1%
material effects	0.3%
extrapolation from electron	0.3%
Additional systematics uncertainties	
non-linearities of the EM cal. electronics	0.15%
lateral energy leakage	0.1%
uncertainties on the resolution	0.15%
migration beween converted and unconverted	0.13%
E_1/E_2	0.2%
angle misalignment	0.03%
background modelling	0.1%

Table 6.7: Systematic uncertainties affecting the mass measurement. The additional systematics uncertainties are not treated as category-dependent. These systematics are used in both datasets.

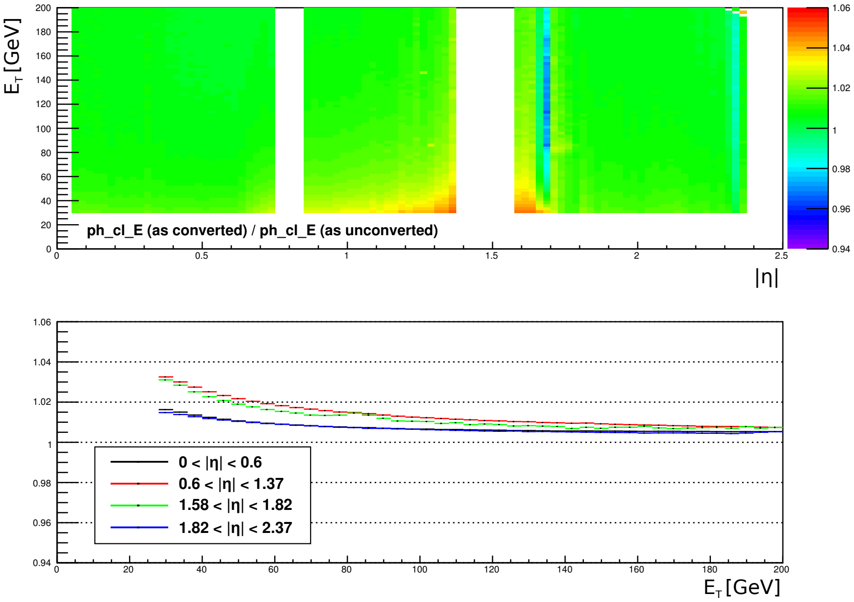

Figure 6.13: Ratio between the energy calibrated as converted photon with the energy calibrated as for unconverted photons.

results are presented separately for the exclusion limit of the SM Higgs boson and for the discovery. This result uses different test statistics based on the profiled likelihood ratio λ.

6.7.1 Exclusion limits

Different signal+background hypotheses are tested changing the values of a strength parameter μ, defined as the ratio of the signal rate (cross section) being tested to that predicted by the SM. That is, $\mu = 0$ correspond to the background-only hypothesis and $\mu = 1$ is the presence of a SM Higgs. At fixed values of the Higgs boson mass m_H, different values of μ are tested using a statistic based on the profile likelihood ratio. This statistic depends on the parameter of interest μ as well as nuisance parameters that characterize the systematic uncertainties described above. Exclusion limits on the Higgs boson production cross section for the decay into two photons are determined using the CLs procedure [125] at 95% confidence level (CL), results are in figure 6.14. The Standard Model Higgs boson ($\mu = 1$) is excluded in the mass regions from 110 to 122.5 GeV and 129.5 to 144.5 GeV. The limit can however not be applied to a second boson since the fit assumes only one contribution.

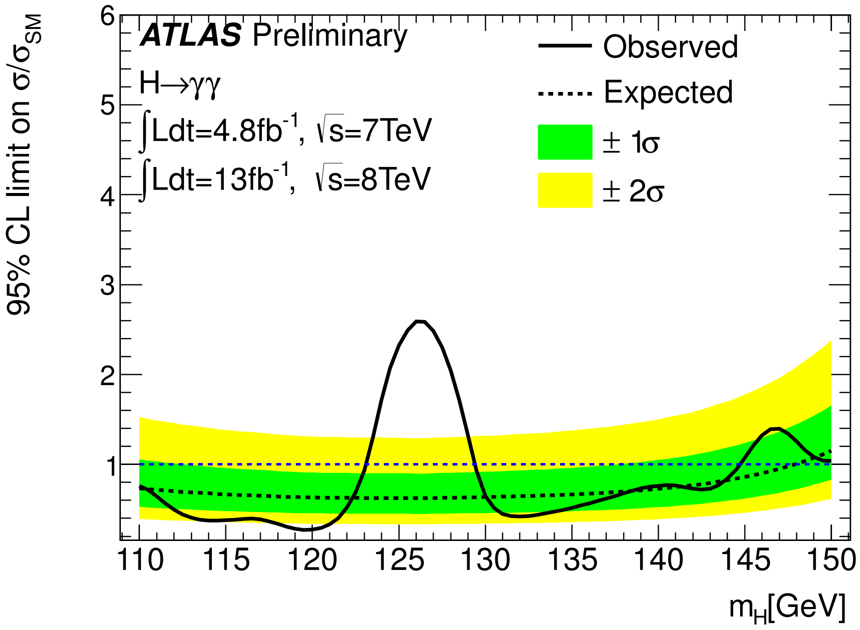

Figure 6.14: The observed 95% CL exclusion of value of μ as a function of mH and the expected (dashed) corresponding to the background-only hypothesis, from the combination of the 7 and 8 TeV data.

6.7.2 Discovery significance

To quantify discovery significance, the p-value of the background-only hypothesis, p_0, is reported. This quantity gives the fraction of background-only experiments which would have a profile likelihood ratio of the zero signal hypothesis relative to the best-fitted signal strength at least as low as the one found in the data. Equivalently, this can be expressed using the discovery significance $Z_0 = \Phi^{-1}(1 - p_0)$, where Φ^{-1} is the standard Gaussian quantile. The p-value is extracted from the distribution of the profile likelihood ratio using the asymptotic approximation [126].

The observed local p_0 values as a function of m_H, as well as the expected p_0 values corresponding to a SM Higgs boson signal plus background hypothesis, are shown in Fig. 6.15. The largest local significance in the combination of 7 TeV data and 8 TeV data is found to be 6.1 σ, corresponding to $p_0 = 4.4 \times 10^{-10}$ at $m_H = 126.5$ GeV, where the expected significance is 3.3σ. The diphoton mass scale systematics (MSS) uncertainty is not included in the evaluation of p_0 value, and a modest reduction in the observed significance at a level of 0.1σ is expected if it were accounted for. Both 7 TeV and 8 TeV data show excesses around $m_H = 126.5$ GeV: the largest observed (expected) local significance for the 7 TeV data is 3.3σ (1.6σ), at $m_H = 126.0$ GeV, while the largest observed (expected) local significance for the 8 TeV data is 5.1σ ($2.9\ \sigma$) at $m_H = 126.5$ GeV. Taking into account the look-elsewhere effect in the mass range 100–150 GeV, the global significance of the excess is 5.4σ, corresponding to $p_0 = 2.8 \times 10^{-8}$ and confirms the observation of the new particle reported in [30] where all the studied Higgs decays are combined. This is the first time the observation of the new boson compatible with the SM Higgs boson is established in the diphoton channel alone [8].

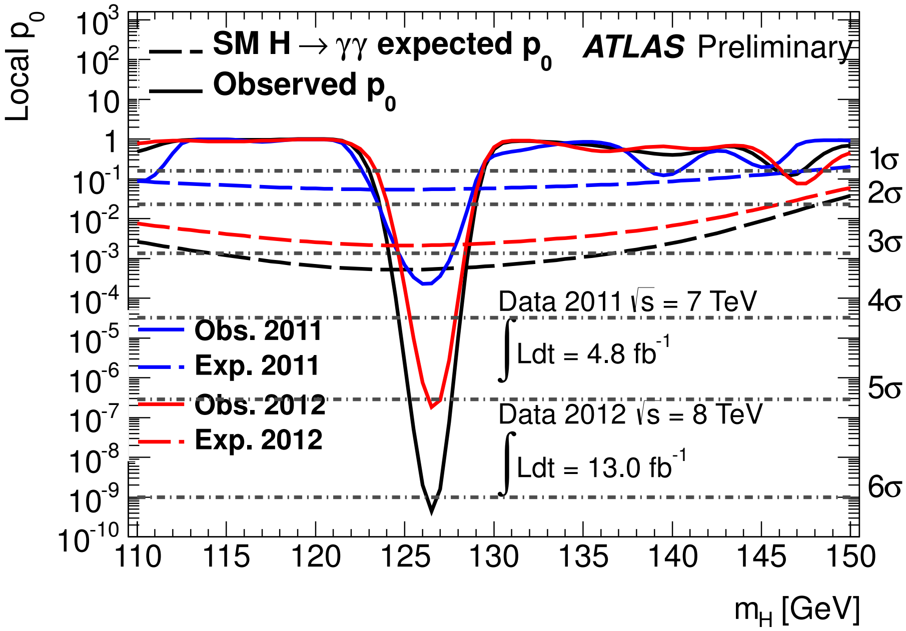

Figure 6.15: The observed local p_0 value as a function of the Higgs mass for the 7 TeV data (solid blue), 8 TeV data (solid red), and their combination (solid black). The corresponding expected local p_0 values for the SM Higgs boson signal plus background hypothesis are shown by the dashed curves.

6.7.3 Mass and signal strength of the excess

The parameter of interest in the test statistic is changed to m_H in order to estimate the mass of the observed new particle, and the signal strength parameter μ is treated here as a nuisance parameter without any constraint. To take into account the photon energy scale uncertainty and other uncertainties that affect the position of the diphoton mass peak (section 6.6), the diphoton mass scale uncertainties are included in the likelihood. The best-fit for the mass value is $m_H = 126.6 \pm 0.3(stat) \pm 0.7(syst)$GeV from the combination of 2011 and 2012 datasets. The statistical error on the measurement is evaluated by fixing all the nuisance parameters, with the exception of the signal strength and the background shape parameters. The dominant systematic uncertainty on the mass measurement is the absolute photon energy scale. The compatibility between the mass from the various category treated separately has been checked.

The best-fit values of m_H and μ, and the corresponding 68% and 95% CL contours are shown in Fig. 6.16. The impact of the systematic uncertainty, and in particular of the diphoton mass scale uncertainty, on the precision of the measurement is shown by the modified 68% and 95% CL contours when these systematic uncertainties are removed (Fig. 6.16). At the best-fit $m_H = 126.6\,\text{GeV}$, $\hat{\mu}$ is found to be $1.80 \pm 0.30(\text{stat})^{+0.21}_{-0.15}(\text{syst})^{+0.20}_{-0.14}(\text{theory})$ which is a 2.4 standard deviations from the SM expectation.

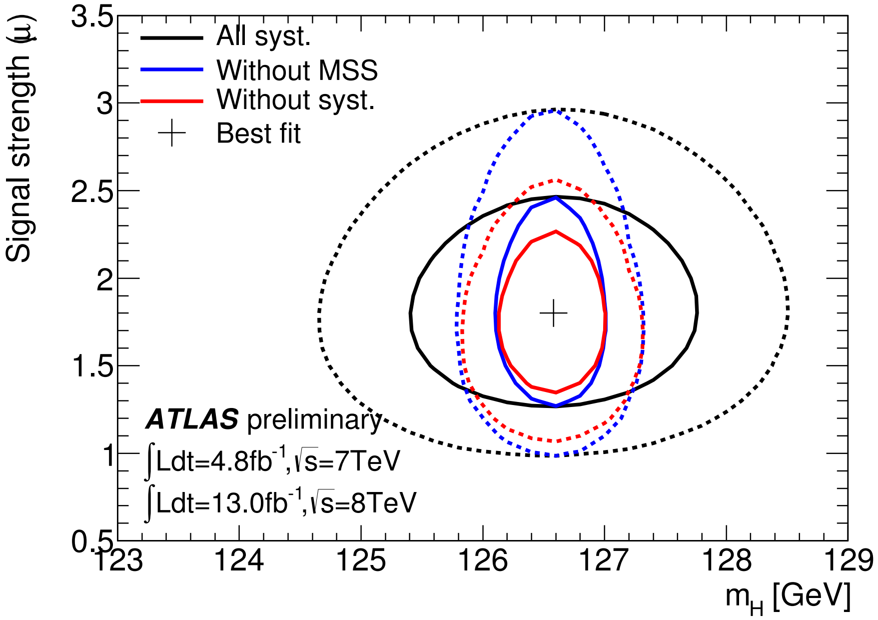

Figure 6.16: The best-fit values of m_H and μ, and the corresponding 68% (solid black) and 95% (dashed black) CL contours. The modified 68% (solid) and 95% (dashed) CL contours when the diphoton mass scale uncertainty MSS (blue) or all the systematic uncertainties (red) are removed are also shown.

The consistency or a deviation of the production and decays of the new particle with the expectation for the SM Higgs boson need to be assessed by quantifying the signal yields in different production modes and decay channels. The categories introduced in the $H \to \gamma\gamma$ analysis not only improve the sensitivity to the SM Higgs boson signal but can also provide some discrimination between different production modes. For example the introduction of low mass di-jet and lepton tagged categories greatly enhanced the sensitivity to the VH production modes. The $t\bar{t}H$ mode remains largely unconstrained due to the limited statistics and therefore is analysed together with the gluon-fusion mode in the following measurements. A profile likelihood ratio using $(\mu_{ggH} + \mu_{t\bar{t}H}, \mu_{\text{VBF}} + \mu_{\text{VH}})$ as parameters of interest is used as test statistic. The 68% and 95% CL contours are shown in Figure 6.17 where the Higgs boson mass is fixed to 126.6 GeV. The results do not show any significant deviation with respect to the SM prediction. Figure 6.18 show the breakdown for the total μ for all the categories for the 8 TeV data.

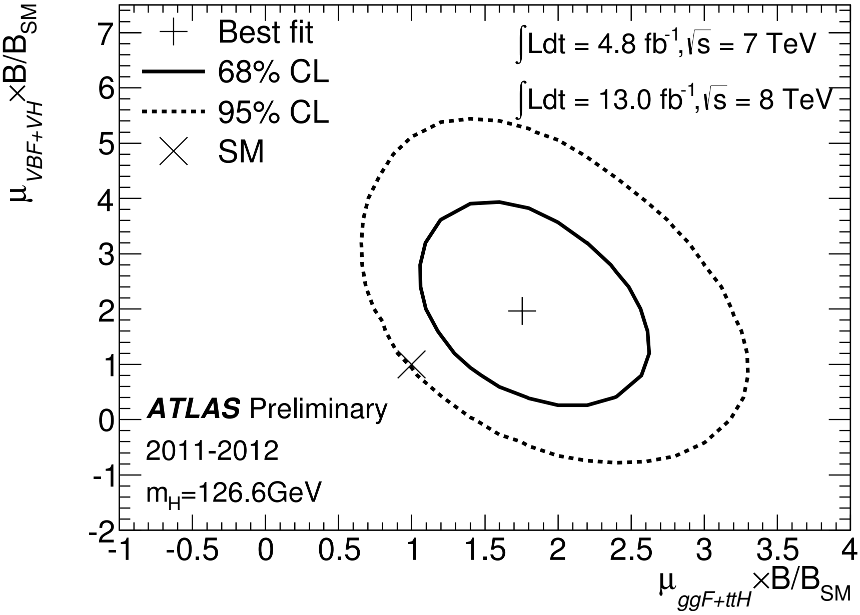

Figure 6.17: The best-fit values (+) of $\mu_{ggF+t\bar{t}H} \times B/B_{\text{SM}}$ and $\mu_{\text{VBF+VH}} \times B/B_{\text{SM}}$ where B is the $H \to \gamma\gamma$ branching ratio, and their 68% (solid) and 95% (dashed) CL contours.

6.7.4 Spin

The observation of a resonance in the diphoton channel implies that the new particle is a boson and excludes the spin-1 hypothesis due to the Landau-Yang theorem [127, 128]. A first comparison of the smallest spin values is summarized. Two spin$^{\text{parity}}$ J^P hypotheses are compared: the 0^+ SM Higgs boson and a graviton-like spin-2 state with minimal couplings (2^+_m). Information about the spin of the new particle can be inferred from the distribution of the polar angle θ^* of the photons with respect to some given reference axis in the resonance rest frame. The chosen reference axis is the z-axis of the Collins-Soper (CS) frame [129]:

$$\cos\theta^* = \frac{(E_1 + p_{z,1})(E_2 - p_{z,2}) - (E_1 - p_{z,1})(E_2 + p_{z,2})}{m\sqrt{m^2 + p_T^2}}, \tag{6.20}$$

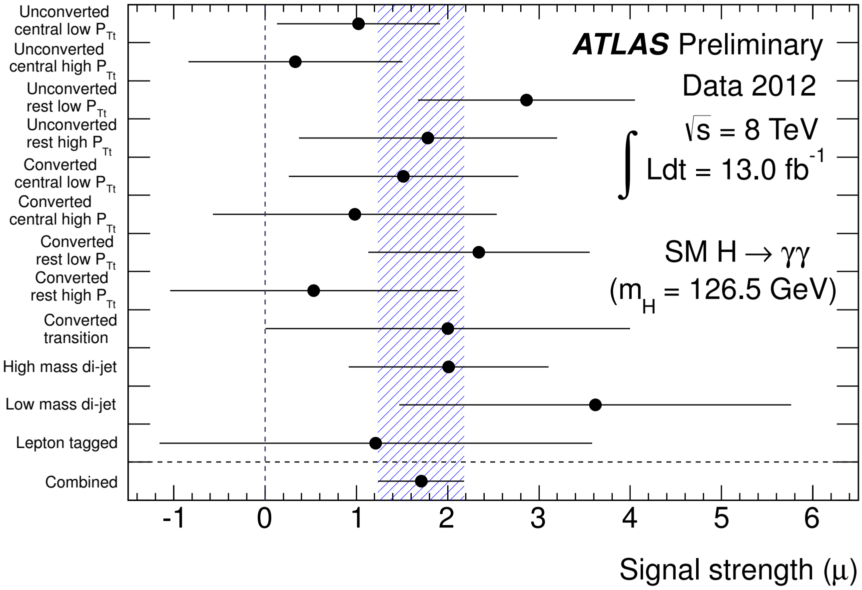

Figure 6.18: The observed signal strength μ and 1σ error for the 12 categories with 8 TeV data only.

where m and p_T are the diphoton mass and transverse momentum and $E_{1/2}, p_{z,1/2}$ are the photon energies and longitudinal momenta. For a 0^+ state, the $|\cos\theta^*|$ distribution is uniform before acceptance cuts. For a 2^+ state, the shape of this distribution depends on the specific model. The analysis is performed without categorisation, on events with diphoton invariant mass in the range [123.8,128.6] GeV which defines the signal region. The background $|\cos\theta^*|$ distribution is determined from data, with events with $m_{\gamma\gamma}$ within [115,135] GeV, but outside the signal region. The shape of the signal distributions are taken from MC simulations.

The compatibility between data and the two different hypotheses is estimated by a likelihood ratio of the 0^+ SM Higgs boson signal plus background hypothesis and the 2^+ signal plus background hypothesis. The expected p-value of a 2^+_m state signal plus background in pseudo-experiments simulating a SM Higgs boson signal plus background, is $p_{2^+_m}$ = 3.4%. The expected p-value of a SM Higgs boson signal plus background hypothesis, in a pseudo-experiment simulating a 2^+_m state signal plus background hypothesis, is p_{0^+} = 3.4%. The data favours a 0^+ state over the 2^+_m on a non-significant level , the observed p-values are: $p_{2^+_m}$ = 8.6% (1.4σ) and $p_{0^+} = 29\%$ (0.55σ).

Conclusions

This thesis focused on the search of the Higgs boson in the diphoton channel and on the energy calibration of electromagnetic particles with the ATLAS detector. Two calibrations have been presented, a simpler method already used by all the ATLAS analyses and a new method based on a multivariate technique.

The standard calibration method is based on the energy loss decomposition in: the energy loss before the calorimeter, into passive material of the calorimeter, the leakage into the hadronic calorimeter and the energy lost laterally, outside of the window used for the cluster reconstruction. All these components are estimated with parametrizations using as input the pseudorapidity, the shower depth and, for the energy lost in front, the fraction of energy in the presampler and the energy reconstructed in the accordion corrected for the other effects. Single particle Monte Carlo simulations with fixed energies have been used. Electrons, unconverted photons and converted photons have been optimized separately. The non-linearity is inside $\pm 0.5\%$ of the true energy for energies greater than 25 GeV in the barrel and 50 GeV in the endcap. Unconverted photons are the best calibrated particles because the energy lost in front is negligible. On the contrary, the worst calibrated particle are converted photons. The relative resolution, taking into account only the core of the distribution of the calibrated energy, depends on the particle, on the pseudorapidity and on the energy. For example at 50 GeV the resolution of electrons varies between 1.5% and 2.5%, except in the region at $|\eta| \sim 1.6$ where it reaches 4%. At this energy the resolution for converted photons is similar, but it is worse at lower energies. The resolution of unconverted photons of 50 GeV is between 1.5% and 2%.

To improve the calibration of converted photons a dedicated correction has been developed. This correction uses the correlation of the radius of conversion with the energy loss outside of the cluster and in front of the calorimeter. The most important effect of this correction is the reduction of the lower tail in the reconstructed energy distribution, defined as the fraction of event with calibrated energy below 95% of the true energy: for example at 100 GeV this reduction is up to 35% in the endcap.

The standard calibration is the method currently used in all the analysis. It has been shown that the only way to improve the calibration is to add additional information, as in the correction using the radius of conversion. With the present implementation it is very difficult to add new inputs, for this reason a new calibration using multivariate technique (MVA) has been developed. Many additional inputs have been considered and some new variables have been developed for this calibration. Since this is the first time such a calibration has been implemented it was chosen to use only the most important variables as input. The improvement with respect to the standard calibration is visible in all the energy ranges and in all the pseudorapidity regions and for all the particle hypotheses. Maximum improvements are in the region $|\eta| \sim 1.6$ where the improvement on the resolution for single particles is about 30%.

A good energy measurement is a key ingredient in the search for new resonances. In 2012 a new resonance, decaying in two photons and compatible with the hypothesised Higgs boson was discovered. This result is described in details in the final part of this thesis. The observation of a resonance in the search for the Higgs boson in the diphoton channel has been described. The analysed dataset corresponds to an integrated luminosity of $4.8\,\mathrm{fb}^{-1}$ collected at $\sqrt{s} = 7\,\mathrm{TeV}$ and $13.0\,\mathrm{fb}^{-1}$ collected at $\sqrt{s} = 8\,\mathrm{TeV}$. The full analysis presented at the CERN council in 2012 has been described where for the first time the observation of the SM Higgs boson is established in the diphoton channel alone. The observed significance of the excess at $m_H = 126.5\,\mathrm{GeV}$ with respect to the background-only hypothesis is 6.1σ and taking into account the look-elsewhere effect it is reduced to 5.4σ. The best-fit for the mass value is $m_H = 126.6 \pm 0.3(stat) \pm 0.7(syst)\mathrm{GeV}$. At the best-fit $m_H = 126.6\,\mathrm{GeV}$, $\hat{\mu}$ is found to be $1.80 \pm 0.30(\mathrm{stat})^{+0.21}_{-0.15}(\mathrm{syst})^{+0.20}_{-0.14}(\mathrm{theory})$.

In addition the effects of the MVA calibration on the Higgs mass reconstruction has been shown using MC simulations. The distribution of the diphoton invariant mass is more centred to the true value of the simulated Higgs mass, it is more symmetric and the resolution is improved by 4% at $m_H = 125\,\mathrm{GeV}$. For categories with two unconverted photons the improvement is $1 \div 2\%$, while for categories with converted photons the improvement is up to 6%.

The first proton-proton run ended on December 17th, 2012 and LHC is preparing for a long shutdown. A new analysis of the diphoton channel is being prepared using the whole statistics. This and future analyses will focus on the determination of the properties of this new resonance, in particular measuring the couplings with all the production modes, the mass and the spin.

The MVA calibration demonstrated that to improve the performance of the calibration additional variables have to be introduced. Many improvements can be done using different methods or introducing additional variables. The usage of new variables is subjected to a proper knowledge of the detector, in particular of the calorimeter and the shower development. For the near future this calibration has to be fully validated on data, in particular all the systematics effects have to be evaluated.

APPENDIX A

Hypothesis testing

In the search for the Higgs boson statistical hypothesis testing play a big role. In particular the final results (exclusion and discovery) are quoted in terms of probability.

The expected SM Higgs boson event yields will be generically denoted as s, backgrounds as b. It has become customary to express null results of the SM-like Higgs searches as a limit on a signal strength modifier μ that is taken to change the SM Higgs boson cross sections of all production mechanisms by exactly the same scale μ. Note that the decay branching ratios are assumed to be unchanged.

In the absence of a Higgs boson, $\mu = 0$, and for the Standard Model expectation, $\mu = 1$. Discovery is claimed when the background only hypothesis ($\mu = 0$) is rejected, and limits can be set if the discovery is not realized by the confidence level (CL) associated with the calculated value for μ. This means that two quantity are provided at the same time:

- the probability that the observed data are compatible with the background-only hypothesis
- the upper limit on the signal strenght

Usually probabilities p are quoted in terms of significance Z, usually called "number of σ", using the convention of a one-sided Gaussian tail, solving the equation:

$$p = \int_Z^\infty N(x|0,1)\,dx = \frac{1}{2}\left(1 - F_{\chi^2_1}(Z^2)\right) \tag{A.1}$$

where N is the probability density function (pdf) of the Normal distribution and $F_{\chi^2_1}$ is the cumulative density function (cdf) of the χ^2 distribution for one degree of freedom. For example 5σ significance ($Z = 5$) corresponds to $p = 2.8 \times 10^{-7}$.

A.1 Quantifying an excess

The presence of the Higgs boson is manifest as an excess in some distribution above the background, for example in the $H \to \gamma\gamma$ decay in the $m_{\gamma\gamma}$ distribution. The presence of the signal is quantified by the background-only p-value, i.e. the probability for the background to fluctuate and give an excess of events as large or larger than the observed one. The model for the null hypothesis for an unbinned analysis is proportional to a Poissonian term and it has the form of:

$$L(\boldsymbol{m}|\mu = 0, \boldsymbol{\theta}) = \mathrm{Pois}(n|b) \prod_j^n f_b(m_k|\boldsymbol{\theta}) \tag{A.2}$$

where $\boldsymbol{\theta}$ represents the nuisance parameters used to incorporate uncertainty in our background model and $\boldsymbol{m}$ is used to indicate we have a measurement of m for each of the n observed events. b is the total expected background and f_b is the pdf for the observable for the background only.

Similarly the rate and the shape for the signal are denoted s and $f_s(m)$. Thus when the signal is purely additive[1], the model for the alternate hypothesis can be written as

$$\begin{aligned} L(\boldsymbol{m}|\mu = 1, \boldsymbol{\theta}) &= \text{Pois}(n|s(\boldsymbol{\theta}) + b(\boldsymbol{\theta})) \prod_j^n f_{s+b}(m_j|\boldsymbol{\theta}) \\ &= \text{Pois}(n|s(\boldsymbol{\theta}) + b(\boldsymbol{\theta})) \prod_j^n \frac{s(\boldsymbol{\theta}) f_s(m_j|\boldsymbol{\theta}) + b(\boldsymbol{\theta}) f_b(m_j|\boldsymbol{\theta})}{s(\boldsymbol{\theta}) + b(\boldsymbol{\theta})} \end{aligned} \tag{A.3}$$

In general the model can be written using the signal strenght modified μ as

$$\begin{aligned} L(\boldsymbol{m}|\mu, \boldsymbol{\theta}) &= \text{Pois}(n|\mu s(\boldsymbol{\theta}) + b(\boldsymbol{\theta})) \prod_j^n f_{\mu s+b}(m_j|\boldsymbol{\theta}) \\ &= \text{Pois}(n|\mu s(\boldsymbol{\theta}) + b(\boldsymbol{\theta})) \prod_j^n \frac{\mu s(\boldsymbol{\theta}) f_s(m_j|\boldsymbol{\theta}) + b(\boldsymbol{\theta}) f_b(m_j|\boldsymbol{\theta})}{\mu s(\boldsymbol{\theta}) + b(\boldsymbol{\theta})} \end{aligned} \tag{A.4}$$

Additional factors are added to the likelihood to constrain the nuisance parameters $p(\theta|\tilde{\theta})$ where $\tilde{\theta}$ is the default value of the nuisance parameter reflecting the degree of belief on what the true value of θ might be. Usually p is a Gaussian or a log-normal function.

$$\begin{aligned} L(\boldsymbol{m}|\mu, \boldsymbol{\theta}) &= \text{Pois}(n|\mu s(\boldsymbol{\theta}) + b(\boldsymbol{\theta})) \prod_j^n f_{\mu s+b}(m_j|\boldsymbol{\theta}) \times \prod_i p(\theta_i|\tilde{\theta}_i) \\ &= \text{Pois}(n|\mu s(\boldsymbol{\theta}) + b(\boldsymbol{\theta})) \prod_j^n \frac{\mu s(\boldsymbol{\theta}) f_s(m_j|\boldsymbol{\theta}) + b(\boldsymbol{\theta}) f_b(m_j|\boldsymbol{\theta})}{\mu s(\boldsymbol{\theta}) + b(\boldsymbol{\theta})} \times \prod_i p(\theta_i|\tilde{\theta}_i) \end{aligned} \tag{A.5}$$

Since the data $\boldsymbol{m}$ are fixed one can introduce a likelihood function where the data are fixed: $\mathcal{L}(\mu, \theta) = L(\boldsymbol{m}|\mu, \boldsymbol{\theta})$

In previous searches different statistic tests have been used. The choice for LHC was driven by the presence of large uncertainties. For a given Higgs boson mass hypothesis m_H, the test statistic used is based on the profile likelihood ratio:

$$q_0 = -2 \log \frac{\mathcal{L}(0, \hat{\theta}_0)}{\mathcal{L}(\hat{\mu}, \hat{\theta})} \quad \text{and } \hat{\mu} \geq 0, \tag{A.6}$$

where $\hat{\theta}_0$ is the value that optimize the likelihood fixing $\mu = 0$, $\hat{\mu}$ and $\hat{\theta}$ are the values optimizing the likelihood without any constrain. The constraint $\hat{\mu} \geq 0$ gives an accumulation of the test statistic at zero for events with downward fluctuations, since we are not interested in interpreting a deficit of events with respect to the expected background on an equal footing with an excess.

Following the frequentist convention for treatment of nuisance parameters we build the distribution $f(q_0|0, \hat{\theta}_0^{\text{obs}})$ by generating pseudo-data for nuisance parameters around

---

[1] an example of non-additive signal is the one for the search of neutrino oscillation

θ_0^{obs} and event counts following Poisson probabilities under the assumption of the background-only hypotheses or using asymptotic approximation. From such a distribution, one can evaluate the p-value corresponding to a given experimental observation q_0^{obs} as follows:

$$p_0 = P(q_0 \geq q_0^{\text{obs}}) = \int_{q_0^{\text{obs}}}^{\infty} f(q_0|0,\hat{\theta}_0^{\text{obs}})\,dq_0 \tag{A.7}$$

where q_0^{obs} and $\hat{\theta}_0^{\text{obs}}$ are computed using the observed data $\boldsymbol{m}^{\text{obs}}$. The procedure is repeated for every m_H.

A.2 Limit setting

The procedure to compute exclusion limits is based on the modified frequentist method, often referred to as CL$_s$ [125].

As to quantity an excess one has to construct the likelihood function $\mathcal{L}(\mu,\theta)$ where μ is the signal strength and θ represent the nuisance parameters as in equation (A.4).

Since one has to test every value of μ the test statistics depends on the tested μ:

$$\tilde{q}_\mu = -2\log\frac{\mathcal{L}(\mu,\hat{\theta}_\mu)}{\mathcal{L}(\hat{\mu},\hat{\theta})} \quad \text{with the requirement } 0 \leq \hat{\mu} \leq \mu \tag{A.8}$$

Here $\hat{\theta}_\mu$ refer to the conditional maximum-likelihood estimators of a given strength parameter, while $\hat{\mu}$ and $\hat{\theta}$ are the values optimizing the likelihood.

For every set of (μ, m_H) it is possible to compute $\tilde{q}_\mu^{\text{obs}}$ using the observed $\boldsymbol{m}^{\text{obs}}$. The exclusion is not quoted simply as p-value under the $s+b$ hypothesis (CL_{s+b} method):

$$p_\mu = CL_{s+b} = P(\tilde{q}_\mu \geq \tilde{q}_\mu^{\text{obs}}|\mu s+b) = \int_{q_\mu^{\text{obs}}}^{\infty} f(\tilde{q}_\mu|\mu,\hat{\boldsymbol{\theta}}_{\boldsymbol{\mu}}^{\text{obs}})\,dq_\mu, \tag{A.9}$$

but it is quoted in terms of CL_s:

$$CL_s = \frac{p_\mu}{1-p_b} \tag{A.10}$$

where

$$p_b = 1 - CL_b = P(\tilde{q}_\mu \leq \tilde{q}_\mu^{\text{obs}}|\mu = 0) \int_{-\infty}^{q_\mu^{\text{obs}}} f(\tilde{q}_\mu|\mu = 0,\hat{\boldsymbol{\theta}}_{\boldsymbol{0}}^{\text{obs}})\,dq_\mu, \tag{A.11}$$

If, for $\mu = 1$, $CL_s \leq 0.05$ the signal hypothesis is excluded with 95% CL_s confidence level (C.L.). It is usual to quote the $\mu^{95\%CL}$ adjusting μ until $CL_s = 0.05$.

The CL_s method is introduced to reduce the exclusion of region where the sensibility is very small. In particular the CL_{s+b} method (equation (A.9)) excludes regions where $p_\mu < 0.05$ also when the expected number of signal events is much less than that of background. In the modified approach, using the CL_s, the p-value is effectively penalized by dividing by $1-p_b$. If the two distributions $f(\tilde{q}_\mu|\mu = 0,\hat{\boldsymbol{\theta}}_{\boldsymbol{0}}^{\text{obs}})$ and $f(\tilde{q}_\mu|\mu,\hat{\boldsymbol{\theta}}_{\boldsymbol{\mu}}^{\text{obs}})$ are widely separated, then $1-p_b$ is only slightly less than unity, the penalty is slight, and thus exclusion based in CL_s is similar to that obtained from the usual p-value p_{s+b}. If, however, one has little sensitivity to the signal model, then the two distributions are close together, $1-p_b$ becomes small, and thus the p-value of $s+b$ is penalized (increased) more. In this way one is prevented from excluding signal models in cases of low sensitivity.

From the definition (A.10), one can see that CL_s is always greater than the p-value p_{s+b}. Thus the models excluded by requiring $CL_s < 0.05$ are a subset of those excluded by the usual criterion $p_{s+b} < 0.05$, and the upper limit from CL_s is therefore higher (weaker). In this sense the CL_s procedure is conservative.

A.3 Look Elsewhere effect

The Look Elsewhere effect is important in particular for the discovery when the signal model depends on a parameter (m_H for example). In fact the probability to find an excess is function of the range of the parameter. To solve the problem a factor (trial factor) is introduced to scale the p value of the maximum excess (the local p-value) to the global p-value taking into account the fact that a fluctuation could occur at any mass within the range.

When settings limit each hypothesis of mass and signal strength is in effect tested individually, and thus the look-elsewhere effect does not come into play.

For very small p-values, a procedure exists [130, 131]. Following these references, the p-value of the global test statistic can be written as follows:

$$p^{\text{global}} = P(q_0(\hat{m}_H) > u) \leq \langle N_u \rangle + \frac{1}{2} P_{\chi_1^2}(u) \tag{A.12}$$

where $\langle N_u \rangle$ is the average number of up-crossing of the likelihood ratio scan $q_0(m_H)$ at a level u chosen to correspond to a particular significance level.

Appendix B

Boosted decision tree

B.1 Decision tree

A decision tree (DT) [132] is a binary tree structured similar to the one sketched in Fig. B.1a. At every interior node of the tree a binary decision (yes/no) is taken usually comparing a variable with a constant when using continuous variable or looking if a particular value belongs to a set in the case of discrete variables. Modern decision trees are described statistically by Breiman et al. [133]. As many multivariate algorithms (MVA) methods decision trees are of two main types: classification tree is when the predicted outcome is the class to which the data belongs (usually signal or background); regression tree analysis is when the predicted outcome can be considered a real number. In case of regression trees, each output node represents a specific predicted value of the target variable.

The effect of the DT is to split the input space in rectangular partition as in Fig.B.1b using a series of rules to identify regions having the most homogeneous responses to the inputs. They are in this similar to rectangular cuts. However, whereas a cut-based analysis is able to select only one hypercube as region of phase space, the decision tree is able to split the phase space into a large number of hypercubes, each of which is identified as either “signal-like” or “background-like”, or attributed a constant (target) value in case of a regression tree, usually the mean of the target values of the items in the node.

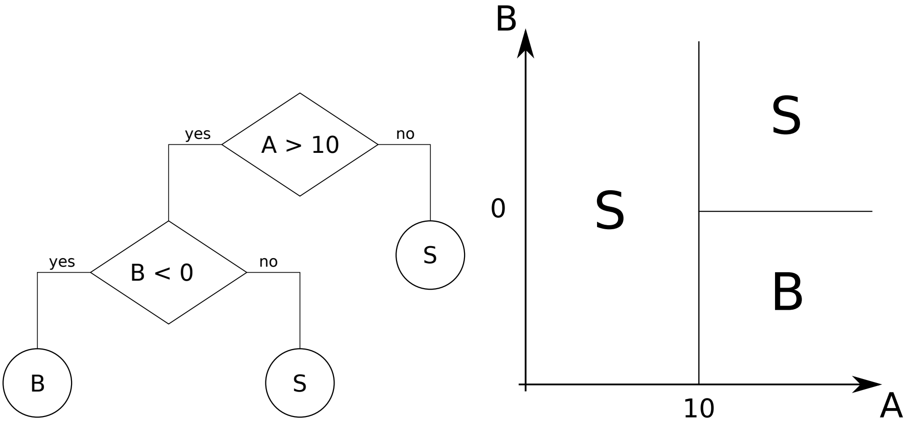

(a) decision tree **(b)** input space partitioning

Figure B.1: Example of a decision tree using only two variables

To find the best decision tree the algorithm recursively splits the data in two until a certain condition is reached. At every step it needs to choose the most powerful cut. The same variable may thus be used at several nodes, while others might not be used at all. Many criteria have been developed, some for separate signal to background, other for regression.

What follow is a brief description on how boosted decision tree (BDT) are trained as in the TMVA framework [93] used in this thesis.

B.2 Training

During the training the algorithm must grow the DT, in particular at every step it has to choose how to split the space. The growing starts with the root node where the space has not been partitioned at all. Then the algorithm splits the space in two ($A > 10$ in Fig. B.1). This procedure is repeated until the whole tree is built. At each node, the split is determined by finding the variable and the corresponding cut value that provides the best performance.

To choose the best variable and the best cut at every splitting step many criteria have been developed to discriminate between signal and background (separation criteria) as the Gini index, the cross entropy, the misclassification error, the statistical significance. For the regression problem the averaged squared error is used:

$$\frac{1}{N}\sum(y-\hat{y})^2 \tag{B.1}$$

where y is the regression target of each event in the node and $\hat{y}$ is its mean value over all events in the node. Since the splitting criterion is always a cut on a single variable, the training procedure selects the variable and cut value that minimize the error between the parent node and the sum of the error of the two daughter nodes, weighted by their relative fraction of events. The cut values are optimised by scanning over the variable range with specified granularity.

DT are unaffected by monotone transformations of the inputs, irrelevant inputs are seldom selected and trees are insensitive to outliers.

One common stopping condition to determine the end of the node splitting is when it has reached a minimum number of events. Another one is to choose the number of splitting. An effective strategy for fitting a single decision tree is to grow a large tree, then prune it by collapsing the weakest links identified through cross-validation.

B.3 Boosting

The motivation for the boosting algorithm is to design a procedure that combines many "weak" classifiers (e.g. decision trees) to achieve a powerful classifier (e.g. BDT). Boosting algorithms can be applied to any classifier. Tecnically a BDT is a machine learning algorithm that iteratively constructs an ensemble of weak decision tree learners through boosting. In boosting, models (e.g. decision trees) are fitted iteratively to the training data, using appropriate methods gradually to increase emphasis on observations modelled poorly by the existing collection of trees.

A shortcoming of decision trees is their instability with respect to statistical fluctuations in the training sample from which the tree structure is derived. For example, if two input variables exhibit similar separation power, a fluctuation in the training sample may cause the tree growing algorithm to decide to split on one variable, while the other variable could have been selected without that fluctuation. In such a case the whole tree structure is altered below this node, possibly resulting also in a substantially different classifier response.

This problem is overcome by constructing a forest of decision trees and classifying an event on a majority vote of the classifications done by each tree in the forest. All trees in the forest are derived from the same training sample, with the events being subsequently subjected to so-called boosting, a procedure which modifies their weights in the sample. Boosting increases the statistical stability of the classifier and typically also improves the separation performance compared to a single decision tree. However, the advantage of the straightforward interpretation of the decision tree is lost.

Boosting is a general way of enhancing the classification and regression performance of typically weak MVA methods by sequentially applying an MVA algorithm to reweighted (boosted) versions of the training data and then taking a weighted majority vote of the sequence of MVA algorithms thus produced. In general, for DT the boosting process uses the training results of the previous tree to increase the weights of candidates with bad results. A new tree is then trained using these weights.

Bibliography

[1] G. Aad et al. (ATLAS Collaboration). "Measurement of the inclusive isolated prompt photon cross section in pp collisions at $\sqrt{s} = 7$ TeV with the ATLAS detector". *Phys.Rev.* D83 (2011), p. 052005. DOI: 10.1103/PhysRevD.83.052005. arXiv: 1012.4389 [hep-ex] (cit. on p. vii).

[2] G. Aad et al. (ATLAS Collaboration). "Measurement of the inclusive isolated prompt photon cross-section in pp collisions at $\sqrt{s} = 7\,\text{TeV}$ using $35\,\text{pb}^{-1}$ of ATLAS data". *Phys.Lett.* B706 (2011), pp. 150–167. DOI: 10.1016/j.physletb.2011.11.010. arXiv: 1108.0253 [hep-ex] (cit. on p. vii).

[3] R. Turra. "Measurements of isolated prompt photons in pp collisions with the ATLAS detector". ATL-PHYS-PROC-2011-159. Geneva, Oct. 2011 (cit. on p. vii).

[4] G. Aad et al. (ATLAS Collaboration). "Measurement of the isolated di-photon cross-section in pp collisions at $\sqrt{s} = 7\,\text{TeV}$ with the ATLAS detector". *Phys.Rev.* D85 (2012), p. 012003. DOI: 10.1103/PhysRevD.85.012003. arXiv: 1107.0581 [hep-ex] (cit. on p. vii).

[5] ATLAS Collaboration. *Search for the Standard Model Higgs boson in the diphoton decay channel with* $4.9\,\text{fb}^{-1}$ *of ATLAS data at* $\sqrt{s} = 7\,\text{TeV}$. Tech. rep. ATLAS-CONF-2011-161. Geneva: CERN, Dec. 2011 (cit. on p. vii).

[6] G. Aad et al. (ATLAS Collaboration). "Search for the Standard Model Higgs boson in the diphoton decay channel with $4.9\,\text{fb}^{-1}$ of pp collisions at $\sqrt{s} = 7\,\text{TeV}$ with ATLAS". *Phys.Rev.Lett.* 108 (2012), p. 111803. DOI: 10.1103/PhysRevLett.108.111803. arXiv: 1202.1414 [hep-ex] (cit. on pp. vii, 141).

[7] ATLAS Collaboration. *Observation of an excess of events in the search for the Standard Model Higgs boson in the gamma-gamma channel with the ATLAS detector*. Tech. rep. ATLAS-CONF-2012-091. Geneva: CERN, July 2012 (cit. on p. vii).

[8] ATLAS Collaboration. *Observation and study of the Higgs boson candidate in the two photon decay channel with the ATLAS detector at the LHC*. Tech. rep. ATLAS-CONF-2012-168. Geneva: CERN, Dec. 2012 (cit. on pp. vii, 139, 164).

[9] R. Turra. "Search for the standard model higgs boson in the decay mode $H \to \gamma\gamma$ with ATLAS". Beyond the standard model in particle physics (July 15, 2012). ATL-PHYS-PROC-2012-289. Rencontres du Vietnam. Geneva, Nov. 2012 (cit. on p. vii).

[10] R. Turra. "Search for the Standard Model Higgs Boson in the Decay Mode $H \to \gamma\gamma$". Lecce: ATLAS Italia, Oct. 2012 (cit. on p. vii).

[11] R. Turra. "Search for the Standard Model Higgs Boson in the Decay Mode $H \to \gamma\gamma$ with ATLAS". Napoli: Società Italiana di Fisica (SIF), Sept. 2012 (cit. on p. vii).

[12] R. Turra. "Search for the Standard Model Higgs Boson in the Decay Mode $H \to \gamma\gamma$ with ATLAS". Beyond the standard model in particle physics (July 15, 2012). ATL-PHYS-SLIDE-2012-485. Quy Nhon (Vietnam), July 2012 (cit. on p. vii).

[13] S. Glashow. "Partial Symmetries of Weak Interactions". *Nucl.Phys.* 22 (1961), pp. 579–588. DOI: `10.1016/0029-5582(61)90469-2` (cit. on p. 1).

[14] S. Weinberg. "A Model of Leptons". *Phys. Rev. Lett.* 19 (21 Nov. 1967), pp. 1264–1266. DOI: `10.1103/PhysRevLett.19.1264` (cit. on p. 1).

[15] *Weak and Electromagnetic Interactions*. (May 19, 1968). Vol. C680519. Eighth Nobel symposium. Lerum, Sweden, 1968, pp. 367–377 (cit. on p. 1).

[16] G. 't Hooft and M. Veltman. "Regularization and Renormalization of Gauge Fields". *Nucl.Phys.* B44 (1972), pp. 189–213. DOI: `10.1016/0550-3213(72)90279-9` (cit. on p. 1).

[17] F. Mandl and G. G. Shaw. *Quantum field theory; 2nd ed.* New York, NY: Wiley, 2010 (cit. on p. 1).

[18] M. E. Peskin and D. V. Schroeder. *An Introduction to Quantum Field Theory; 1995 ed.* Boulder, CO: Westview, 1995 (cit. on pp. 1, 8).

[19] A. Pich. "The Standard model of electroweak interactions" (2007). arXiv: `0705.4264 [hep-ph]` (cit. on p. 1).

[20] A. Djouadi. "The Anatomy of electro-weak symmetry breaking. I: The Higgs boson in the standard model". *Phys.Rept.* 457 (2008), pp. 1–216. DOI: `10.1016/j.physrep.2007.10.004`. arXiv: `hep-ph/0503172 [hep-ph]` (cit. on pp. 1, 8, 9).

[21] F. Englert and R. Brout. "Broken Symmetry and the Mass of Gauge Vector Mesons". *Phys.Rev.Lett.* 13 (1964), pp. 321–323. DOI: `10.1103/PhysRevLett.13.321` (cit. on p. 5).

[22] P. W. Higgs. "Broken symmetries, massless particles and gauge fields". *Phys.Lett.* 12 (1964), pp. 132–133. DOI: `10.1016/0031-9163(64)91136-9` (cit. on p. 5).

[23] G. Guralnik, C. Hagen, and T. Kibble. "Global Conservation Laws and Massless Particles". *Phys.Rev.Lett.* 13 (1964), pp. 585–587. DOI: `10.1103/PhysRevLett.13.585` (cit. on p. 5).

[24] *The LEP Electroweak Working Group*. URL: `http://lepewwg.web.cern.ch/LEPEWWG/` (visited on 2013) (cit. on pp. 7, 8, 12).

[25] C. Amsler et al. "Review of particle physics". *Phys. Lett.* B667 (2008), p. 1. DOI: `10.1016/j.physletb.2008.07.018` (cit. on pp. 7, 8).

[26] J. Alcaraz. "Precision Electroweak Measurements and Constraints on the Standard Model" (2009). arXiv: `0911.2604 [hep-ex]` (cit. on p. 8).

[27] *A Generic Fitter Project for HEP Model Testing*. URL: `http://project-gfitter.web.cern.ch` (visited on 2013) (cit. on pp. 8, 12).

[28] C. press office. *CERN experiments observe particle consistent with long-sought Higgs boson*. 2012. URL: `http://press.web.cern.ch/press-releases/2012/07/cern-experiments-observe-particle-consistent-long-sought-higgs-boson` (cit. on pp. 8, 27).

[29] S. Chatrchyan et al. (CMS Collaboration). "Observation of a new boson at a mass of 125 GeV with the CMS experiment at the LHC". *Phys.Lett.* B716 (2012), pp. 30–61. DOI: `10.1016/j.physletb.2012.08.021`. arXiv: `1207.7235 [hep-ex]` (cit. on pp. 8, 19, 139).

[30] G. Aad et al. (ATLAS Collaboration). "Observation of a new particle in the search for the Standard Model Higgs boson with the ATLAS detector at the LHC". *Phys.Lett.* B716 (2012), pp. 1–29. DOI: `10.1016/j.physletb.2012.08.020`. arXiv: `1207.7214 [hep-ex]` (cit. on pp. 8, 19, 20, 139, 164).

[31] R. Barate et al. "Search for the standard model Higgs boson at LEP". *Phys. Lett.* B565 (2003), pp. 61–75. DOI: `10.1016/S0370-2693(03)00614-2`. arXiv: `0306033 [hep-ex]` (cit. on pp. 9, 10).

[32] C. Group et al. "Updated Combination of CDF and D0 Searches for Standard Model Higgs Boson Production with up to 10.0 fb^{-1} of Data" (2012). arXiv: `1207.0449 [hep-ex]` (cit. on pp. 11–13).

[33] M. Baak et al. "The Electroweak Fit of the Standard Model after the Discovery of a New Boson at the LHC". *Eur.Phys.J.* C72 (2012), p. 2205. DOI: `10.1140/epjc/s10052-012-2205-9`. arXiv: `1209.2716 [hep-ph]` (cit. on pp. 12, 14).

[34] LHC Higgs Cross Section Working Group et al. "Handbook of LHC Higgs Cross Sections: 2. Differential Distributions". *CERN-2012-002* (CERN, Geneva, 2012). arXiv: `1201.3084 [hep-ph]` (cit. on pp. 15, 16, 18).

[35] M. Spira et al. "Higgs boson production at the LHC". *Nucl.Phys.* B453 (1995), pp. 17–82. DOI: `10.1016/0550-3213(95)00379-7`. arXiv: `hep-ph/9504378 [hep-ph]` (cit. on pp. 16, 149).

[36] A. Djouadi. "The Higgs in the Standard Model: status and expectations". CERN Theoretical Seminar. Apr. 2010. URL: `http://indico.cern.ch/conferenceDisplay.py?confId=92290` (cit. on p. 16).

[37] "Inauguration workshop of the LHC Higgs Cross Section Working Group". Freiburg, Apr. 2010. URL: `http://james.physik.uni-freiburg.de/~warsinsk/xsfrhiggs/` (cit. on p. 18).

[38] G. Aad et al. (ATLAS Collaboration). "Higgs Boson" (2009), pp. 1197–1511. arXiv: `0901.0512 [hep-ex]` (cit. on pp. 19, 22).

[39] G. L. Bayatian et al. "CMS technical design report, volume II: Physics performance". *J. Phys.* G34 (2007), pp. 995–1579. DOI: `10.1088/0954-3899/34/6/S01` (cit. on pp. 19, 24).

[40] ATLAS Collaboration. *Search for the Standard Model Higgs boson in produced in association with a vector boson and decaying to bottom quarks with the ATLAS detector*. Tech. rep. ATLAS-CONF-2012-161. Geneva: CERN, Nov. 2012 (cit. on p. 19).

[41] G. Aad et al. (ATLAS Collaboration). "Search for the Standard Model Higgs Boson via Vector Boson Fusion Production Process in the Di-Tau Channels" (2009), pp. 1271 –1305. arXiv: `0901.0512 [hep-ex]` (cit. on p. 21).

[42] A. Elagin et al. "A New Mass Reconstruction Technique for Resonances Decaying to di-tau". *Nucl.Instrum.Meth.* A654 (2011), pp. 481–489. DOI: `10.1016/j.nima.2011.07.009`. arXiv: `1012.4686 [hep-ex]` (cit. on p. 21).

[43] R. Ellis et al. "Higgs decay to $\pi^+\pi^-$: A possible signature of intermediate mass Higgs bosons at high energy hadron colliders". *Nuclear Physics B* 297.2 (1988), pp. 221 –243. ISSN: 0550-3213. DOI: `10.1016/0550-3213(88)90019-3` (cit. on p. 21).

[44] ATLAS Collaboration. *Search for the Standard Model Higgs boson in $H \to \tau\tau$ decays in proton-proton collisions with the ATLAS detector*. Tech. rep. ATLAS-CONF-2012-160. Geneva: CERN, Nov. 2012 (cit. on p. 21).

[45] ATLAS Collaboration. *Search for the Higgs boson in the $H \to WW \to l\nu jj$ decay channel using* 4.7 fb^{-1} *of pp collisions at* $\sqrt{s} = 7$ TeV *with the ATLAS detector*. Tech. rep. ATLAS-CONF-2012-018. Geneva: CERN, Mar. 2012 (cit. on p. 22).

[46] ATLAS Collaboration. *Update of the $H \to WW^{(*)} \to e\nu\mu\nu$ Analysis with* 13 fb^{-1} *of* $\sqrt{s} = 8$ TeV *Data Collected with the ATLAS Detector*. Tech. rep. ATLAS-CONF-2012-158. Geneva: CERN, Nov. 2012 (cit. on p. 22).

[47] M. Vesterinen and T. Wyatt. "A Novel Technique for Studying the Z Boson Transverse Momentum Distribution at Hadron Colliders". *Nucl.Instrum.Meth.* A602 (2009), pp. 432–437. DOI: `10.1016/j.nima.2009.01.203`. arXiv: `0807.4956 [hep-ex]` (cit. on p. 22).

[48] ATLAS Collaboration. "Search for a Standard Model Higgs in the $H \to ZZ \to ll\nu\nu$ decay channel with 4.7 fb^{-1} with the ATLAS detector". ATLAS-CONF-2012-016 (Mar. 2012) (cit. on p. 22).

[49] ATLAS Collaboration. *Study of the channel $H \to Z^*Z \to \ell^+\ell^- q\bar{q}$ in the mass range 120-180 GeV with the ATLAS Detector at* $\sqrt{s} = 7$ TeV. Tech. rep. ATLAS-CONF-2012-163. Geneva: CERN, Nov. 2012 (cit. on p. 22).

[50] ATLAS Collaboration. *Search for a Standard Model Higgs in the mass range 200-600 GeV in the channel $H \to ZZ \to llqq$ with with the ATLAS detector*. Tech. rep. ATLAS-CONF-2012-017. Geneva: CERN, Mar. 2012 (cit. on p. 22).

[51] ATLAS Collaboration. *Observation of an excess of events in the search for the Standard Model Higgs boson in the $H \to ZZ^{(*)} \to 4l$ channel with the ATLAS detector*. Tech. rep. ATLAS-CONF-2012-169. Geneva: CERN, Dec. 2012 (cit. on p. 22).

[52] G. Aad et al. (ATLAS Collaboration). *Expected Performance of the ATLAS Experiment - Detector, Trigger and Physics*. 2009. arXiv: `0901.0512 [hep-ex]` (cit. on pp. 24, 48, 49, 55).

[53] G. Aad et al. (ATLAS Collaboration). "Sensitivity to an Invisibly Decaying Higgs Boson" (2009), pp. 1419 –1450. arXiv: `0901.0512 [hep-ex]` (cit. on p. 24).

[54] L. Evans and P. Bryant. "LHC Machine". *JINST* 3 (2008), S08001 (cit. on p. 25).

[55] J. D. Jackson. "Classical Electrodynamics". first. Wiley, 1962. Chap. 14, p. 475 (cit. on p. 26).

[56] M Bajko et al. *Report of the Task Force on the Incident of 19th September 2008 at the LHC*. Tech. rep. LHC-PROJECT-Report-1168. CERN-LHC-PROJECT-Report-1168. Geneva: CERN, Mar. 2009 (cit. on p. 28).

[57] C. Amsler et al. "Kinematics". *Phys. Lett.* B667 (2008), pp. 321 –324. DOI: `10.1016/j.physletb.2008.07.018` (cit. on p. 33).

[58] G. Aad et al. (ATLAS Collaboration). "The ATLAS Experiment at the CERN Large Hadron Collider". *JINST* 3 (2008), S08003. DOI: `10.1088/1748-0221/3/08/S08003` (cit. on pp. 33, 40, 55, 61, 62).

[59] J.-F. Arguin, M Elsing, and B Heinemann. *ATLAS Tracking Performance in the Presence of Pile-up*. Tech. rep. ATL-INDET-INT-2010-001. Geneva: CERN, Feb. 2010 (cit. on p. 37).

[60] *ATLAS: Detector and physics performance technical design report*. Vol. 1. CERN-LHCC-99-14, 1999 (cit. on pp. 41, 55).

[61] *ATLAS liquid-argon calorimeter: Technical Design Report*. Geneva: CERN, 1996. ISBN: 9789290830900 (cit. on p. 44).

[62] ATLAS Collaboration. *A Search for High Mass Diphoton Resonances in the Context of the Randall-Sundrum Model in* $\sqrt{s} = 7\,\text{TeV}$ *pp Collisions*. Tech. rep. ATLAS-CONF-2011-044. Geneva: CERN, Mar. 2011 (cit. on p. 46).

[63] G. Aad et al. (ATLAS Collaboration). "Search for Extra Dimensions in diphoton events using proton-proton collisions recorded at $\sqrt{s} = 7\,\text{TeV}$ with the ATLAS detector at the LHC" (2012). arXiv: `1210.8389 [hep-ex]` (cit. on p. 46).

[64] G. Aad et al. (ATLAS Collaboration). "Search for extra dimensions using diphoton events in 7 TeV proton–proton collisions with the ATLAS detector". *Physics Letters B* 710.4–5 (2012), pp. 538 –556. ISSN: 0370-2693. DOI: `10.1016/j.physletb.2012.03.022` (cit. on p. 46).

[65] G. Aad et al. (ATLAS Collaboration). "Search for Dark Matter Candidates and Large Extra Dimensions in Events with a Photon and Missing Transverse Momentum in *pp* Collision Data at $\sqrt{s} = 7\,\text{TeV}$ with the ATLAS Detector". *Phys. Rev. Lett.* 110 (1 Jan. 2013), p. 011802. DOI: `10.1103/PhysRevLett.110.011802` (cit. on p. 46).

[66] Y.-S. Tsai. "Pair production and bremsstrahlung of charged leptons". *Rev. Mod. Phys.* 46 (4 Oct. 1974), pp. 815–851. DOI: `10.1103/RevModPhys.46.815` (cit. on p. 46).

[67] S. R. Klein. "Pair production from 10 GeV to 10 ZeV". *Radiation Physics and Chemistry* 75.6 (2006). Pair Production, pp. 696 –711. ISSN: 0969-806X. DOI: `10.1016/j.radphyschem.2005.09.005` (cit. on p. 47).

[68] D Varouchas and D Rousseau. "Study of the Higgs boson discovery potential, produced by the vector boson fusion with the ATLAS detector and commissioning of calorimetric transverse missing energy". PhD thesis. Orsay, France, Universite Paris 11, 2009 (cit. on p. 47).

[69] W Lampl et al. *Calorimeter Clustering Algorithms: Description and Performance*. Tech. rep. ATL-LARG-PUB-2008-002. ATL-COM-LARG-2008-003. Geneva: CERN, Apr. 2008 (cit. on pp. 47, 48, 53).

[70] Wikipedia. *Probability integral transform — Wikipedia, The Free Encyclopedia*. 2012. URL: `http://en.wikipedia.org/wiki/Probability_integral_transform` (cit. on p. 52).

[71] Wikipedia. *Inverse transform sampling — Wikipedia, The Free Encyclopedia*. 2012. URL: `http://en.wikipedia.org/wiki/Inverse_transform_sampling` (cit. on p. 52).

[72] G. Aad et al. (ATLAS Collaboration). "Measurement of the inclusive isolated prompt photon cross-section in pp collisions at using of ATLAS data". *Physics Letters B* 706.2-3 (2011), pp. 150 –167. ISSN: 0370-2693. DOI: `10.1016/j.physletb.2011.11.010` (cit. on p. 52).

[73] G. Aad et al. (ATLAS Collaboration). "Measurement of isolated-photon pair production in pp collisions at $\sqrt{s} = 7\,\text{TeV}$ with the ATLAS detector" (2012). arXiv: 1211.1913 [hep-ex] (cit. on p. 52).

[74] D. Green. *At the Leading Edge. The Atlas and Cms Lhc Experiments*. World Scientific Pub Co Inc, Dec. 2009. ISBN: 9814304670 (cit. on p. 52).

[75] M. Cacciari, G. P. Salam, and G. Soyez. "The Catchment Area of Jets". *JHEP* 0804 (2008), p. 005. DOI: 10.1088/1126-6708/2008/04/005. arXiv: 0802.1188 [hep-ph] (cit. on p. 53).

[76] M. Cacciari, G. Salam, and S. Sapeta. "On the characterisation of the underlying event". *Journal of High Energy Physics* 2010 (4 2010), pp. 1–42. DOI: 10.1007/JHEP04(2010)065 (cit. on p. 53).

[77] S. D. Ellis and D. E. Soper. "Successive combination jet algorithm for hadron collisions". *Phys. Rev. D* 48 (7 Oct. 1993), pp. 3160–3166. DOI: 10.1103/PhysRevD.48.3160 (cit. on p. 53).

[78] S. Catani et al. "Longitudinally invariant K_t clustering algorithms for hadron hadron collisions". *Nucl.Phys.* B406 (1993), pp. 187–224. DOI: 10.1016/0550-3213(93)90166-M (cit. on p. 53).

[79] *ATLAS muon spectrometer: Technical Design Report*. Geneva: CERN, 1997 (cit. on p. 55).

[80] *The ATLAS Computing Technical Design Report*. CERN-LHCC/2005-022, 2005 (cit. on pp. 63, 65).

[81] *ROOT - An Object Oriented Data Analysis Framework*. URL: http://root.cern.ch (visited on 2013) (cit. on p. 65).

[82] *The Physics Analysis Tools project for the ATLAS experiment*. Proceedings of the ICCMSE Symposium: Computing in Experimental High Energy Physics, to appear. ICCMSE Symposium. 2010 (cit. on p. 65).

[83] S. Agostinelli and al. "Geant4: a simulation toolkit". *Nuclear Instruments and Methods in Physics Research Section A: Accelerators, Spectrometers, Detectors and Associated Equipment* 506.3 (2003), pp. 250 –303. ISSN: 0168-9002. DOI: 10.1016/S0168-9002(03)01368-8. URL: http://www.sciencedirect.com/science/article/pii/S0168900203013688 (cit. on pp. 65, 149).

[84] *ATLAS computing workbook*. URL: https://twiki.cern.ch/twiki/bin/view/Atlas/WorkBook (cit. on p. 66).

[85] *PROOF - Parallel ROOT Facility*. URL: http://root.cern.ch/drupal/content/proof (cit. on p. 66).

[86] *GPFS - General Parallel File System*. URL: http://www-03.ibm.com/systems/software/gpfs/ (cit. on p. 66).

[87] M. Aharrouche et al. "Measurement of the response of the ATLAS liquid argon barrel calorimeter to electrons at the 2004 combined test-beam". *Nucl.Instrum.Meth.* A614.3 (2010), pp. 400–432. DOI: 10.1016/j.nima.2009.12.055 (cit. on p. 69).

[88] L. Courneyea et al. *Computation and validation of the electronic calibration constants for the ATLAS Liquid Argon Calorimeters*. Tech. rep. ATL-LARG-INT-2010-007. Geneva: CERN, July 2010 (cit. on p. 69).

[89] G. Aad et al. (ATLAS Collaboration). "Electron performance measurements with the ATLAS detector using the 2010 LHC proton-proton collision data". *Eur.Phys.J.* C72 (2012), p. 1909. DOI: `10.1140/epjc/s10052-012-1909-1`. arXiv: `1110.3174 [hep-ex]` (cit. on p. 69).

[90] M. Agustoni et al. *Electromagnetic energy scale in-situ calibration and performance: Supporting document for the egamma performance paper*. Tech. rep. ATL-COM-PHYS-2011-263. Geneva: CERN, Mar. 2011 (cit. on p. 69).

[91] Y. Benjamini. "Opening the Box of a Boxplot". English. *The American Statistician* 42.4 (1988), pp. 257–262. ISSN: 00031305. URL: `http://www.jstor.org/stable/2685133` (cit. on p. 72).

[92] G. Aad et al. (ATLAS Collaboration). "Performance of Missing Transverse Momentum Reconstruction in Proton-Proton Collisions at 7 TeV with ATLAS". *Eur.Phys.J.* C72 (2012), p. 1844. DOI: `10.1140/epjc/s10052-011-1844-6`. arXiv: `1108.5602 [hep-ex]` (cit. on p. 75).

[93] A. Hoecker et al. "TMVA: Toolkit for Multivariate Data Analysis". *PoS* ACAT (2007), p. 040. arXiv: `physics/0703039`. URL: `http://tmva.sourceforge.net/` (cit. on pp. 107, 176).

[94] W Lampl et al. *Calorimeter Clustering Algorithms: Description and Performance*. Tech. rep. ATL-LARG-PUB-2008-002. ATL-COM-LARG-2008-003. Geneva: CERN, Apr. 2008 (cit. on p. 141).

[95] M. Cacciari, G. P. Salam, and G. Soyez. "The Anti-k(t) jet clustering algorithm". *JHEP* 0804 (2008), p. 063. DOI: `10.1088/1126-6708/2008/04/063`. arXiv: `0802.1189 [hep-ph]` (cit. on p. 147).

[96] P. Nason. "A New method for combining NLO QCD with shower Monte Carlo algorithms". *JHEP* 0411 (2004), p. 040 (cit. on p. 149).

[97] T. Sjostrand et al. "High-energy-physics event generation with PYTHIA 6.1". *Comput. Phys. Commun.* 135 (2001), pp. 238–259. DOI: `10.1088/1126-6708/2006/05/026`. eprint: `0010017` (hep-ph) (cit. on pp. 149, 154).

[98] A. Djouadi, J. Kalinowski, and M. Spira. "HDECAY: A Program for Higgs boson decays in the Standard Model and its supersymmetric extension". *Comput. Phys. Commun.* 108 (1998), pp. 56–74. DOI: `10.1016/S0010-4655(97)00123-9`. arXiv: `hep-ph/9704448 [hep-ph]` (cit. on p. 149).

[99] R. V. Harlander and W. B. Kilgore. "Next-to-next-to-leading order Higgs production at hadron colliders". *Phys. Rev. Lett.* 88 (2002), p. 201801. DOI: `10.1103/PhysRevLett.88.201801`. arXiv: `hep-ph/0201206 [hep-ph]` (cit. on p. 149).

[100] C. Anastasiou and K. Melnikov. "Higgs boson production at hadron colliders in NNLO QCD". *Nucl. Phys.* B646 (2002), pp. 220–256. DOI: `10.1016/S0550-3213(02)00837-4`. arXiv: `hep-ph/0207004 [hep-ph]` (cit. on p. 149).

[101] V. Ravindran, J. Smith, and W. L. van Neerven. "NNLO corrections to the total cross-section for Higgs boson production in hadron hadron collisions". *Nucl.Phys.* B665 (2003), pp. 325–366. DOI: `10.1016/S0550-3213(03)00457-7`. arXiv: `hep-ph/0302135 [hep-ph]` (cit. on p. 149).

[102] M. Ciccolini, A. Denner, and S. Dittmaier. "Strong and electroweak corrections to the production of Higgs + 2jets via weak interactions at the LHC". *Phys.Rev.Lett.* 99 (2007), p. 161803. DOI: `10.1103/PhysRevLett.99.161803`. arXiv: `0707.0381 [hep-ph]` (cit. on p. 149).

[103] M. Ciccolini, A. Denner, and S. Dittmaier. "Electroweak and QCD corrections to Higgs production via vector-boson fusion at the LHC". *Phys.Rev.* D77 (2008), p. 013002. DOI: `10.1103/PhysRevD.77.013002`. arXiv: `0710.4749 [hep-ph]` (cit. on p. 149).

[104] K. Arnold et al. "VBFNLO: A Parton level Monte Carlo for processes with electroweak bosons". *Comput.Phys.Commun.* 180 (2009), pp. 1661–1670. DOI: `10.1016/j.cpc.2009.03.006`. arXiv: `0811.4559 [hep-ph]` (cit. on p. 149).

[105] P. Bolzoni et al. "Higgs production via vector-boson fusion at NNLO in QCD". *Phys.Rev.Lett.* 105 (2010), p. 011801. DOI: `10.1103/PhysRevLett.105.011801`. arXiv: `1003.4451 [hep-ph]` (cit. on p. 149).

[106] T. Han and S. Willenbrock. "QCD correction to the $pp \to WH$ and ZH total cross-sections". *Phys. Lett.* B273 (1991), pp. 167–172. DOI: `10.1016/0370-2693(91)90572-8` (cit. on p. 149).

[107] O. Brein, A. Djouadi, and R. Harlander. "NNLO QCD corrections to the Higgs-strahlung processes at hadron colliders". *Phys. Lett.* B579 (2004), pp. 149–156. DOI: `10.1016/j.physletb.2003.10.112`. arXiv: `hep-ph/0307206 [hep-ph]` (cit. on p. 149).

[108] M. Ciccolini, S. Dittmaier, and M. Krämer. "Electroweak radiative corrections to associated WH and ZH production at hadron colliders". *Phys. Rev.* D68 (2003), p. 073003. DOI: `10.1103/PhysRevD.68.073003`. arXiv: `hep-ph/0306234 [hep-ph]` (cit. on p. 149).

[109] W. Beenakker et al. "Higgs radiation off top quarks at the Tevatron and the LHC". *Phys. Rev. Lett.* 87 (2001), p. 201805. DOI: `10.1103/PhysRevLett.87.201805`. arXiv: `hep-ph/0107081 [hep-ph]` (cit. on p. 149).

[110] W. Beenakker et al. "NLO QCD corrections to $t\bar{t}H$ production in hadron collisions". *Nucl. Phys.* B653 (2003), pp. 151–203. DOI: `10.1016/S0550-3213(03)00044-0`. arXiv: `hep-ph/0211352 [hep-ph]` (cit. on p. 149).

[111] S. Dawson et al. "Next-to-leading order QCD corrections to $pp \to t\bar{t}h$ at the CERN Large Hadron Collider". *Phys. Rev.* D67 (2003), p. 071503. DOI: `10.1103/PhysRevD.67.071503`. arXiv: `hep-ph/0211438 [hep-ph]` (cit. on p. 149).

[112] S. Dawson et al. "Associated Higgs production with top quarks at the large hadron collider: NLO QCD corrections". *Phys. Rev.* D68 (2003), p. 034022. DOI: `10.1103/PhysRevD.68.034022`. arXiv: `hep-ph/0305087 [hep-ph]` (cit. on p. 149).

[113] M. Botje et al. "The PDF4LHC working group interim recommendations" (2011). arXiv: `1101.0538 [hep-ph]` (cit. on p. 149).

[114] H.-L. Lai et al. "New parton distributions for collider physics". *Phys. Rev.* D82 (2010), p. 074024. DOI: `10.1103/PhysRevD.82.074024`. arXiv: `1007.2241 [hep-ph]` (cit. on p. 149).

[115] A. Martin et al. "Parton distributions for the LHC". *Eur. Phys. J.* C63 (2009), pp. 189–285. DOI: `10.1140/epjc/s10052-009-1072-5`. arXiv: `0901.0002 [hep-ph]` (cit. on p. 149).

[116] R. D. Ball et al. "Impact of heavy quark masses on parton distributions and LHC phenomenology". *Nucl. Phys.* B849 (2011), pp. 296–363. DOI: `10.1016/j.nuclphysb.2011.03.021`. arXiv: `1101.1300 [hep-ph]` (cit. on p. 149).

[117] S. Actis et al. "NNLO computational techniques: The cases $H \to \gamma\gamma$ and $H \to gg$". *Nucl. Phys.* B811 (2009), pp. 182–273. DOI: `10.1016/j.nuclphysb.2008.11.024`. arXiv: `0809.3667 [hep-ph]` (cit. on p. 149).

[118] A. Denner et al. "Standard Model Higgs-boson branching ratios with uncertainties". *Eur. Phys. J.* C71 (2011), p. 1753. DOI: `10.1140/epjc/s10052-011-1753-8`. arXiv: `1107.5909 [hep-ph]` (cit. on p. 149).

[119] LHC Higgs Cross Section Working Group et al. "Handbook of LHC Higgs Cross Sections: 1. Inclusive Observables". *CERN-2011-002* (CERN, Geneva, 2011). arXiv: `1101.0593 [hep-ph]` (cit. on p. 149).

[120] LHC Higgs Cross Section Working Group et al. "Handbook of LHC Higgs Cross Sections: 2. Differential Distributions". *CERN-2012-002* (CERN, Geneva, 2012). arXiv: `1201.3084 [hep-ph]` (cit. on p. 149).

[121] S. Bernstein. "Démonstration du théorème de Weierstrass fondée sur le calcul des probabilities." *Comm. Soc. Math. Kharkov* 13 (1912), pp. 1–2 (cit. on p. 154).

[122] C. Balazs et al. "Calculation of prompt diphoton production cross-sections at Tevatron and LHC energies". *Phys.Rev.* D76 (2007), p. 013009. DOI: `10.1103/PhysRevD.76.013009`. arXiv: `0704.0001 [hep-ph]` (cit. on p. 154).

[123] T. Binoth et al. "A Full next-to-leading order study of direct photon pair production in hadronic collisions". *Eur.Phys.J.* C16 (2000), pp. 311–330. DOI: `10.1007/s100520050024`. arXiv: `hep-ph/9911340 [hep-ph]` (cit. on p. 154).

[124] T. Gleisberg et al. "Event generation with SHERPA 1.1". *JHEP* 0902 (2009), p. 007. DOI: `10.1088/1126-6708/2009/02/007`. arXiv: `0811.4622 [hep-ph]` (cit. on p. 154).

[125] A. L. Read. "Presentation of search results: the CL s technique". *J.Phys.* G28.10 (2002), pp. 2693–2704. DOI: `10.1088/0954-3899/28/10/313` (cit. on pp. 163, 173).

[126] G. Cowan et al. "Asymptotic formulae for likelihood-based tests of new physics". English. *The European Physical Journal C* 71 (2 2011), pp. 1–19. ISSN: 1434-6044. DOI: `10.1140/epjc/s10052-011-1554-0` (cit. on p. 164).

[127] L. D. Landau. "On the angular momentum of a two-photon system". *Dokl.Akad.Nauk Ser.Fiz.* 60 (1948), pp. 207–209 (cit. on p. 166).

[128] C. N. Yang. "Selection Rules for the Dematerialization of a Particle into Two Photons". *Phys. Rev.* 77 (2 Jan. 1950), pp. 242–245. DOI: `10.1103/PhysRev.77.242` (cit. on p. 166).

[129] J. C. Collins and D. E. Soper. "Angular distribution of dileptons in high-energy hadron collisions". *Phys. Rev. D* 16 (7 1977). DOI: `10.1103/PhysRevD.16.2219` (cit. on p. 166).

[130] E. Gross and O. Vitells. "Trial factors or the look elsewhere effect in high energy physics". *Eur.Phys.J.* C70 (1-2 2010), pp. 525–530. ISSN: 1434-6044. DOI: `10.1140/epjc/s10052-010-1470-8`. arXiv: `1005.1891 [physics.data-an]` (cit. on p. 174).

[131] R. B. Davies. "Hypothesis testing when a nuisance parameter is present only under the alternative". *Biometrika* 74.1 (1987), pp. 33–43. DOI: `10.1093/biomet/74.1.33` (cit. on p. 174).

[132] J. Quinlan. "Simplifying decision trees". *International journal of man-machine studies* 27.3 (1987), pp. 221–234 (cit. on p. 175).

[133] L. Breiman, J. Friedman, and R. Olshen. *Classification and regression trees*. Chapman & Hall, New York, NY, 1984. ISBN: 0-412-04841-9 (cit. on p. 175).

Acknowledgements

First of all I must thank my supervisors, Chiara Meroni and Marcello Fanti. Thank you, Chiara, for your advices, for your support and for the trust you put in me. Thank you, Marcello, for all the help during these years, for all your very detailed explanations and interesting discussions from which a lot of ideas have come out. Thanks to my external referee, Daniel Fournier, for all the interest he showed to my work about the energy calibration of "his" calorimeter. In addition thanks to Chiara and Francesco to give me the opportunity to spend one year (and more) at CERN.

Special thanks to Leonardo for all the time dedicated to my work about the calibration and to offer me what he calls "opportunities": often they are, sometimes it is only a nice way to give me additional tasks. Thanks Luciano for the interest you demonstrate about my progress. Even if I have never worked with them, I want to thank Donatella for all her support and Attilio for his prompt answers to my random questions about the inner detector.

Many thanks to all the colleagues I have met at CERN, Guillaume for his wide expertise and willingness, the e/gamma conveners, Fabrice, Andrea and Marco, Maarten, Giovanni, Iro, Narei and all the people from the HSG1 group. A very special thank to Bruno, for all his help, without him an important part of this thesis would not have been possibile. I thank all the people from the LAr operational group, starting from Francesco, who seems to be the only one who can solve some kind of problems, Valerio, who taught me the right way to deal with electronics when it is not working, Isabelle (I've never thank you for the cheese), Luis, Hass and all the people in the satellite control room. I want to thank my very first student, Ladislav, for being much better than I would have ever imagined.

Of course I have to thank my friends at CERN for all the happy moments we have had together, I hope we can have many more. First of all my flatmate, Federico, without him probably I would have died of hunger, Rosa who forced me to write these acknowledgements, Andrea for all the funny moments (and yes, to remember me all the bureaucratic deadlines about the PhD), Roberta (I did not get dengue fever), Damiana, Umberto, Sofia, Simone and Luca.

Thanks to my family, my friends in Italy and to my girlfriend, Alessandra, she tried to read my thesis, but it is "too boring".

Finally I have to thank all the people who designed, developed, build this amazing machine and gave us the opportunity to get such historic achievement.